

**LIGHTWEIGHT COMPOSITE STRUCTURE
FOR SOLAR CENTRAL RECEIVER
HELIOSTATS**

Sulaiman Omer Fadlallah

A thesis submitted to

Auckland University of Technology

in fulfilment of the requirements for the degree of

Doctor of Philosophy (PhD)

2020

School of Engineering, Computer and Mathematical Sciences

ABSTRACT

Of all Concentrating Solar Power (CSP) technologies available today, central tower CSP systems are moving to the forefront as they have the capability to become the technology of choice for the generation of renewable electricity. The potential of central tower systems to achieve high temperatures offers a path to higher efficiencies, thereby providing an inherent advantage versus the other CSP systems. Achieving these high temperatures requires a large number of heliostats, and therefore the heliostats are considered the most crucial cost element of central tower CSP systems amounting up to 50% of a plant's total cost. To address this issue and in order for the cost of energy from central tower plants to be competitive with that of other energy systems, there is a need for innovative heliostat designs that can reduce the heliostats' cost without affecting its performance. One way of reducing this cost is by utilizing lightweight honeycomb sandwich composites in the heliostat structure, reducing the size of the drive units and their energy consumption. However, one of the challenges faced in implementing such systems is ensuring that they are able to cope with the aerodynamic forces imposed upon them during operation.

Despite the progress in heliostat development, a comprehensive review of literature revealed a lack of work undertaken on investigating the suitability of honeycomb sandwich composites for use as a heliostat mirror structure. This gap indicated a need to deliver a better understanding on the interaction between the wind and honeycomb sandwich composites employed as a heliostat mirror support structure by investigating their aero-structural robustness and behaviour characteristics.

The research first studied the flow behaviour and aerodynamic loads on a stand-alone heliostat using computational fluid dynamics (CFD), with particular emphasis on the effect of wind direction and its impact on the aerodynamic loading of a heliostat. This

aspect of loading had not previously been explored in any detail. The model was validated by comparing the computation predictions of the heliostat's aerodynamic coefficients with both experimental measurements and numerical results from previously published work. The study showed that, for a 0° wind incidence angle, the drag and base overturning moment coefficients decrease as the tilt angle alters from vertical to horizontal. The lift and hinge moment coefficients, on the other hand, showed an asymmetric behaviour about the 0° tilt angle with maximum values occurring at tilt angles of 30° and -30° . Increasing wind incidence angle affected the wind loading coefficients (drag, lift, base overturning moment and hinge moment coefficients) by decreasing their magnitudes at different rates. A subsequent non-linear regression analysis delivered a correlation for each of the coefficients based on the heliostat's tilt and wind incidence angle was developed. These formulations provide a useful analytical tool for heliostat designers to determine the wind loads on heliostats and to assess structural forces and moments on the frame of the heliostat and its reflective surface. In summary, it was shown that wind incidence had a significant impact on the aerodynamic loads encountered by a heliostat and, therefore, needs to be accounted for when examining the structural integrity of heliostats.

Secondly, the study investigated the aero-structural behaviour characteristics of a proposed honeycomb sandwich composite-based heliostat structure by performing numerical fluid-structure interaction (FSI) simulations for several loading conditions at various tilt and wind incidence angles. The structural response of the heliostat's honeycomb sandwich panel showed markedly different behaviour characteristics at various operational conditions. From the results, it was shown that the effect of heliostat's tilt orientation on the sandwich panel's maximum deflection and stresses becomes more pronounced as wind velocity increases above 10 m/s. This effect becomes more vital and the difference in the maximum displacement and stress values at different tilt angles

escalates to a maximum at wind velocity of 20 m/s. Moreover, the wind velocity effect on the heliostat panel for the case of 0° tilt angle was negligible. This is because of the flow uniformity (the projected area of the reflector directly facing the wind is at its minimum) that leads to a significant decrease in the wind loading effect on the panel at this tilt orientation for all wind velocities (5-20 m/s). The study showed that increasing wind incidence angle affected the recorded maximum displacement and stress results by reducing their magnitudes at different rates. This is due to the fact that the heliostat's projected area directly facing the wind decreases with the increase in wind incidence angle. This consequently reduces the effect of the blockage, causing a decrease in the wind loading effect on the heliostat. As the wind incidence angle gradually increases from 45° to 90° (the projected area of the reflector continues to decrease) for all tilt angles, the wind incidence angle influence on the maximum displacement and stress values gradually increased and the values notably decreased thus reaching its minimum at $\beta = 90^\circ$. This implies that the heliostat panel at 90° wind incidence angle, regardless of any tilt angle, is not significantly influenced by wind loadings at wind velocities of 20 m/s and below. The study also showed that when wind strikes the heliostat structure at 0° and 45° incidence angles, the shielding effect caused by the supporting components and torque tube was clearly noticeable. When the incoming wind acted on the reflector's back surface, the maximum displacement and stress values were slightly lower compared to the ones recorded when the flow acted on the heliostat's mirror surface. In all of the operational conditions studied, it was concluded that the worst case was found to be at a tilt angle of 30° under the effect of wind flow at 0° to the heliostat surface with a velocity of 20 m/s. Despite this observation, it was found that the heliostat managed to maintain its structural integrity according to relevant optical and material failure standards.

Taking the worst case operational condition as a basis, and given that the mechanical properties of honeycomb core-based sandwich composites are highly dependent upon the

honeycomb's geometric configuration (e.g., cell wall angle (ϕ), cell wall length (a), cell wall thickness (t)) and the core thickness (D), a comprehensive parametric study was performed to investigate the effect that each of these parameters has on the aero-structural behaviour characteristics of the honeycomb sandwich composite-based heliostat. The study was carried out for three different core thicknesses (D) with various honeycomb configurations. From this the study revealed that varying the honeycomb's cellular geometry significantly affected both the strength and stiffness properties of the sandwich composite-based heliostat structure, illustrating that it is attainable to control suitably the strength of the heliostat's honeycomb sandwich panel to achieve superior mechanical properties by varying the cell's configuration.

These variations in the heliostat's structural response highlighted the necessity for a generalized model that can capture the influence of each of the honeycomb core's geometrical parameters on the heliostat structure's performance (i.e. optical, material failure and weight reduction). Having a predictive model that estimates the heliostat's structural performance, under the worst case operational condition and based on the desired site's maximum recorded wind speed, eradicates the need of going through the hurdles of establishing an FSI model for each of the honeycomb core's geometrical parameters. This, in turn, runs down the implementation time and keeps off unnecessary computations. In this sense, and given that this approach is one of the prominent tools for modelling complex non-linear relationships, particularly in situations where the development of phenomenological or conventional regression models becomes impractical or cumbersome, artificial neural network (ANN) technique was utilized to establish a novel predictive model that predicts the structural performance of the honeycomb sandwich composite-based heliostat based on its honeycomb core's physical parameters. The results showed that the established ANN model was capable of

accurately predicting the structural performance of the honeycomb sandwich composite-based heliostat.

Finally, a rigorous investigation was carried out on the utilization of particle swarm optimization (PSO) algorithm to establish a novel prediction-optimization model that predicts and optimizes the structural performance of honeycomb sandwich composite-based heliostats. The model couples the ANN predictive model with the PSO algorithm for determining the optimum honeycomb core configuration leading to minimum self-weight of the heliostat's sandwich composite panel while satisfying the structural performance requirements (i.e. optical and material failure). It was shown that the proposed integrated ANN-PSO model, which was encompassed as a user-friendly graphical user interface (GUI), delivers a useful, flexible and time-efficient tool for heliostat designers to predict and optimize the structural performance of honeycomb sandwich composite-based heliostats as per desired requirements.

In summary, the work presented is a significant milestone in the quest to develop cheaper lightweight heliostats that are strong and capable of withstanding wind loads and other environmental conditions, and a major step on the way to move central tower CSP systems to the forefront to become the technology of choice for energy production.

ACKNOWLEDGMENTS

I am extremely grateful to the **Almighty ALLAH** for providing me the ability and understanding to carry out this research.

This thesis would not have been possible without the generous support of the wonderful people around me. This thesis would not have been possible without the help, support and patience of my Supervisor **Dr. Timothy Anderson** throughout these years. The good advice and support of my second supervisor **Dr. Roy Nates** has been invaluable for which I am extremely grateful. The knowledge, skills and encouragement I have received from both supervisors have been of enormous value and I attribute the completion of my thesis to their influence.

I extend my gratitude to the **Auckland University of Technology (AUT)** and the **School of Engineering, Computer and Mathematical Sciences** to provide me the comfortable working space and facilities to conduct this research.

I am also very thankful to my research colleagues and amazing friends **Muhammad Uzair, Delight Morkporkpor, Si Thu Paing, Muhammad Asif, and Mehrdad Khamooshi** for their valuable suggestions throughout the research.

I would like to thank my parents, my backbone, **Dr. Omer Sulaiman** and **Awatif Hashim**, my brother **Sufiyan** and my gorgeous little sister **Aya**, who always supported and encouraged me during my difficult time.

Finally, my heartfelt thanks to my other half **Remaz Hayder** and my best friends **Khalid Boulbrachene, Djamel Benhadji** and **Yaseen Hago** for patiently putting up with me during the hardship of these years.

CONTENTS

ABSTRACT	i
ACKNOWLEDGMENTS	vi
LIST OF FIGURES	x
LIST OF TABLES	xv
ATTESTATION OF AUTHORSHIP	xvi
Chapter 1: Introduction	1
1.1 Line-focus concentrating systems	3
1.2 Point-focus concentrating systems	5
1.3 Central tower CSP systems: Current status, challenges and improvement opportunities.....	8
1.3.1 Heliostat primary elements	9
1.3.1.1 Reflective mirror module	9
1.3.1.2 Mirror support structure	10
1.3.1.3 Drives (rotation of mirror panel).....	10
1.3.1.4 Pylon and foundation (ground connection).....	11
1.3.1.5 Tracking control system.....	12
1.3.2 Review of existing heliostat technologies.....	12
1.3.2.1 ATS 150.....	12
1.3.2.2 ASM-150.....	13
1.3.2.3 PSI 120 and Colon 70	15
1.3.2.4 SAIC	16
1.3.2.5 Sanlucar 90.....	17
1.3.2.6 ASUP 140	18
1.3.2.7 Solaflect Energy	19
1.3.2.8 eSolar	20
1.3.2.9 Vast Solar.....	21
1.3.2.10 Stellio	22
1.3.3 Heliostat cost reduction opportunities.....	23
1.4 Summary and research objective.....	25
Chapter 2: Flow behaviour and aerodynamic loading on a stand-alone heliostat: Wind incidence effect	27
2.1 Numerical setup.....	30
2.2 Validation with available data of wind loading coefficients.....	34
2.3 Effect of tilt on flow field.....	38
2.4 Effect of wind incidence on the aerodynamic loading characteristics	42
2.5 Effect of wind incidence on flow field.....	45

2.6	Force-coefficient and moment-coefficient correlations	51
2.7	Chapter Summary	54
Chapter 3: Structural behaviour of honeycomb sandwich composite-based heliostat structure under wind effects		56
3.1	Numerical setup.....	56
3.2	Wind pressure distribution characteristics	63
3.3	Heliostat structural behaviour	69
3.3.1	Deflections	70
3.3.2	Stress distributions	83
3.4	Chapter Summary.....	102
Chapter 4: Effect of the geometric configuration of honeycomb on the aero-structural behaviour characteristics of the sandwich composite-based heliostat		105
4.1	Numerical setup.....	106
4.2	Effect of honeycomb cell geometry on the structural behaviour of the sandwich composite-based heliostat	107
4.3	Effect of honeycomb core thickness on the structural behaviour of the sandwich composite-based heliostat	119
4.4	Chapter Summary.....	123
Chapter 5: Artificial neural network-based modelling of the honeycomb core geometry effect on the structural behaviour characteristics of the sandwich composite-based heliostat		125
5.1	Numerical setup.....	128
5.2	Results and discussions	135
5.2.1	Predictive performance of the ANN model within the training dataset bounds 137	
5.2.2	Predictive performance of the ANN model outside the training dataset bounds 140	
5.3	Chapter Summary.....	143
Chapter 6: Particle swarm-based structural optimization of the honeycomb sandwich composite-based heliostat		145
6.1	Numerical setup.....	149
6.1.1	Optimization problem formulation (objective function, decision variables and restrictions).....	151
6.1.1.1	Objective function.....	151
6.1.1.2	Decision variables	151
6.1.1.3	Constraints	152
6.1.2	ANN-PSO optimization procedure	153
6.2	Results and discussions	156
6.3	Chapter Summary.....	171

Chapter 7: Conclusion and Recommendations	173
7.1 Recommendations for future work.....	177
References	179
Appendix A: Wind profile development.....	197
Appendix B: CFD mesh sensitivity analysis.....	199
Appendix C: Size selection analysis of the heliostat supporting steel attachments	201
Appendix D: FEA mesh sensitivity analysis.....	203
Appendix E: Equations used for calculating the mechanical properties of the sandwich composite's honeycomb core	205
Appendix F: FSI results for wind flow at $\beta = 22.5^\circ$ and $\beta = 67.5^\circ$ to the heliostat surface	207
• Pressure distribution	207
• Deflections	209
• Stress distributions	212
Appendix G: Dataset used in establishing the ANN model.....	218

LIST OF FIGURES

Figure 1: Classification of solar thermal technologies.....	2
Figure 2: Non-concentrating solar thermal systems.....	3
Figure 3: Linear Fresnel collector schematic.....	4
Figure 4: Parabolic trough system schematic.....	5
Figure 5: Parabolic dish system schematic.....	6
Figure 6: Solar central tower system schematic.....	7
Figure 7: Heliostat field in solar central tower power plant.....	8
Figure 8: Heliostat main elements.....	9
Figure 9: ATS 150 heliostat.....	13
Figure 10: ASM-150 heliostat.....	14
Figure 11: PSI 120 and Colon 70 heliostats.....	16
Figure 12: SAIC heliostat.....	17
Figure 13: Sanlucar 90 heliostat.....	18
Figure 14: Abengoa ASUP 140 heliostat.....	19
Figure 15: Solaflect suspension heliostat.....	20
Figure 16: eSolar® SCS5 heliostat.....	21
Figure 17: Vast Solar heliostats.....	22
Figure 18: Stellio heliostat.....	23
Figure 19: Honeycomb sandwich composite structure.....	24
Figure 20: Geometric description of load coefficients.....	27
Figure 21: Heliostat geometrical configuration.....	31
Figure 22: Computational domain.....	32
Figure 23: Coordinate system of heliostat model.....	33
Figure 24: Comparison of drag and lift coefficients at different tilt angles.....	35
Figure 25: Comparison of base overturning moment and hinge moment coefficients at different tilt angles.....	36
Figure 26: CFD streamlines around the heliostat for 90° tilt angle.....	38
Figure 27: CFD streamlines around the heliostat for 60° tilt angle.....	39
Figure 28: CFD streamlines around the heliostat for 30° tilt angle.....	40
Figure 29: CFD streamlines around the heliostat for 0° tilt angle.....	40
Figure 30: CFD streamlines around the heliostat for -30° tilt angle.....	41
Figure 31: CFD streamlines around the heliostat for -60° tilt angle.....	42
Figure 32: CFD streamlines around the heliostat for -90° tilt angle.....	42
Figure 33: Wind incidence angle comparison of drag coefficient for different tilt angles.....	43
Figure 34: Wind incidence angle comparison of lift coefficient for different tilt angles.....	44
Figure 35: Wind incidence angle comparison of base overturning moment coefficient for different tilt angles.....	44
Figure 36: Wind incidence angle comparison of hinge moment coefficient for different tilt angles.....	45
Figure 37: CFD streamlines around the heliostat at 90° and -90° tilt angles for a range of wind incidence angles.....	48
Figure 38: CFD streamlines around the heliostat at 30° and -30° tilt angles for a range of wind incidence angles.....	50

Figure 39: Comparison of drag, lift, base overturning moment and hinge moment coefficients obtained from correlation and numerical results	53
Figure 40: Sandwich composite-based heliostat in full-scale	57
Figure 41: Close-up view of the heliostat's honeycomb sandwich composite structure	58
Figure 42: Definition of tilt and wind incidence angles.....	59
Figure 43: Geometric model of the honeycomb core and equivalent core sandwich panel (Aydincak and Kayran, 2009).....	60
Figure 44: Honeycomb main geometrical properties.....	61
Figure 45: Pressure distribution on the heliostat at wind velocity of 15 m/s approaching at 0° incidence angle (β).....	65
Figure 46: Pressure distribution on the heliostat at wind velocity of 15 m/s approaching at 45° incidence angle (β).....	66
Figure 47: Pressure distribution on the heliostat at wind velocity of 15 m/s approaching at 90° incidence angle (β).....	68
Figure 48: Pressure distribution on the heliostat at 30° tilt angles (θ) and 0° incidence angle (β) for a range of wind velocities	69
Figure 49: Displacement distribution of the heliostat surface for different tilt angles (θ) at wind velocity of 15 m/s approaching at 0° incidence angle (β).....	72
Figure 50: Displacement distribution of the heliostat surface for different tilt angles (θ) at wind velocity of 15 m/s approaching at 45° incidence angle (β).....	74
Figure 51: Displacement distribution of the heliostat surface for different tilt angles (θ) at wind velocity of 15 m/s approaching at 90° incidence angle (β).....	75
Figure 52: Wind velocity and tilt angle effects on the heliostat surface's maximum recorded displacement for 0° wind incidence angle	77
Figure 53: Pressure and displacement distribution of the heliostat surface for 90°, 60° and 30° tilt angles (θ) at wind velocity of 20 m/s approaching at 0° incidence angle (β)	78
Figure 54: Wind velocity and tilt angle effects on the heliostat surface's maximum recorded displacement for 45° wind incidence angle	79
Figure 55: Pressure and displacement distribution of the heliostat surface for 90°, 60° and 30° tilt angles (θ) at wind velocity of 20 m/s approaching at 45° incidence angle (β) ...	80
Figure 56: Wind velocity and tilt angle effects on the heliostat surface's maximum recorded displacement for 90° wind incidence angle	81
Figure 57: Interpretation of the reflective surface's maximum allowable deflection (reproduced from Björkman (2014)).....	82
Figure 58: Pressure and stress distribution of the heliostat surface for 90°, 60°, 30° and 0° tilt angles (θ) at wind velocity of 15 m/s approaching at 0° incidence angle (β).....	85
Figure 59: Pressure and stress distribution of the heliostat surface for 0° tilt angles (θ) at wind velocity of 15 m/s approaching at 0° incidence angle (β).....	86
Figure 60: Pressure and stress distribution of the heliostat surface for -30°, -60° and -90° tilt angles (θ) at wind velocity of 15 m/s approaching at 0° incidence angle (β).....	87
Figure 61: Stress distribution of the heliostat surface for different tilt angles at wind velocity of 15 m/s approaching at 45° incidence angle	89
Figure 62: Wind incidence angle effect on the heliostat's maximum recorded stress for different tilt angles at wind velocity of 15 m/s	90
Figure 63: Stress distribution of the heliostat surface for different tilt angles at wind velocity of 15 m/s approaching at 90° incidence angle (β).....	92
Figure 64: Wind velocity and tilt angle effects on the heliostat's maximum recorded stress for 0° wind incidence angle	94

Figure 65: Pressure and stress distribution results for 90°, 60°, 30° and 0° tilt angles (θ) at wind velocity of 20 m/s approaching at 0° incidence angle (β)	95
Figure 66: Wind velocity and tilt angle effects on the heliostat's maximum recorded stress for 45° wind incidence angle	97
Figure 67: Pressure and stress distribution results for 90°, 60°, 30° and 0° tilt angles (θ) at wind velocity of 20 m/s approaching at 45° incidence angle (β)	98
Figure 68: Wind velocity and tilt angle effects on the heliostat's maximum recorded stress for 90° wind incidence angle	100
Figure 69: Common failure forms of honeycomb sandwich panels (reproduced from Galletti et al. (2008) and Gibson and Ashby (1997))	101
Figure 70: Geometrical parameters investigated in the study	107
Figure 71: Cell geometry effect on the heliostat panel's maximum recorded displacement for a core with a thickness of 300 mm	108
Figure 72: Cell geometry effect on the heliostat panel's maximum recorded stress for a core with a thickness of 300 mm	109
Figure 73: Displacement and stress distribution results for different cell wall lengths (a)	111
Figure 74: Supporting steel attachments' displacement contribution for different cell wall lengths (a)	112
Figure 75: Cell wall thickness (t) effect on the heliostat panel's maximum recorded displacement and stress for a core with a thickness of 300 mm and cell wall angle (φ) of 10°	113
Figure 76: Displacement and stress distribution results for different cell wall thicknesses (t)	114
Figure 77: Supporting steel attachments' displacement contribution for different cell wall thicknesses (t)	114
Figure 78: Cell wall angle effect (φ) on the heliostat panel's maximum recorded displacement for a core with a thickness of 300 mm	116
Figure 79: Displacement and stress distribution results for different cell wall angles (φ)	117
Figure 80: Supporting steel attachments' displacement contribution for different cell wall angles (φ)	118
Figure 81: Core thickness effect on the heliostat panel's maximum recorded displacement at multiple cell wall angles for a core with a cell wall thickness of 0.05 mm	119
Figure 82: Core thickness effect on the heliostat panel's maximum recorded stress at multiple cell wall angles for a core with a cell wall thickness of 0.05 mm	120
Figure 83: Displacement and stress distribution results for different core thicknesses (D)	122
Figure 84: Supporting steel attachments' displacement contribution for different core thicknesses (D)	123
Figure 85: Schematic diagram of a typical artificial neural network	128
Figure 86: Configurations used for the network design input dataset	131
Figure 87: Inputs and outputs of the ANN model for the prediction of the structural performance of the honeycomb sandwich composite-based heliostat	132
Figure 88: Flowchart of the proposed methodology	134
Figure 89: Determination of optimum network architecture for different neurons in the hidden layer	136

Figure 90: Predicted values from the established ANN model versus the actual values for all datasets	137
Figure 91: ANN model predictions of the heliostat's attainable weight reduction and maximum structural displacement at multiple cell wall angles for unseen cell wall thicknesses of 0.025, 0.035 and 0.045 mm	138
Figure 92: ANN model predictions of the heliostat's recorded maximum stress at the lower aluminium sheet and core crush index at multiple cell wall angles for unseen cell wall thicknesses of 0.025, 0.035 and 0.045 mm	139
Figure 93: ANN model predictions of the heliostat's attainable weight reduction and maximum structural displacement at multiple cell wall angles for unseen cell wall thickness 0.01 mm.....	141
Figure 94: ANN model predictions of the heliostat's recorded maximum stress at the lower aluminium sheet and core crush index at multiple cell wall angles for unseen cell wall thickness of 0.01 mm	142
Figure 95: Design variables of optimization study with their search ranges	152
Figure 96: Flowchart of the ANN-PSO methodology	154
Figure 97: Objective function evolution (weight reduction percentage) according to the number of iterations performed for various swarm sizes (case of configuration 1)	157
Figure 98: Effect of honeycomb cellular configuration on the heliostat surface's maximum recorded displacement, lower aluminum sheet's maximum recorded stress and core crush index for a core with a thickness of 150 mm.....	159
Figure 99: Effect of honeycomb cellular configuration on the mirror support structure's attainable weight reduction for a core with a thickness of 150 mm.....	160
Figure 100: Effect of honeycomb cellular configuration on the heliostat surface's maximum recorded displacement, lower aluminum sheet's maximum recorded stress and core crush index for a core with a thickness of 300 mm.....	162
Figure 101: Effect of honeycomb cellular configuration on the mirror support structure's attainable weight reduction for a core with a thickness of 300 mm.....	163
Figure 102: Effect of honeycomb cellular configuration on the heliostat surface's maximum recorded displacement, lower aluminum sheet's maximum recorded stress and core crush index for a core with a thickness of 450 mm.....	165
Figure 103: Effect of honeycomb cellular configuration on the mirror support structure's attainable weight reduction for a core with a thickness of 450 mm.....	166
Figure 104: Evolution of the optimum along the iterative procedure (case of configuration 1)	167
Figure 105: Screenshots of the established GUI for the three case scenarios.....	170
Figure 106: Incident velocity and turbulence intensity profiles.....	198
Figure 107: Grid independency test	199
Figure 108: Mesh around the heliostat.....	200
Figure 109: Attachment sizes investigated in the study.....	201
Figure 110: Displacement and weight reduction percentage variations with attachment size.....	202
Figure 111: Point analysed in the grid independency test.....	203
Figure 112: FEA grid independency test	204
Figure 113: FEA model of the heliostat structure.....	204
Figure 114: Pressure distribution on the heliostat at wind velocity of 15 m/s approaching at 22.5° incidence angle	208

Figure 115: Pressure distribution on the heliostat at wind velocity of 15 m/s approaching at 67.5° incidence angle	209
Figure 116: Displacement distribution of the heliostat surface for different tilt angles (θ) at wind velocity of 15 m/s approaching at 22.5° incidence angle (β).....	210
Figure 117: Displacement distribution of the heliostat surface for different tilt angles (θ) at wind velocity of 15 m/s approaching at 67.5° incidence angle (β).....	211
Figure 118: Wind velocity and tilt angle effects on the heliostat surface's maximum recorded displacement for 22.5° wind incidence angle	211
Figure 119: Wind velocity and tilt angle effects on the heliostat surface's maximum recorded displacement for 67.5° wind incidence angle	212
Figure 120: Stress distribution of the heliostat surface for different tilt angles at wind velocity of 15 m/s approaching at 22.5° incidence angle	213
Figure 121: Stress distribution of the heliostat surface for different tilt angles at wind velocity of 15 m/s approaching at 67.5° incidence angle	215
Figure 122: Wind velocity and tilt angle effects on the heliostat's maximum recorded stress for 22.5° wind incidence angle.....	216
Figure 123: Wind velocity and tilt angle effects on the heliostat's maximum recorded stress for 67.5° wind incidence angle.....	217

LIST OF TABLES

Table 1: Material properties	62
Table 2: Former studies on ANN modelling of sandwich composites	126
Table 3: ANN model performance for training, testing and all datasets	136
Table 4: Former studies on the optimization of sandwich composites	147
Table 5: PSO algorithm characteristics	155
Table 6: Description of the three cases to be optimized	156
Table 7: PSO optimization results of the three cases	169

ATTESTATION OF AUTHORSHIP

I hereby declare that this submission is my own work and that, to the best of my knowledge and belief, it contains no material previously published or written by another person (except where explicitly defined in the acknowledgments), nor material which to a substantial extent has been submitted for the award of any other degree or diploma of a university or other institution of higher learning.

Auckland

Signature _____

Sulaiman Omer Fadlallah

Chapter 1: Introduction

By 2030, the world is projected to consume two-thirds more energy than today (Dorian et al., 2006). As fossil sources of energy are starting to diminish, the search for alternative energy solutions has become vital. Among diverse energy resources, solar energy is by far the largest exploitable resource (Lewis and Nocera, 2006). The sun emits energy at an extremely high and relatively constant rate. The estimated rate of energy produced by the Sun is about 3.8×10^{20} megawatts (MW). While only a fraction reaches earth (around 1.8×10^{11} MW), the amount of solar energy striking the earth in one hour (4.3×10^{20} joules (J)) is more than the energy consumed by humans in an entire year, which is around 4.1×10^{20} J (Philibert, 2011; Foster et al., 2010). If all of this energy could be converted into usable forms on earth, it would be more than enough to supply the world's energy demand (Al-Qubaisi et al., 2009). This rapidly growing demand, in addition to the untapped solar energy's full potential, significantly encouraged solar power generation technologies to grow faster than any other renewable technology. According to a forecast, solar energy power generation systems should be able to provide up to one-third of the world's total energy demand after 2060 (Philibert, 2011). While proven fossil reserves represent 150 years (coal), 58 years (natural gas) and almost 46 years (oil) of consumption at current rates, the amount of solar energy received in one year can cover the total energy consumption of 6,000 years (Philibert, 2014).

The incoming solar radiation can be utilized to produce useful electricity through a variety of technologies, categorized into two main systems: photovoltaic (PV) systems based on converting photons in sunlight to electricity via the photovoltaic effect, and thermal systems that operate using the sun's heat to drive thermal power systems. Compared to photovoltaic systems, solar thermal energy conversion systems are considered to be the most promising available solar power generation technologies due to their higher solar to power conversion efficiencies (up to 35 percent compared to PV technologies that provide

efficiency of 10 to 15 percent) and relatively low cost per unit produced energy (Uzair, 2018; Goswami, 2015). As demonstrated in Figure 1, these solar thermal technologies can be classified into two main categories: non-concentrating and concentrating solar systems.

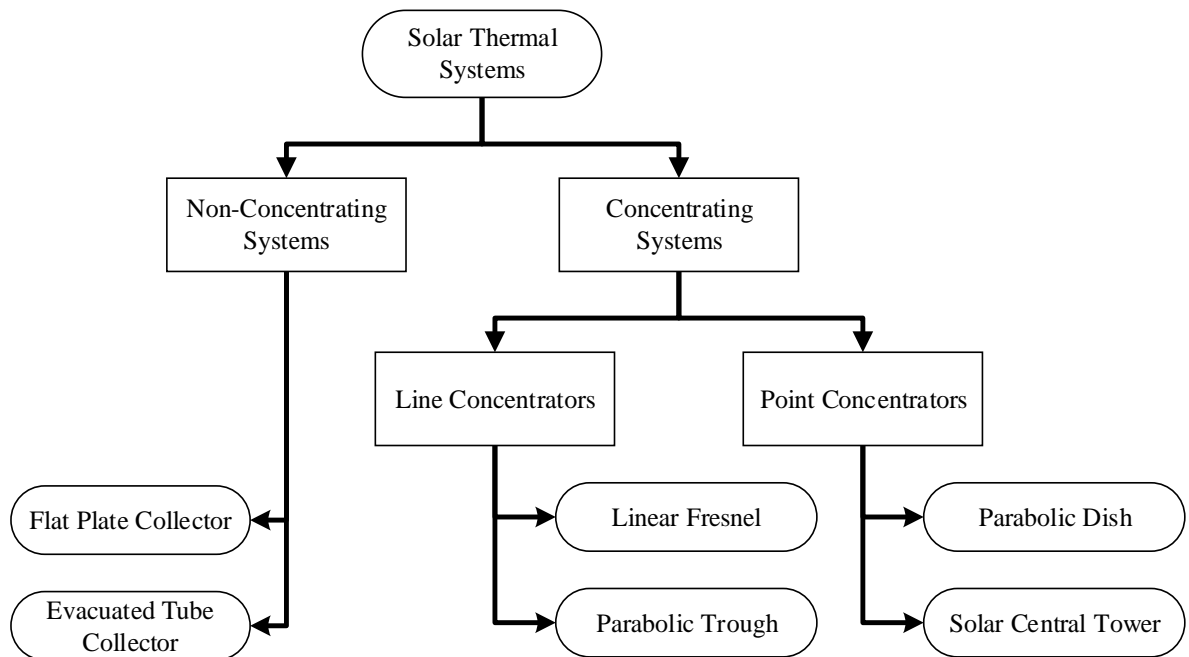


Figure 1: Classification of solar thermal technologies

Flat plate and evacuated tube collectors (Figure 2), which fall under the former category, are rarely used for electricity generation, since their maximum operational temperature is usually lower than 120 °C and the resulting efficiency is very low (Kosmadakis et al., 2013). The most common and prevalent technique for power production employing solar thermal technology is the concentrating solar power (CSP) technology. CSP systems concentrate the direct solar irradiation to produce high thermal energy density and temperature using various arrangements of optical lenses and mirrors. Based on the optical configurations, CSP systems can be divided into two main categories: line and point concentrating systems.



(a) Flat plate collector



(b) Evacuated tube collector

Figure 2: Non-concentrating solar thermal systems

(Mahendran, 2016)

1.1 Line-focus concentrating systems

This type of concentrating systems capture the sun's energy with large mirrors that reflect and focus the incoming radiation onto a linear receiver tube located at the focal axis of the reflector. Linear Fresnel and parabolic trough collectors, shown in Figures 3 and 4, are the two most popular line-focus CSP technologies.

Linear Fresnel collectors (Figure 3), consisting of long rows of single-axis tracking flat or slightly curved mirrors, concentrate the solar beam radiation onto a fixed downward-facing linear receiver that heats up a circulating fluid (Philibert, 2011). The resulting vapour is fed to a turbine that produces electricity through a generator. Initially, when Fresnel thermal plants were designed, the purpose targeted was low to medium

temperature applications, such as heat generation for commercial or residential demand and water treatment. The current status of the technology surpassed the first level, and now is more often designed to produce high-temperature heat for large-scale industrial heat processes or utility-scale electricity generation (Zhu et al., 2014).

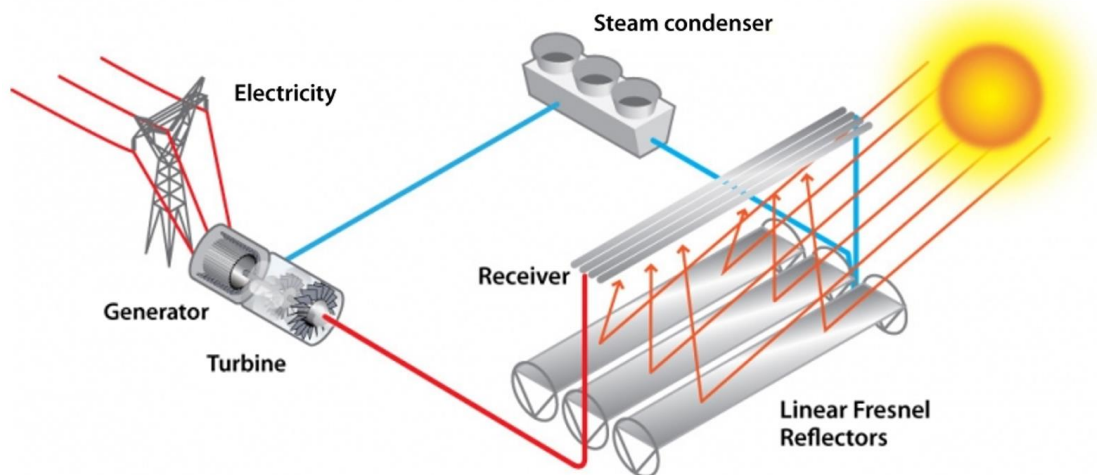


Figure 3: Linear Fresnel collector schematic

(<https://www.energy.gov/eere/solar/articles/linear-concentrator-system-basics-concentrating-solar-power>)

Parabolic trough collectors (Figure 4), on the other hand, consist of parallel rows of single-axis tracking reflectors curved in one dimension (i.e. semi-cylindrical) to focus the solar beam radiation onto a receiver tube located along the focal line of each parabola-shaped reflector. The mirror arrays can be more than 100 m long with the curved surface 5 m to 6 m across (Philibert, 2011). The receiver tube converts the solar radiation projected onto it into thermal energy by heating up a working fluid that runs through the tube. This heated fluid is then pumped down to a conventional thermal power generation system to produce electricity. Usually a thermal-storage unit is included in the parabolic trough power plant configuration to stabilize the power production and operate during the night as well.

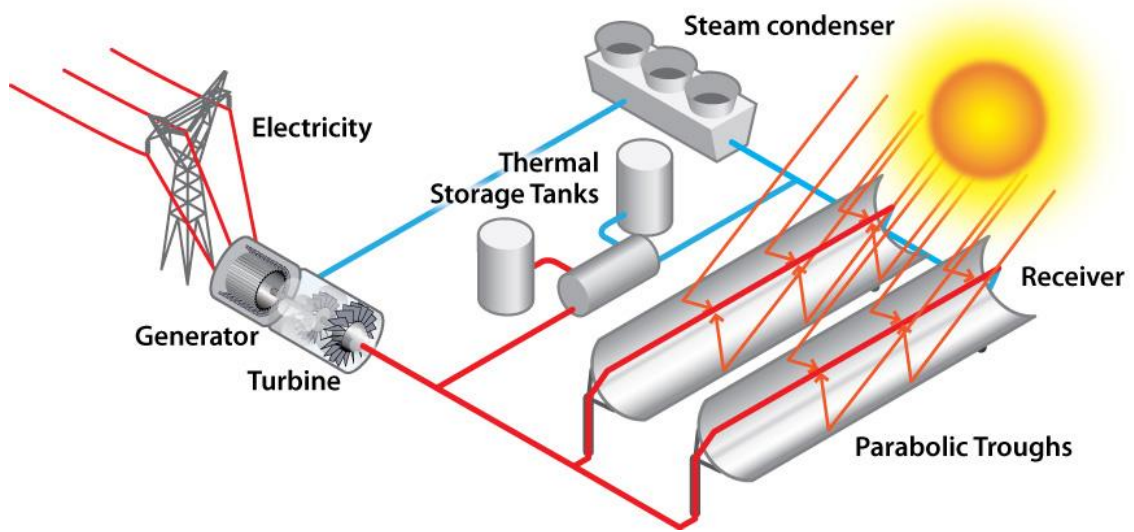


Figure 4: Parabolic trough system schematic

(<https://www.energy.gov/eere/solar/articles/linear-concentrator-system-basics-concentrating-solar-power>)

1.2 Point-focus concentrating systems

In the case of the point-focus concentrating systems, the sun is tracked along two axes, and the incoming solar radiation is focused on a single point receiver. In view of the fact that the solar beam radiation is concentrated at a point instead of along a line, these systems can achieve far higher temperatures comparatively, owing to the concentration of a larger fraction of the solar irradiation. The two most common point-focus CSP technologies are parabolic dish collectors and solar central tower systems.

Considered to be the oldest solar technology, parabolic dish collectors (Figure 5) are comprised of paraboloid-shaped mirrors that concentrate the direct solar radiation onto a receiver mounted at the focal point of each dish. The entire apparatus tracks the sun in two axes, with the dish and receiver moving in tandem. The dish's receiver captures the high temperature thermal energy into a fluid that is either the working fluid for a receiver-

mounted Stirling engine/generator module, or is used to transport the energy to ground-based processes (Lovegrove and Stein, 2012). A single parabolic dish system has the potential to produce from approximately 10 kilowatts to approximately 100 kilowatts of electricity (Goswami, 2015). Each parabolic dish is a complete power-producing unit, and may function either independently or as part of a group of linked modules. The modular usability of solar dish systems allows large scale applications with an output capacity that can reach up to 1.5 megawatts (MW) (Zhang et al., 2013). In addition to electricity generation, parabolic dish collectors are also used in desalination plants utilising the reverse osmosis (RO) process to deliver energy input to the system's pumping and heat recovery section (Uzair, 2018).

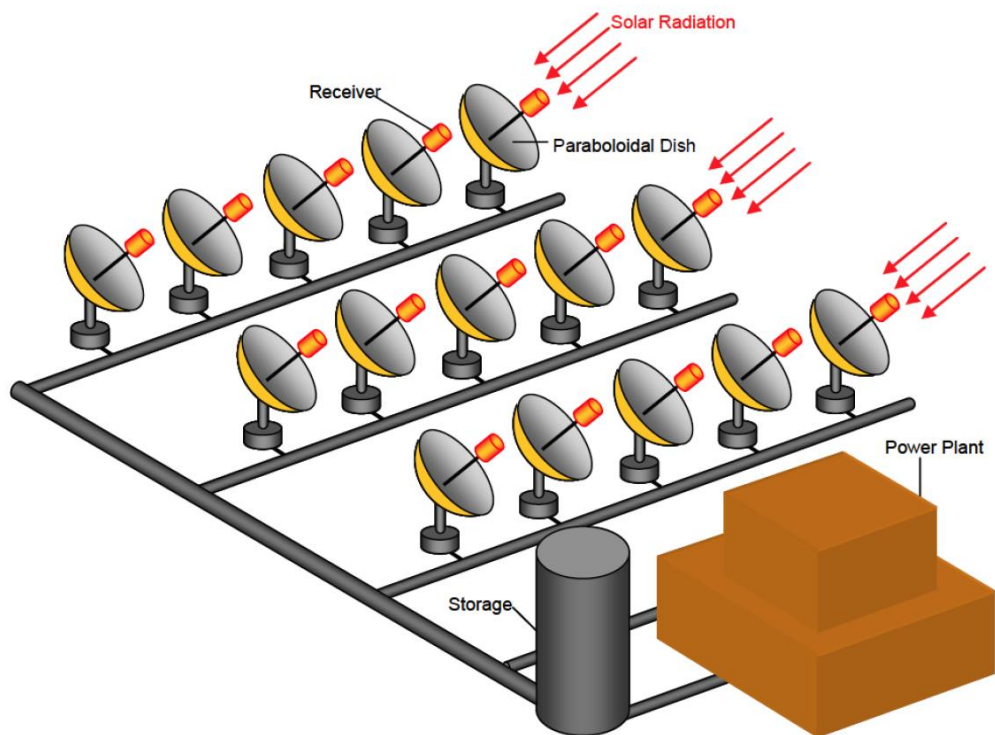


Figure 5: Parabolic dish system schematic

(Uzair, 2018)

Central tower systems (Figure 6), which also fall into the classification of point-focus technologies, are comprised of a field of flat mirrors, also known as heliostats, that track the sun along two axes and reflect and concentrate the solar beam radiation onto a central receiver located at the top of a large tower. The receiver heats up and transmits heat to a heat transfer fluid due to the incoming solar radiation flux. The heated fluid is then pumped down to conventional thermal power generation systems for electricity production. A thermal-storage unit is normally included in the central tower power plant for power production stabilization and operation during the night as well. Central tower CSP systems can achieve high operating temperatures of the order of 1000°C or even higher. Hence, a central tower plant is suitable for thermal electric power production in the range of 10-1000 megawatts (MW) (Goswami, 2015).

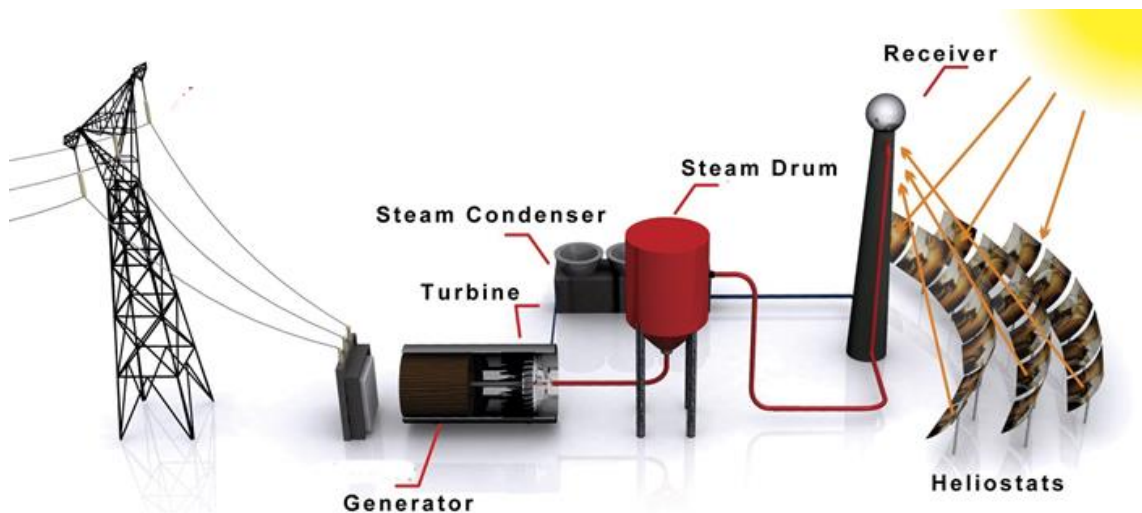


Figure 6: Solar central tower system schematic

(Tiba et al., 2014)

1.3 Central tower CSP systems: Current status, challenges and improvement opportunities

Of all CSP technologies available today central tower systems are moving to the forefront and they have the capability to become the technology of choice (Behar et al., 2013). The potential of solar central tower systems to achieve high temperatures offers a path to higher efficiencies, thereby providing an inherent advantage versus the other CSP systems. However, achieving these high temperatures requires a large number of heliostats (Figure 7). A 100 MW central tower power plant would require nearly one million square meters of glass heliostats, corresponding to approximately 10000, 100 m² heliostats (Mancini, 2000). Due to this large number of reflectors, heliostats represent the largest cost element of central tower CSP systems: almost 50% of the plant's total cost (Kolb et al., 2007). This significant influence has encouraged the development of new innovative heliostat designs and solutions, aimed at reducing the heliostats' cost without affecting its tracking performance in order for the cost of energy from central tower plants to be competitive with that of fossil fuels (Mancini, 2000; Pfahl et al., 2017).



Figure 7: Heliostat field in solar central tower power plant

(Pfahl et al., 2017)

1.3.1 Heliostat primary elements

Reducing the cost of heliostats requires a full understanding of the heliostat's main elements and the effect of each component on the cost of production. In general, a typical heliostat mainly consists of the following components: reflective mirror module, mirror support structure, drive mechanism, pylon and foundation (ground connection) and tracking control system (Téllez et al., 2014) as shown in Figure 8.

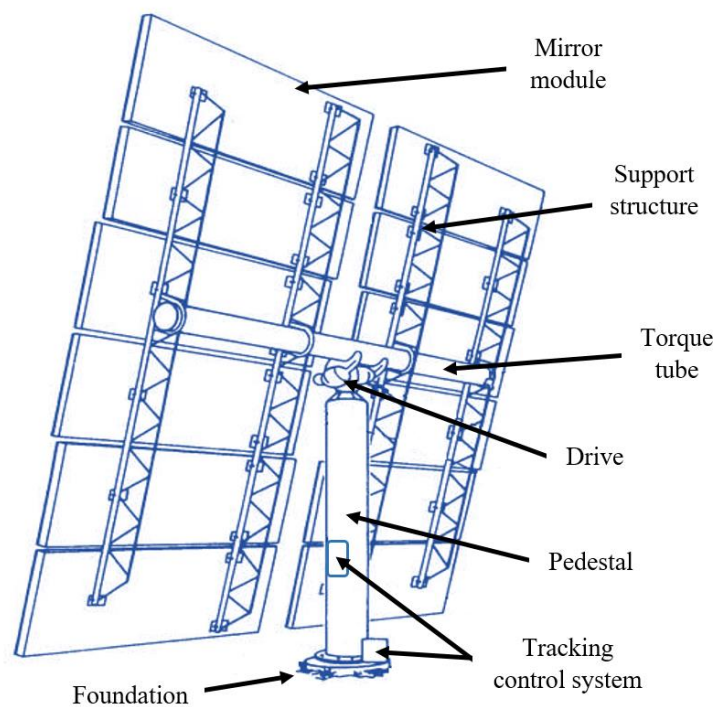


Figure 8: Heliostat main elements

(Téllez et al., 2014; Mancini, 2000)

1.3.1.1 Reflective mirror module

Consisting of one or multiple concaved facets, the reflective module's main purpose is to concentrate the reflected sunlight onto the central receiver (Téllez et al., 2014). Ideally, a reflector would have a low specific weight and maintenance costs, high durability, and

high optical performance. In most recently developed heliostats, mirrored glass and reflective films are the most suitable current options for heliostat reflectors (Pfahl et al., 2017). Between the two aforementioned options and despite their high specific weight, glass mirrors are considered the default reflector, as they are relatively inexpensive, have high reflectance (0.93-0.94), durable (20-25 years' lifespan), and accepted by industry (Pfahl et al., 2017; Téllez et al., 2014).

1.3.1.2 Mirror support structure

State-of-the-art central tower CSP plants generally use T-type heliostats with steel-based support structure and glass facets (Pfahl et al., 2017; Téllez et al., 2014). The heliostat's mirror support structure often comprises of multiple cross beams mounted to a horizontal torque tube. Both the torque tube and the pylon (pedestal) together form a "T" and are coupled to each other by the drive system for azimuth and elevation movement (Pfahl et al., 2017). To accommodate differences in thermal expansion between the glass facets and the metallic support structure, the mirrors are often connected to the support structure either via flexible pins and pads or flexible adhesives (Pfahl et al., 2017; Rumsey-Hill et al., 2019).

1.3.1.3 Drives (rotation of mirror panel)

Composed of a transmission system and a power source, drives are the reason for controlling and providing the heliostat structure with the necessary rotations in order to direct the solar irradiation to the specified point location. In most of the existing heliostats, the drive's rotation is about two axes to provide both elevation and azimuth rotations. Based on the power source specifications, different transmission solutions can be considered for providing the heliostat with the necessary torque and velocity to fulfil the tracking mode. Two of the commonly employed technologies are the rotary

electromagnetic motors and the hydraulic actuators (either linear or rotary) (Téllez et al., 2014).

Rotary electromagnetic motors provide multiple advantages, including satisfactory performance in heliostat motion control, exceptional maintenance characteristics and lifetime, and flexible motor characteristics in terms of power capabilities. In addition to this, mass-producing rotary electromagnetic motors will provide opportunities to minimize the heliostat's total cost (Téllez et al., 2014).

Hydraulic actuators consist of hydraulic pumps, servo-valves, rotary hydraulic motors or telescopic cylinders and the control system. In comparison to the rotary electromagnetic motors, hydraulic actuators are relatively more expensive. This can be related to the fact that fluid characteristics, sealing, and wear resistivity are all important factors that must be considered in maintenance (Téllez et al., 2014).

1.3.1.4 Pylon and foundation (ground connection)

Whether implemented with a concrete foundation or mounted on an above-ground ballasted frame (Pfahl et al., 2017), heliostats' foundation is one of the crucial elements that requires fair consideration because it chains the heliostat to the ground (Téllez et al., 2014). For large heliostats, a concrete foundation is the most common option due to its reasonable cost. Generally, a concrete foundation consists of a ground-buried concrete base attached to the heliostat's pedestal (Coventry and Pye, 2014). This approach can also be achieved by inserting the pedestal into a ground-drilled hole that filled with concrete. For an extensive network of smaller heliostats, concrete foundations are economically unfavourable and alternatives such as the above-ground ballasted frame structure presented by eSolar® and ground anchors (Téllez et al., 2014) are often preferred. However, ground anchors are not suitable for all ground types and require a great deal of effort to avoid heliostat rotation about the vertical axis (Pfahl, 2013). Additionally,

providing stability for the heliostat requires digging deep holes based on the heliostat size. Therefore, implementing this approach on large heliostats will increase the material costs, since long pedestals are needed.

1.3.1.5 Tracking control system

This element involves all mandatory sensors, controllers, processors, limit switches, and encoders in order to provide the desired signals for tilting and orienting the heliostat's drive accurately into the proper facet position. Various control strategies are identified by the mechanism's technology and tracking modes including continuous current, step by step, hydraulics and synchronous. Based on the employed inverter type, controlling the drive's motion can be accomplished by two modes: current or torque. The control algorithm can be carried out by applying a sensor-based control system for heliostat position control (closed-loop) or by providing an accurate calculation of the solar orientation (Télez et al., 2014).

1.3.2 Review of existing heliostat technologies

Over the past several years, in the field of heliostats' development, various innovative designs and prototypes have been developed with different sizes, features, and design specifications. In the following section, current heliostat designs known to the author are presented with particular emphasis on the special design features of each heliostat.

1.3.2.1 ATS 150

Designed in 1984 by Advanced Thermal Systems, Inc., the ATS 150 heliostat (Figure 9) has been successfully operated for the last 20 years in Albuquerque, USA. With a reflectivity of 94%, ATS 150's reflective area is approximately 148 m², and the facet is made of silvered glass second surface mirrors bonded to formed sheet metal back. The mirrors are attached and supported by a steel support structure that consists of several

cross beams which are mounted to a horizontal torque tube. The torque tube and the pylon together are connected to each other by the drive system (Mancini, 2000).

One of the issues related to this model is the cost of a unit, which is proportionally related to its weight. The heliostat has a total weight of 6385 kg. Around 87% of the ATS 150 (e.g., reflective mirror module, back support structure, torque tube and pedestal) was manufactured from steel components (4006 kg) and mirrors (1518 kg) (Kolb et al., 2007). This weight requires expensive drives with high torque capabilities to provide accurate sun tracking.

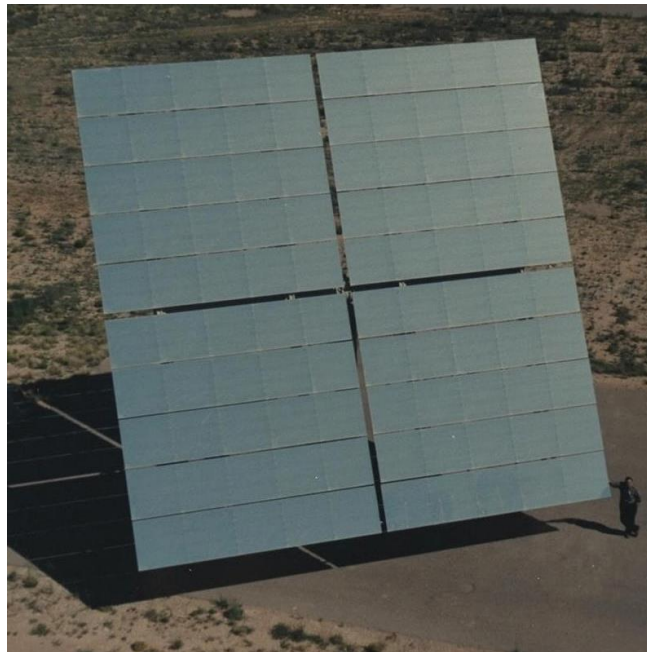


Figure 9: ATS 150 heliostat

(Mancini, 2000)

1.3.2.2 ASM-150

In 1995, Babcock Borsig Power Environment developed a circular heliostat with a total reflective area of 150 m², also known as ASM-150 (Figure 10). The reflector is made of

a 0.9 mm thin glass mirror and metal stretched-membrane with a reflectivity that can reach up to 94%. With a total weight of 3,300 kg, the heliostat azimuth drive is based on an electrically driven turntable with absolute position encoder. As for the elevation drive, it is electric driven spoke wheel with absolute position encoder. The ASM-150 is controlled using a pulse-width modulated 4-quadrant servo controller using measured sun vector as an input (Mancini, 2000).

Although the stretched-membrane facet of the ASM-150 heliostat proved to be mechanically sound, the polymer mirror quickly degraded due to ultraviolet (UV) damage and the face-up stow position led to hail-induced membrane denting (Kolb et al., 2007). Moreover, the circular shape of the heliostat, considering a field of heliostats arranged close to each other, is not favourable due to the gaps between each heliostat.



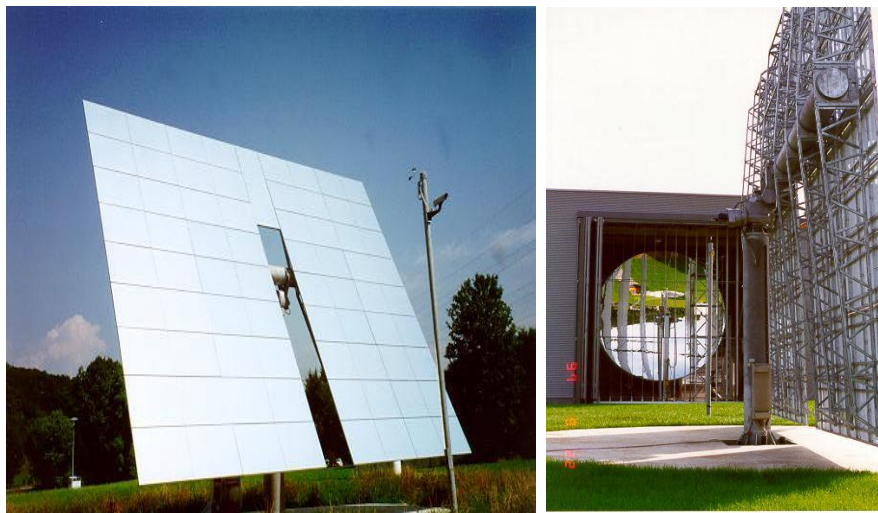
Figure 10: ASM-150 heliostat

(Mancini, 2000)

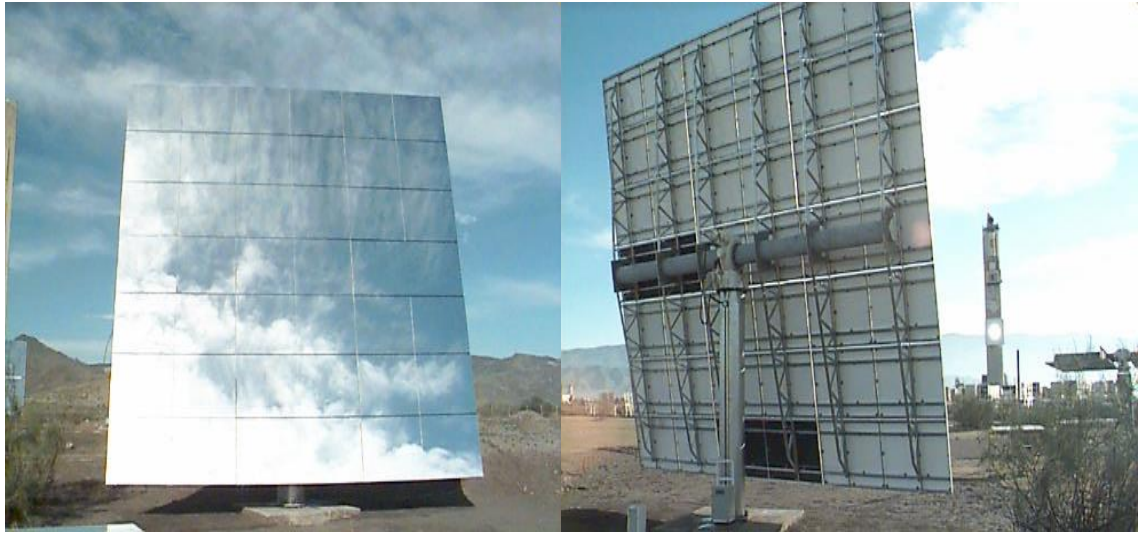
1.3.2.3 PSI 120 and Colon 70

Inabensa, Instalaciones Abengoa, S.A. manufactured in 1996 a heliostat named PSI 120 (Figure 11a). With a reflective surface area of 122.1 m^2 and reflectivity of 93%, the facet is constructed by fixing a mirror to a steel frame with steel nails on the facets jig table (Mancini, 2000). Despite the heliostat's satisfactory optical performance, its cost remains very high due to the heliostat's weight of approximately 6,500 kg. Most of this weight is from the steel structure and the mirror. This heavy frame requires expensive drives with high torque capabilities. Moreover, and since the objective of heliostats is to reflect as much solar radiation as possible with minimal losses, the hollow in the middle of the mirror is wasteful and unfavourable.

With the intention of reducing the cost, Inabensa, Instalaciones Abengoa, S.A. managed to manufacture in 1997 another heliostat design: the Colon 70 (Figure 11b). The facet specifications are almost identical to PSI 120 with the exception of the reflective surface area being reduced to 69.3 m^2 and both azimuth and elevation drives being modified. Despite the cost being reduced in comparison to the PSI 120, this lower cost is size-dependent and uncompetitive for large solar thermal power plants.



(a) Front and back view of the PSI 120 heliostat



(b) Front and back view of the Colon 70 heliostat

Figure 11: PSI 120 and Colon 70 heliostats

(Mancini, 2000)

1.3.2.4 SAIC

SAIC Energy Products Division developed a multi-facet stretched membrane heliostat (Figure 12) in 1998. The 10,000 kg heliostat consists of 22 round mirror facets; each measuring 3.2 meters in diameter and fixed to a steel frame. The reflective surface is made of back-silvered standard glass adhesively applied to stretched membrane (stainless steel ring welded to stainless steel membrane). The total reflective area is approximately 170.72 m² with a reflectivity reaching 89.6% (Mancini, 2000).

Several drawbacks have been identified with this heliostat. The heliostat's main objective is to reflect as much as possible of solar radiation with minimum losses. The circular shape of the heliostat mirrors in SAIC, considering a field of heliostats arranged close to each other, is not favourable due to the gaps between each reflective surface. Another

issue with this heliostat is the high manufacturing cost, where the facet and the heliostat steel-based support hold approximately 72% of the total cost. Not to mention also the drawbacks associated with using stretched-membrane facets, including fast polymer mirror degrading due to ultraviolet (UV) damage and the hail-induced membrane denting (Kolb et al., 2007).

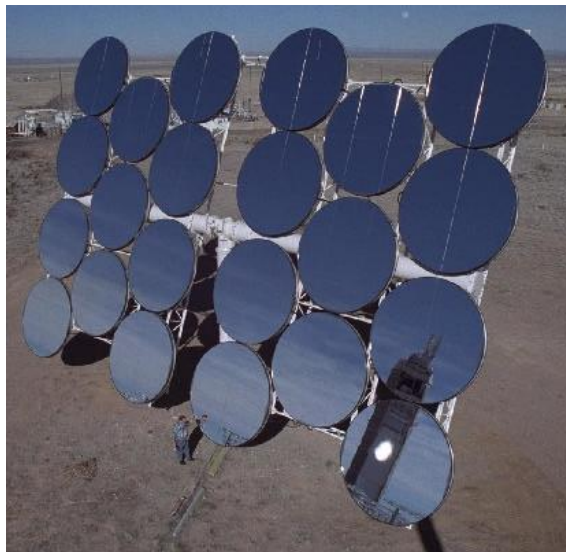


Figure 12: SAIC heliostat

(Télliez et al., 2014; Mancini, 2000)

1.3.2.5 Sanlucar 90

In 1999, Inabensa, Instalaciones Abengoa, S.A. constructed another heliostat design with the name Sanlucar 90, as demonstrated in Figure 13. With a reflective surface area of 91 m² and reflectivity around 92%, the facet is constructed by fixing mirror facets to a steel frame with steel nails on the facets jig table (Mancini, 2000).

Despite the cost being reduced compared to the first two attempts (i.e. PSI 120 and Colon 70) presented earlier (Figure 11), it is still considered high. The heliostat weighs around

3,500 kg; most of this weight is from the steel structure and the mirror and requires expensive motors with high torque capabilities to provide accurate sun tracking.

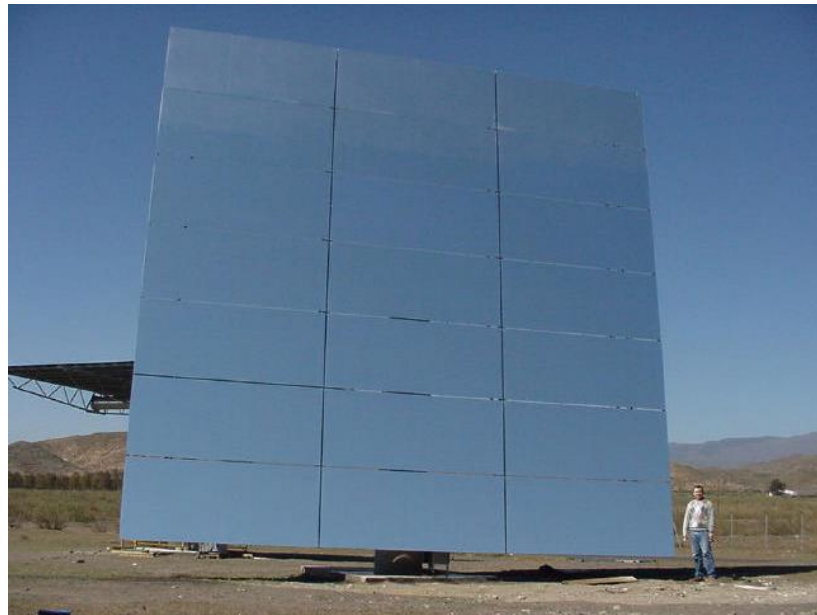


Figure 13: Sanlucar 90 heliostat

(Mancini, 2000)

1.3.2.6 ASUP 140

As a result of the continuing drive to reduce power generating costs from central tower CSP systems, 2012 saw Abengoa unveil the development of a new 138.7 m² hydraulic heliostat named ASUP 140 (Figure 14) (Abengoa, 2012; Pfahl et al., 2017). Using a new concept of facet that combines a 2 mm sheet of glass with a foam support, this model offers a series of innovative features including reflectivity levels of over 95 %, complete protection against rust and wear and improved mechanical resistance. In addition, the ASUP 140's new hydraulic tracking system provides unrivalled reliability and precision in comparison to the previously developed heliostats (i.e. PSI 120, Colon 70 and Sanlucar 90) (Figures 11 and 13).

Despite the cost savings that reached up to 30%, the heliostat still relies on the heavy steel-based support structure to provide the mirror facets with the necessary rigidity and support. This heavyweight support structure requires expensive drives with high torque capabilities to provide accurate sun tracking.



Figure 14: Abengoa ASUP 140 heliostat

(Abengoa, 2012)

1.3.2.7 Solaflect Energy

Solaflect developed a new design of heliostats with the intention of reducing the amount of steel in the heliostat structure. The new design is built like a suspension bridge, stabilizing the mirror structure with steel cables from the front and rear, as seen in Figure 15 (Bender, 2013). The reflective surface area of Solaflect's heliostat is 16 m² and composed of a four-by-four matrix of facets; each 1 meter by 1 meter in size.

Although the design managed to reduce the amount of steel by approximately 60%, the drawbacks of this model are the bi-directional shading from the components in front of the mirror as well as the cable adjustment difficulties.



Figure 15: Solaflect suspension heliostat

(Bender, 2013)

1.3.2.8 eSolar

eSolar® introduced in 2014 its new heliostat system: the SCS5 (Ricklin et al., 2014; eSolar®, 2014). SCS5 consists of three main components: the structure, the reflector module, and the drive. The SCS5 has an optimized triangular truss structure which provides better stiffness and requires a significantly lower steel composition. As can be seen in Figure 16, the tripod configuration (triangle with three heliostats) reduced ground preparation costs while maintaining structural stability. The reflector module consists of a mirrored glass with an area of 2.2 m². The reflector module is supported with a non-

complicated metallic frame that can be easily connected to the drive and controlled accurately. The SCS5's drive houses two inexpensive stepper motors which provide a two-axes movement.

Several drawbacks have been identified in the SCS5 heliostat such as exposed actuation mechanisms, clumsy height adjustment, and reflector durability. Moreover, for large thermal solar power plants producing between 50 to 100 MW of energy, the eSolar's small reflective area means that hundreds of thousands of heliostats must be installed in order to provide these energy rates.



Figure 16: eSolar® SCS5 heliostat

(Ricklin et al., 2014; eSolar®, 2014)

1.3.2.9 Vast Solar

Vast Solar's heliostats, following the same approach of manufacturing small-area reflectors, consist of a single 3.6 m² mirror and an azimuth-elevation drive that are mounted on a pylon rammed directly into the ground (Figure 17) (Vast Solar, 2017; Pfahl et al., 2017). The pylons are connected to each other by vertical tubes. These tubes increase the stability of the pylons and reduces the effort of installing the cables for power

supply and control below ground level by connecting them to the tubes (Vast Solar, 2017; Pfahl et al., 2017).

However, and similar to eSolar’s heliostats, providing high energy rates would require installing hundreds of thousands of Vast Solar heliostats due to its small reflector area. This will significantly increase the total cost of power generation.

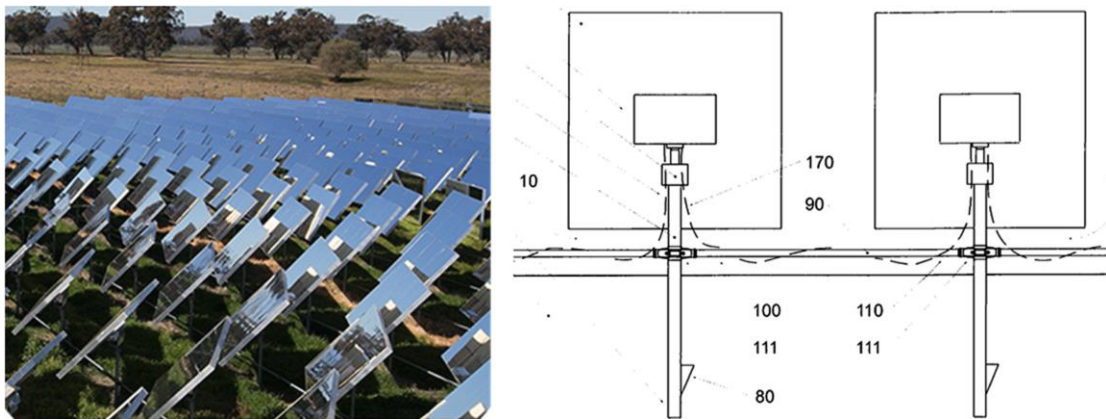


Figure 17: Vast Solar heliostats

(Vast Solar, 2017; Pfahl et al., 2017)

1.3.2.10 Stellio

Presented by Balz et al. (2015), the new heliostat “Stellio” of schlaich bergemann partner (sbp) (Figure 18) consists of a 48 m² pentagonal-shaped mirror fixed to a steel-based support structure that consists of 10 cantilever arms and a central hub (Pfahl et al., 2017). The Stellio heliostat’s mirror support structure is mounted to a torque tube similar to the ones used in conventional T-type heliostats but smaller in size. The torque tube and the pedestal together are connected to each other by a drive system that consists of two linear actuators (von Reeken et al., 2016).

Despite the weight savings achieved by reducing the load path through the support structure, the Stellio heliostat still depends on the heavy steel-based support structure to provide the reflective module with the essential rigidity. This heavyweight back support structure requires expensive heavy duty drives to provide accurate sun tracking.



Figure 18: Stellio heliostat

(von Reeken et al., 2016; Pfahl et al., 2017)

1.3.3 Heliostat cost reduction opportunities

Amongst the major components that a typical heliostat consists of (e.g., reflective mirror module, back support structure, drive, torque tube and pedestal) (Figure 8), it was reported that for both large and small-area heliostats, the drive element (the component responsible for applying the necessary rotations to the structure in order to direct the solar irradiation to the specified point location) holds the most influence on the production cost of heliostats (Kolb et al., 2011). Large-area heliostats require a high-torque drive, due in part to the heavy mirror support structure that is generally designed from steel. Kolb et al. (2007) provided a relation between the drive's torque capacity and the heliostat's drive

cost. It was found that the torque capacity had a substantial impact on the drive cost and, therefore, a promising opportunity arises for reducing the cost of heliostats by reducing the mirror support structure's total weight while maintaining the heliostat's tracking performance and rigidity.

One possible solution is to use sandwich composites due to their lightweight properties and high flexural stiffness (Heimbs et al., 2008; Ayub et al., 2011; Cheng et al., 2016; Lande and Patil, 2015). This type of composite is frequently used in automotive, marine and aerospace structures (Birman and Kardomateas, 2018) and consists of a lightweight core sandwiched between two thin facing layers using a strong adhesive. The core is produced from thick and lightweight materials with the capability of withstanding normal and shear loads (Zenkert, 1997). On the other hand and generally made of high-strength materials, the faces handle both compressive and tensile loads due to bending. For such type of composites, the honeycomb-shaped configuration (Figure 19) has been commonly utilized as a core because it benefits from its voids for mass reduction while preserving stiffness. Added also to the previously mentioned advantage, various properties can be obtained by a simple variation in the honeycomb's geometrical configuration.

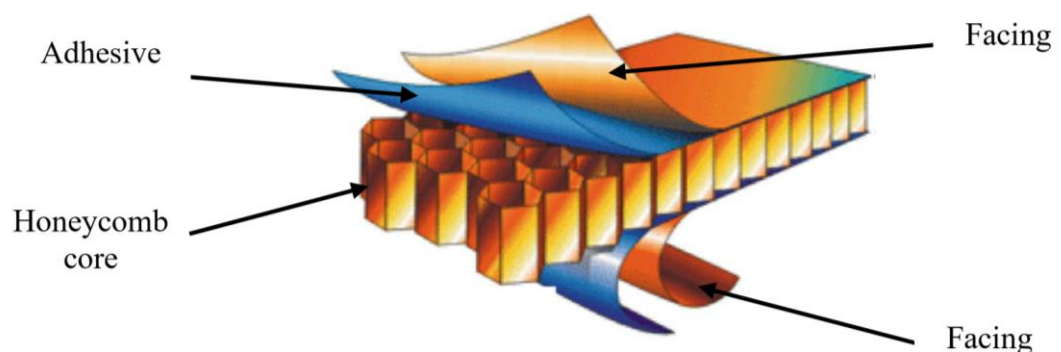


Figure 19: Honeycomb sandwich composite structure

(Abbadi et al., 2009)

Heliostats are exposed to the atmospheric conditions prevailing on the field. They experience aerodynamic forces caused by wind that can lead to structural deformations, affecting the heliostat's optical performance. One of the challenges faced in implementing such systems is ensuring that they are able to cope with these aerodynamic loads imposed upon them. Although much research has been devoted to investigate the aerodynamic forces encountered by heliostats (Peterka et al., 1986; Peterka and Derickson, 1992; Wu et al., 2010; Pfahl et al., 2011; Emes et al., 2017), it is surprising that there is a dearth of research studies that attempted on investigating the suitability of honeycomb sandwich composites for use as a heliostat mirror structure. Moreover, despite very few attempts found in literature that utilized sandwich composites but with different core materials and configurations (Diver and Grossman, 1998; Aldaz et al., 2018; Liedke et al., 2018), they did not investigate in great detail the interaction between the wind and sandwich composites employed as a heliostat mirror support structure. In addition, the aforementioned attempts lacked details concerning material properties, the influence of the utilized sandwich composite's physical parameters on the structural performance of the heliostat and considered only small-area heliostats (in particular, 8 m² size in Aldaz et al. (2018) and 9 m² size in Liedke et al. (2018)) and did not take into account large-area heliostats (>100 m²).

1.4 Summary and research objective

According to what has been covered in the literature, including the opportunity of reducing the heliostat's cost by minimizing the total weight of the structure, and the fact that honeycomb sandwich composites have been used in a wide range of applications due to their high stiffness to weight ratios, clearly there is a marked absence of research studies that attempted on assessing the suitability of honeycomb sandwich composites as a heliostat structure. Given that heliostats are sensitive to wind loads, there is a need for

a better understanding on how honeycomb sandwich composites respond under wind effects when utilized as the structure for heliostat mirror. In addressing this, the central question for this work is:

“How can honeycomb sandwich composites be utilized to develop a robust, lightweight heliostat mirror support structure that is capable of withstanding wind loads at various operational conditions?”

Chapter 2: Flow behaviour and aerodynamic loading on a stand-alone heliostat: Wind incidence effect

In the preceding chapter it was noted that a promising opportunity arises for reducing the cost of heliostats by diminishing the mirror support structure's total weight using honeycomb sandwich composites instead of conventional steel in designing the heliostat's support structure. One of the challenges in realising this goal is the issue of wind loads (Peterka and Derickson, 1992). The fact that heliostats are typically located in open terrain sites means they are constantly exposed to wind loads that cause structural deformations which could affect the heliostat's optical and tracking accuracy. To begin to address the research question posed in the previous chapter, an understanding is required of the airflow which cause the aerodynamic loads acting on a heliostat.

The aerodynamic loads encountered by heliostats can be determined by utilizing normalized load coefficients which are a function of the structure's shape and orientation. These represent the four major loadings that act on the heliostat structure: drag, lift and base overturning and hinge moments (Figure 20). Investigations into these aerodynamic loadings have historically been using scaled heliostat models in wind tunnels (Peterka et al., 1986; Peterka and Derickson, 1992; Wu et al., 2010; Pfahl et al., 2011; Emes et al., 2017), or numerically by means of computational fluid dynamics (CFD) (Marais et al., 2015; Mammar et al., 2017; Ghanadi et al., 2017a).

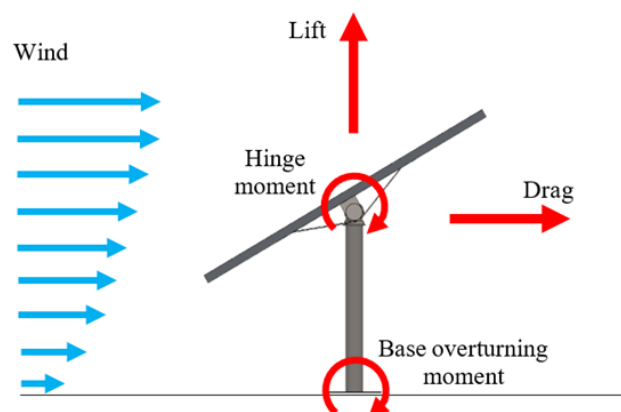


Figure 20: Geometric description of load coefficients

In their wind tunnel study Wu et al. (2010) investigated the effect of mirror spacing on the wind loads experienced by a faceted heliostat. The study revealed that the gaps between the mirror facets did not influence the wind loads experienced by the heliostat. Pfahl et al. (2011) used wind tunnel testing to undertake an extensive investigation of the impact of the aspect ratio of mirror panels (width to height) on the wind loads of heliostats, while more recently, Emes et al. (2017) used this approach to explore the peak wind loads experienced by a heliostat in the stow position as a function of the winds turbulence characteristics.

In parallel with these wind tunnel studies, a number of researchers have used CFD in their heliostat investigations. In their work, Mammar et al. (2017) performed CFD simulations of the air flow around an isolated full-size heliostat to provide a quantitative assessment of mean wind loads at varying tilt angles. Using a similar approach Ghanadi et al. (2017a) determined the drag force on a single square heliostat at various tilt angles within the atmospheric boundary layer under varying turbulence intensities. From this it was shown that the aerodynamic loads encountered by a heliostat varied significantly with turbulence intensity. In a subsequent study (Ghanadi et al., 2017b), the same authors demonstrated that the variation in wind loads experienced by a heliostat could be determined by specifying a design mean wind load and a gust factor (defined as the ratio of actual wind gust to mean wind velocity).

Given the role that wind plays on the design of heliostats it is surprising that the issue of the wind incidence angle on their aerodynamic coefficients has not been widely considered. For instance, the studies conducted by Emes et al. (2017), Mammar et al. (2017) and Ghanadi et al. (2017a) considered only 0° wind incidence angle (the wind directly striking the reflective surface of the heliostat structure) in their heliostat investigations. Pfahl et al. (2011), on the other hand, considered 0° , 60° , and 90° wind incidence angles in their study. However, only 90° (wind flow perpendicular to the mirror

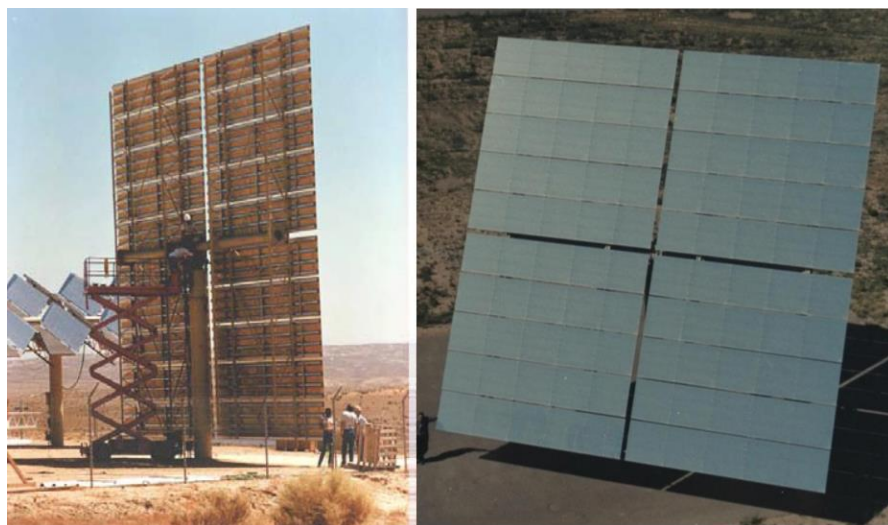
surface) and 0° (stow position) tilt angles were examined for the 60° and 90° wind incidence angles, respectively.

As for the wind tunnel tests conducted by Peterka et al. (1986) and Peterka and Derickson (1992), their investigations into wind loads on heliostats were carried out for wind incidence angles between 0° to 180° in increments of 22.5° and a range of tilt angles between 90° and 0° . Wu et al.'s (2010) study considered also the same range of wind incidence angles (i.e. 0° to 180°) but in increments of 30° and a range of tilt angles between 90° and 0° . However, these wind tunnel tests conducted by Peterka et al. (1986), Peterka and Derickson (1992) and Wu et al. (2010) only reported wind load coefficients without relating their findings of the variation in wind loads with heliostat orientation to the airflow characteristics around the structure. Added to that, the aforementioned studies did not explore in any detail the wind incidence effect and the impact that has on the aerodynamic behaviour of a heliostat. Furthermore, various existing heliostat suppliers have performed wind tunnel tests and extracted aerodynamic loading data with even higher angular resolution ($\sim 10^\circ$) for wind incidence angle. However, such data typically is not published, but kept as proprietary information.

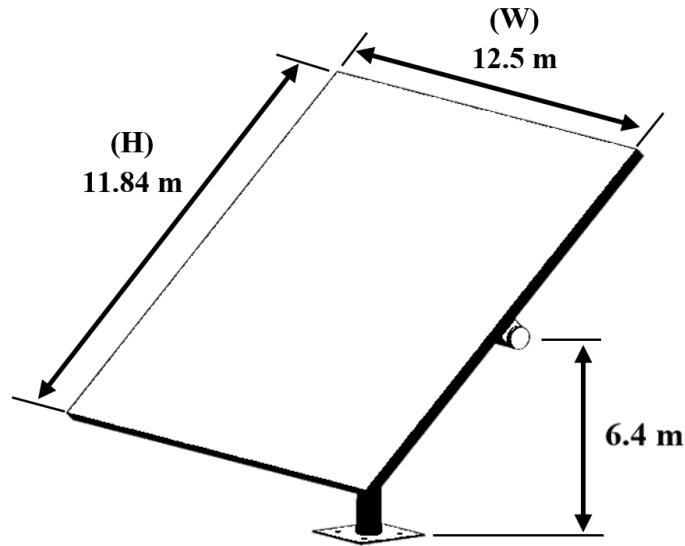
Hence, there is clearly a gap in knowledge and a need to deliver a better understanding of the effect of wind direction on the aerodynamic loading of a heliostat, relate the loads to the wind flow field around the structure, and to deliver a non-dimensional relationship for the wind loading coefficients (drag, lift, base overturning moment and hinge moment coefficients) to heliostat designers. This will assist in the development of lightweight heliostat mirror support structure with the capability to endure winds approaching from different directions.

2.1 Numerical setup

In this study, a computational fluid dynamics (CFD) analysis of the flow around a single heliostat with a geometry similar to an existing large-area heliostat manufactured by Advanced Thermal Systems (ATS) (Figure 21a) (Mancini, 2000; Kolb et al., 2007) was undertaken. Investigating the aerodynamic loads acting on a stand-alone heliostat serves as an upper design limit, as the vast majority of the energy from the wind is mainly handled by the heliostats at the edges of a heliostat field. CFD has proven to be a powerful tool for obtaining reliable predicted aerodynamic forces and moments on structures. It has been utilized in heliostat studies (Wu et al., 2010; Marais et al., 2015; Mammam et al., 2017) due to its flexibility when examining a diversity of heliostats designs and modifications and exploring their impact on the airflow around them (Bendjebbas et al., 2016). The selected heliostat has a reflecting area of 148 m^2 ($11.84 \text{ m (H)} \times 12.5 \text{ m (W)}$) and a vertical distance from the ground to the hinge axis of 6.4 m , as shown in Figure 21b. This size of reflector was chosen as a basis for this study, as Sandia National Laboratories' analysis of heliostat cost versus size (Kolb et al., 2007) indicated that heliostats with sizes around 150 m^2 show best economy compared to other heliostat sizes.



(a) Existing ATS 150 heliostat (Mancini, 2000; Kolb et al., 2007)



(b) Model geometry

Figure 21: Heliostat geometrical configuration

In undertaking the analysis, three-dimensional simulations of the wind flow over the heliostat structure were performed using ANSYS's commercial CFD software, FLUENT 16.2. Since the aerodynamic coefficients (i.e. lift, drag, hinge moment and base overturning moment coefficients) are Reynolds number independent over the typical wind velocities (Pfahl and Uhlemann, 2011), in conducting the simulations it was assumed that wind entered the domain at a free stream velocity (V_∞) of 5 m/s (a Reynolds number of $\sim 4.05 \times 10^6$, taking the heliostat chord length ($H = 11.84$ m) as the characteristic length). To ensure a sufficiently accurate simulation of the flow, the computational domain around the heliostat (Figure 22) was extended $10H$ downstream, to capture the wake of the heliostat, $5H$ upstream to allow the development of a boundary layer on the ground (a description and validation of this technique is provided in Appendix A) and $4H$ and $6H$ in the vertical and span-wise directions respectively, where H is the heliostat chord length ($H = 11.84$ m). Because of the turbulent nature of the flow, the Shear Stress Transport (SST) $k-\omega$ turbulence model was selected for this study. This model has been successfully employed in atmospheric boundary layer flow simulations

previously (Jubayer and Hangan, 2014; Rafiee et al., 2016; Uzair et al., 2017) because of its ability to predict flow separation, and given that it combines the advantages of both the $k-\epsilon$ model in the freestream and standard $k-\omega$ close to the wall (ANSYS, 2015).

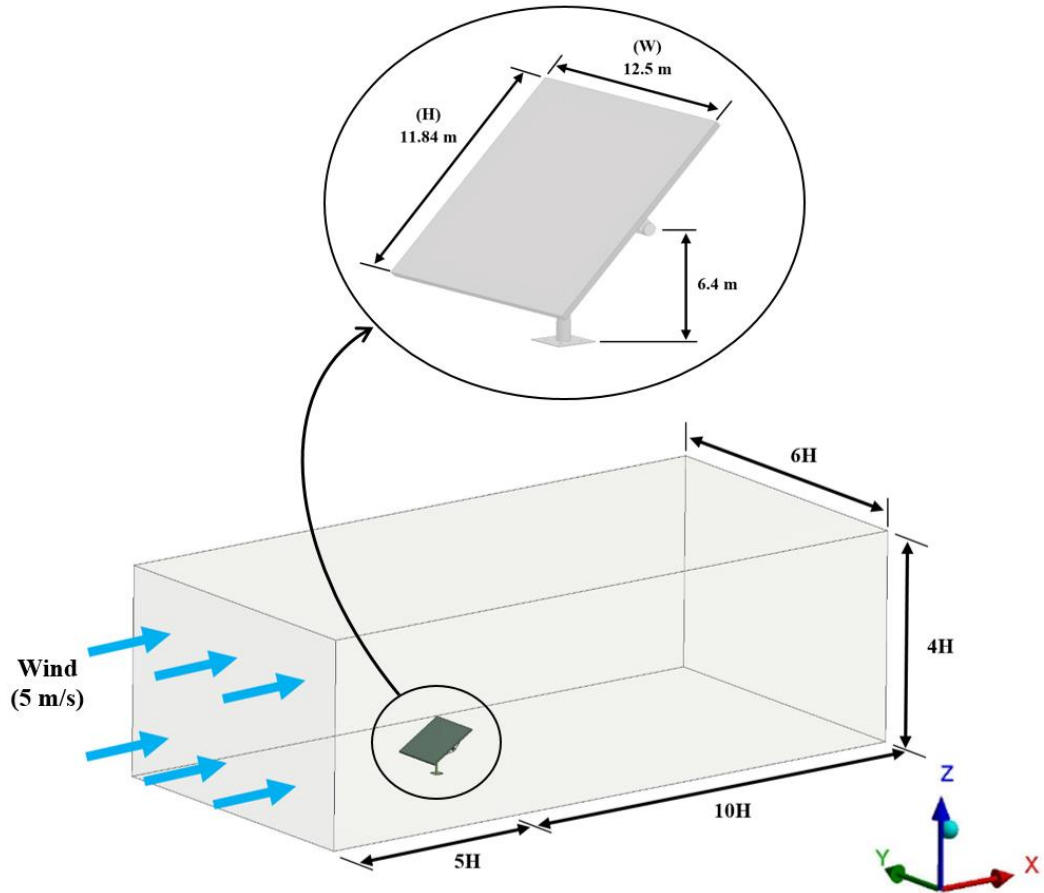
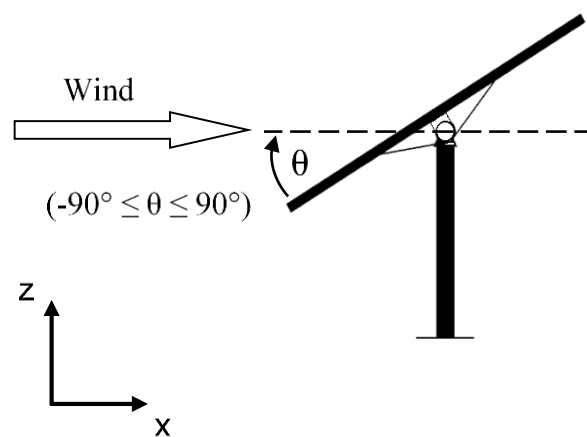


Figure 22: Computational domain

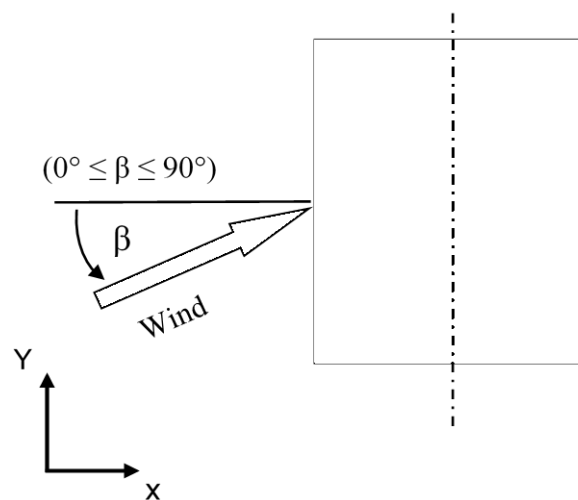
Furthermore, the domain's inlet was set as a velocity boundary condition, the outlet set as a zero gauge pressure boundary and both the heliostat and the ground were taken to be non-slip walls. A symmetry boundary was set at the remaining three sides of the computational domain, as suggested by Jubayer and Hangan (2014) in their numerical study of wind effects on a stand-alone ground mounted photovoltaic (PV) system. The domain was discretised in space with an un-structured mesh, where finer grid elements were employed near the heliostat and in its wake region and the regions away from the heliostat were meshed with larger grid sizes. A detailed mesh sensitivity analysis was performed to investigate the effect of grid sizes on the numerical results and is presented

in Appendix B. The grid independency test led to a domain consisting of approximately 13 million elements being used.

In determining the loading simulations were carried out for a range of tilt angles (θ) between 90° (wind flow perpendicular to the mirror surface) and -90° (wind impinging on the heliostat's back surface) and several wind incidence angles (β) between 0° to 90° in small increments of 11.25° as shown in Figure 23. Wind incidence can vary from 0° to 360° , but due to the symmetrical structure of the heliostat about a vertical axis and the consideration of both positive and negative tilt angles, the range of wind incidence angles (β) only needs to be varied from 0° to 90° . In this sense, a full range of tilt angles (positive and negative) and incidence angles ranging from 0° to 90° were evaluated.



(a) Side elevation



(b) Plan view

Figure 23: Coordinate system of heliostat model

2.2 Validation with available data of wind loading coefficients

To evaluate the numerical model's accuracy, the heliostat structure's predicted drag, lift, base overturning moment and hinge moment coefficients were compared with experimental and numerical results from previously published work for wind approaching at an angle (β) of 0° (Cermak et al., 1978; Peterka et al., 1986; Pfahl et al., 2011; Google, 2011; Wu et al., 2010; Mammam et al., 2017), as shown in Figures 24 and 25.

The aerodynamic coefficients, drag (C_D), lift (C_L), base overturning moment (C_{My}) and hinge moment (C_{MHy}) coefficients are defined as:

$$C_D = \frac{F_D}{\frac{1}{2} \rho V^2 A} \quad (1)$$

$$C_L = \frac{F_L}{\frac{1}{2} \rho V^2 A} \quad (2)$$

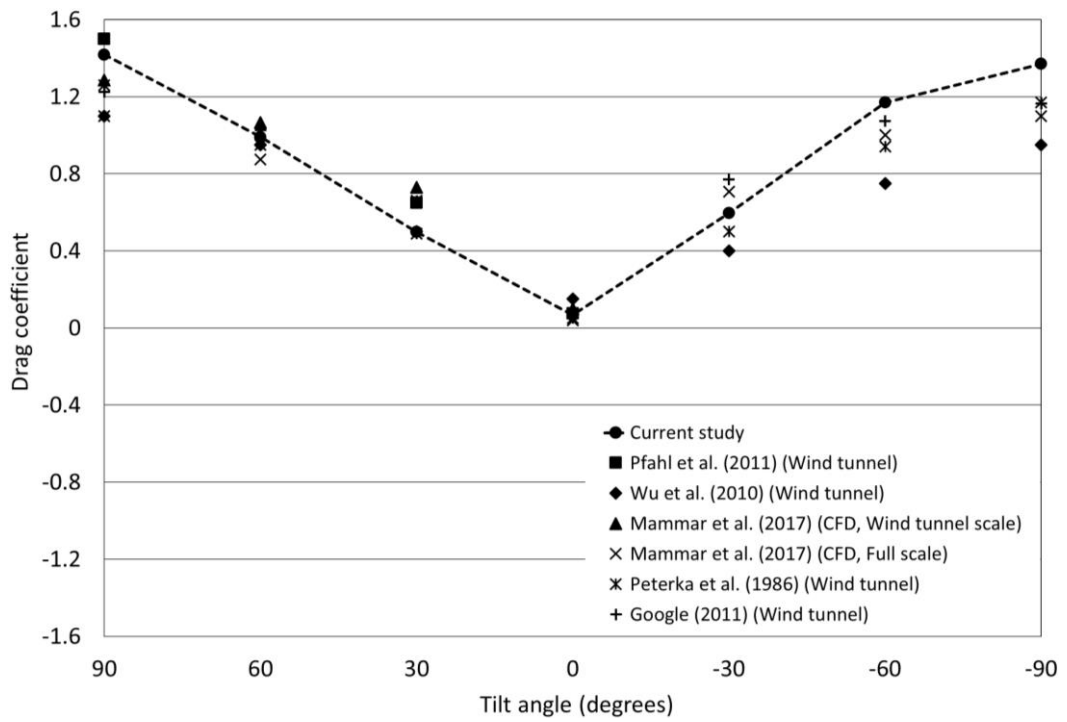
$$C_{My} = \frac{M_y}{\frac{1}{2} \rho V^2 A H} \quad (3)$$

$$C_{MHy} = \frac{M_{Hy}}{\frac{1}{2} \rho V^2 A h} \quad (4)$$

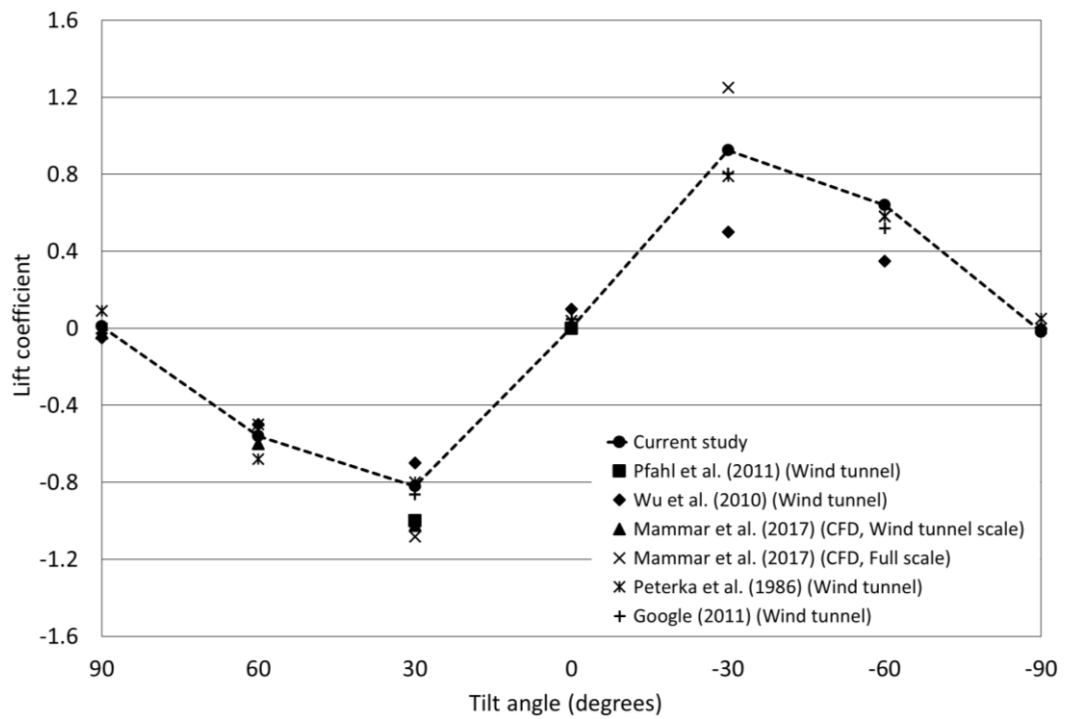
Where F_D and F_L are the drag and lift forces experienced by the heliostat, M_y and M_{Hy} are the base overturning and hinge moments, ρ is the density of air, V is the speed of the wind, A is the projected area of the reflector, H is the heliostat chord length and h is the vertical distance from the ground to the hinge axis ($h = 6.4$ m).

For this study, it can be seen that the results in Figures 24 and 25 correspond well with the drag, lift, base overturning moment and hinge moment coefficients of these previous studies. This implies that the CFD can quantitatively match the flow effects of the

heliostat. This is significant as it supports the use of such a technique in exploring the aerodynamic loads acting on such systems.

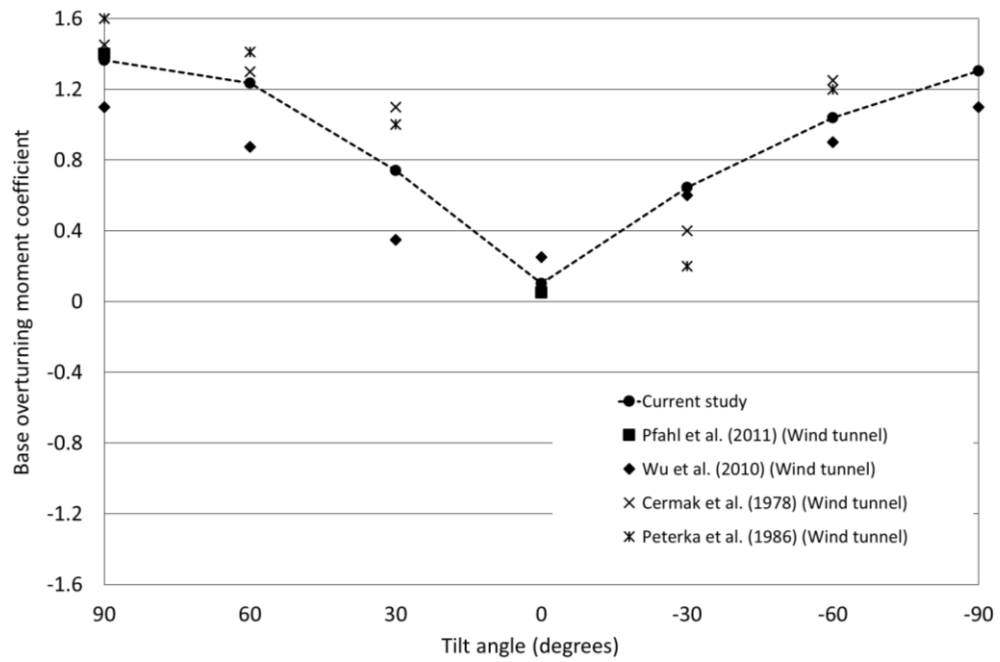


(a) Drag coefficient

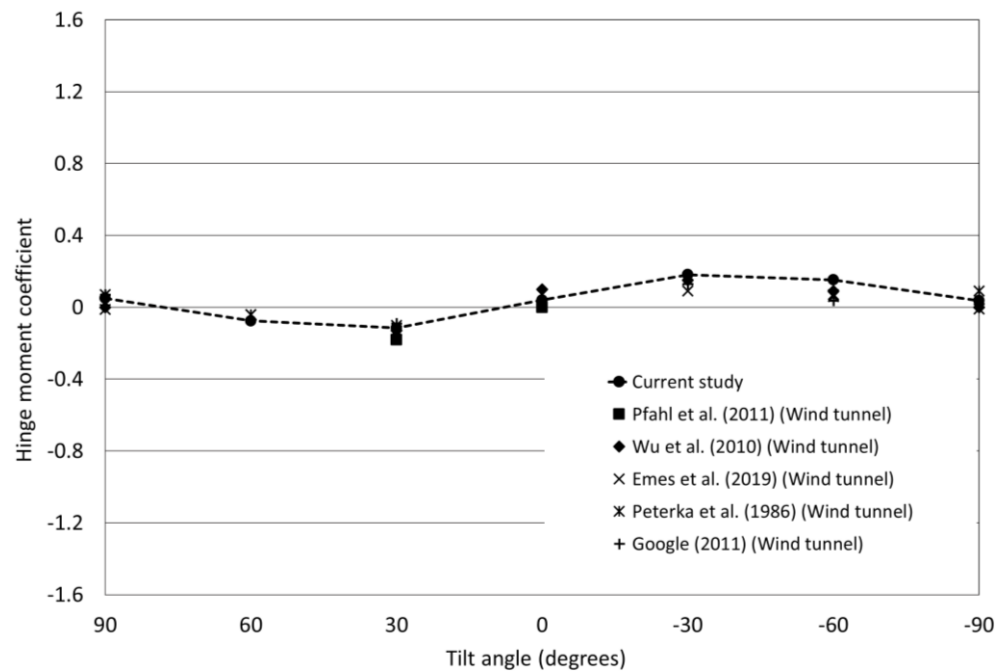


(b) Lift coefficient

Figure 24: Comparison of drag and lift coefficients at different tilt angles



(a) Base overturning moment coefficient



(b) Hinge moment coefficient

Figure 25: Comparison of base overturning moment and hinge moment coefficients at different tilt angles

The curves show that the heliostat receives the maximum drag force (Figure 24a) when the heliostat structure was tilted at an angle of $\theta = 90^\circ$. The maximum drag force with the maximum frontal projected area of the heliostat surface to the wind causes the structure

to experience the maximum base overturning moment (Figure 25a). As the heliostat structure is moved towards the stow position ($\theta = 0^\circ$), the drag value decreases until it reaches its minimum at this condition due to the decrease in the projected area of the heliostat. Due to the reduced influence of drag, the base overturning moment also decreases with a similar trend and reaches its lowest value at $\theta = 0^\circ$. However, by altering the structure's tilt angle from the stow position to a -90° tilt angle (heliostat's back surface facing the wind), the opposite occurs, and the values of both drag and base overturning moment increase. However, it is interesting to note that they reach a slightly lower drag and base overturning moment coefficients' values than the ones recorded at an angle of $\theta = 90^\circ$, due to the influence of the heliostat's pedestal and torque tube.

Opposed to drag forces, Figure 24b demonstrates that the heliostat experiences approximately zero lift force at 90° and -90° tilt angles as a result of minimum lift area (maximum drag area). By varying the tilt angles from 90° and -90° , the negative (downward directed) and positive (upward directed) lift forces are experienced by the heliostat structure. In case of positive tilt angles, the negative lift force reaches its maximum when the structure is tilted at an angle of 30° due to the high pressure on the heliostat's front side and the low pressure below the reflector. Due to the increased influence of negative lift forces, the negative (anti-clockwise direction of rotation) hinge moment also increases with a similar trend and reaches its maximum value at $\theta = 30^\circ$ (Figure 25b). As the structure is moved towards $\theta = 0^\circ$ (stow position), the pressure difference between the heliostat's front and rear surfaces becomes very small and the heliostat experiences almost zero lift force at this orientation. This causes the structure to experience the minimum hinge moment. In case of negative tilt angles, both the lift force and hinge moment first increase to a maximum value at $\theta = -30^\circ$ and then due to the progressive decrease in the lift area as the structure's tilt angle approaches $\theta = -90^\circ$, the lift force decreases to a zero value causing the hinge moment value to drop.

2.3 Effect of tilt on flow field

Relating the aforementioned wind load variations with tilt angle to the flow field around the heliostat, Figures 26-32 illustrate the velocity streamlines around the heliostat along the domain's center plane (with flow moving from left to right) at different tilt angles. The flow around the heliostat demonstrates noticeably different flow structures with various tilt angles.

Starting from the case when flow is perpendicular to the heliostat's reflective surface, i.e. 90° tilt angle (Figure 26), the structure blocks the horizontal movement of air. This interception causes the flow's velocity in the front of heliostat structure to move towards a stagnation condition (zero wind velocity), producing high-pressure in the front of the heliostat. Moreover, the blockage to wind flow provided by the heliostat structure causes also the flow to separate at the edges facing the windward direction, generating two strong recirculating vortices generated as a result of the reduced pressure in the heliostat's wake thus explaining the maximum drag force and base overturning moment and minimum lift force and hinge moment.

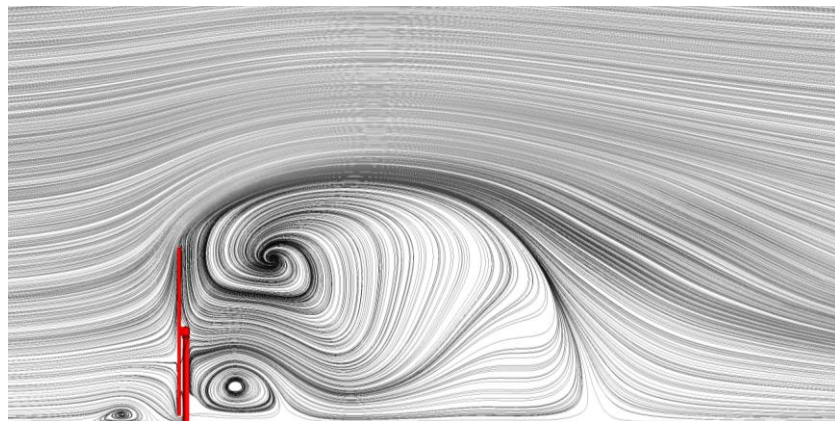


Figure 26: CFD streamlines around the heliostat for 90° tilt angle

By changing the tilt angle to $\theta = 60^\circ$ (Figure 27), again two large vortices are formed at the back of the heliostat as a result of the flow separation that occurs at the edges of the heliostat. However their intensities are lower compared to the 90° tilt angle case. This indicates the gradual decrease in the pressure difference between the heliostat's windward and leeward surfaces and explains the reduction in the drag and base overturning moment coefficients. In turn and due to the high pressure generated in the front of heliostat by the deceleration of the flow and the low pressure below the structure, the heliostat at this orientation experiences a downward directed lift force (negative lift coefficient) that causes an increase in the negative hinge moment.

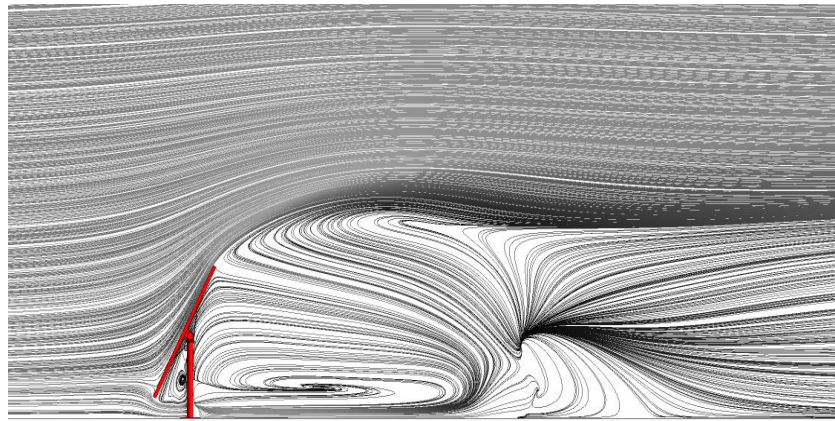


Figure 27: CFD streamlines around the heliostat for 60° tilt angle

As the tilt angle decreases to 30° (Figure 28), the projected area of the heliostat directly facing the wind decreases and the influence of the blockage becomes less, causing the drag and base overturning moment coefficients to drop. Similar to the 60° tilt angle and as a result of the flow separation that takes place at the upper and lower edges of the structure, two recirculating vortices are generated at the back of the heliostat. However their sizes are smaller compared to the aforementioned operational conditions i.e. 90° and 60° tilt angles. At $\theta = 30^\circ$, the structure experiences the maximum negative lift force due to the high pressure on the front side of the heliostat and the low pressure and high

velocities below the structure. Due to the increased influence of negative lift forces, the negative hinge moment also increases and reaches its highest value at the same tilt angle.

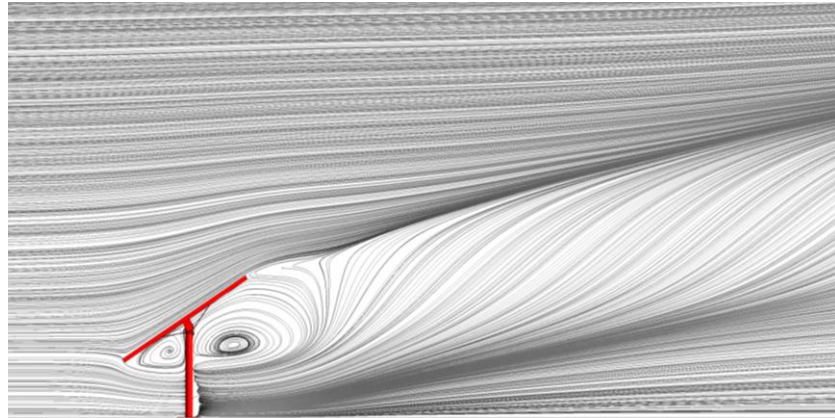


Figure 28: CFD streamlines around the heliostat for 30° tilt angle

As the heliostat structure reaches a 0° tilt angle (Figure 29), the projected area of the reflector directly facing the wind becomes very small, which allows the flow to become uniform and attached to the heliostat's surface. The uniformity of the flow causes a significant reduction in the pressure difference between the heliostat's front and rear surfaces, which would lead the wind loading coefficient values of drag, lift, base overturning moment and hinge moment coefficients to drop and reach their minimum.

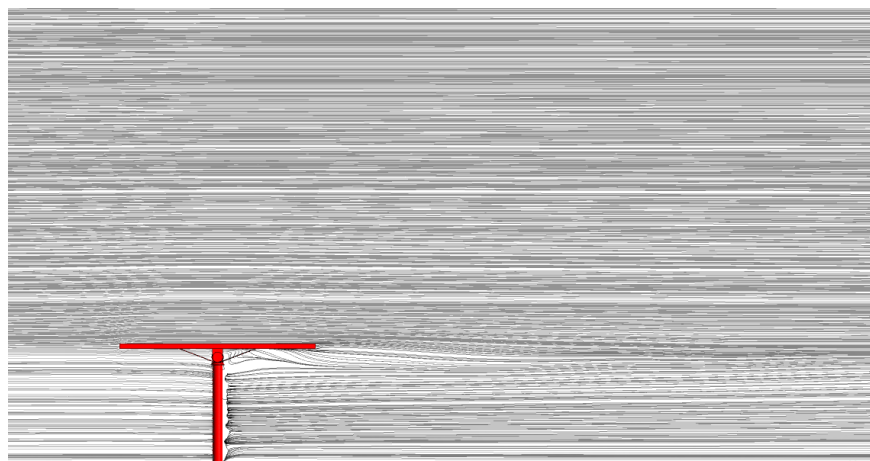


Figure 29: CFD streamlines around the heliostat for 0° tilt angle

By altering the tilt angle from $\theta = 0^\circ$ to $\theta = -30^\circ$ (Figure 30), such that the flow is from the backside of the heliostat structure, the heliostat's windward projected area increases and consequently the blockage effect increases, causing an increase in the drag and base overturning moment coefficients. Furthermore, and as a result of the flow interception by the structure, a strong vortex that covers the entire leeward side of the heliostat, and a small one located at the lower edge of the reflector are formed. At this operational condition ($\theta = -30^\circ$), the heliostat experiences the maximum lift force because of the high pressure generated in the back of heliostat by the deceleration of the flow and the low pressure above the structure caused by flow separation. As a result, the hinge moment also increases and reaches its maximum value at the same tilt angle.

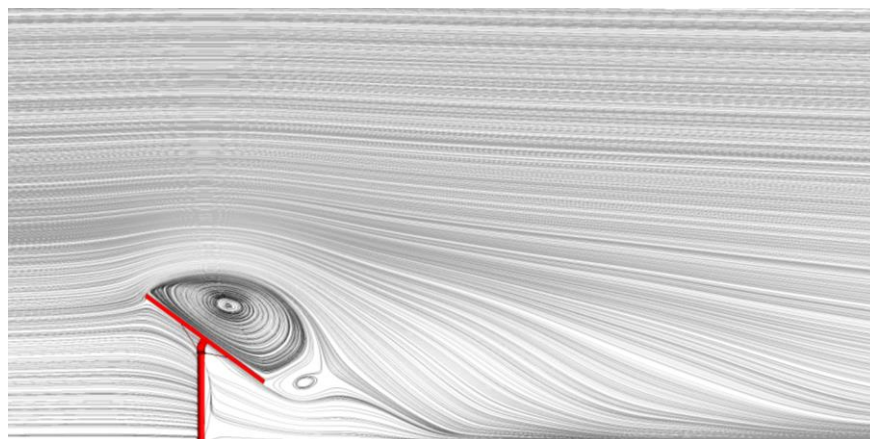


Figure 30: CFD streamlines around the heliostat for -30° tilt angle

As the tilt angle gradually changes from $\theta = -30^\circ$ to $\theta = -90^\circ$ (Figures 31 and 32), the projected area increases and the circulation region behind the heliostat structure increases sharply as a result of an increase in the pressure difference between the heliostat's windward and leeward surfaces, generating two large vortices at the back of the heliostat due to the reduced pressure in the heliostat's wake and explaining the increase in the drag and base overturning moment coefficients. In turn and due to the decrease in the heliostat

structure's lift area as the tilt angle moves from -30° to -90° , the lift force decreases until it reaches its minimum at $\theta = -90^\circ$. As a result of the reduced influence of lift force, the hinge moment also drops with a similar trend and reaches its minimum at $\theta = -90^\circ$.

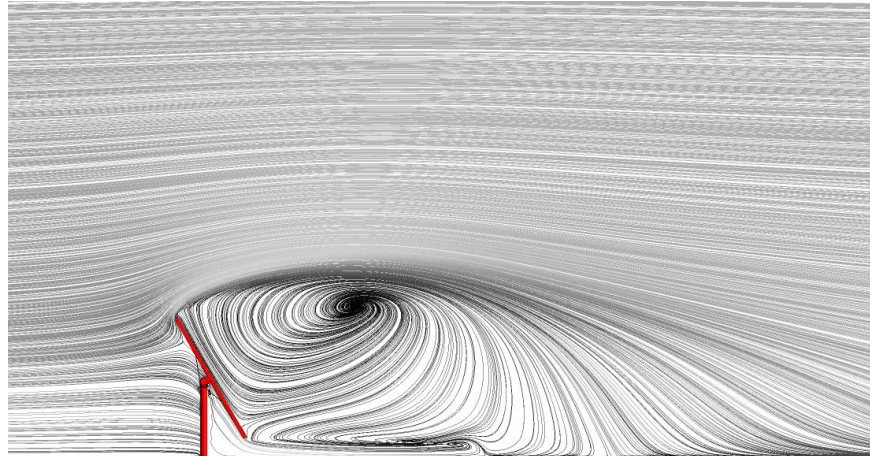


Figure 31: CFD streamlines around the heliostat for -60° tilt angle

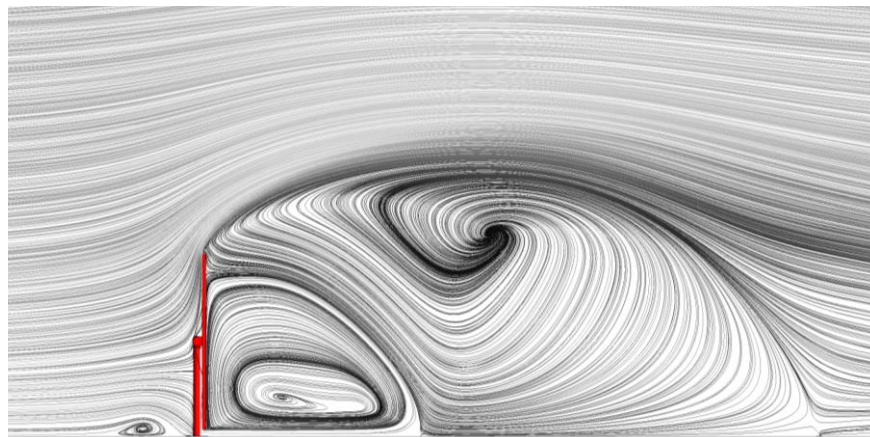


Figure 32: CFD streamlines around the heliostat for -90° tilt angle

2.4 Effect of wind incidence on the aerodynamic loading characteristics

Having validated the method and discussed the effect of tilt angle on the aerodynamic loading of the heliostat and the flow field around the structure, the effect of varying the wind incidence angle on the drag, lift, base overturning moment and hinge moment

coefficients is shown in Figures 33-36. It can be seen that as the wind incidence angle changes from $\beta = 0^\circ$ to $\beta = 22.5^\circ$, the drag (Figure 33) and base overturning moment (Figure 35) values do slightly decrease. On the other hand, and under the same conditions, it is apparent that the increase in the wind incidence angle has little influence on the lift coefficient (Figure 34) and hinge moment coefficient values (Figure 36). However, a wind incidence angle of 45° results in a significant reduction in the drag and base overturning moment coefficient values and a very slight decrease in the lift and hinge moment coefficients' magnitudes. Moreover, as the wind incidence angle increases from 45° to 67.5° , only the lift coefficient values occurred at a tilt angle of 30° and -30° are significantly affected, and their values notably decrease compared to the remaining angles of operation. Despite this observation, it can be clearly noted that this decrease in the lift forces does not strongly affect the hinge moment coefficient values at the aforementioned tilt angles. Increasing the wind incidence angle to 90° leads to a significant drop in the coefficients' values, which approach zero.

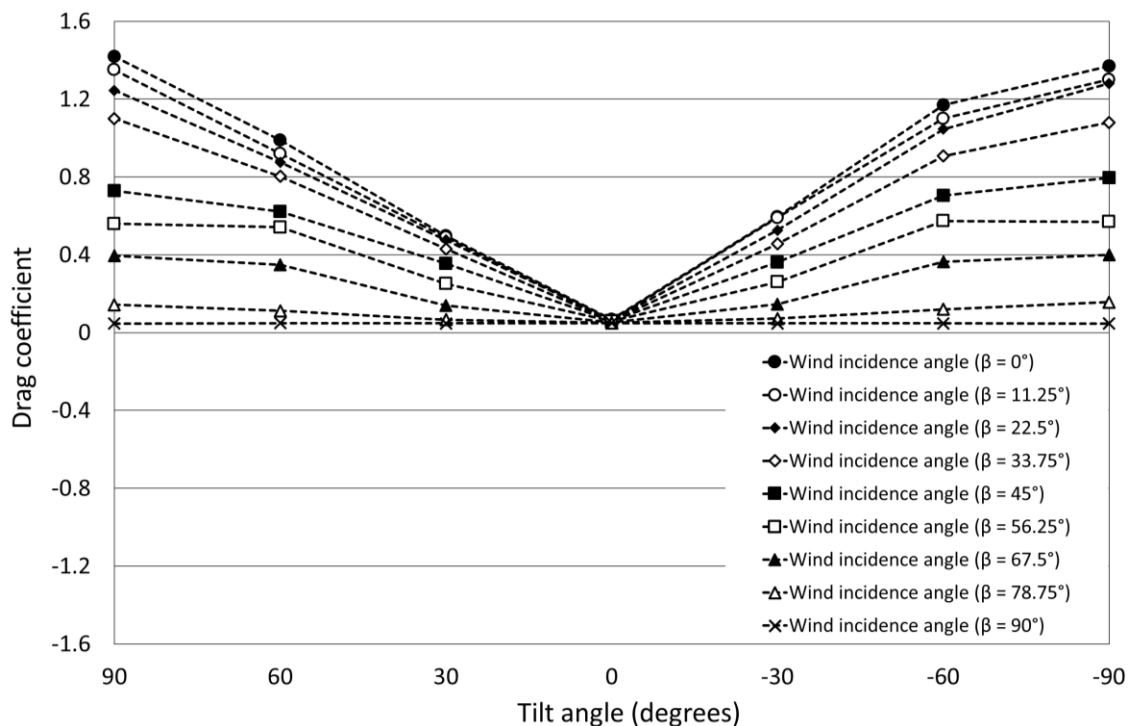


Figure 33: Wind incidence angle comparison of drag coefficient for different tilt angles

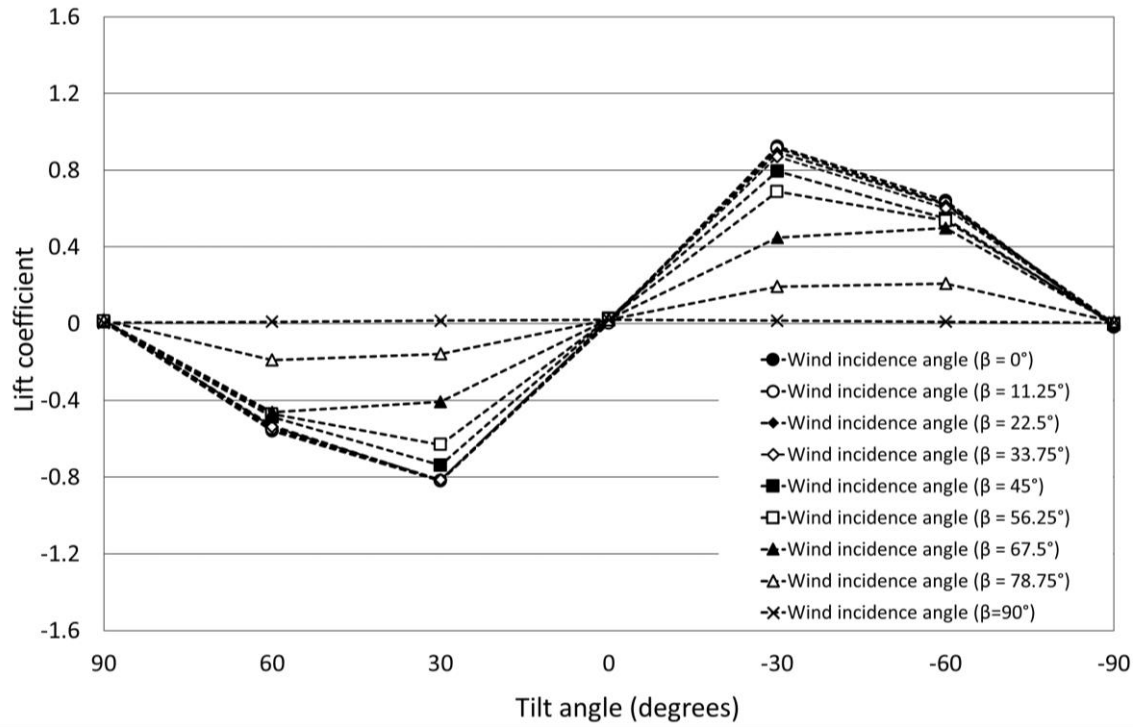


Figure 34: Wind incidence angle comparison of lift coefficient for different tilt angles

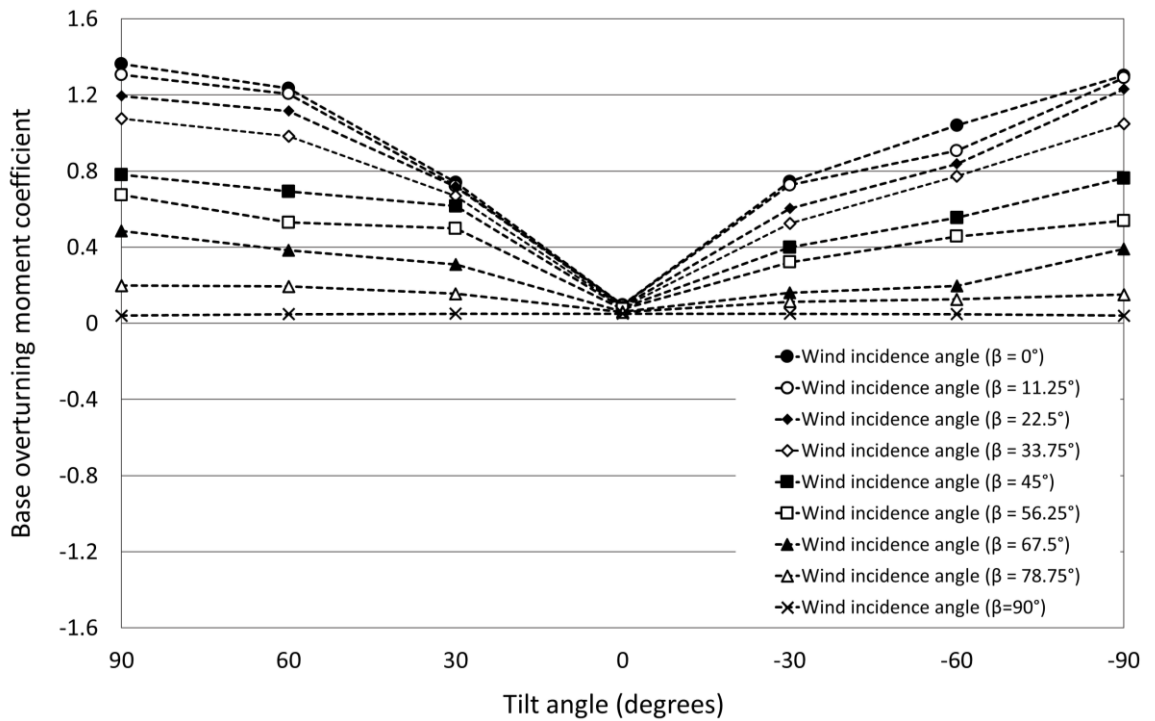


Figure 35: Wind incidence angle comparison of base overturning moment coefficient for different tilt angles

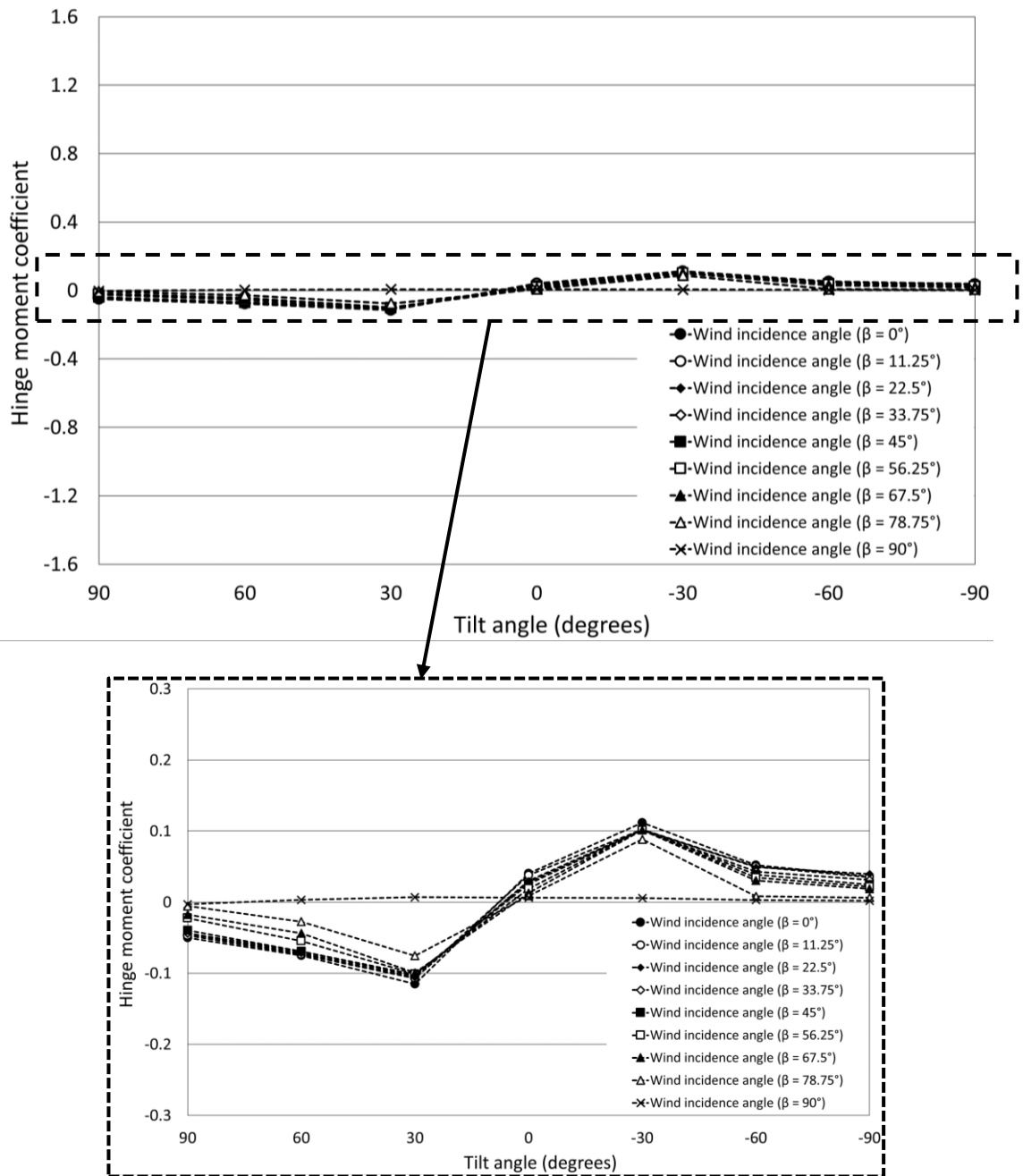
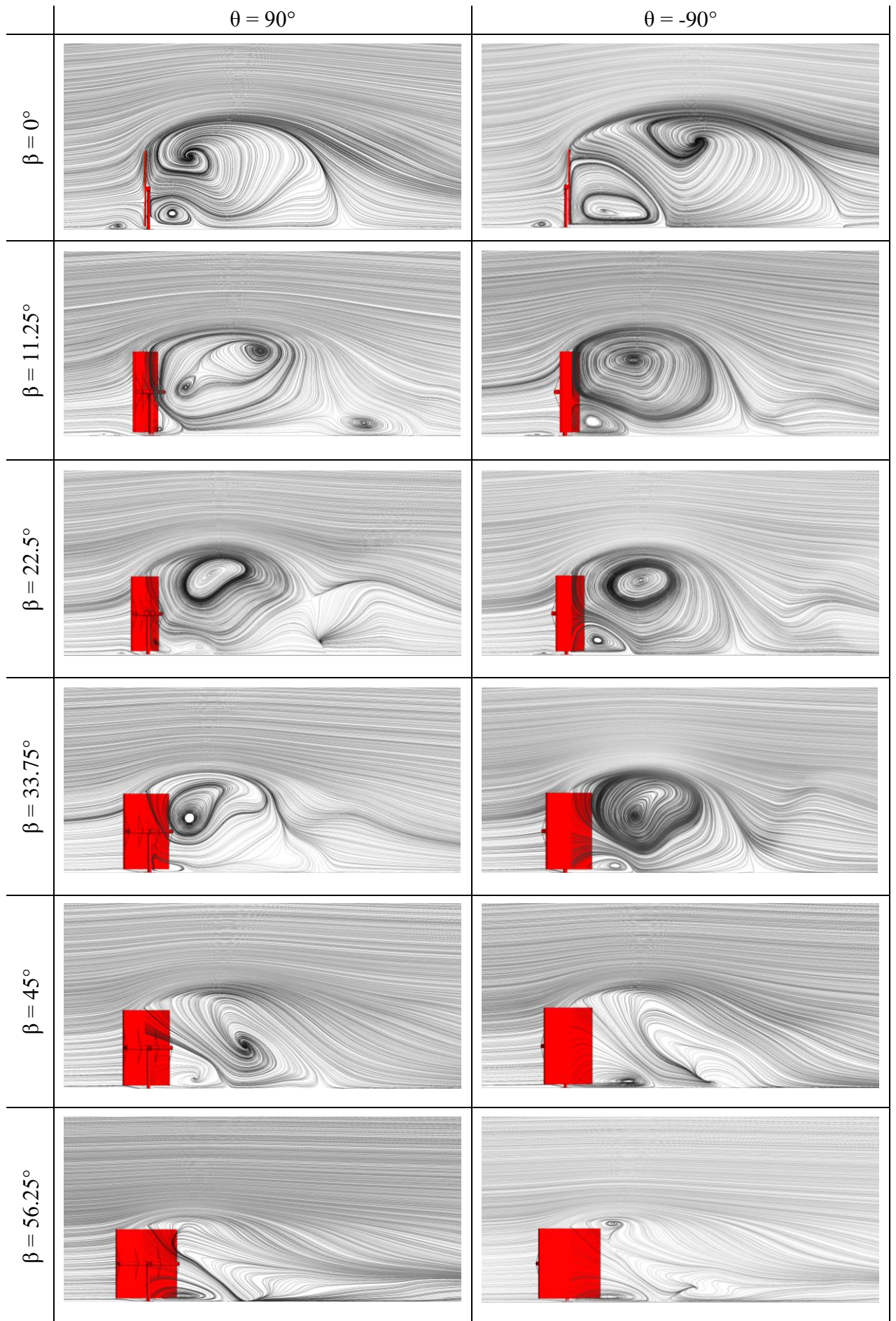


Figure 36: Wind incidence angle comparison of hinge moment coefficient for different tilt angles

2.5 Effect of wind incidence on flow field

Having discussed the wind load variations with wind incidence it was decided to explore the influence of the wind incidence angle on the aerodynamic behaviour of the heliostat in detail. Figures 37 and 38 present the velocity streamlines around the heliostat along the domain's center plane for various wind incidences.

When the drag and base overturning moment coefficients' results from the validation simulations were at a maximum i.e. $\pm 90^\circ$ tilt angle and 0° wind incidence angle; the CFD streamlines (Figure 37) illustrate the heliostat structure blocking the air's horizontal movement. Due to this interception as discussed earlier, the flow separates at the edges facing the windward direction, creating two strong recirculating vortices generated as a result of the reduced pressure in the heliostat's wake thus explaining the maximum drag force and base overturning moment and minimum lift force and hinge moment. Exploring this further, the intensity of the recirculating vortices generated at the back corners of the heliostat's structure reduces as the wind incidence angle (β) moves from 0° to 45° . This would imply that the drag forces reduce due to a decrease in the pressure difference between the heliostat's windward and leeward surfaces, causing a decrease in the base overturning moment experienced by the heliostat. Taking this further, as the incidence angle increases from 45° to 67.5° , the recirculation region almost disappears. Once the wind incidence reaches an angle of 90° , the incoming flow becomes uniform and attached to the heliostat's surface, resulting in the effective demise of the recirculation regions. This is due to a reduction in the pressure gradient between the heliostat's front and rear surfaces, which lead to a significant drop in the drag and base overturning moment coefficients' values.



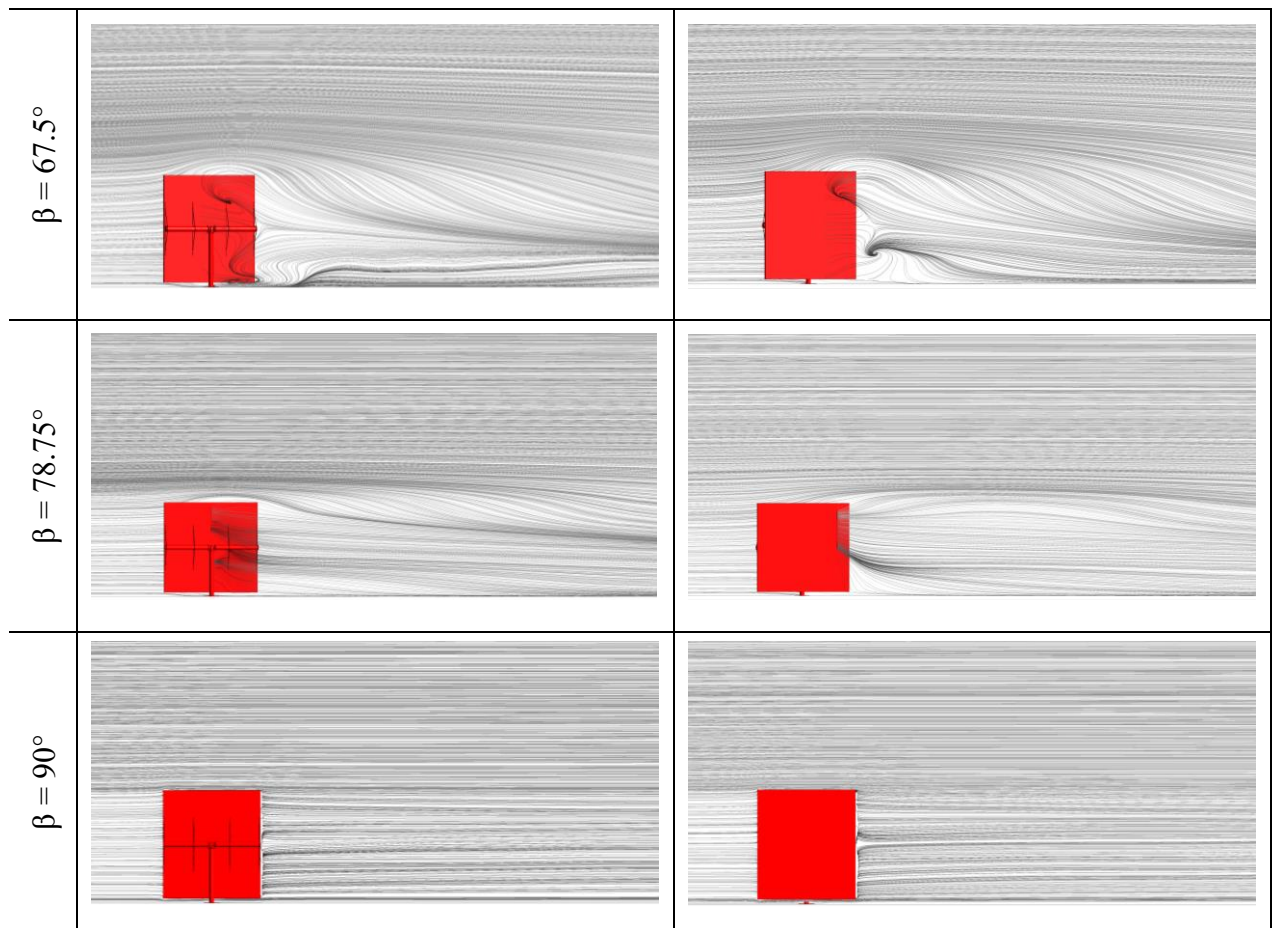
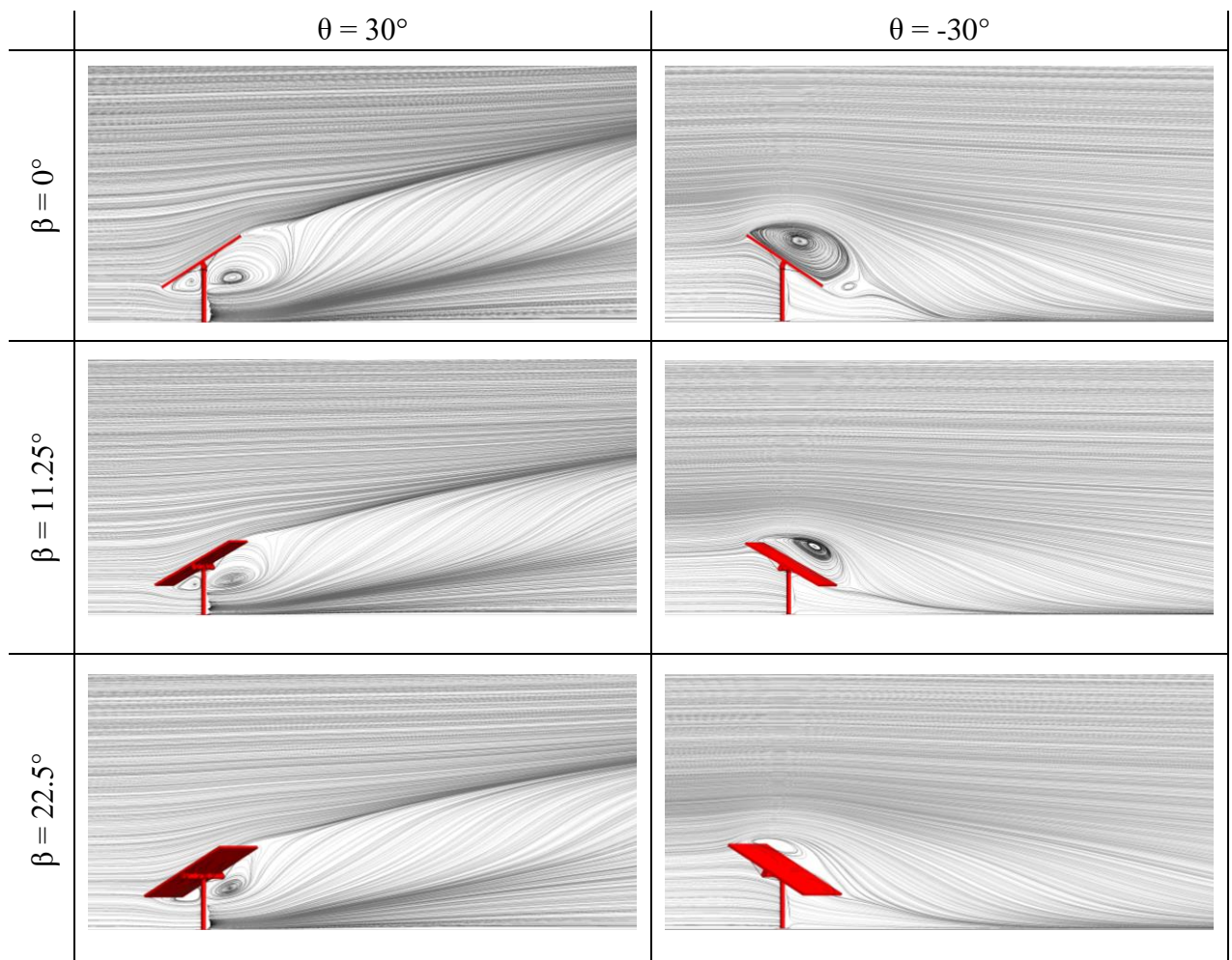


Figure 37: CFD streamlines around the heliostat at 90° and -90° tilt angles for a range of wind incidence angles

Moving to the case where the lift and hinge moment coefficients' results were at a maximum in the validation simulations, i.e. $\pm 30^\circ$ tilt angle and 0° wind incidence angle, the streamlines (Figure 38) show that as the flow approaches the structure, flow separation occurs at the heliostat's upper and lower edges. This results in two large vortices located at the back of the heliostat. Taking the same wind incidence angle but changing the tilt angle to $\theta = -30^\circ$ results in a strong vortex that covers the entire leeward side of the heliostat, and a small one located at the lower edge of the reflector. However, varying the wind incidence angle from $\beta = 0^\circ$ to $\beta = 22.5^\circ$ does not affect the flow pattern greatly when the structure is tilted at an angle of 30° . This suggests that an increase in wind incidence angle have a very minor influence on the lift and hinge moment coefficients' values at that angle of operation. For the -30° tilt angle operational condition experiencing

the same wind incidence angle changes described, the pressure difference between the heliostat's windward and leeward surfaces decreases, which leads to a reduction in intensity of the strong vortex that covers the entire leeward side of the heliostat. As a result, this lead to a noticeable decrease in the lift coefficient's absolute magnitude.

As the wind incidence angle gradually increases until it reaches $\beta = 90^\circ$, the flow becomes more uniform for both orientations ($\theta = 30^\circ$, $\theta = -30^\circ$) with no major flow separation except a small recirculation located near the torque tube's leeward side. This flow uniformity leads to a significant reduction in the pressure difference between the windward and leeward surfaces of the heliostat, which causes the lift coefficient to drop and consequently reduces the hinge moment experienced by the heliostat structure.



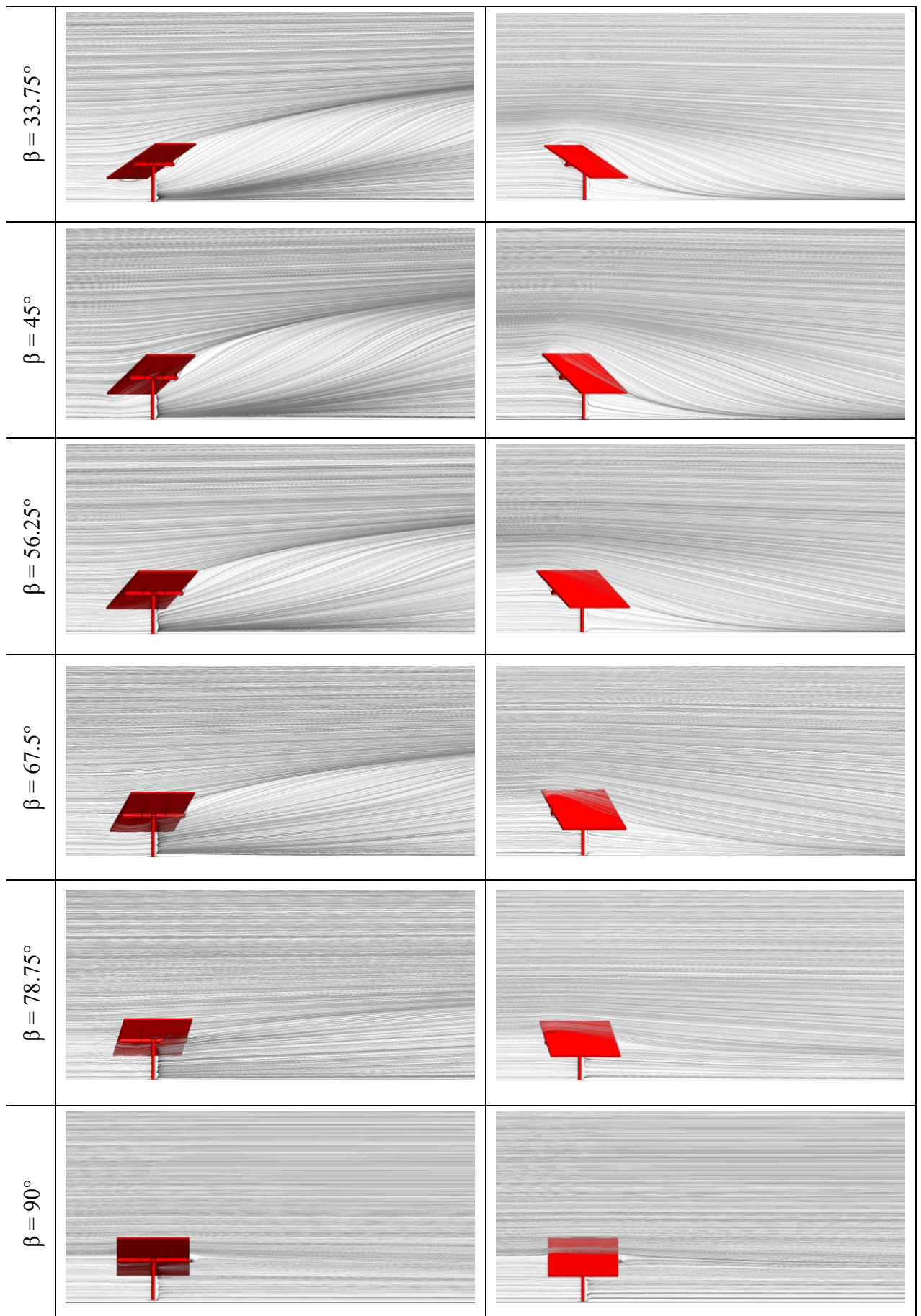


Figure 38: CFD streamlines around the heliostat at 30° and -30° tilt angles for a range of wind incidence angles

2.6 Force-coefficient and moment-coefficient correlations

From the results it is clear that the orientation of a heliostat with respect to wind has a significant impact on the aerodynamic coefficients. On this basis, there is a need to draw together the analysis performed earlier to develop a correlation to describe these with respect to both the tilt (θ) and wind incidence (β) angles. These formulations provide a useful analytical tool for heliostat designers to determine the wind loads on heliostats and to assess structural loads on the frame of the heliostat and its reflective surface.

Hence, using non-linear regression, drag (C_D), lift (C_L), base overturning moment (C_{My}) and hinge moment (C_{MHy}) coefficients' correlations can be given by Eqs. (5) to (8):

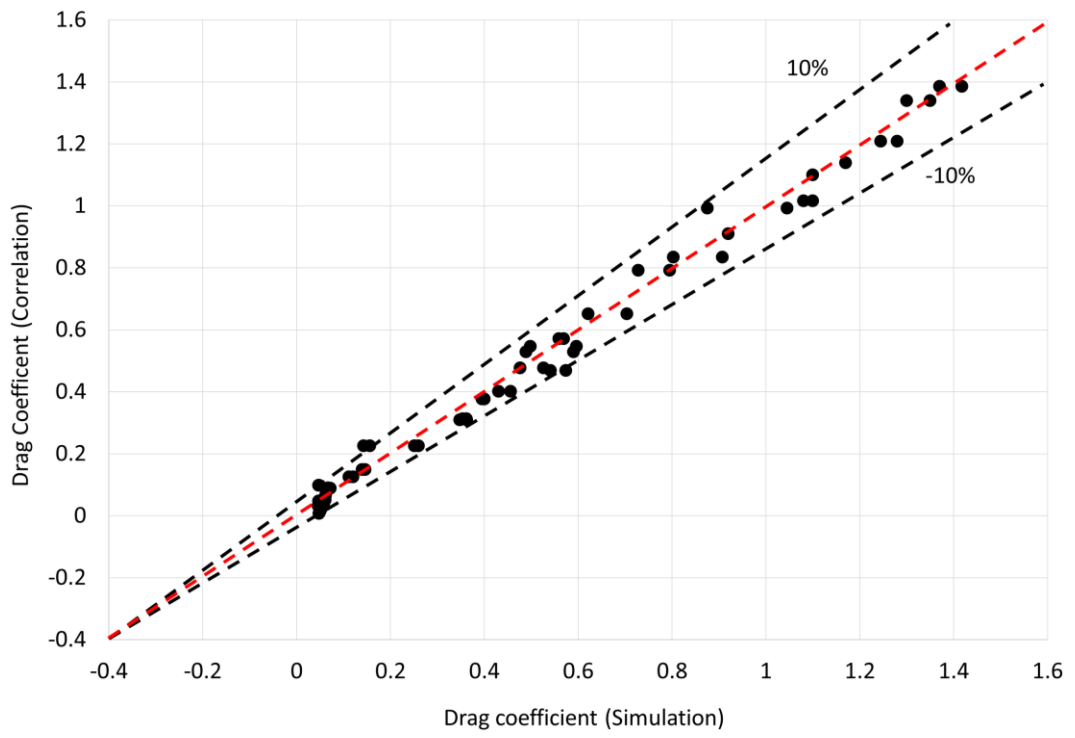
$$C_D = 0.12 (1 - 0.98 \cos^2 \theta)^{0.7} (1 + \cos \beta)^{3.53} \quad (5)$$

$$C_L = 1.2 (0.02 - \sin^3 2.05\theta) (\cos^{0.64} \beta) \quad (6)$$

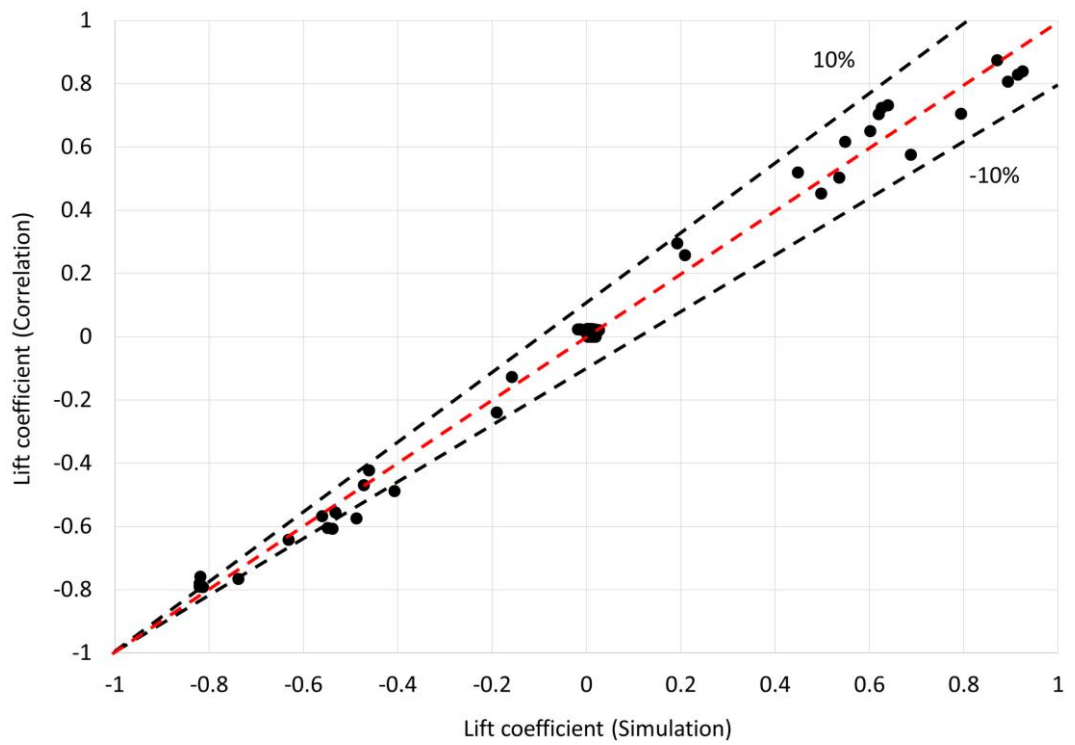
$$C_{My} = \begin{cases} 0.13 (1 - 0.99 \cos^{3.5} \theta)^{0.53} (1 + \cos^{0.92} \beta)^{3.35} & 90^\circ \geq \theta \geq 0^\circ \\ 0.1 (1 - 0.99 \cos^{1.85} \theta)^{0.5} (1 + \cos^{0.95} \beta)^{3.7} & 0^\circ > \theta \geq -90^\circ \end{cases} \quad (7)$$

$$C_{MHy} = \begin{cases} 0.168 (0.1 - \sin^2 2.32\theta) (0.57 + \cos^{0.28} \beta) + 0.001 e^{(4.8 \sin^2 2.32\theta)} & 90^\circ \geq \theta \geq 0^\circ \\ -0.13 (0.5 + \sin^7 2.23\theta) (\cos^{0.1} \beta) + 0.01 e^{(2.3 \cos^{0.1} \beta)} & 0^\circ > \theta \geq -90^\circ \end{cases} \quad (8)$$

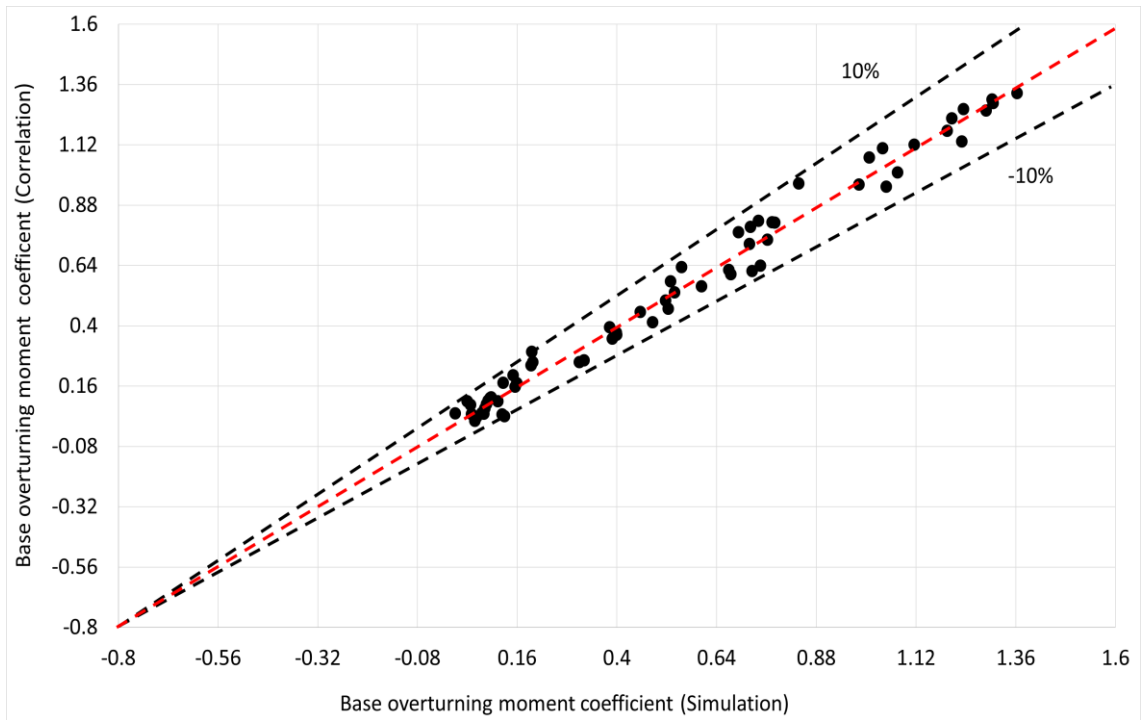
Where the coefficient of determination (R^2) for Eq. (5) is 98.6%, 98.4% for Eq. (6), 98.37% for Eq. (7) and 98.25% for Eq. (8), indicating that the effect of the heliostat's tilt and wind incidence angle values is adequately explained by the derived correlations. Figure 39 shows the calculated values of drag, lift, base overturning moment and hinge moment coefficients from Eqs. (5), (6), (7) and (8) compared to the values determined numerically. It can be seen that most of the predicted data from the correlations lie between 10% of the numerical values obtained from the simulation results.



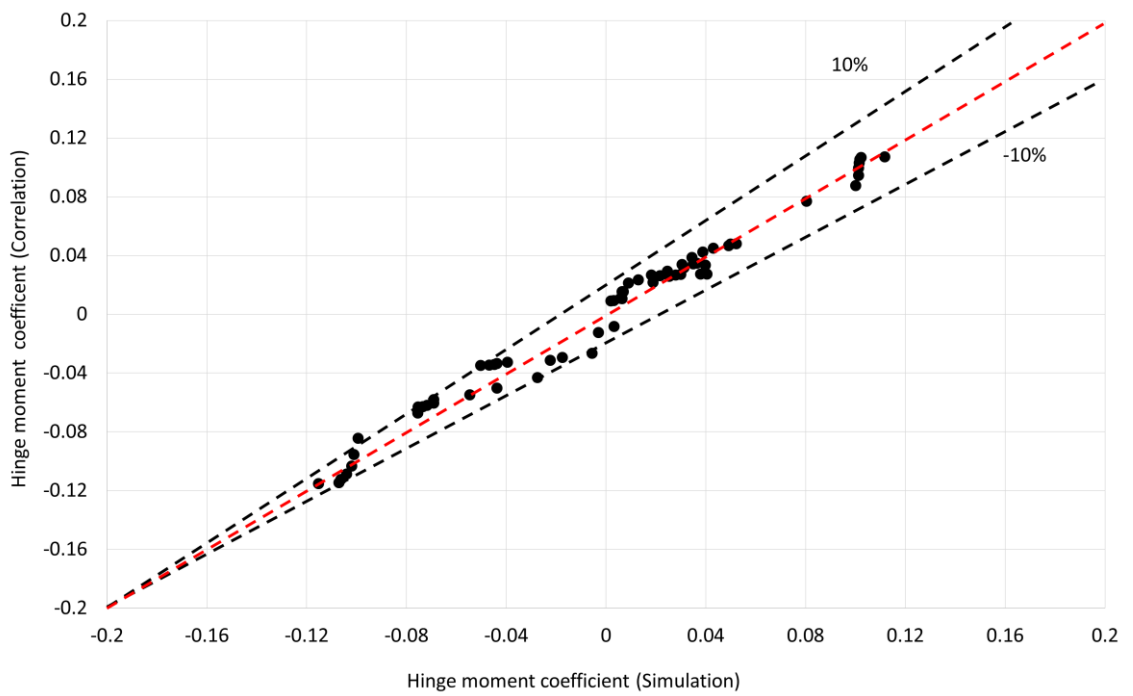
(a) Drag coefficient



(b) Lift coefficient



(c) Base overturning moment coefficient



(d) Hinge moment coefficient

Figure 39: Comparison of drag, lift, base overturning moment and hinge moment coefficients obtained from correlation and numerical results

2.7 Chapter Summary

With the advance in technology and the necessity to reduce the heliostats' cost without affecting its tracking performance so that central tower CSP systems become the technology of choice for the generation of renewable electricity, the industry is forced to consider new innovative designs, leading to new materials, such as sandwich composites, and joining techniques being implemented into the development of heliostats. However, the physical behaviour of such materials is quite dissimilar from that of most common engineering materials that are homogeneous and isotropic. The makeup and physical properties of composites vary with location and orientation of principal axes, making it difficult with the current available characterization of wind loads to ensure that these innovative heliostat designs and prototypes are able to cope with the aerodynamic forces imposed upon them during operation. Previous studies only reported the aerodynamic loads encountered by heliostats without linking their outcomes of the variation in wind loads with heliostat orientation to the airflow characteristics around the structure. In addition, the studies did not explore in any detail the wind incidence effect and the impact that has on the aerodynamic behaviour of a heliostat. Furthermore, several existing heliostat suppliers have conducted wind tunnel tests and extracted aerodynamic loading data with small angular resolution for wind incidence angle. However, such data typically is not available, but kept as proprietary information.

In this chapter, we attempted to deliver a better understanding of the effect of wind direction on the aerodynamic loading of a heliostat, relate the loads to the wind flow field around the structure, and to deliver a non-dimensional relationship for the wind loading coefficients to heliostat designers.

Computational fluid dynamics (CFD) was utilized to investigate the effect of wind incidence angles on a heliostat operating at varying tilt angles, to better characterise the

aerodynamic loading of these structures. The numerical model's accuracy was verified by comparing the computation predictions of the heliostat's drag, lift, base overturning moment and hinge moment coefficients with both experimental measurements and numerical results from previously published work. The obtained results showed reasonable agreement, confirming the validity of the CFD model and improving our confidence in utilizing it in the upcoming heliostat analyses.

From this the study showed that, for a 0° wind incidence angle, the drag and base overturning moment coefficients decrease as the tilt angle alters from vertical to horizontal. The lift and hinge moment coefficients, on the other hand, showed an asymmetric behaviour about the 0° tilt angle with maximum values occurring at tilt angles of 30° and -30° . Increasing wind incidence angle affected the wind loading coefficients (drag, lift, base overturning moment and hinge moment coefficients) by decreasing their magnitudes at different rates.

A subsequent non-linear regression analysis delivered a correlation for each of the coefficients based on the heliostat's tilt and wind incidence angle was developed. These formulations provide a more accurate and a better quantified description of the wind incidence effect on wind loads than what has been found in former studies, and offer a useful analytical tool for heliostat designers, in conjunction with Pfahl et al.'s (2011) aspect ratio (width to height) relationships, to determine the wind loads on heliostats with different sizes and to assess structural forces and moments on the frame of the heliostat and its reflective surface.

In summary, it was shown that the aerodynamic coefficients vary strongly with respect to the wind incidence angle and it is crucial to consider this variation when examining the performance of heliostat systems in order to avoid any structural deformations that can lead to potential mechanical failure.

Chapter 3: Structural behaviour of honeycomb sandwich composite-based heliostat structure under wind effects

Based on the validated simulation scheme in the previous chapter, it was shown that wind incidence had a significant impact on the aerodynamic loads encountered by a heliostat and, therefore, needs to be accounted for when examining the structural integrity of heliostats. Proceeding further into answering the main research question in Chapter 1, and taking into account the wind incidence effect, this chapter set out to deliver an understanding on how honeycomb sandwich composites respond under wind-loaded conditions when utilized as the structure for heliostat mirror.

3.1 Numerical setup

To investigate the aero-structural robustness and behaviour characteristics of honeycomb sandwich composites when employed as a heliostat mirror support structure, it was decided to perform a fluid-structure interaction (FSI) study (combined computational fluid dynamics (CFD) and finite element analysis (FEA)). This approach has been successfully employed in a number of prior research studies conducted on the interaction of structures such as wind turbines and photovoltaic systems with wind (MacPhee and Beyene, 2013; Wang et al., 2016; Lee et al., 2017; Lin et al., 2013). It is considered to be an effective way, especially during the development stage, to explore and examine a variety of designs and modifications at real scale, as field and wind tunnel experiments are time-consuming and expensive to set up.

In doing this, and considering the geometry chosen in Chapter 2 of the existing large-area ATS heliostat, it was assumed that the heliostat would consist of a 148 m^2 (11.84 m (H) \times 12.5 m (W)) rectangular sandwich composite plate (Figure 40). As discussed earlier, this size of reflector was selected since heliostats with reflective areas around 150 m^2 offer best economy compared to other heliostat dimensions as reported by Kolb et al.

(2007). The sandwich composite plate is supported by four steel attachments, each with a length of about 6 m and a width of 0.15 m. Unlike the ATS heliostat where the steel-based trusses extend along the entire height of the reflector, the attachments were made smaller to reduce the amount of steel in the heliostat structure, considering that the sandwich panel should be capable enough of providing the reflective mirror module with the necessary rigidity and support without fully relying on the heavy steel-based support structure. A detailed analysis on the attachments' size selection is described in Appendix C. Both the panel and the attachments are mounted to a steel-based torque tube/pedestal configuration, also known as T-type heliostat configuration (both the torque tube and the pedestal together form a "T" and are coupled to each other by the drive system). This configuration was chosen, since state-of-the-art central tower CSP plants mostly use T-type heliostats with azimuth-elevation tracking mechanism (Pfahl et al., 2017; Téllez et al., 2014).

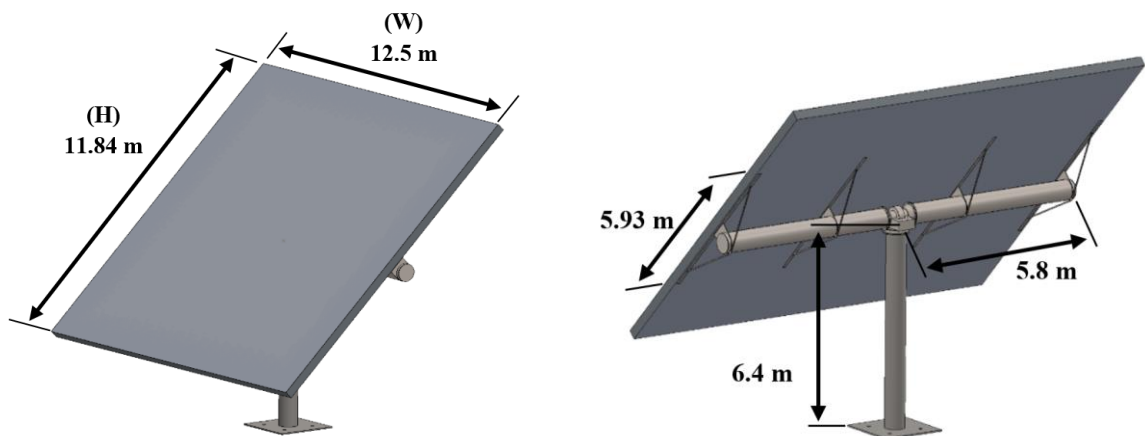


Figure 40: Sandwich composite-based heliostat in full-scale

The heliostat's sandwich composite structure (Figure 41) was assumed to consist of a 300 mm thick aluminum honeycomb core sandwiched between two 0.3 mm aluminum skins. Amongst the various materials that can be utilized to manufacture honeycomb sandwich panels, aluminum is the most widely used option (Araújo et al., 2019). Aluminum honeycomb sandwich panels have been extensively adopted in the motorsport,

construction, marine and aerospace industries (applications where reducing weight whilst maintaining or improving the strength of a structure is of key importance) due to their comparatively low cost, high strength to weight ratio, corrosion resistance and good energy absorbing capabilities (Paik et al., 1999; Castellon, 2012).

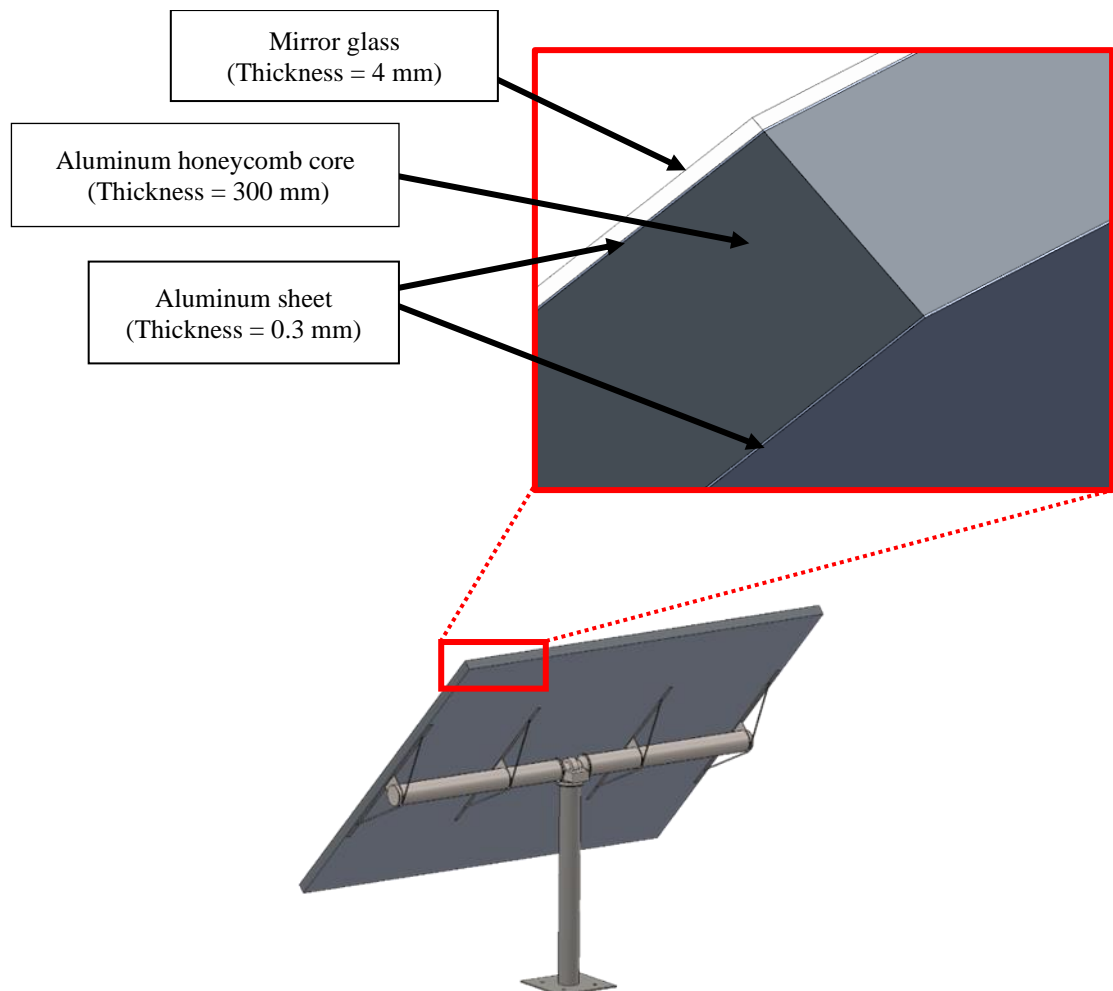


Figure 41: Close-up view of the heliostat's honeycomb sandwich composite structure

Furthermore, and taking into account the heliostat's large reflective area and market availability, the selection of the sandwich panel's thickness was based on preliminary analysis carried out to determine an initial structural configuration that reduces the mirror support structure's total weight (in comparison to the existing 148 m² steel-based ATS heliostat's mirror support structure that weighs around 1550 kg as reported by Kolb et al. (2007)) while maximizing its structural strength and robustness. A detailed analysis was

performed to investigate the effect of the geometric configuration of the honeycomb core thickness on the heliostat panel's structural behaviour and is presented in Chapter 4. A 4 mm thick glass mirror, which is similar to the one used in the ATS heliostat, was mounted on top surface of the sandwich composite. Mirrored glass was selected as the reflective surface, as they are relatively inexpensive, have high reflectance (0.93-0.94), durable (20-25 years' lifespan), and accepted by industry in comparison to reflective films (Pfahl et al., 2017; Téllez et al., 2014).

In undertaking the analysis, the wind (i.e. the fluid) flow around the heliostat was simulated using the validated numerical CFD model in Chapter 2. To determine the aerodynamic loads on the heliostat adequately simulations were carried out for a range of tilt angles (θ) between 90° (wind flow perpendicular to the mirror surface) and -90° (wind impinging on the heliostat's back surface) and wind incidence angles (β) ranging from 0° to 90° , with a wind velocity (V) range of 5-20 m/s (Reynolds number varying from 4.05×10^6 to 1.62×10^7 taking the chord length of the panel ($H = 11.84$ m) as the characteristic length) as shown in Figure 42.

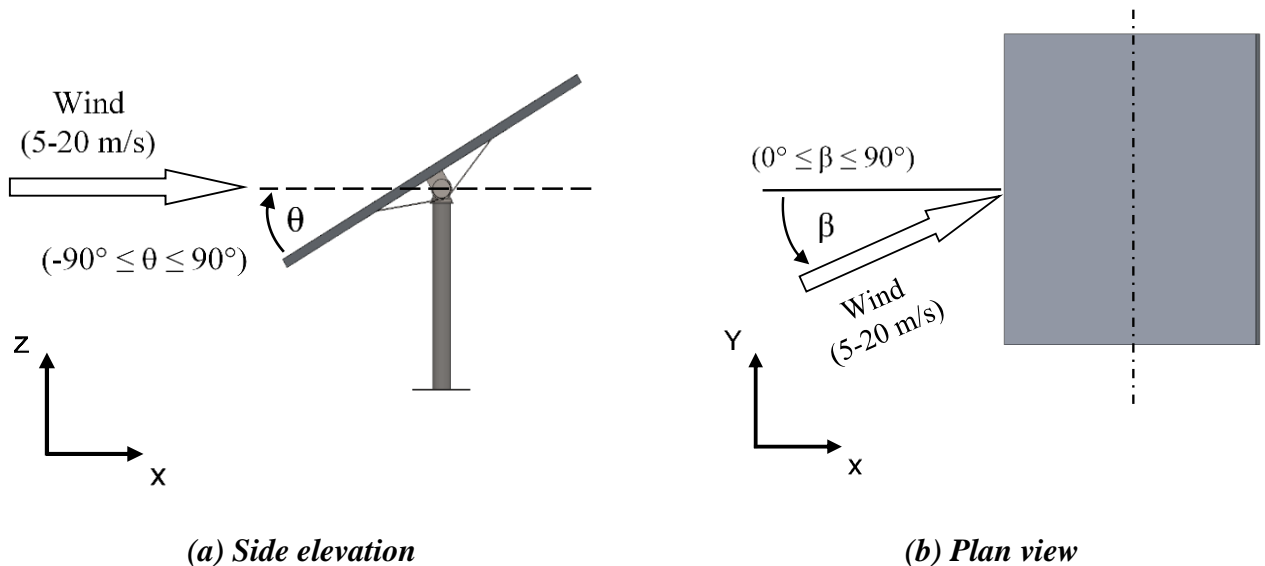


Figure 42: Definition of tilt and wind incidence angles

To investigate the behaviour characteristics of the honeycomb sandwich composite-based heliostat structure under wind loads, the predicted aerodynamic loads were then mapped to an FEA model of the sandwich composite-based heliostat developed in the ANSYS/Static Structural package. This coupling strategy is a one-way coupling method, which is less computationally intensive compared than the more complex unsteady two-way approach. In addition, obtaining and verifying the flow characteristics and aerodynamic loads is simpler but more reliable than two-way FSI, where assuring solution convergence and accurate results cannot be guaranteed (Wang et al., 2016; Lee et al., 2017). That said, for the FEA fine meshes were generated (about 650,000 elements after performing mesh sensitivity analysis described in Appendix D) to reduce any numerical instabilities when importing the aerodynamic loads from the CFD solver.

Furthermore, instead of developing a fully detailed multi-cell honeycomb core model, the common practice, which was selected for this study, is to replace those cells with an equivalent three-dimensional orthotropic material model (has different material properties in three mutually perpendicular directions) (Figure 43). This approach has been effectively employed in previous studies (Schwingshackl et al., 2006; Aydincak and Kayran, 2009; Soroohan et al., 2016) due to the substantial advantages that can be obtained, besides delivering the same results as the actual fully detailed multi-cell honeycomb model, including ease of modelling and model modification, reduced solution time, and less hardware resources.

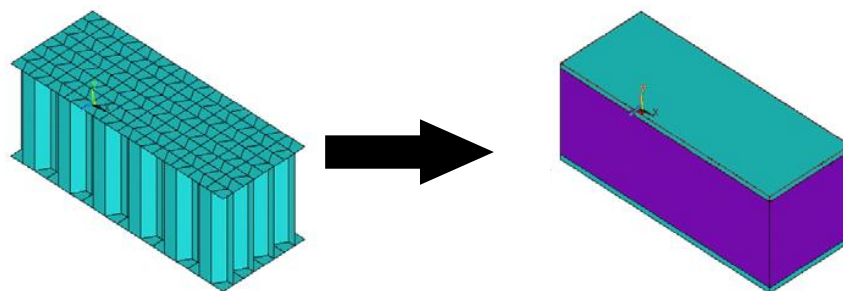


Figure 43: Geometric model of the honeycomb core and equivalent core sandwich panel (Aydincak and Kayran, 2009)

In doing this, the honeycomb core's mechanical properties were calculated based on the geometrical properties of the honeycomb shape (Figure 44) (e.g., cell wall angle (φ), cell wall length (a) and cell wall thickness (t)) and the material characteristics using the relationships described by Nast (1997) and Gibson and Ashby (1997) (Appendix E).

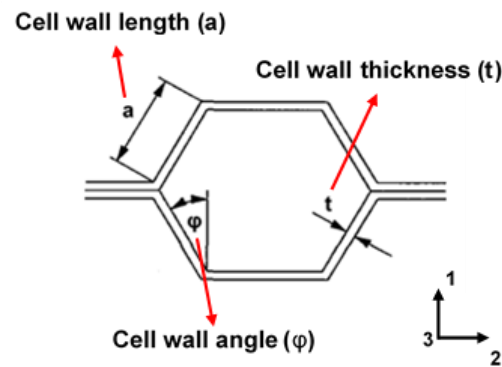
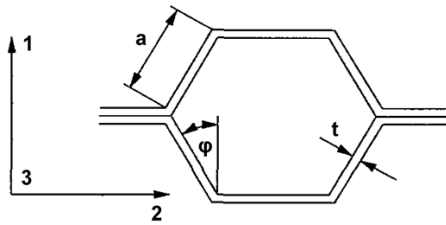


Figure 44: Honeycomb main geometrical properties

When designing a product using honeycomb cores, it is typical to select the most appropriate one from the restricted variations of ready-made honeycomb. In this regard, it was assumed that the panel consists of a honeycomb core formed by regular hexagonal cells (has a cell wall angle of $\varphi = 30^\circ$). Honeycombs formed by regular hexagonal cells are the most commonly used structures for sandwich panel cores in the industry applications, because of their ability to be easily manufactured and their good out-of-plane properties (Hu et al., 2013; Araújo et al., 2019). Moreover, and based on the preliminary analysis mentioned earlier to determine an initial structural configuration that provides a sensible trade-off between the panel's structural integrity and weight reduction, the length and the thickness of the honeycomb cell wall were selected to be $a = 6$ mm and $t = 0.03$ mm, respectively. These selected dimensions fall within the range of the commercially available honeycomb cell sizes (Hexcel, 1999; Yamashita and Gotoh, 2005; Nayak, 2012). A comprehensive investigation was performed to explore the effect of the honeycomb's cellular geometry (a , t , φ) on the aero-structural behaviour characteristics of the honeycomb sandwich composite-based heliostat and is presented in

Chapter 4. The material properties of the mirror glass, steel attachments, pedestal and torque tube, and the aluminum sheets, along with the honeycomb's geometrical properties and the core's calculated properties are listed in Table 1.

Table 1: Material properties

	Mirror glass	Steel	Aluminum	Unit
Young's modulus (E)	68.94	200	69	GPa
Poisson's ratio (ν)	0.23	0.3	0.33	-
Shear modulus (G)	28.02	76.92	27	GPa
Density (ρ)	2457.6	7850	2700	kg/m ³
Aluminum honeycomb core calculated mechanical properties				
				
Honeycomb cell geometry	Cell wall angle (φ)	30	deg	
	Cell wall length (a)	6	mm	
	Cell wall thickness (t)	0.03	mm	
Calculated mechanical properties	Young's modulus of the honeycomb core in direction 1 (E_1)	29.11	kPa	
	Young's modulus of the honeycomb core in direction 2 (E_2)	22.35	kPa	
	Young's modulus of the honeycomb core in direction 3 (E_3)	531.16	MPa	
	Poisson's ratio of the honeycomb core in plane 1–2 (ν_{12})	1	-	
	Poisson's ratio of the honeycomb core in plane 2–3 (ν_{23})	0	-	
	Poisson's ratio of the honeycomb core in plane 1–3 (ν_{13})	0	-	
	Shear modulus of the honeycomb core in plane 1–2 (G_{12})	5.16	kPa	
	Shear modulus of the honeycomb core in plane 2–3 (G_{23})	153.96	MPa	
	Shear modulus of the honeycomb core in plane 1–3 (G_{13})	207.85	MPa	
	Density of the honeycomb core ($\rho_{\text{honeycomb}}$)	15.59	kg/m ³	

3.2 Wind pressure distribution characteristics

Evaluating the structural responses of the honeycomb sandwich composite-based heliostat requires an understanding of the pressure loads acting on the surfaces of the panel due to wind forces. Therefore, and having set up the numerical FSI model, it was decided to explore the wind pressure distribution characteristics on the heliostat's sandwich composite panel in detail. Figures 45-47 show an example of the wind pressure distributions on the heliostat's reflective and back surfaces under a wind velocity of 15 m/s for 0° , 45° , and 90° wind incidence angles (β), respectively, and a range of tilt angles (θ). Pressure distribution results for the remaining wind incidence angles (i.e. $\beta = 22.5^\circ$ and $\beta = 67.5^\circ$) can be viewed in Appendix F.

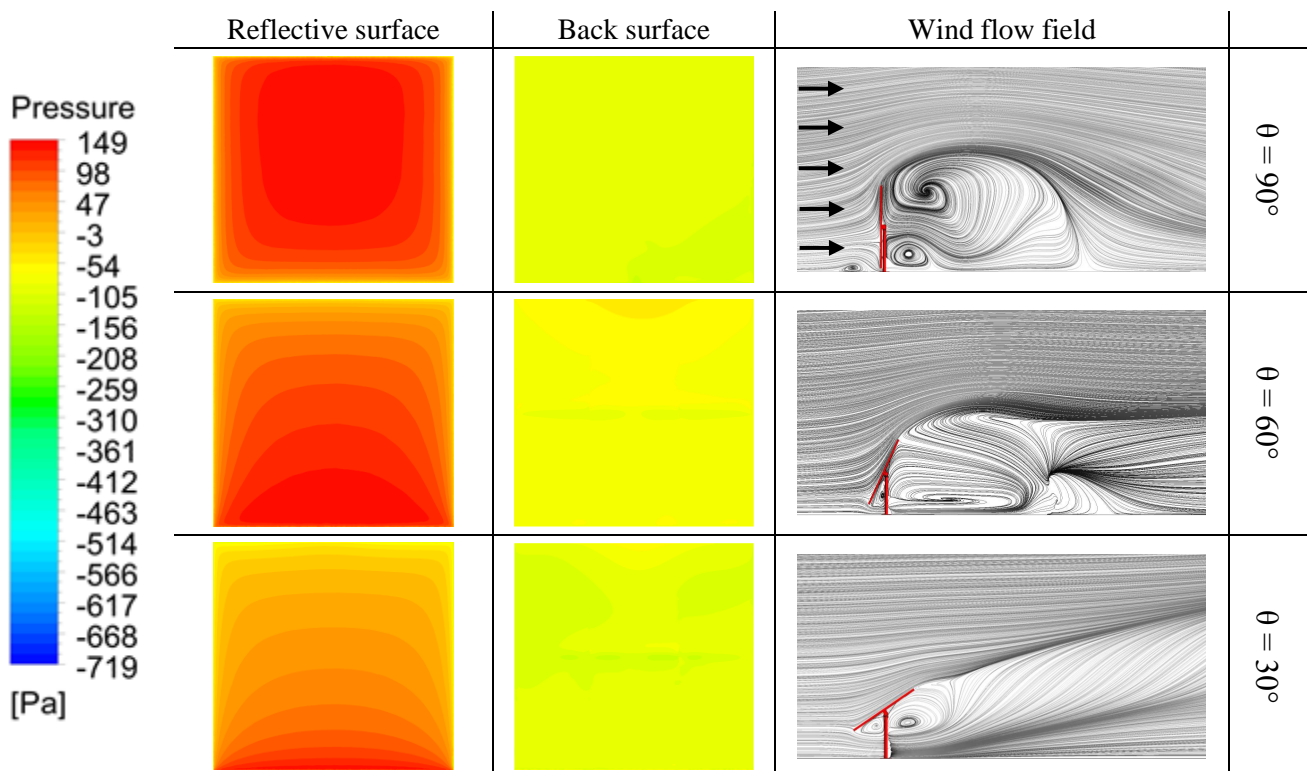
Starting from the case when the flow approaches the heliostat at 0° incidence angle (Figure 45), the structure intercepts the air's horizontal movement when flow is perpendicular to the heliostat's mirror surface, i.e. 90° tilt angle. This causes the flow's velocity in the front of heliostat structure to move towards a stagnation condition (zero wind velocity), resulting in high-pressure values, as stated by Bernoulli's law (pressure has a largest value when the velocity of the fluid is zero), at the middle of a span-wise line and decrease towards the edges. This is expected as the flow accelerates at the edges to maintain continuity; it creates low-pressure regions on the reflector's surface.

Taking the same wind incidence angle but progressively changing the tilt angle from $\theta = 90^\circ$ to $\theta = 30^\circ$ results in a shift in the high pressure region towards the lower edge of the reflector, causing the structure to experience large wind pressures at the mirror surface's lower edge.

Now for the 0° tilt angle operational condition (stow position) experiencing wind at the same incidence angle, the wind loading has no noticeable effect on the structure at this configuration compared to the remaining angles of operation. This is due to the fact that

the area in the front side of the reflector directly facing the wind is very small, allowing the incoming flow to become uniform and attached to the heliostat's surface. However, what is noticeable from the pressure distributions on the heliostat at this configuration ($\theta = 0^\circ$) is that from the windward side the reflector's back surface has greater wind pressures compared to the upper surface. This pressure difference results in large lift forces close to the windward edge. From the leeward side of the heliostat, on the other hand, the opposite occurs and wind pressures are higher at the reflective surface compared to the back surface. This is due to the depression region formed within the torque tube and the reflector's back surface, causing high suction to occur at the heliostat's leeward side.

As the heliostat structure is moved from the stow position to a -90° tilt angle, the incoming wind at the same incidence angle acts on the back surface of the heliostat directly, resulting in high-pressure values at the middle of the heliostat's back surface.



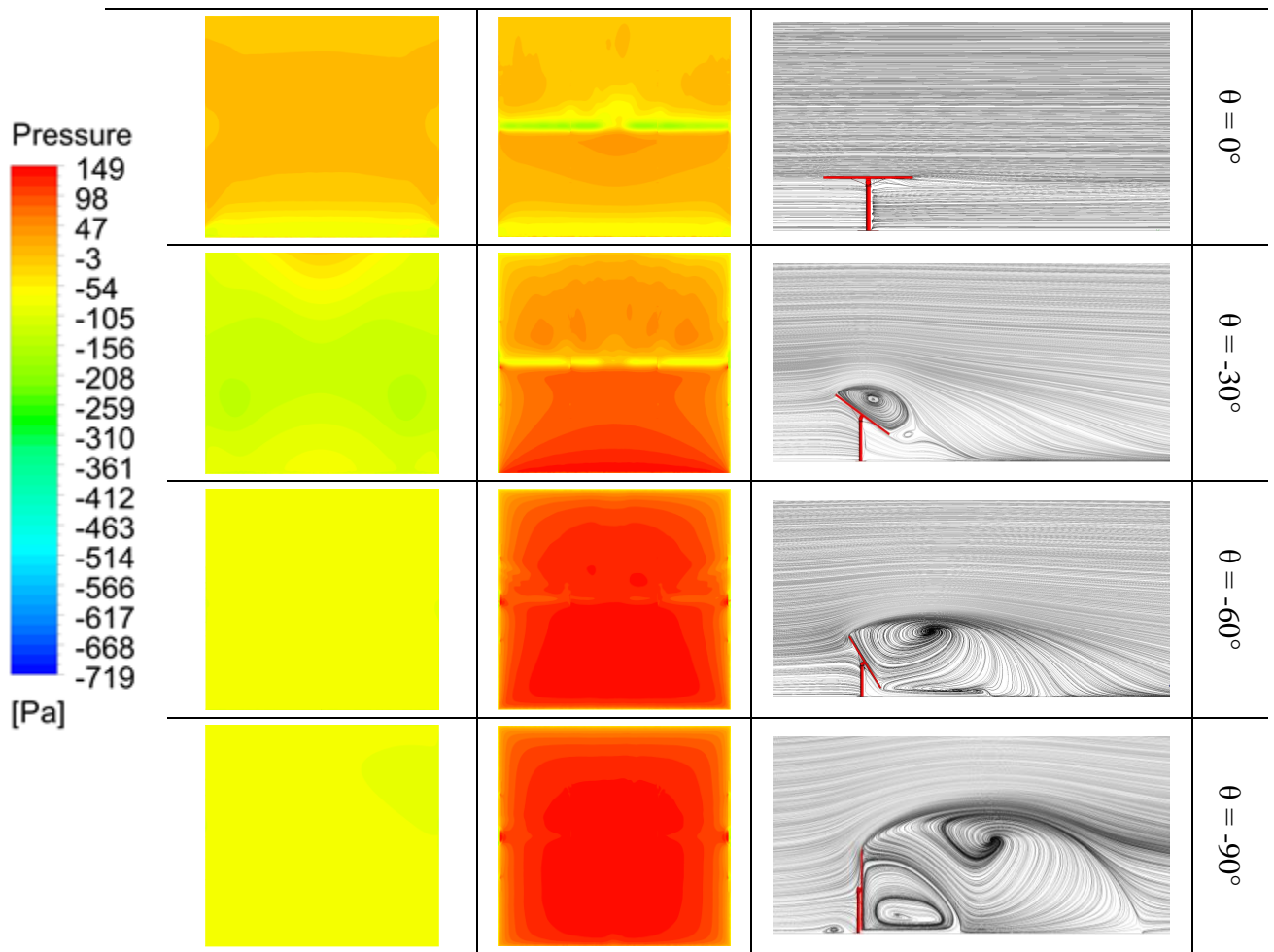


Figure 45: Pressure distribution on the heliostat at wind velocity of 15 m/s approaching at 0° incidence angle (β)

Varying the wind incidence angle (β) from 0° to 45° for all tilt angles (Figure 46) causes the high-pressure regions located at the reflector's surface to shift towards the right edge. For all tilt angles excluding $\theta = 0^\circ$, a reduction in wind loading was observed compared to the same angles of operation when the flow approaches the heliostat at 0° incidence angle. This can be attributed to the fact that the heliostat's projected area directly facing the wind decreases with the increase in wind incidence angle. This consequently reduces the effect of the blockage, causing a decrease in the wind loading effect on the heliostat.

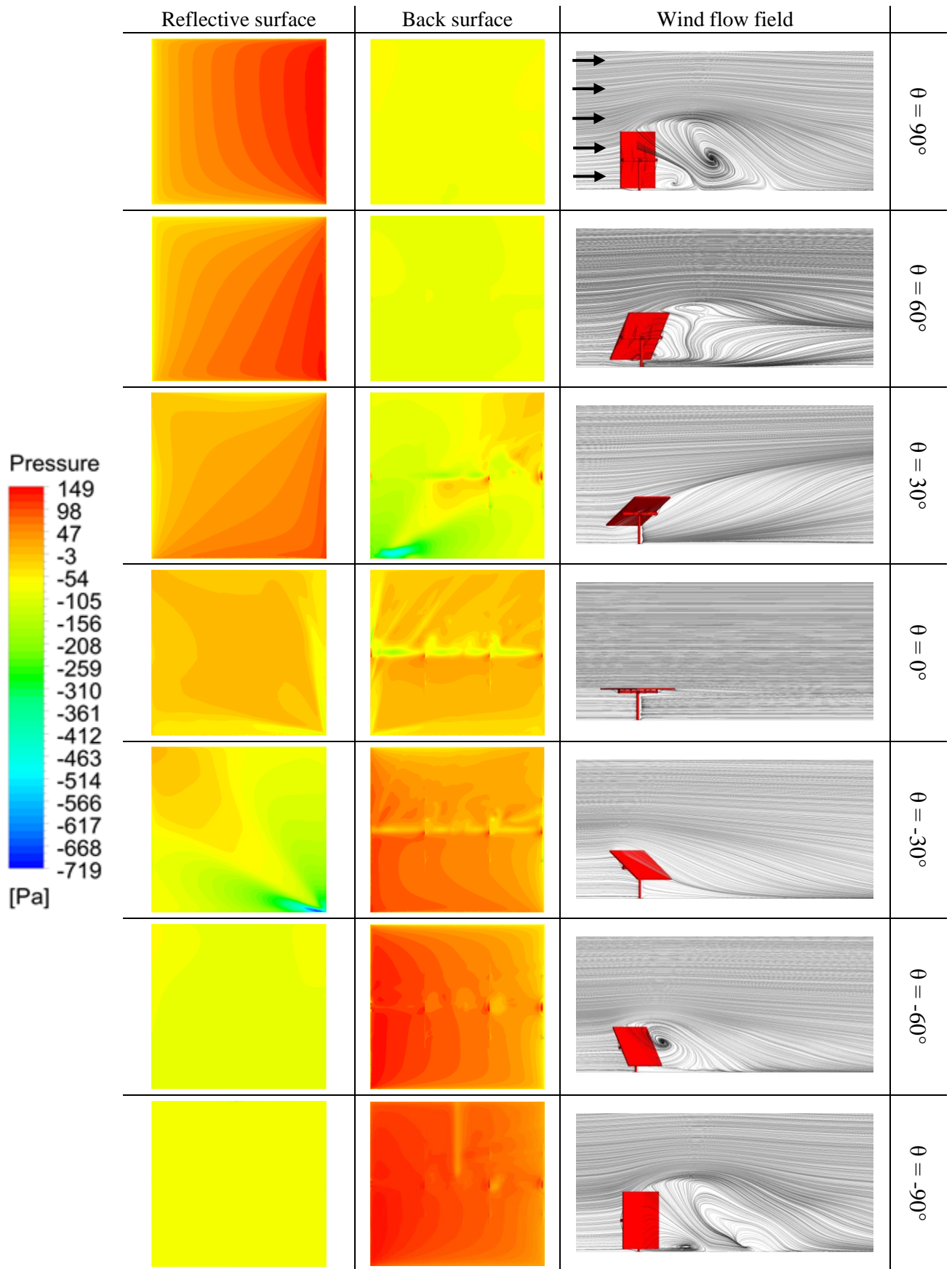
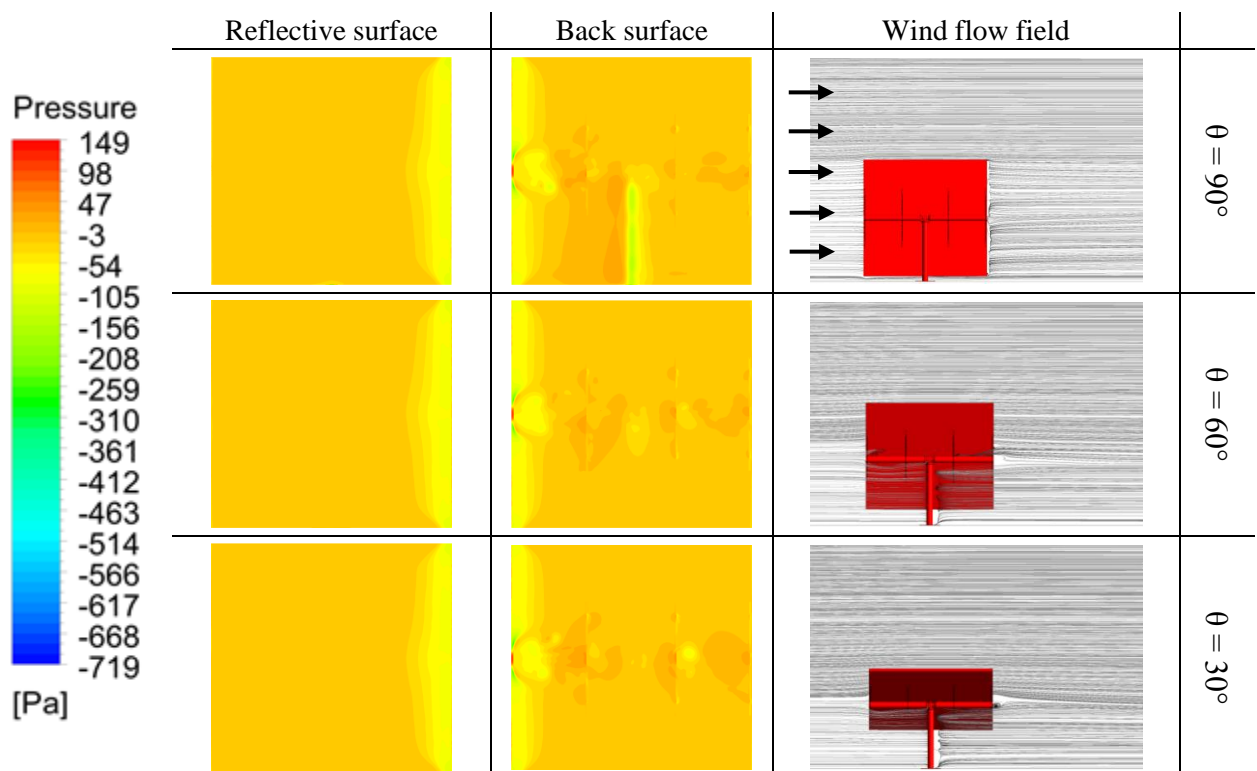


Figure 46: Pressure distribution on the heliostat at wind velocity of 15 m/s approaching at 45° incidence angle (β)

As the wind incidence angle gradually increases from $\beta = 45^\circ$ until it reaches $\beta = 90^\circ$ (Figures 47), the wind loading has no noticeable effect on the structure at this configuration for all given tilt angles. This is due to, as discussed in the stow position case, the area in the front side of the reflector directly facing the wind is very small, allowing the incoming flow to become uniform and attached to the heliostat's surface. In addition, and again similar to the 0° tilt angle operational condition experiencing wind at $\beta = 0^\circ$, the reflector's back surface from the windward side has greater wind pressures compared to the reflective surface. This pressure difference results in large lift forces close to the windward edge. However, what is noticeable from the pressure distributions on the heliostat's back surface at this configuration ($\beta = 90^\circ$) is that both the pedestal and torque tube have an influence on the pressure distributions at the back of the reflector. At the tilt angles 90° and -90° , a depression region forms within the pedestal and the reflector, causing high suction to occur at the heliostat's back surface. This depression region starts to demise as the heliostat structure moves toward the stow position ($\theta = 0^\circ$).



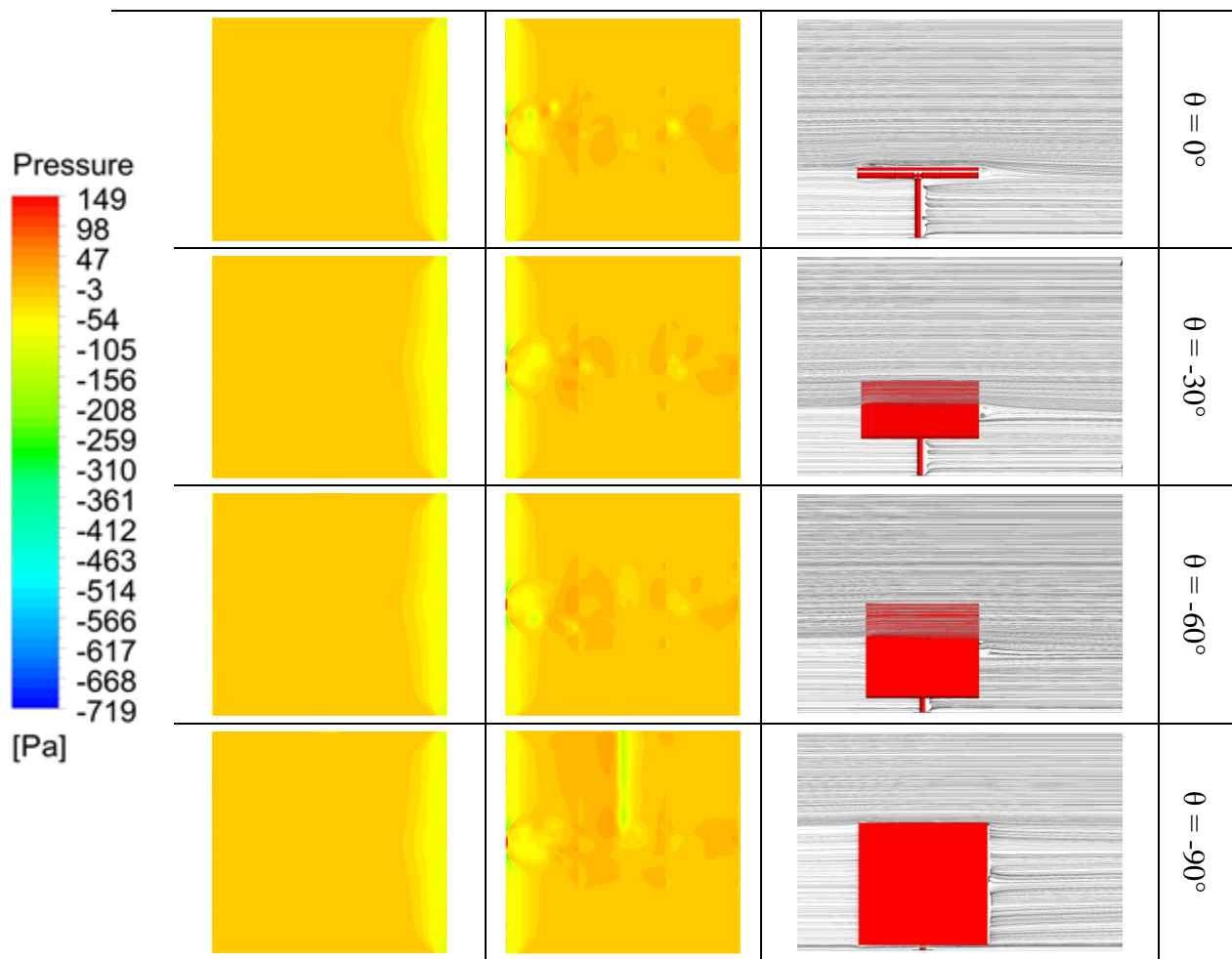


Figure 47: Pressure distribution on the heliostat at wind velocity of 15 m/s approaching at 90° incidence angle (β)

For the complete range of wind velocities (5-20 m/s), the wind pressure distribution patterns on the heliostat were observed almost the same for all the tilt and wind incidence angles except the magnitudes were different. To illustrate this, Figure 48 shows an example of the pressure contours at a tilt angle of 30° under the effect of wind flow at 0° to the heliostat surface. From these, it can be seen that the distribution patterns of wind pressure on the heliostat surface for the cases of 5 m/s, 10 m/s, and 20 m/s were similar to that of 15 m/s discussed earlier.

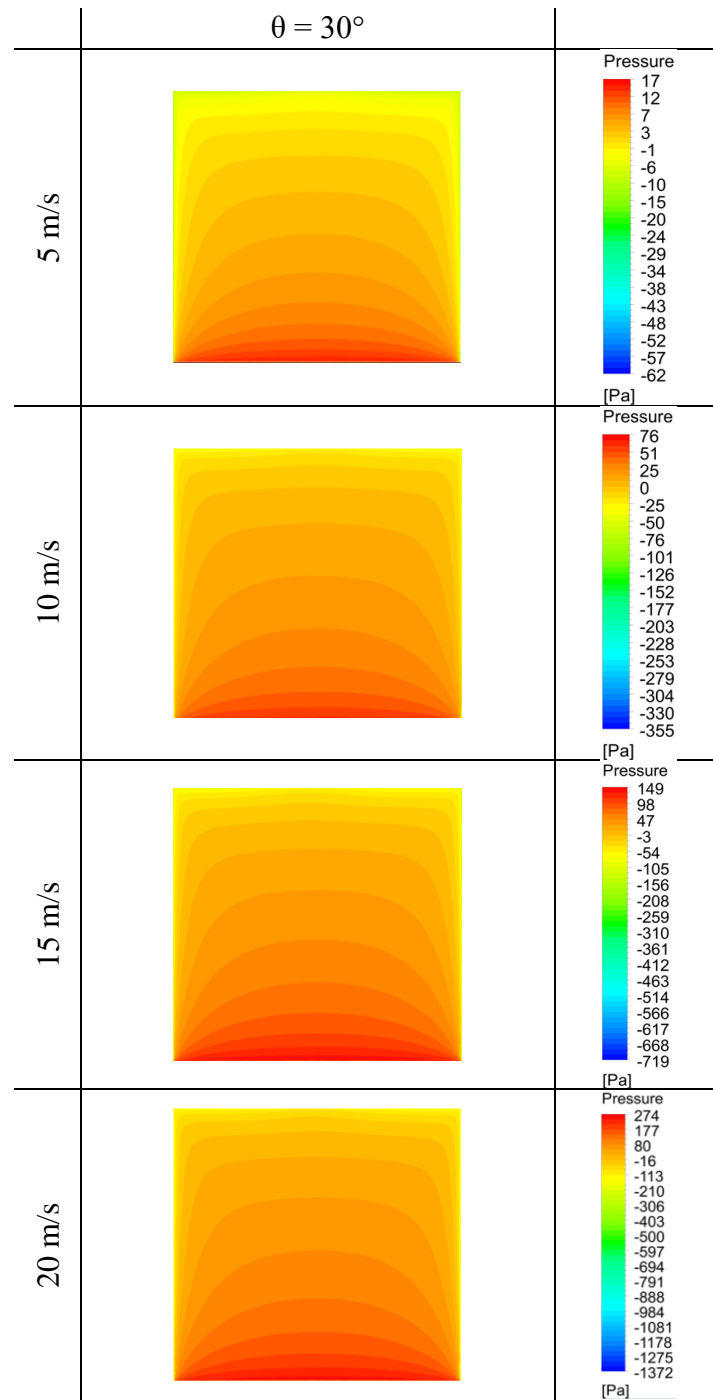


Figure 48: Pressure distribution on the heliostat at 30° tilt angles (θ) and 0° incidence angle (β) for a range of wind velocities

3.3 Heliostat structural behaviour

Having discussed the wind pressure distributions on the heliostat surfaces at varying tilt and incidence angles, it was decided to evaluate the structural behaviour characteristics of the heliostat's sandwich composite panel under those wind-loaded conditions in great detail.

3.3.1 Deflections

As discussed earlier, the aerodynamic loads experienced by heliostats can lead to structural deformations that could strongly affect the mirror quality (the sunlight is reflected with less accuracy). Therefore, the stiffness of the heliostat panel has a direct impact on the final plant efficiency. In this regard, this part focuses on analysing the heliostat panel deformations caused by wind loads at varying conditions.

Figures 49-51 present the displacement distributions of the heliostat panel (calculated normal to the surface of the reflector) for different tilt angles at wind velocity of 15 m/s approaching at 0° , 45° , and 90° wind incidence angles (β), respectively. Displacement distribution results for the remaining wind incidence angles (i.e. $\beta = 22.5^\circ$ and $\beta = 67.5^\circ$) can be found in Appendix F. Positive displacement values indicate that the deflection of the panel is inward to the plane (i.e. the surface of the reflector), and negative displacement values indicate that the deflection is outward to the plane of action. Since the study is focusing on understanding the structural behaviour of the heliostat's composite structure, it was assumed that both the pedestal and torque tube are rigid enough to withstand those wind conditions. Therefore, both components were constrained to obtain just the heliostat's sandwich composite panel behaviour.

Starting with the $\theta = 90^\circ$ tilt angle operational condition experiencing wind at $\beta = 0^\circ$ incidence angle (Figure 49), the areas with maximum displacement values are located at the heliostat's lower and upper edge regions, with higher displacement values located at the upper edge. These two regions are not fully supported by the steel attachments and majorly rely on the sandwich panel's stiffness for providing the reflective mirror module with the necessary rigidity and support. At this tilt orientation, it was found that the sandwich panel deformation contributes around 63% to the total displacement experienced by the heliostat and the remaining 37% is handled by the supporting steel

attachments. As the structure's tilt angle gradually decreases from $\theta = 90^\circ$ to $\theta = 30^\circ$ for the same 0° wind incidence angle results, the structure experiences larger displacement values at the reflector surface's lower edge. This is due to the progressive shift in the high-pressure regions at the heliostat's structure towards the lower edge as the tilt angle varies from 90° to 30° . This increase in displacement with the decrease in tilt angle triggers the supporting steel attachments to act upon the pressure concentration at the lower edge to preserve the deformations of the heliostat, causing the contribution of the attachments to increase to about 42%.

Taking the same wind incidence angle but changing the tilt angle from $\theta = 30^\circ$ to $\theta = 0^\circ$, the recorded maximum displacement values significantly decrease. This is due to the small windward facing area, causing a significant reduction in the wind load on the heliostat structure and consequently reduces the deformation contribution of the steel attachments to the total deformation to about 36%. Having said that, the resultant lift forces close to the panel's windward edge and the high suction that occur at the leeward edge's side causes its windward and leeward edges to deform in the upward and downward directions respectively.

When the structure's tilt angle alters from the stow position to a -90° tilt angle (heliostat's back surface facing the wind) under the same incidence angle ($\beta = 0^\circ$), it is interesting to note that the maximum displacement values were slightly lower than the ones recorded when the flow is acting on the heliostat's mirror surface, i.e. $\theta = 90^\circ$ to $\theta = 30^\circ$. This is due to the influence of the heliostat's supporting components (i.e. pedestal, torque tube, steel attachments) on the incoming flow, causing a shielding effect.

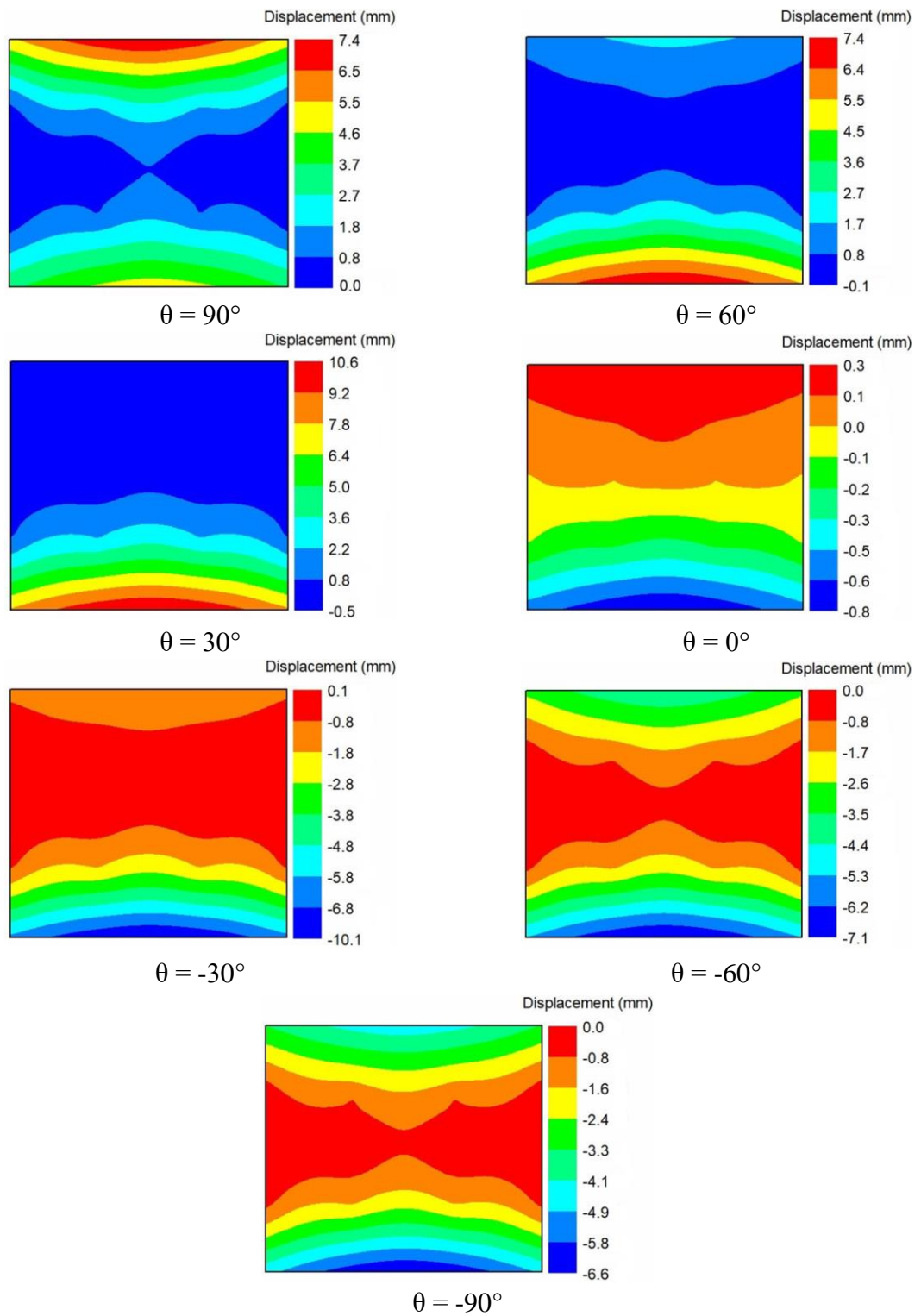
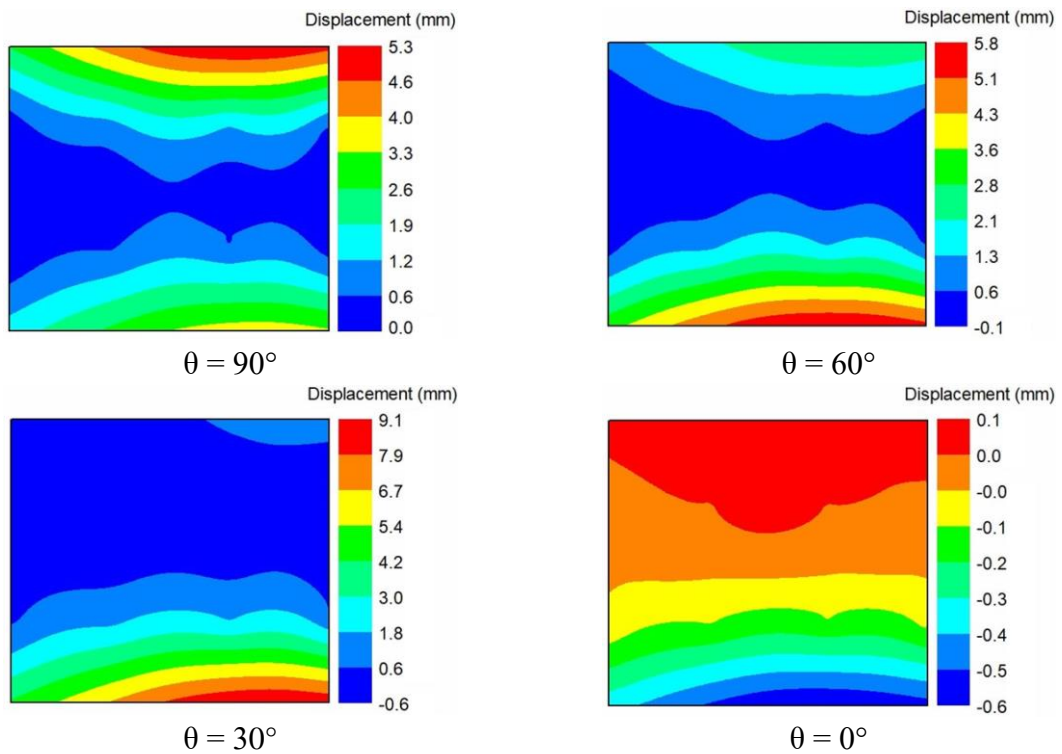


Figure 49: Displacement distribution of the heliostat surface for different tilt angles (θ) at wind velocity of 15 m/s approaching at 0° incidence angle (β)

The progressive shift in the high-pressure regions, observed in the flow modelling, towards the right edge as the incidence angle vary from 0° to 45° led to the same

behaviour being observed in the maximum-recorded displacement regions (Figure 50). However, the displacement values were lower in magnitude than the 0° incidence angle operational condition for all tilt angles. This is due to a reduction in the pressure gradient between the heliostat's reflective and back surfaces as the wind incidence angle changes from $\beta = 0^\circ$ to $\beta = 45^\circ$. The same trend of change was observed in the supporting steel attachments' deformation contribution as the tilt angle alters from vertical to horizontal. Having said that, the identified decrease in the wind pressure imposed upon the panel was reflected on the contribution of the supporting steel attachments to the total displacement experienced by the heliostat, and the deformation percentage values were lower than the ones recorded when the flow approaches the heliostat at 0° incidence angle. Moreover, the same shielding effect has been noticed at this configuration, and the maximum displacement values recorded when the heliostat's back surface facing the wind were slightly lower than the ones recorded when the flow is acting on the heliostat's mirror surface, i.e. $\theta = 90^\circ$ to $\theta = 30^\circ$.



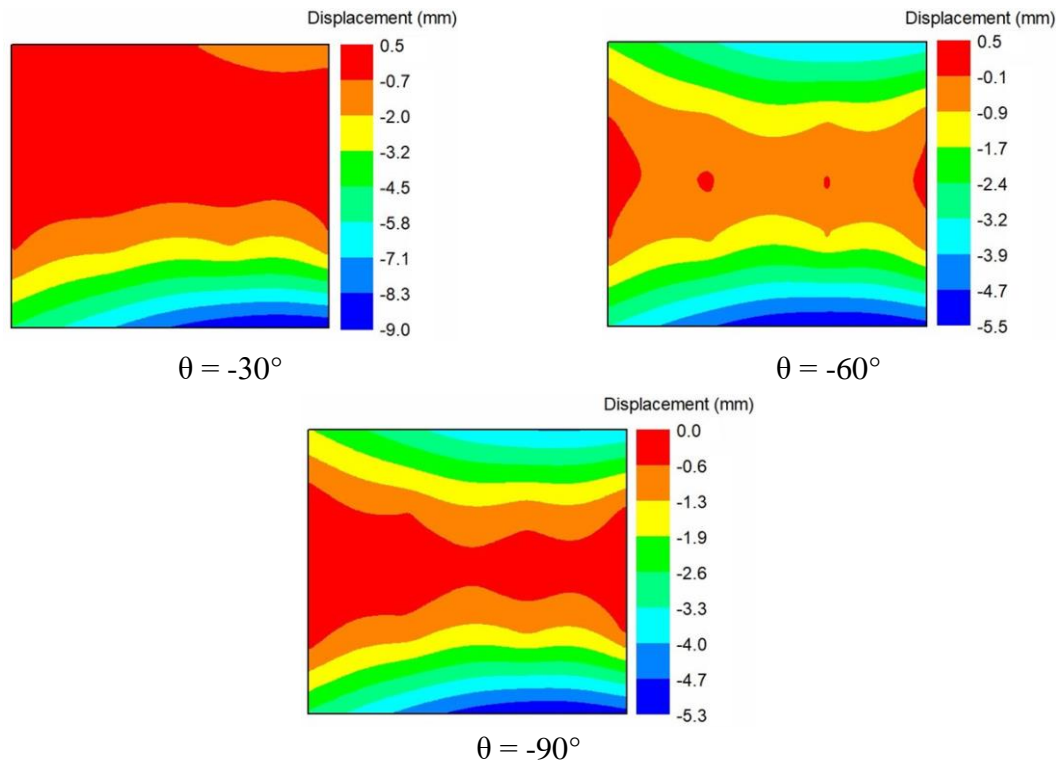


Figure 50: Displacement distribution of the heliostat surface for different tilt angles (θ) at wind velocity of 15 m/s approaching at 45° incidence angle (β)

The recorded maximum displacement values significantly decrease as the wind incidence angle gradually increases until it reaches $\beta = 90^\circ$ for all tilt angles (Figure 51). This is due to the very small area in the front side of the reflector directly facing the wind that allows incoming flow to become uniform and attached to the heliostat's surface, causing a significant reduction in the wind loading effect on the heliostat structure. At this configuration ($\beta = 90^\circ$), the resultant lift forces close to the panel's windward edge and the high suctions that occur at the leeward edge's side causes its windward and leeward edges to deform in the upward and downward directions respectively. However, the displacement distribution is not the same for all tilt angles. At the tilt angles 90° and -90° , the areas with maximum displacement values are located at the heliostat's lower and upper edge regions respectively. This is due to the depression region that forms within the pedestal and the reflector. This region starts to reduce in size as the heliostat structure

moves toward the stow position from $\theta = \pm 90^\circ$, and the displacement distribution tends to become symmetric about the torque tube axis.

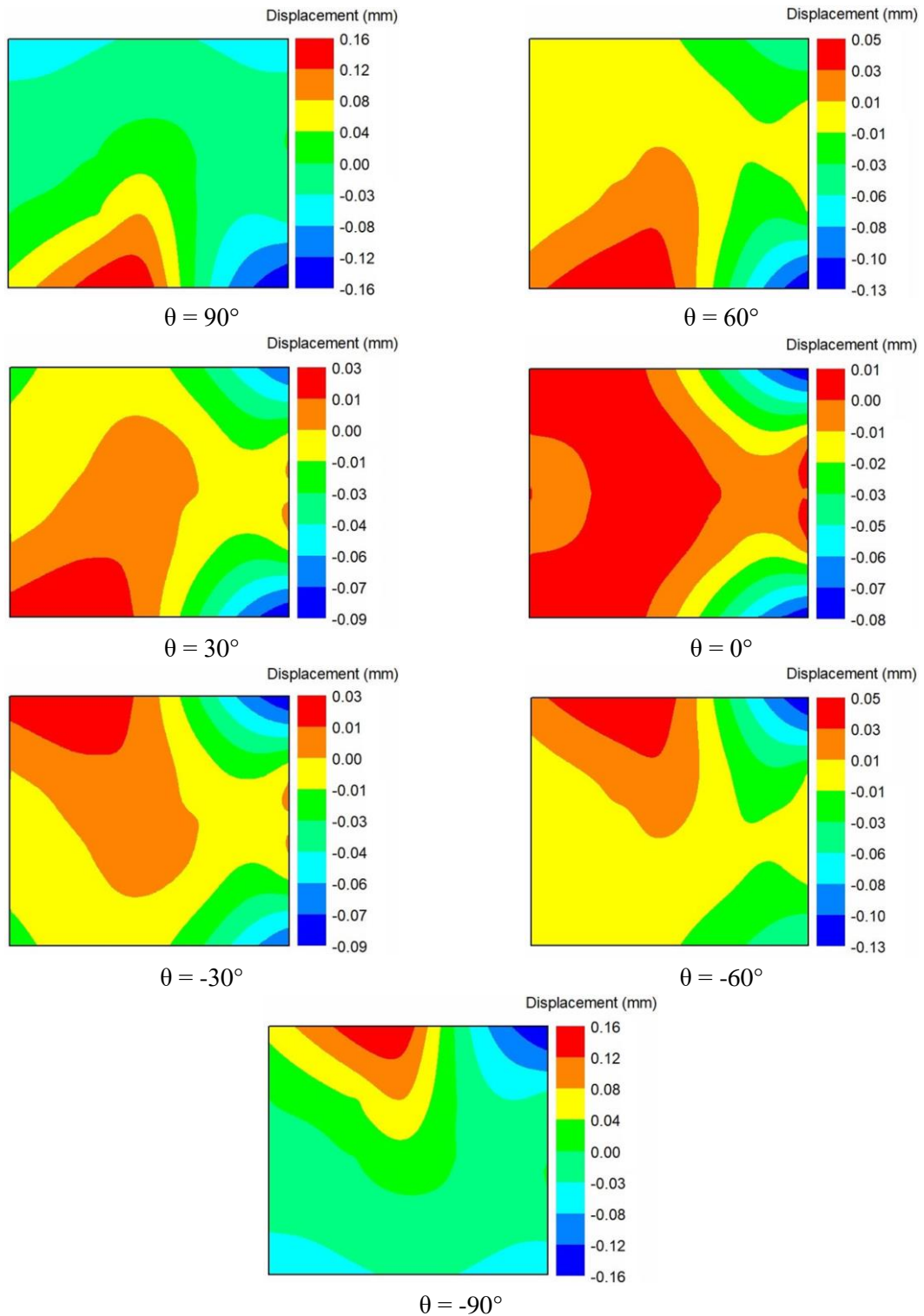


Figure 51: Displacement distribution of the heliostat surface for different tilt angles (θ) at wind velocity of 15 m/s approaching at 90° incidence angle (β)

Having discussed the displacement distribution of the heliostat's sandwich composite panel for the 15 m/s case, the influence of varying wind velocity on the heliostat surface's maximum resultant displacement at varying tilt and incidence angles is illustrated in Figures 52-56.

For the 0° wind incidence angle results (Figure 52), the trends of variation in maximum resultant displacement at the sandwich composite panel are similar among the four wind velocity cases, except when the heliostat structure is at the stow position ($\theta = 0^\circ$). The effect of wind velocity on the structural deformation of the heliostat panel for the case of $\theta = 0^\circ$ was negligible. This is because of the flow uniformity (the projected area of the reflector directly facing the wind is at its minimum) that leads to a significant decrease in the wind loading effect on the panel at this tilt orientation for all wind velocities (5-20 m/s).

At wind velocity of 5 m/s, it can be seen that there is a relatively small difference in the sandwich panel's maximum recorded displacement at different tilt angles. This implies that the heliostat orientation has no significant effect on the recorded maximum deflections of the heliostat panel when subjected to a wind of 5 m/s. For higher wind velocities, greater than 10 m/s, this effect becomes more pronounced and the difference in the maximum displacement values at different tilt angles increases to a maximum at wind velocity of 20 m/s.

Comparing the negative tilt angles ($\theta = -30^\circ$ to $\theta = -90^\circ$) with the positive ones ($\theta = 90^\circ$ to $\theta = 30^\circ$), it can be seen that the maximum displacement values were slightly lower. This is because of, as discussed earlier, the effect of the supporting components of the heliostat (i.e. pedestal, torque tube, steel attachments) on the incoming wind, causing a shielding effect.

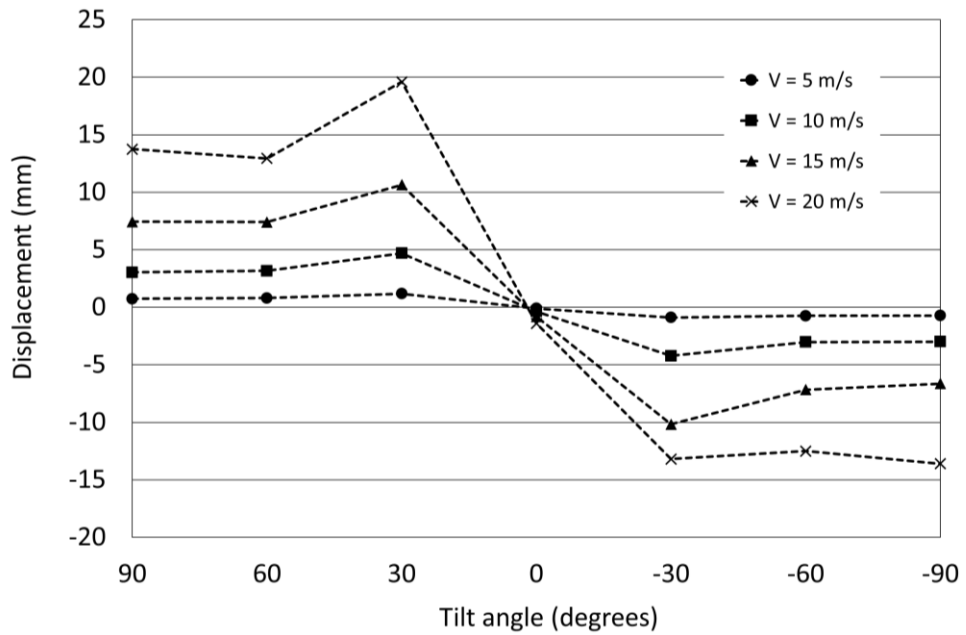


Figure 52: Wind velocity and tilt angle effects on the heliostat surface's maximum recorded displacement for 0° wind incidence angle

For the positive tilt angles, between $\theta = 90^\circ$ (heliostat facing directly at the air flow) and $\theta = 30^\circ$, the aerodynamic loads imposed upon the heliostat at $\theta = 30^\circ$ tilt angle generate a more detrimental effect on the heliostat's sandwich composite panel than do the other tilt angles. Figure 53 shows the pressure and displacement distribution of the heliostat surface from 90° to 30° tilt angles for a wind velocity of 20 m/s approaching at 0° wind incidence angle. When the structure is tilted at an angle of 90° and 60° , the high wind pressure is distributed over a relatively large area of the heliostat's panel compared with the 30° tilt angle condition. However, with the case of 30° tilt angle, the wind directly strikes the panel's lower edge region. Because this region mainly relies on the stiffness of the sandwich panel only (not fully supported by the steel attachments), the structure experiences larger displacement values compared to the 90° and 60° operational conditions.

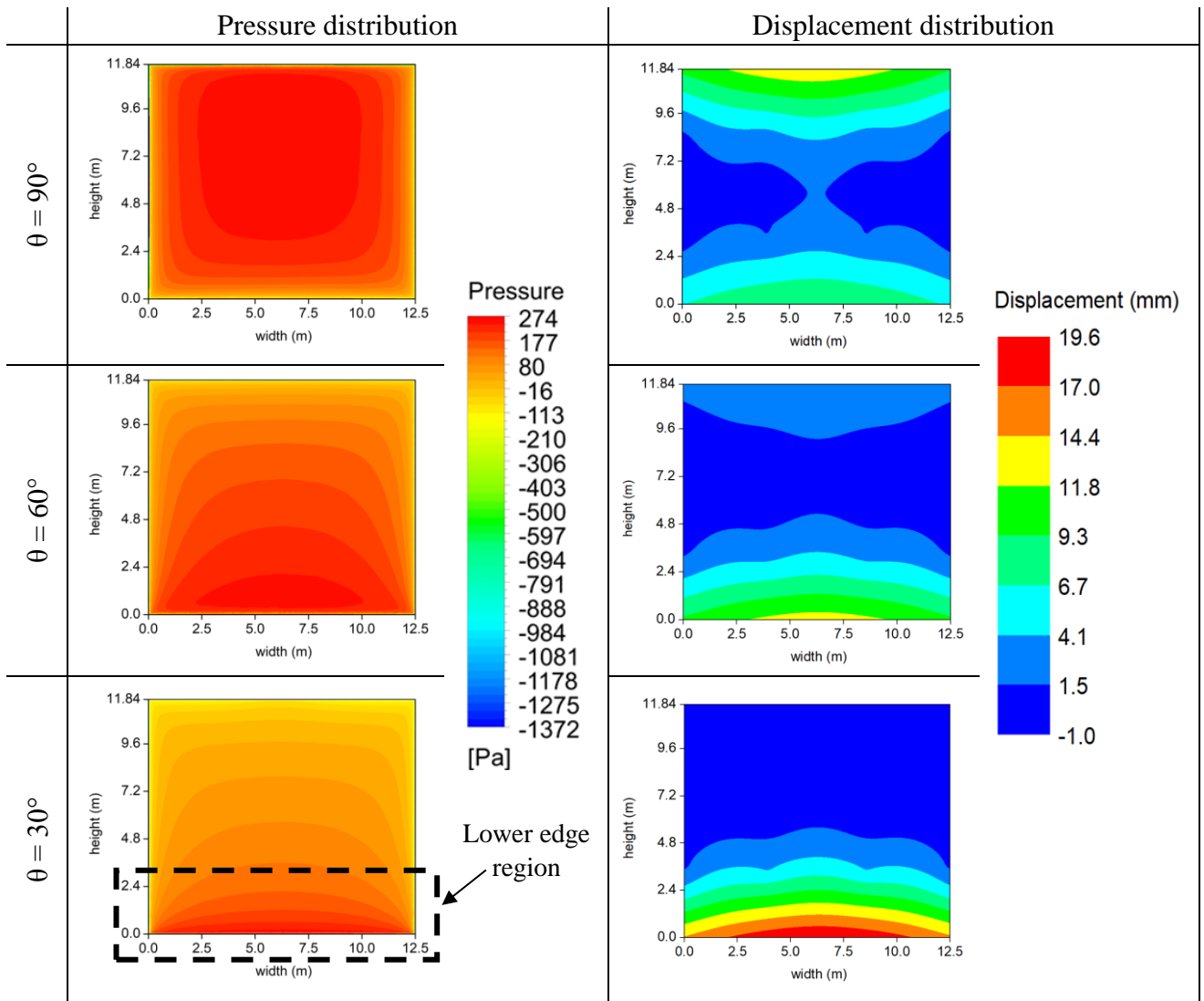


Figure 53: Pressure and displacement distribution of the heliostat surface for 90°, 60° and 30° tilt angles (θ) at wind velocity of 20 m/s approaching at 0° incidence angle (β)

As illustrated for the 0° wind incidence angle operational condition, the recorded maximum displacement results for a wind incidence angle of $\beta = 45^\circ$ (Figure 54) revealed the same patterns of variation but lower in magnitudes in comparison to the $\beta = 0^\circ$ condition illustrated earlier (Figure 52). This is expected as discussed previously that the blockage to wind flow provided by the heliostat structure decrease with the increase in wind incidence angle. This, in turn, causes a decrease in the aerodynamic loads imposed upon the heliostat panel, resulting in lower structural deflections.

Similar to the case of 0° wind incidence angle, it can be clearly observed that the maximum displacement values recorded for the negative tilt angles ($\theta = -30^\circ$ to $\theta = -90^\circ$) are lower than those observed for the positive tilt angles ($\theta = 90^\circ$ to $\theta = 30^\circ$) (Figure 54), confirming again the shielding effect of the heliostat's supporting components and torque tube on the incoming wind.

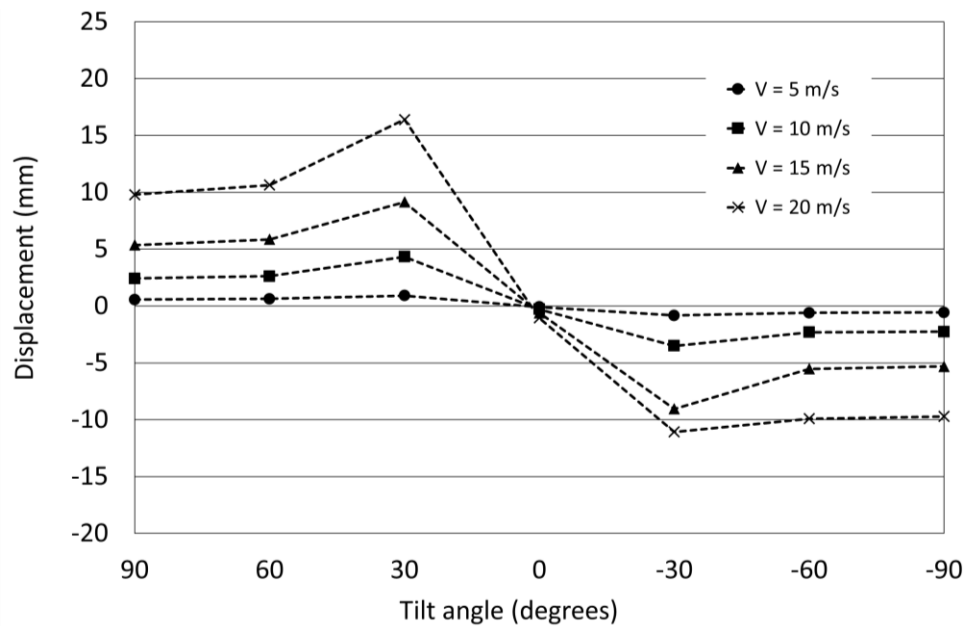


Figure 54: Wind velocity and tilt angle effects on the heliostat surface's maximum recorded displacement for 45° wind incidence angle

From the results in Figure 54, it is clear that the effect of heliostat's tilt orientation on the sandwich panel's maximum deflection becomes more vital as wind velocity increases above 10 m/s, particularly when the heliostat structure is tilted at an angle of $\theta = 30^\circ$ and subjected to a wind of 20 m/s. Expanding on this, the pressure and displacement distribution of the heliostat surface from 90° to 30° tilt angles for a wind velocity of 20 m/s approaching at 45° incidence angle is shown in Figure 55. When wind strikes the heliostat panel at this incidence angle, the high wind pressure is distributed along almost the entire right edge region of the panel when the structure is tilted at an angle of 90° and 60° . This region is supported by both the stiffness of the sandwich panel and also the steel attachment thus explaining the lower structural deflections in comparison to the 30° tilt

angle condition. As the heliostat structure is moved from $\theta = 60^\circ$ to a 30° tilt angle, the incoming wind at the same incidence angle acts on the lower right corner region of the panel directly, resulting in higher wind pressures at that region than those on other regions. As a result, and as described previously that the panel's lower edge region is not fully supported by the steel attachments and majorly rely on the sandwich panel's stiffness, the panel experiences larger displacement values compared to the aforementioned operational conditions i.e. 90° and 60° tilt angles.

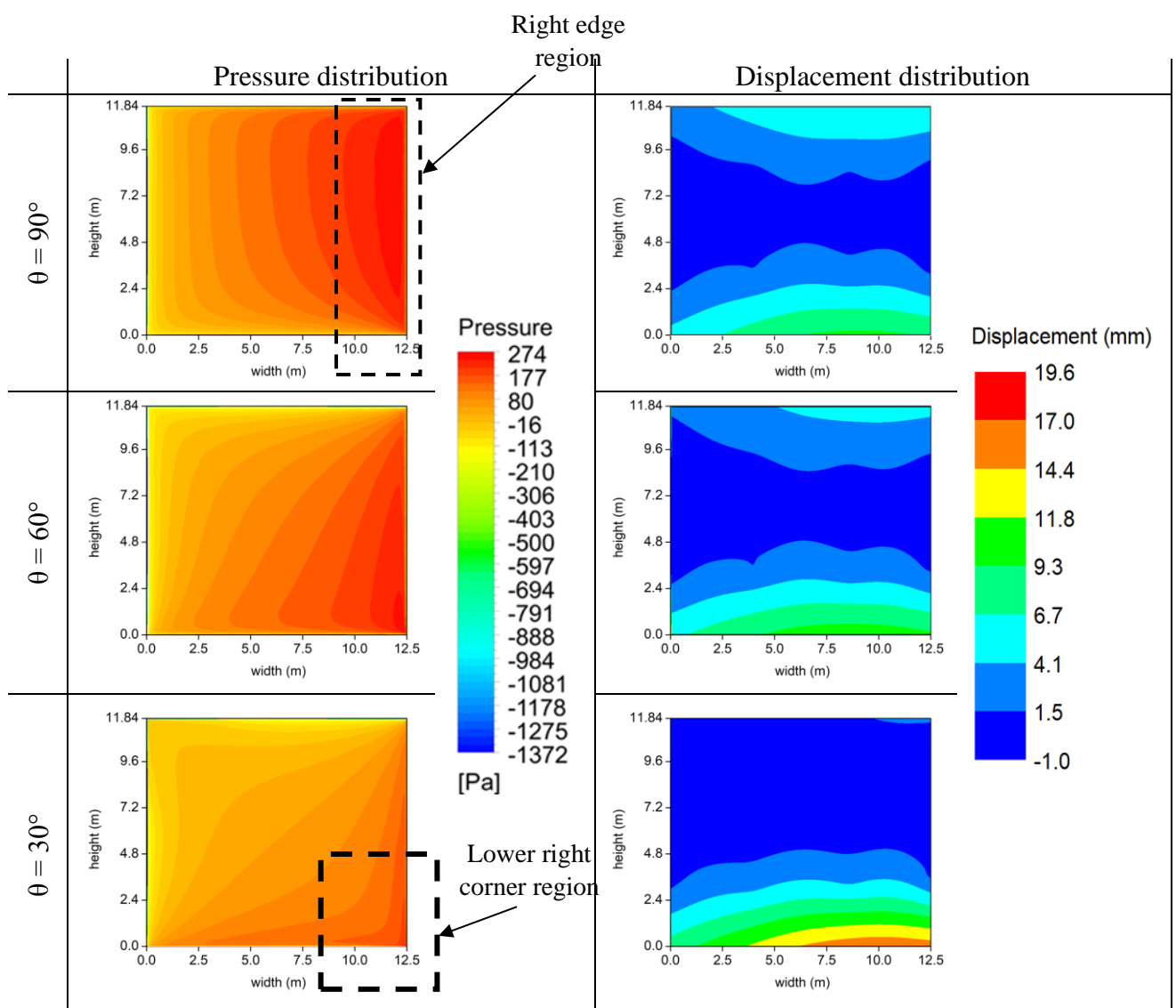


Figure 55: Pressure and displacement distribution of the heliostat surface for 90° , 60° and 30° tilt angles (θ) at wind velocity of 20 m/s approaching at 45° incidence angle (β)

The reduction in the recorded maximum displacement results of the heliostat's sandwich composite panel carries on as the wind incidence angle gradually increases until it reaches $\beta = 90^\circ$ for all tilt angles (Figure 56). This significant drop in the recorded maximum displacement values is due to the flow uniformity that causes a major reduction in the wind loading effect on the structure. This implies that the heliostat panel at 90° wind incidence angle, irrespective of any tilt angle, is not affected by wind loadings at wind velocities of 20 m/s and below.

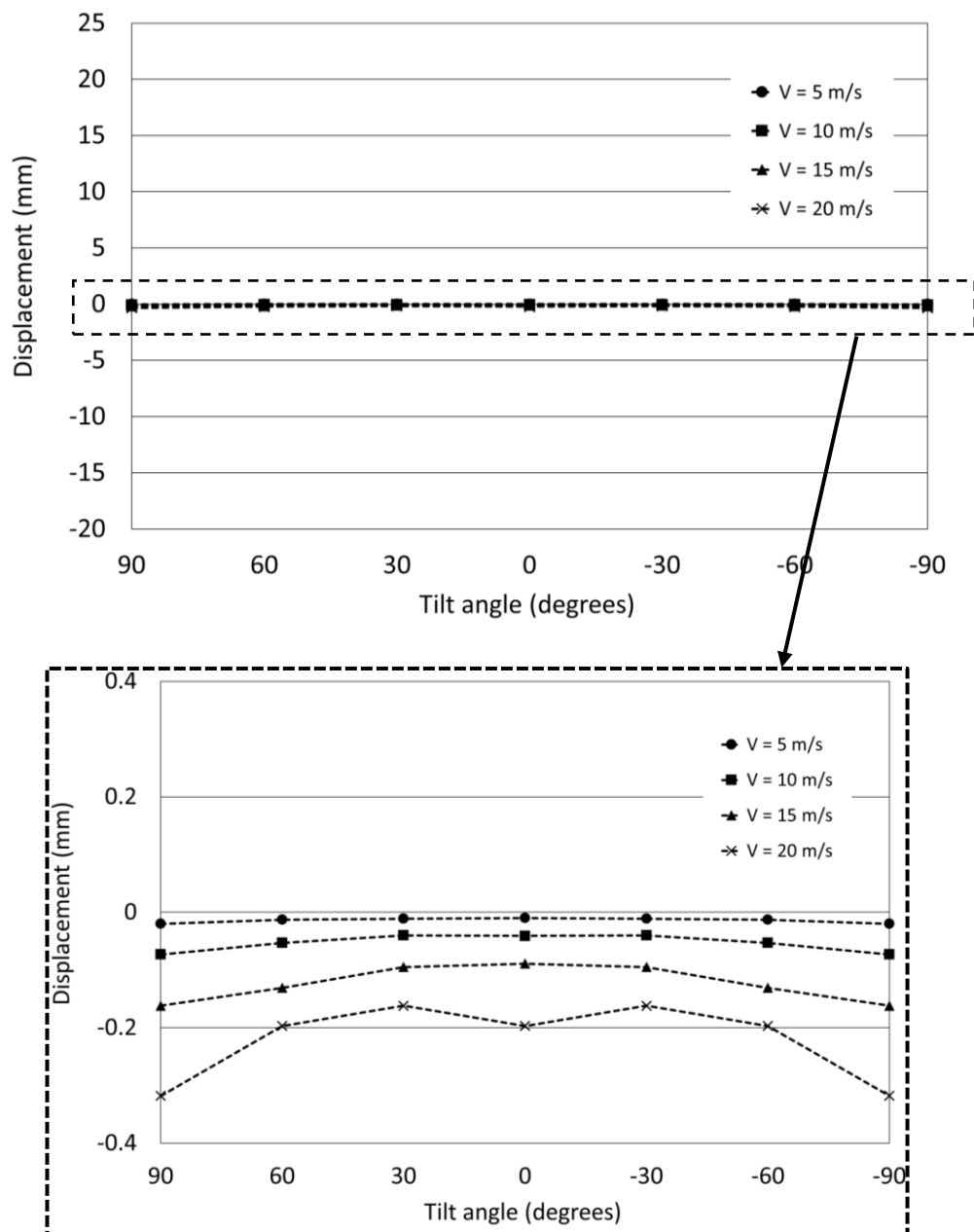


Figure 56: Wind velocity and tilt angle effects on the heliostat surface's maximum recorded displacement for 90° wind incidence angle

Compared to all of the other velocities explored, wind loadings at a wind velocity of 20 m/s have the most substantial effects on the resultant displacement of the given heliostat system for the operational conditions investigated. In all of the conditions studied, the largest resultant displacement is of 19.6 mm taking place at tilt angle of 30° under the effect of wind approaching at 0° incidence angle. For reliable operation of a heliostat, it is required that its structure should be able to keep its deformation below a certain threshold such that the acceptance angle loss of its reflective surface resides within certain tolerable limits. According to Strachan and Houser (1993) and Kolb et al. (2007), the Sandia requirements defined the maximum allowable reflective surface displacement angle caused by wind to be ± 3.6 mRad. Based on the aforementioned requirement, Björkman (2014) presented an approach, demonstrated in Figure 57, to evaluate the performance of the heliostat’s reflective surface using the following triangular relationship (Eq. 19) to calculate the maximum allowable displacement:

$$\tan(\pm 3.6 \text{ mRad}) = \frac{\text{Displacement}}{\frac{1}{2}(\text{Heliostat chord length})} \quad (19)$$

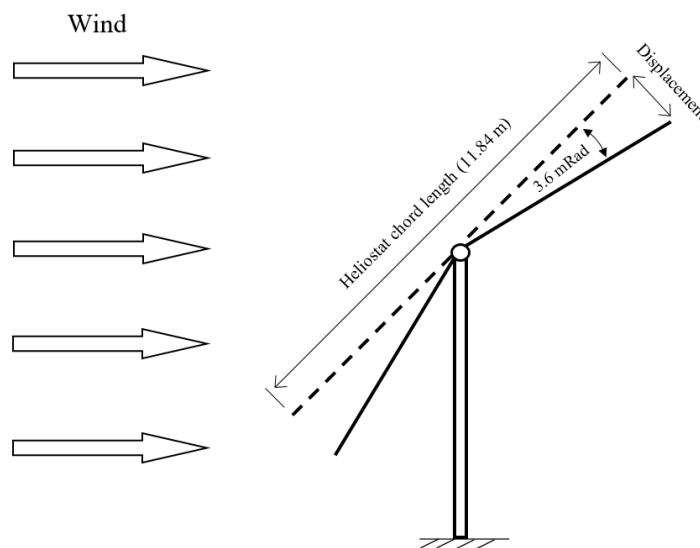


Figure 57: Interpretation of the reflective surface’s maximum allowable deflection (reproduced from Björkman (2014))

In this study, and in order to verify whether the proposed sandwich composite-based heliostat structure provides a good optical performance, the same approach was used. Given that the heliostat's chord length is 11.84 m, the maximum allowable displacement was found to be approximately ± 21.3 mm. On this basis, the deformation of the structure from the simulation suggests that it is within the allowable threshold, and may be suitable for use as a heliostat.

3.3.2 Stress distributions

Having discussed the deflection of the heliostat's sandwich composite panel at varying operational conditions, it was decided to explore the stress distribution characteristics of the heliostat's sandwich composite panel under those conditions in detail, to better understand and evaluate the structural strength of the sandwich panel. By locating regions of high stress in the sandwich panel, it was found that the highly stressed regions are located at the junction between the sandwich panel and the supporting steel attachments. Consequently, the two highly stressed components of the sandwich panel that have a higher probability of experiencing material failure are the lower aluminum sheet and the aluminum honeycomb core. In this sense, the study focused on evaluating the stress distribution characteristics of those two layers. The von Mises stress was selected to be the indicator of the stress field in this study, as it has been previously employed in a large number of studies that assessed the performance of aluminum honeycomb sandwich panels in various applications (Jen and Chang, 2009; Sadowski and Bęc, 2011; Zhang et al., 2011; Araújo et al., 2019; Upreti et al., 2019). Figures 58-63 show the stress distributions of the heliostat panel's lower aluminum sheet and the honeycomb core for different tilt angles (θ) under a wind velocity of 15 m/s approaching at 0° , 45° , and 90° wind incidence angles (β), respectively. Stress distribution results for the remaining wind incidence angles (i.e. $\beta = 22.5^\circ$ and $\beta = 67.5^\circ$) are provided in Appendix F.

Starting from the case when flow is perpendicular to the heliostat's reflective surface, i.e. 90° tilt angle and 0° wind incidence angle (Figure 58), the high stress regions are located at the upper and lower ends of the interface between the steel attachments and the back surface of the panel, with higher stresses seen at the upper ends. This is expected because, as demonstrated in Figure 102 in Appendix A, the heliostat panel is subjected to a wind gradient (the wind strength increases with the height above ground). This explains the higher stresses at the upper ends of the interface compared to the lower ends.

Taking the same wind incidence angle but gradually decreasing the tilt angle from $\theta = 90^\circ$ to $\theta = 30^\circ$ (Figure 58), it can be observed that higher stress concentrations are located near the lower ends of the interface, corresponding to the progressive shift in the high-pressure regions at the heliostat's mirror surface towards the lower edge as the structure's tilt angle (θ) moves from 90° to 30° . At this operational condition ($\theta = 30^\circ$, $\beta = 0^\circ$), the panel experiences the maximum stress. This can be attributed to the fact that the heliostat at this orientation experiences the maximum downward directed lift force due to the high pressure on the front side of the heliostat and the low pressure and high velocities below the structure. Moreover, the wind at this tilt orientation ($\theta = 30^\circ$) strikes the panel's lower edge region directly. As discussed earlier, this region is predominantly dependant on the sandwich panel's stiffness only (not fully supported by the steel attachments) for delivering the necessary rigidity and support for the reflective mirror module. This, therefore, causes an increase in the structural deflection of the panel's lower edge region, resulting in higher stresses at the lower ends of the interface between the steel attachments and the panel's back surface.

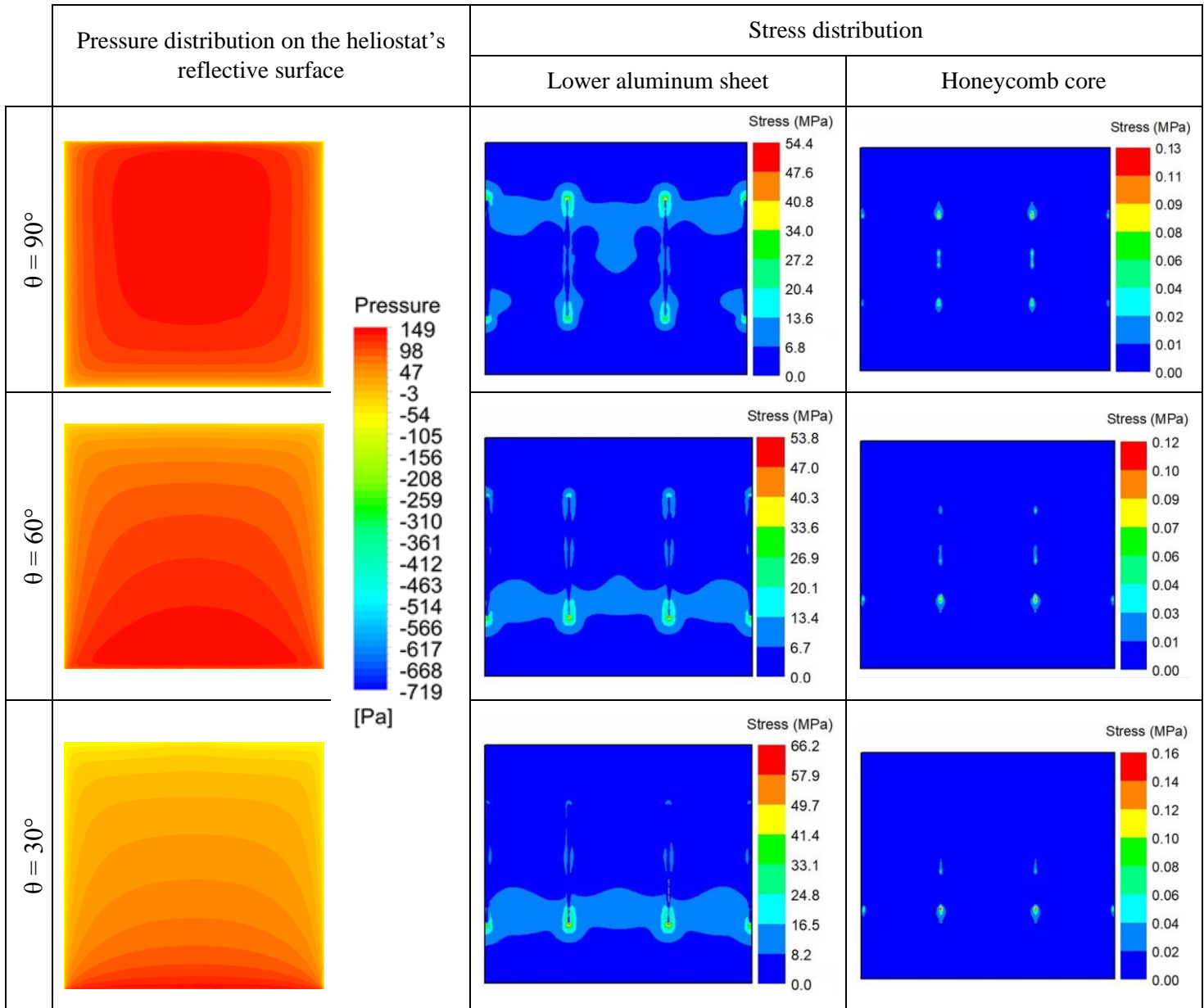


Figure 58: Pressure and stress distribution of the heliostat surface for 90°, 60°, 30° and 0° tilt angles (θ) at wind velocity of 15 m/s approaching at 0° incidence angle (β)

For the same incidence angle ($\beta = 0^\circ$), the recorded maximum stress values drop significantly when the heliostat's tilt angle decreases from $\theta = 30^\circ$ to $\theta = 0^\circ$ (Figure 59).

This is because, as previously explained, the projected area of the reflector directly facing

the wind at this operational condition becomes very small, allowing the uniformity of the flow that causes a significant decrease in the wind loading effect on the heliostat structure.

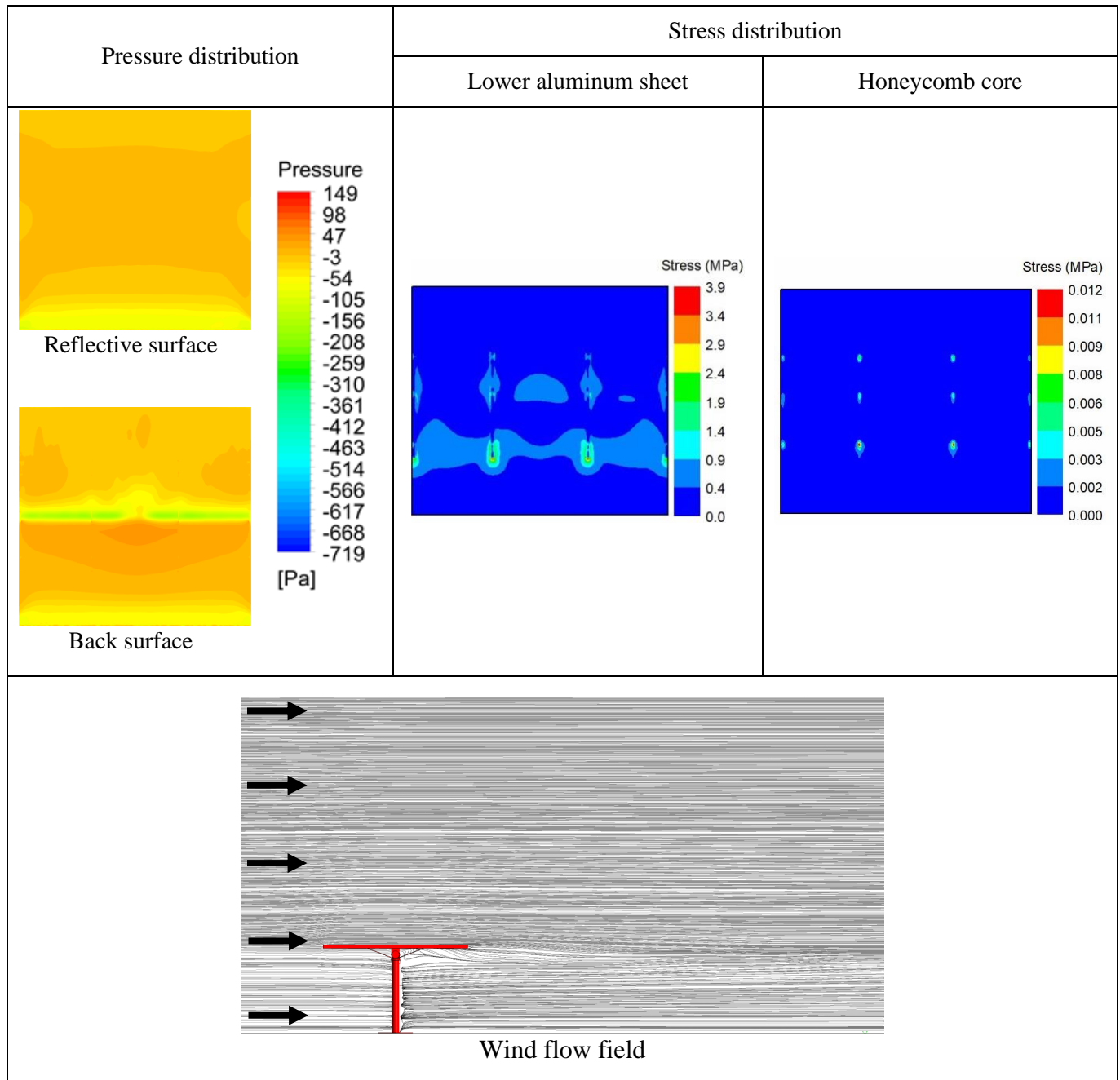


Figure 59: Pressure and stress distribution of the heliostat surface for 0° tilt angles (θ) at wind velocity of 15 m/s approaching at 0° incidence angle (β)

By altering the tilt angle gradually from $\theta = 0^\circ$ to $\theta = -90^\circ$ (Figure 60), such that the flow is from the backside of the structure, the heliostat's windward projected area increases and consequently the wind loading effect on the heliostat structure increases, causing an

increase in stress at the ends of the interface between the steel attachments and the panel's back surface. However, with that being said, the recorded maximum stress values were lower in comparison with the ones recorded when the flow is acting on the heliostat's mirror surface, i.e. $\theta = 90^\circ$ to $\theta = 30^\circ$ (Figure 58). This can be attributed, as previously noted, to the shielding effect caused by the heliostat's supporting components.

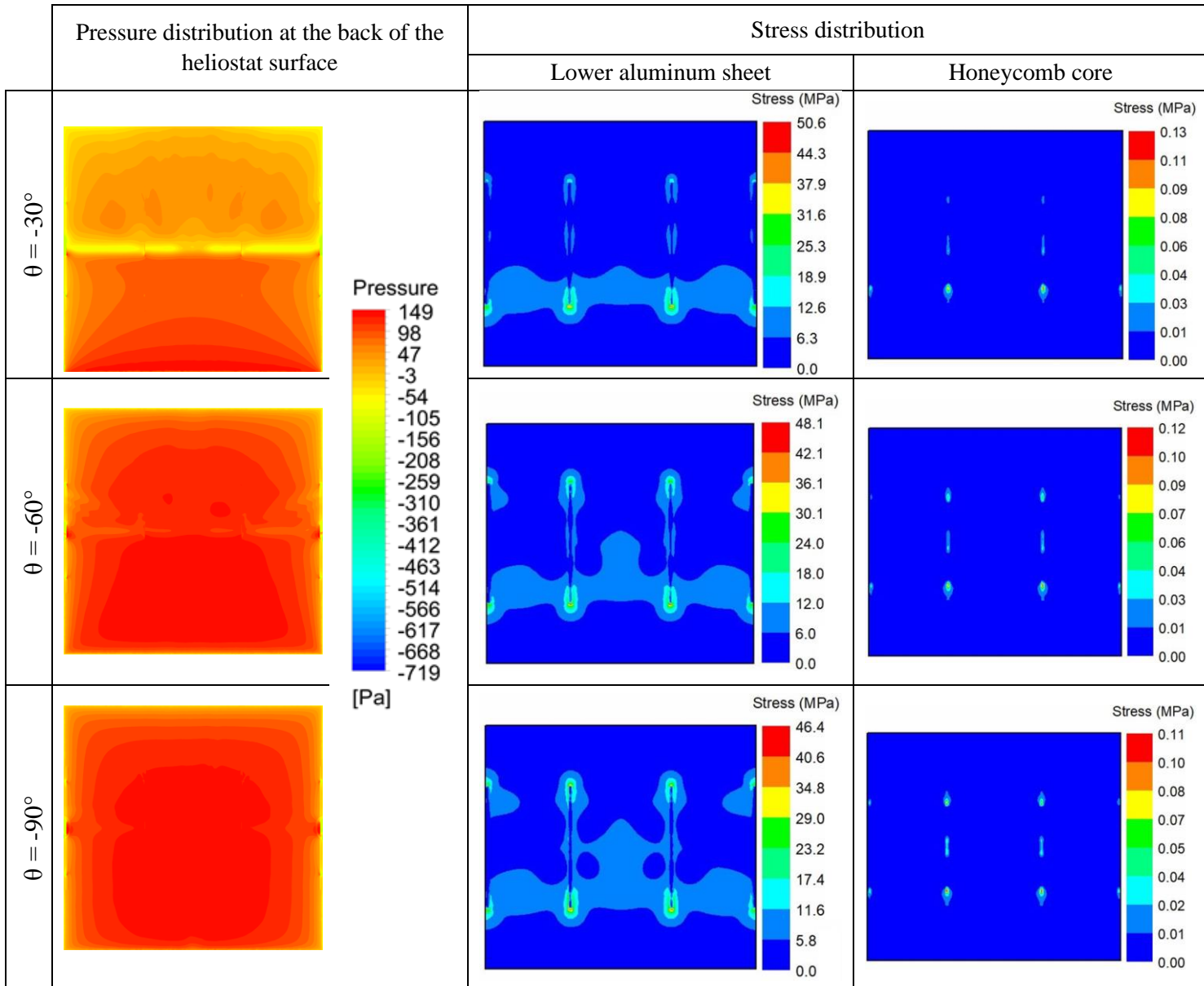
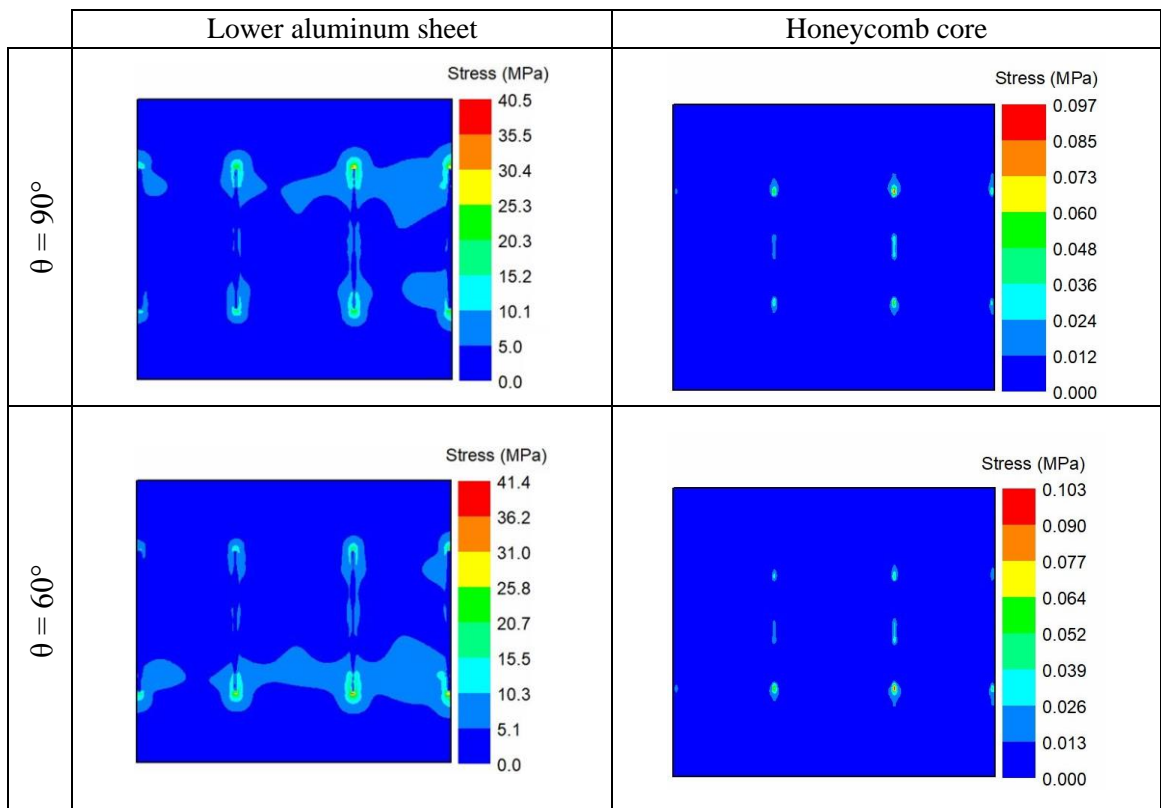


Figure 60: Pressure and stress distribution of the heliostat surface for -30° , -60° and -90° tilt angles (θ) at wind velocity of 15 m/s approaching at 0° incidence angle (β)

The gradual variation in the wind incidence angle (β) from 0° to 45° for all tilt angles (Figures 61) causes the high-stress regions located at the interface between the steel attachments and the back surface of the panel to shift progressively towards the two attachments to the right. Furthermore, and as a result of the decrease in the wind-induced forces caused by the reduction in the pressure gradient between the heliostat's reflective and back surfaces, the stress levels gradually decrease as the wind incidence angle changes from $\beta = 0^\circ$ to $\beta = 45^\circ$ (Figure 62). In addition, and again similar to the 0° wind incidence operational condition, the same shielding effect has been observed at this configuration ($\beta = 45^\circ$) (Figures 61 and 62), and the maximum stress values recorded when the heliostat's back surface facing the wind ($\theta = -30^\circ$ to $\theta = -90^\circ$) were slightly lower than the ones recorded when the flow is acting on the heliostat's mirror surface ($\theta = 90^\circ$ to $\theta = -30^\circ$).



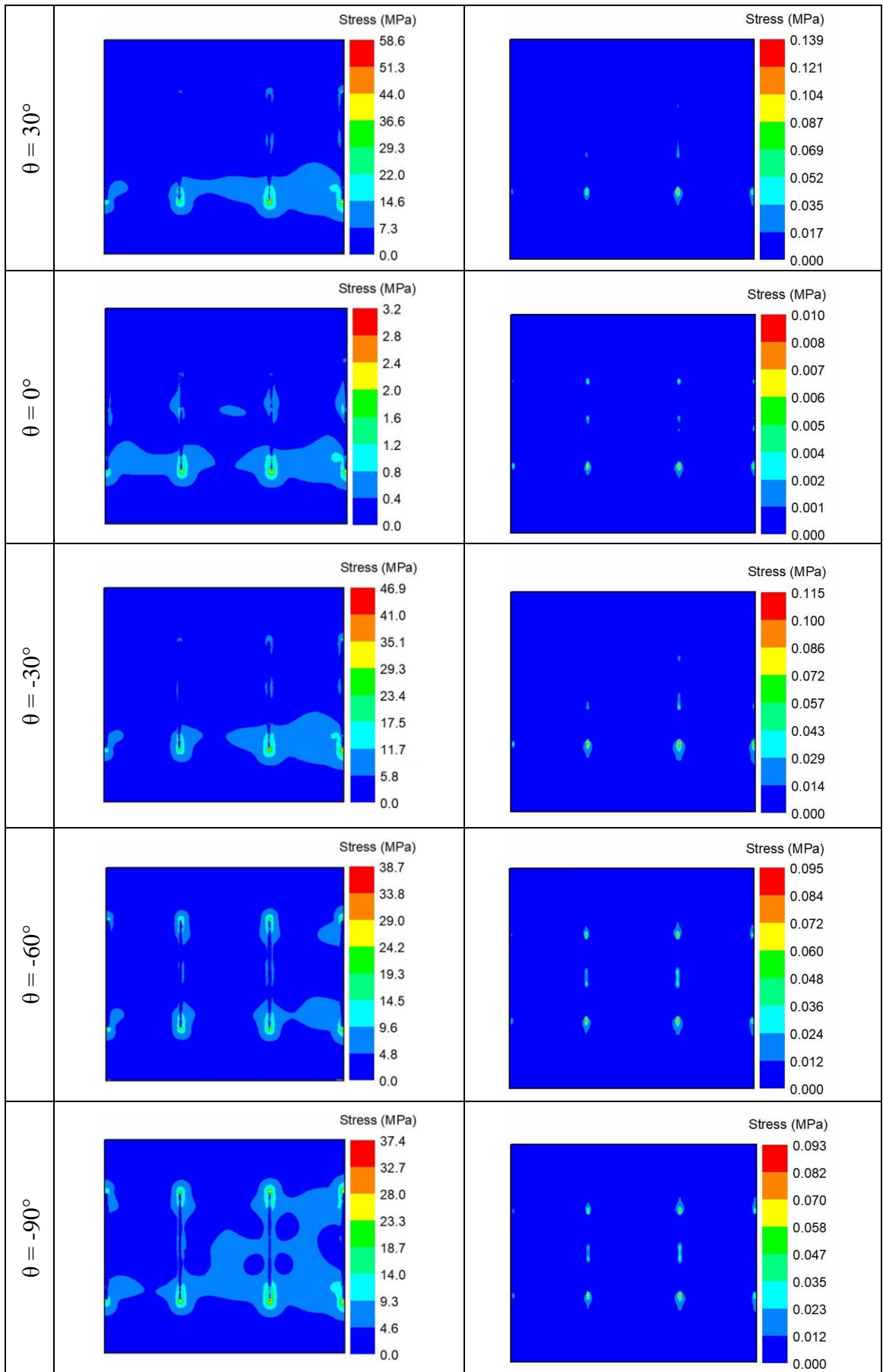
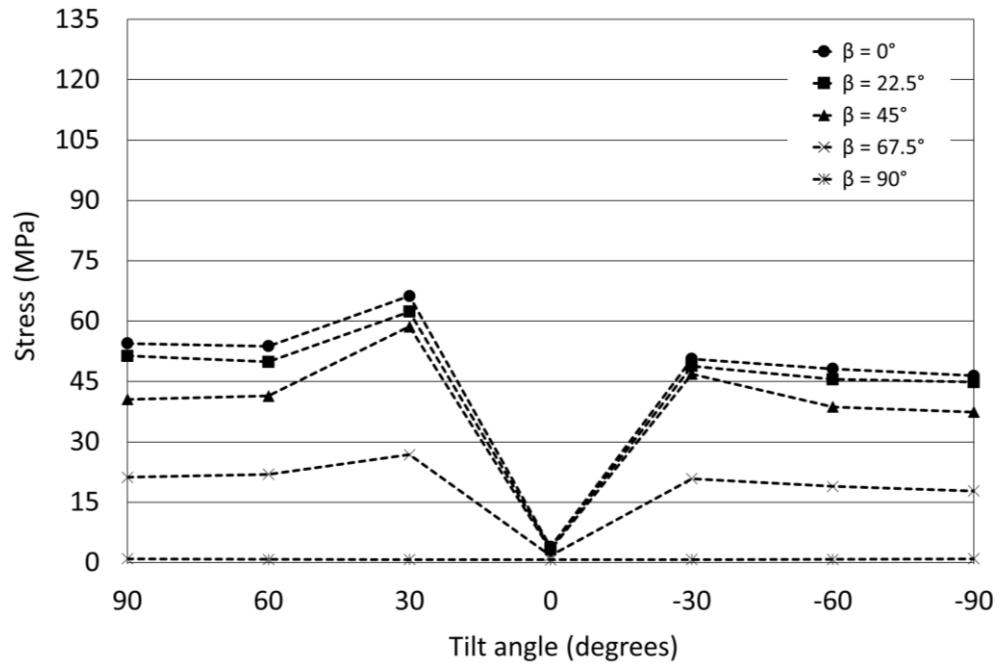
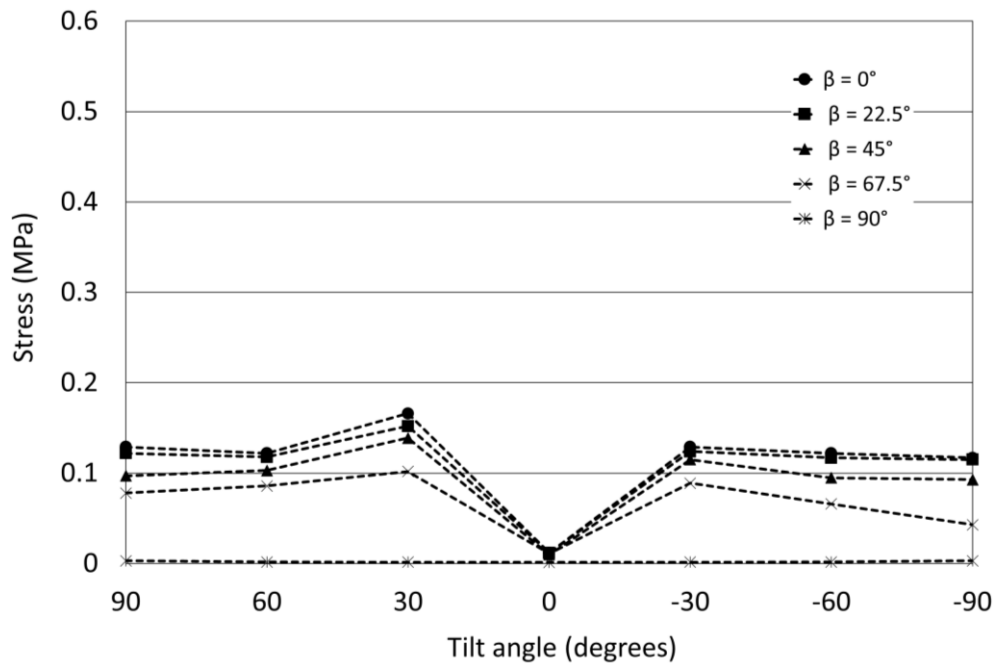


Figure 61: Stress distribution of the heliostat surface for different tilt angles at wind velocity of 15 m/s approaching at 45° incidence angle



(a) Lower aluminum sheet

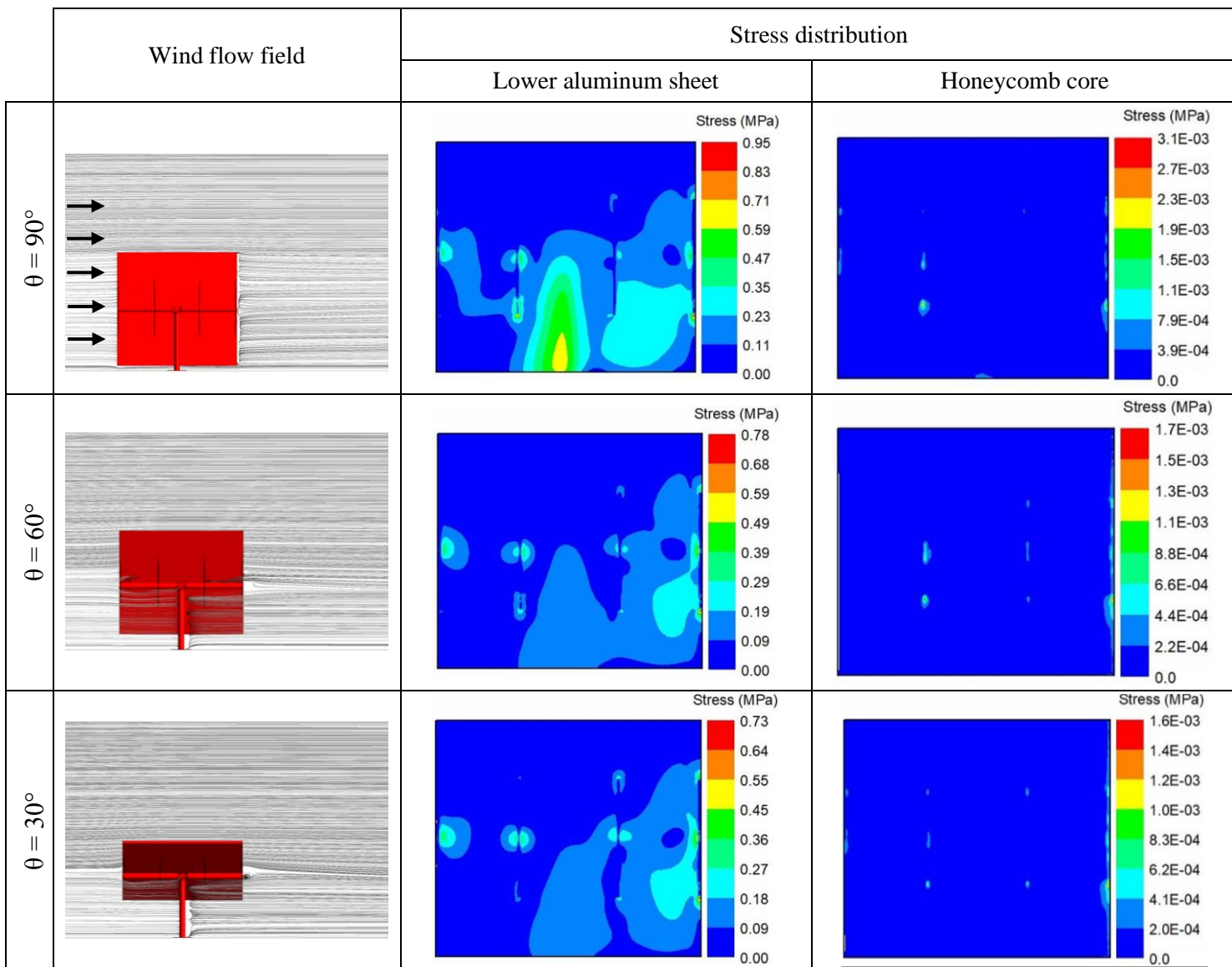


(b) Honeycomb core

Figure 62: Wind incidence angle effect on the heliostat's maximum recorded stress for different tilt angles at wind velocity of 15 m/s

The reduction in stress values continues as the wind incidence increases from 45° to 90° (Figures 62 and 63) and as noted previously, this can be attributed to the significant

decrease in the projected area of the heliostat directly facing the wind at this operational condition, permitting the uniformity of the flow that causes a significant drop in the wind loading effect on the structure. However, what is interesting to note is that for tilt angles 90° and -90° , high stress regions are observed at the aluminum sheet's lower and upper edge regions respectively. This is because of, as discussed previously, the depression region that forms within the pedestal and the panel. This region starts to demise as the structure moves toward the stow position from $\theta = \pm 90^\circ$.



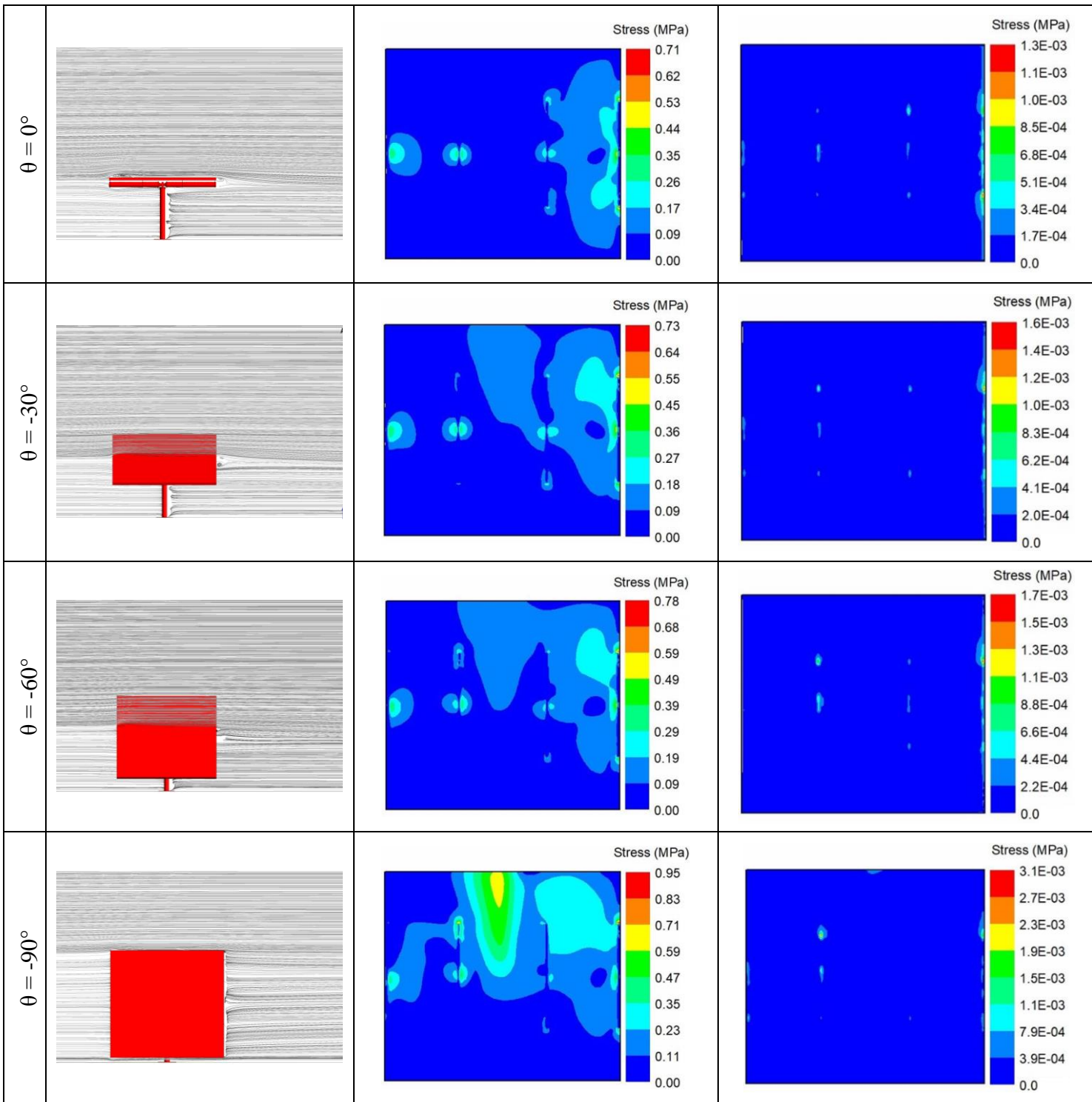
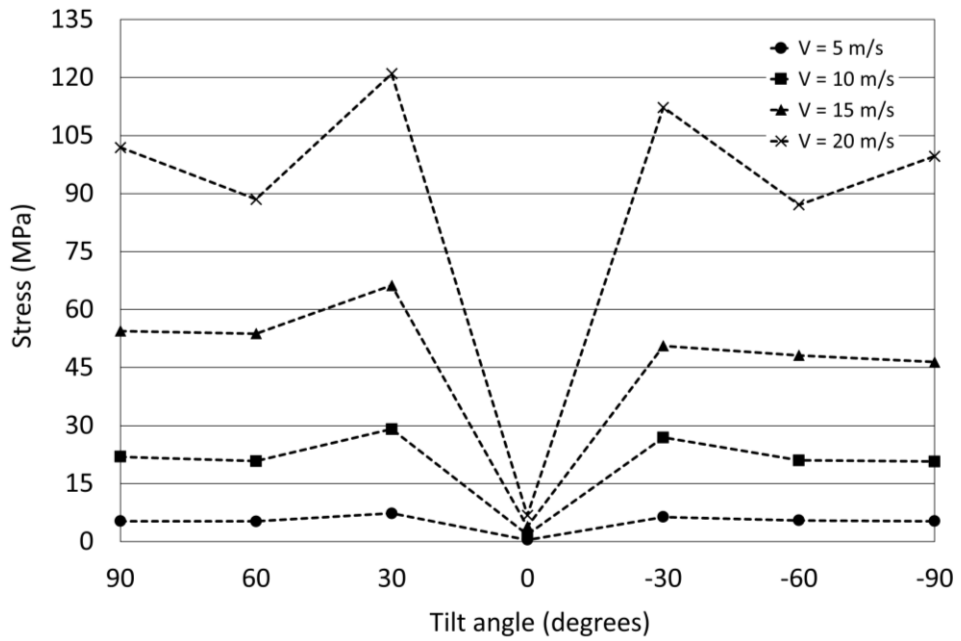


Figure 63: Stress distribution of the heliostat surface for different tilt angles at wind velocity of 15 m/s approaching at 90° incidence angle (β)

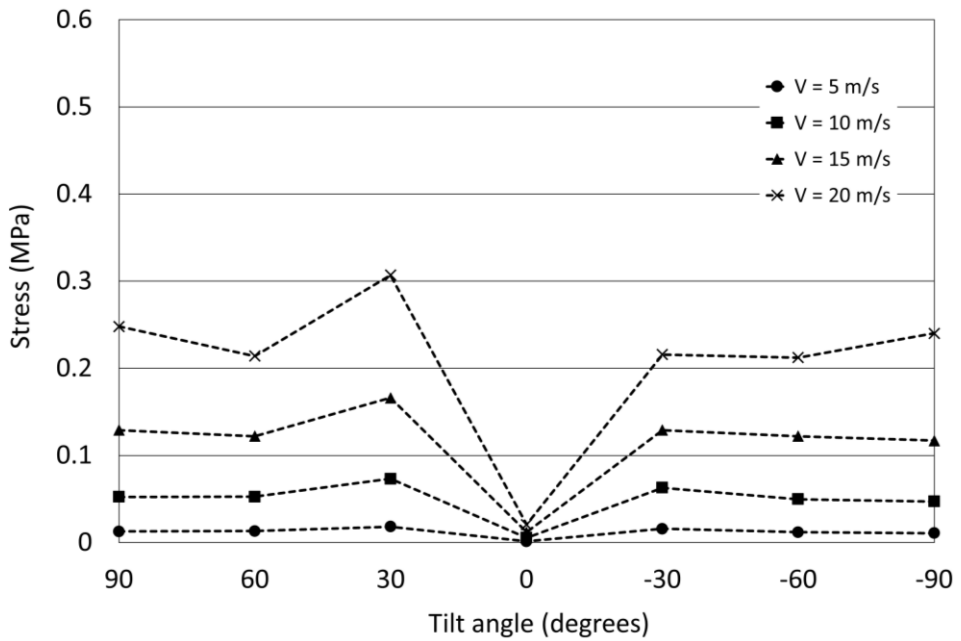
Having investigated the stress distribution of the heliostat's sandwich composite panel for the 15 m/s loading condition, the effect of changing wind velocity on the maximum stresses at the heliostat panel's lower aluminum sheet and honeycomb core for different tilt and incidence angles is shown in Figures 64-68.

Starting with the 0° wind incidence angle results (Figure 64), it was observed that, as one may expect, increasing wind velocity affects the recorded maximum stress values at both the lower aluminum sheet and the honeycomb core by increasing their magnitudes but at different rates. As anticipated, and because of the decrease in the wind loading effect on the panel at this tilt orientation, the effect of increase in wind velocity on the maximum stress values recorded at the panel's lower aluminum sheet and honeycomb core for the case of $\theta = 0^\circ$ was insignificant.

As wind velocity increases above 10 m/s, it can be seen that the effect of heliostat's tilt orientation on the maximum stresses at both the lower aluminum sheet and the aluminum honeycomb core becomes more noticeable, and the variance in the maximum stress values at different tilt angles escalates to a maximum when wind strikes the heliostat panel with a velocity of 20 m/s. With the gradual increase in wind velocity, the shielding effect caused by the heliostat's supporting components on the maximum stress values becomes more pronounced, and the maximum stress values recorded for the negative tilt angles ($\theta = -30^\circ$ to $\theta = -90^\circ$) were lower than those observed for the positive tilt angles ($\theta = 90^\circ$ to $\theta = 30^\circ$) (Figure 64).



(a) Lower aluminum sheet



(b) Honeycomb core

Figure 64: Wind velocity and tilt angle effects on the heliostat's maximum recorded stress for 0° wind incidence angle

From the results (Figure 64), and among the various tilt angles investigated, wind loadings with a velocity of 20 m/s striking the heliostat structure at $\theta = 30^\circ$ tilt angle causes more harmful effect on the sandwich panel than any other tilt angle. Expanding on this, Figure 65 illustrates both pressure and stress distribution results for a wind velocity of 20 m/s approaching at 0° wind incidence angle. Unlike for the 90° and 60° tilt angle conditions

where the loads are distributed over a large area of the heliostat's panel, the high wind pressure for the 30° tilt angle operational condition is concentrated in a particular region i.e. the panel's lower edge region. Because of this, and given that this region is dependent upon the sandwich panel's stiffness only, the panel experiences larger deflections at the lower edge region. This high bending due to wind loads, in addition to the strong wind pressure imposed upon that region, induces higher stresses than do the other tilt angles; located at the lower ends of the interface between the steel attachments and the panel's back surface.

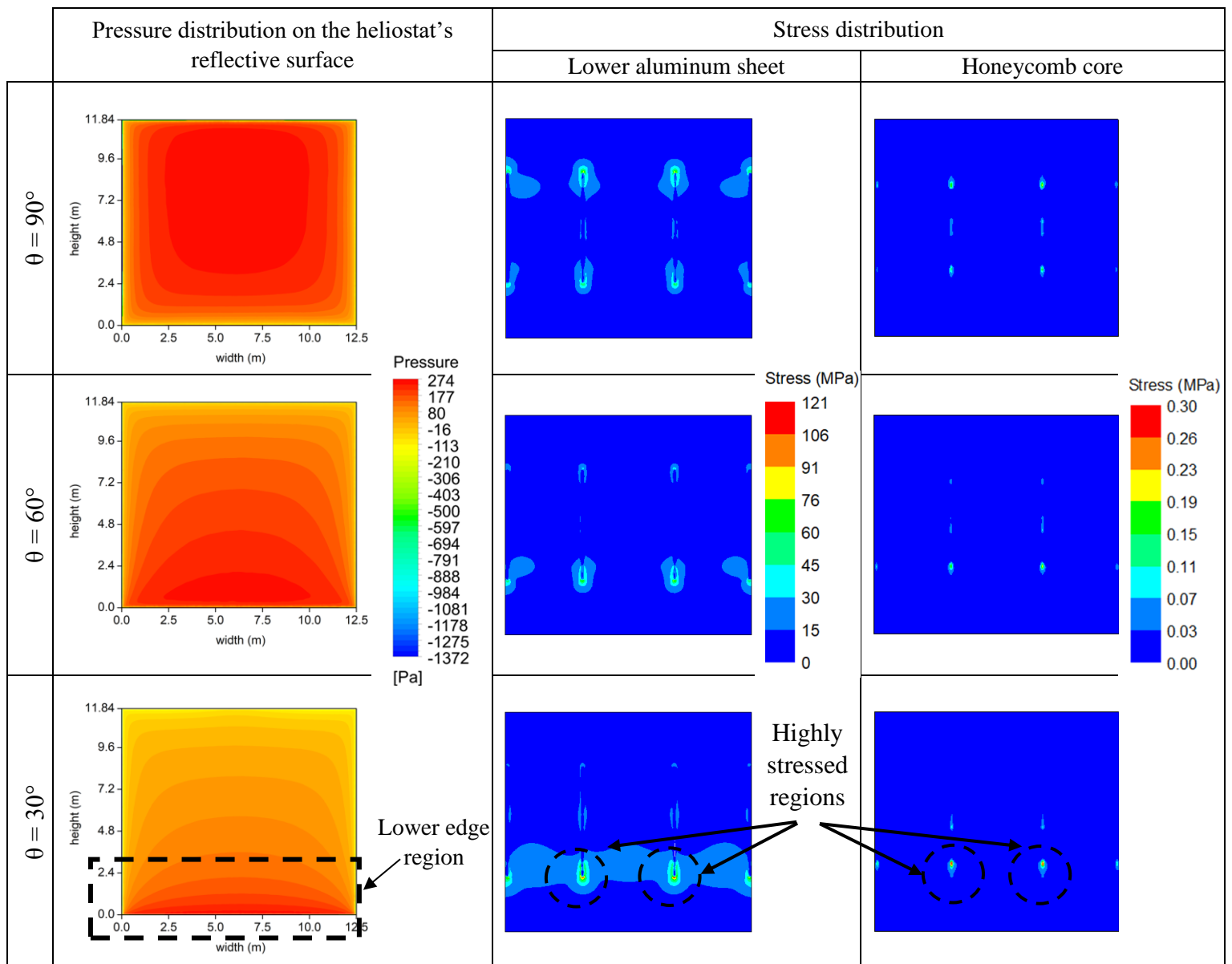
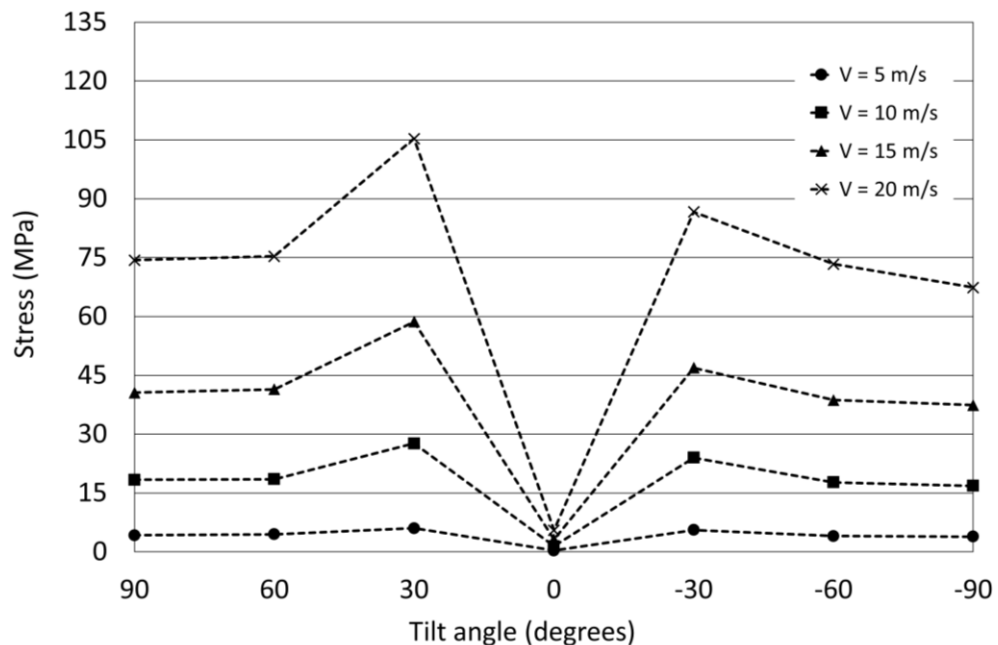


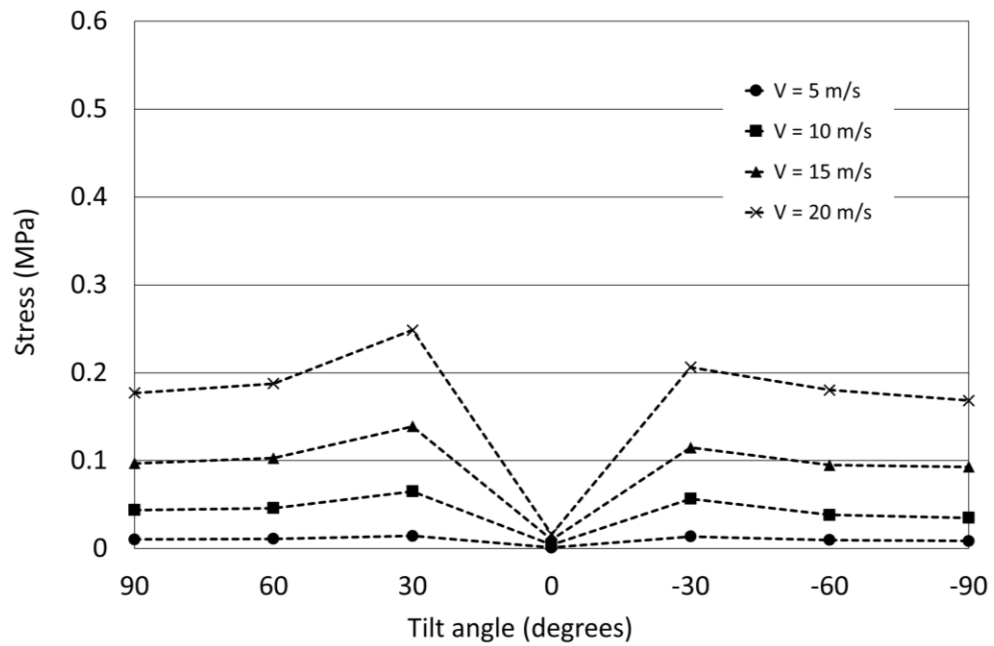
Figure 65: Pressure and stress distribution results for 90°, 60°, 30° and 0° tilt angles (θ) at wind velocity of 20 m/s approaching at 0° incidence angle (β)

The recorded maximum stress values when the flow approaches the heliostat at 45° incidence angle (Figure 66) showed the same variation patterns as the 0° wind incidence angle case but lower. This reduction corresponds to the decrease in the wind loading effect on the heliostat that occurs as a result of the reduced blockage effect (the heliostat's projected area directly facing the wind decreases with the increase in wind incidence angle), resulting in lower stresses in comparison to the $\beta = 0^\circ$ operational condition demonstrated earlier in Figure 64.

At this operational condition ($\beta = 45^\circ$) (Figure 66), again the same shielding effect caused by the heliostat's supporting components on the maximum stress values can be noticed when comparing the negative tilt angles ($\theta = -30^\circ$ to $\theta = -90^\circ$) with the positive ones ($\theta = 90^\circ$ to $\theta = 30^\circ$). This effect develops more strongly at higher wind velocities (greater than 10 m/s).



(a) Lower aluminum sheet



(b) Honeycomb core

Figure 66: Wind velocity and tilt angle effects on the heliostat's maximum recorded stress for 45° wind incidence angle

The heliostat at this wind incidence angle ($\beta = 45^\circ$) experiences the maximum stress intensity when the panel is subjected to a wind of 20 m/s and tilted at an angle of 30° . Going into detail about this, the pressure and stress distribution results for a wind velocity of 20 m/s approaching at 45° wind incidence angle is presented in Figure 67.

For the 30° tilt angle operational condition, the high wind pressure is concentrated over a smaller area (the lower right corner region of the panel) relative to that shown in the 90° and 60° tilt angle operational conditions, which puts direct pressure on the regions located at the junction between the sandwich panel and the two supporting steel attachments to the right. This causes the stresses to escalate and concentrate at the lower right ends of the interface between the steel attachments and the panel's back surface.

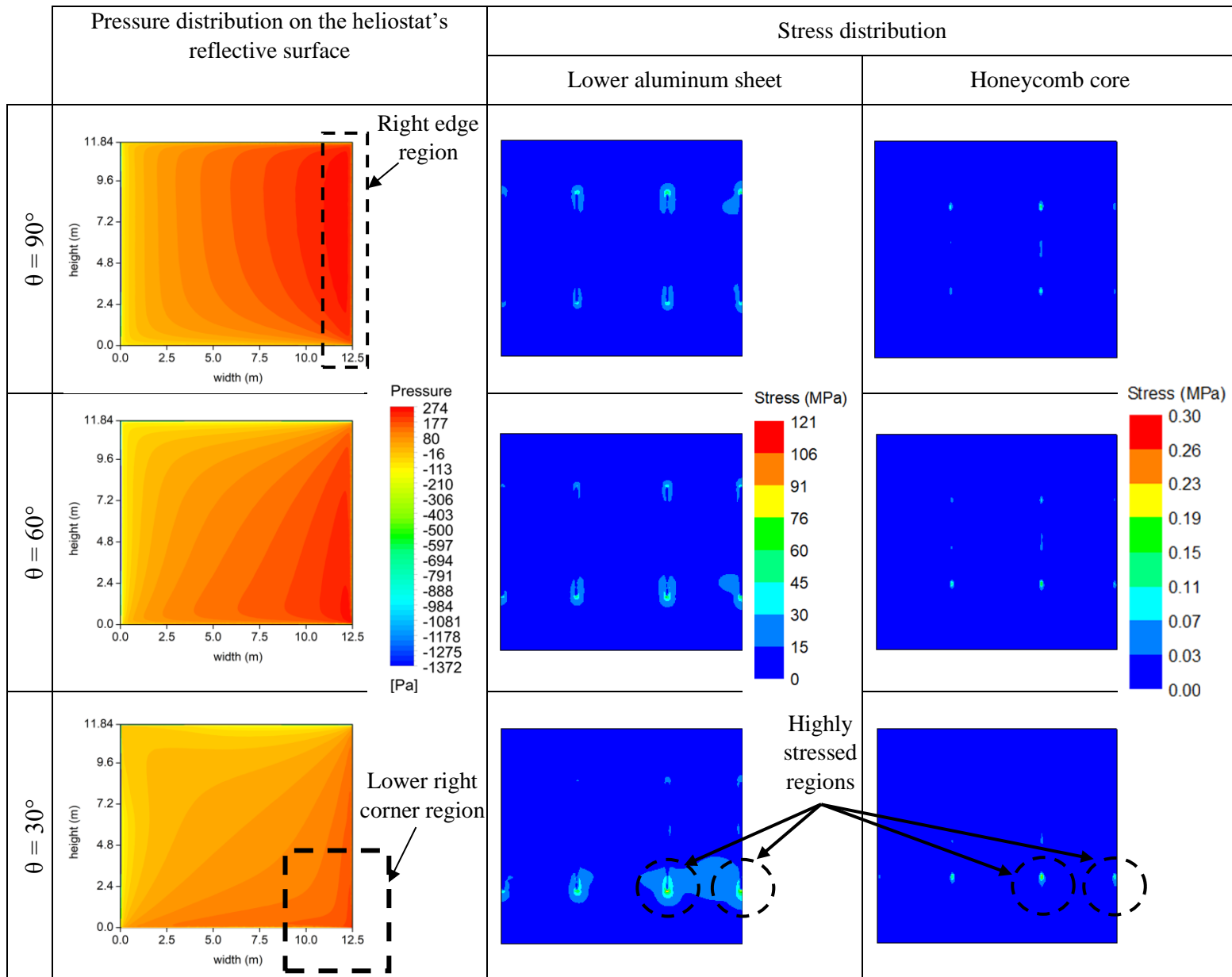
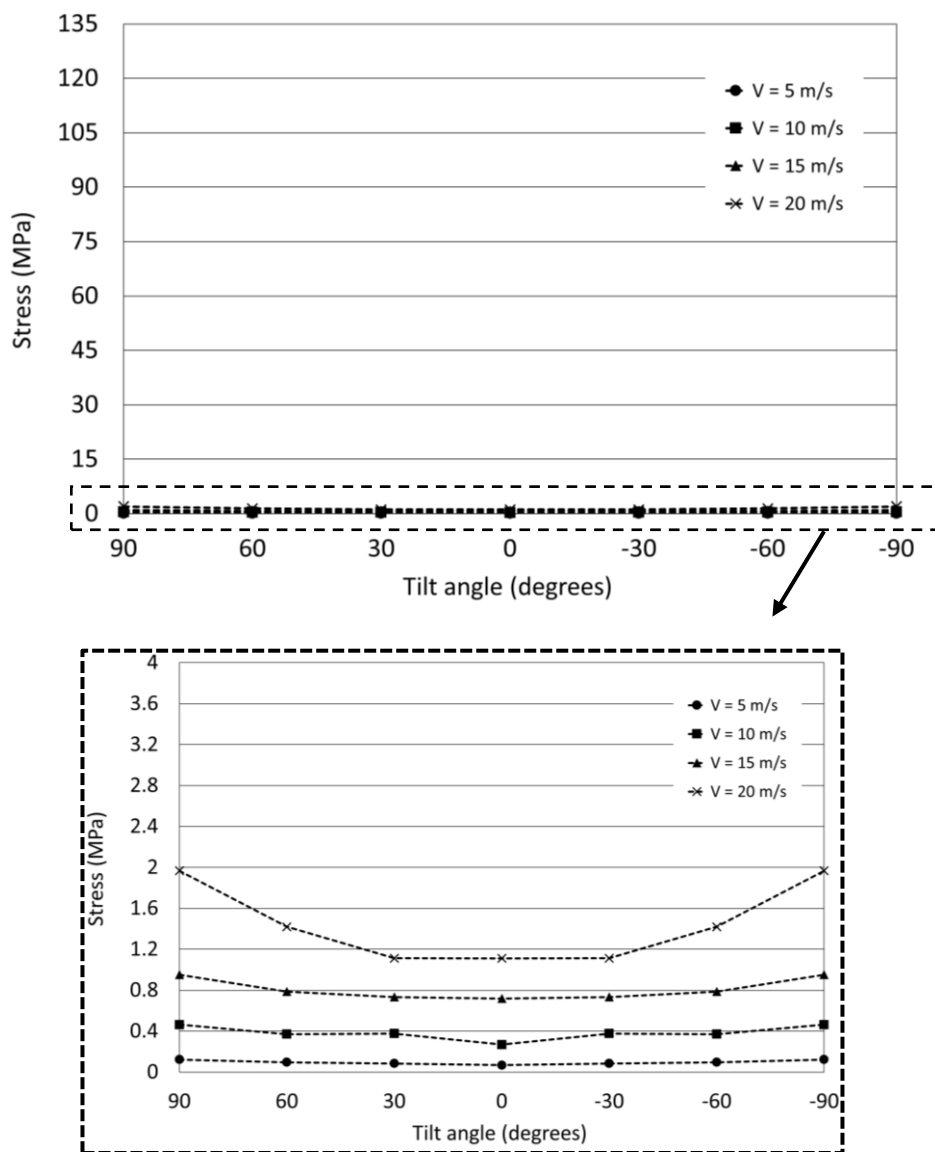
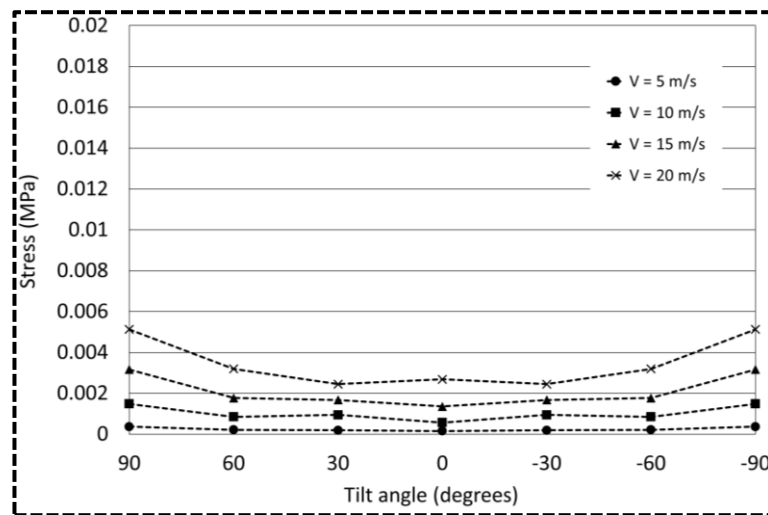
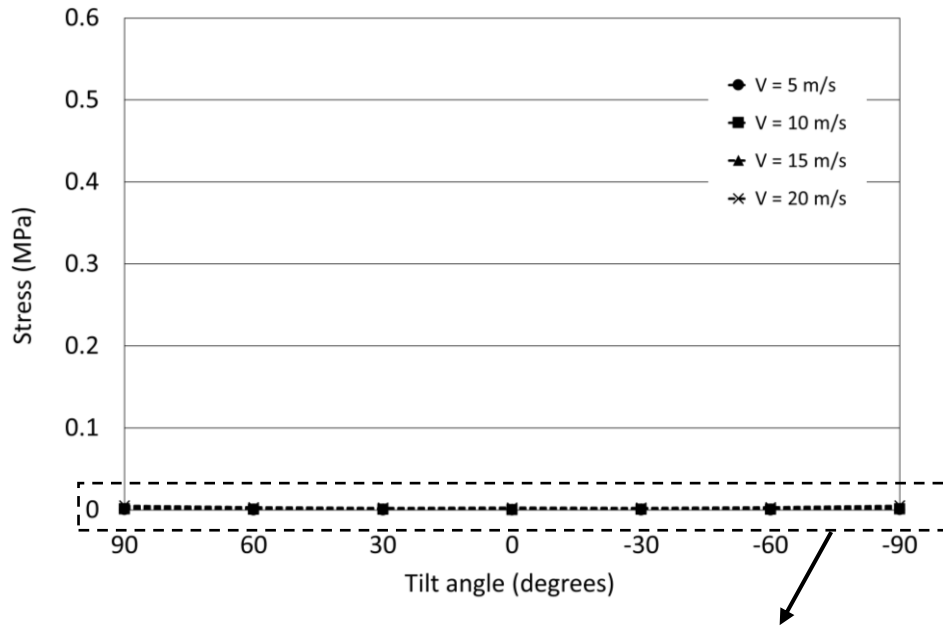


Figure 67: Pressure and stress distribution results for 90° , 60° , 30° and 0° tilt angles (θ) at wind velocity of 20 m/s approaching at 45° incidence angle (β)

As the wind incidence angle gradually increases from 45° until it reaches 90° for all tilt angles (Figures 68), the wind incidence angle influence on the stress values gradually increases and the values notably decrease and reach their minimum at $\beta = 90^\circ$. This is because of the uniformity of the flow that causes a significant decrease in the wind loading effect on the heliostat panel. This suggests that the heliostat panel's lower aluminum sheet and honeycomb core at 90° wind incidence angle, regardless of any tilt angle, are not significantly influenced by wind loadings at wind velocities of 20 m/s and below.



(a) Lower aluminum sheet

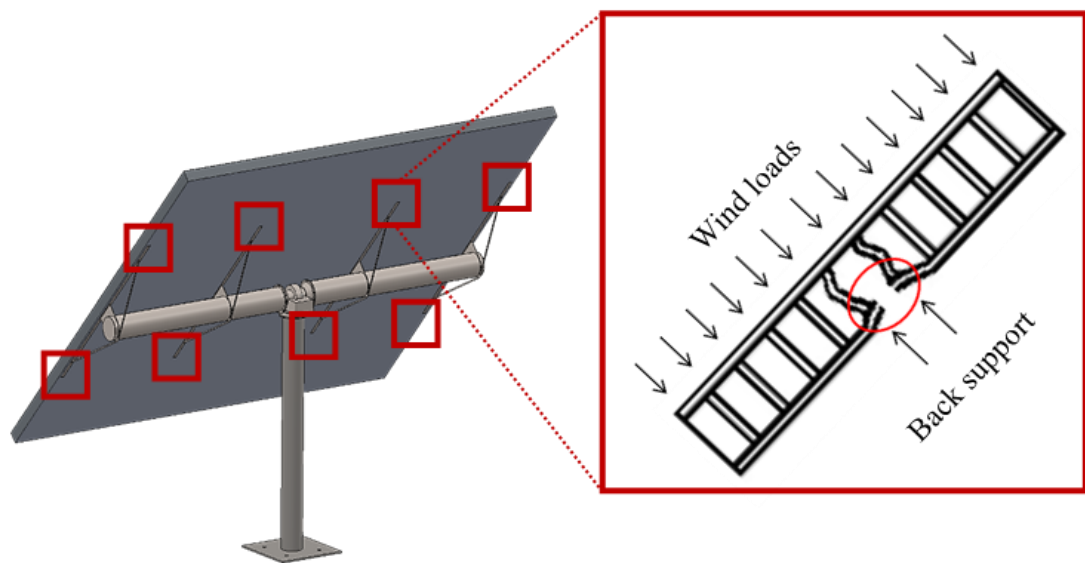


(b) Honeycomb core

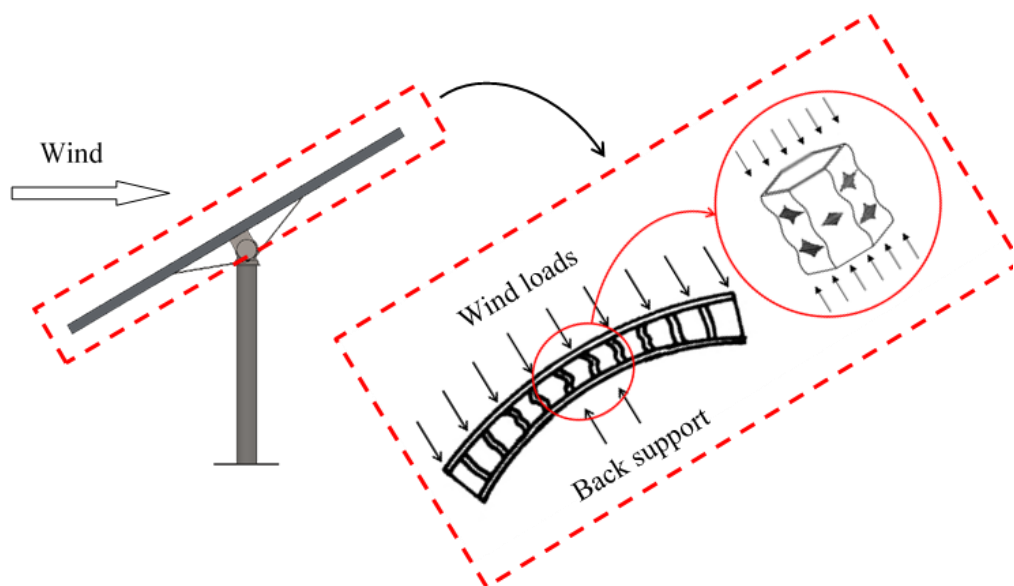
Figure 68: Wind velocity and tilt angle effects on the heliostat's maximum recorded stress for 90° wind incidence angle

Similarly, and corresponding to the maximum resultant deformation of the structure, the worst case was found also to be at a tilt angle of 30° under the effect of wind flow at 0° to the heliostat surface with a velocity of 20 m/s. At this operational condition, the calculated maximum stresses at both the lower aluminum sheet and the aluminum honeycomb core are of 121.62 MPa and 0.307 MPa, respectively. The stresses imposed upon the panel can cause two of the most common forms of failure for honeycomb

sandwich panels: face yielding and core crushing (Figure 69). Face yielding is the plastic collapse of the metal face sheet when the stress exceeds the yield strength of the material (Totten et al., 2018). Core crushing, on the other hand, is a core failure mode that is caused by cell-wall collapse due to cell-wall buckling when the flexure-induced compressive loading exerted upon the core exceeds the critical collapse strength of the core (Staal et al., 2009; Haghpanah et al., 2014).



(a) Face yielding



(b) Core crushing

Figure 69: Common failure forms of honeycomb sandwich panels (reproduced from Galletti et al. (2008) and Gibson and Ashby (1997))

According to Gibson and Ashby (1997), the critical collapse strength of honeycombs ($\sigma_{collapse}$) can be estimated by means of the following relationship (Eq. 20):

$$\sigma_{collapse} = \frac{3t}{2a \cos \varphi (1 + \sin \varphi)} \sigma_y \quad (20)$$

Where φ is the cell wall angle, a is the cell wall length, t is the cell wall thickness and σ_y is the yield strength of the honeycomb's solid material. Given that σ_y for aluminum is 280 MPa, the core's critical collapse strength was found to be approximately 1.62 MPa. On this basis, the maximum stresses at both the lower aluminum sheet and the aluminum honeycomb core from the simulation suggest that they are within the permissible limits. This indicates the given heliostat's composite structure, with an achieved weight reduction of approximately 20% compared to the existing 148 m² steel-based ATS heliostat (Kolb et al., 2007), is unlikely to experience material failure and is expected to maintain a very high optical performance when subjected to a wind of 20 m/s and below. Based on these observations, it can be concluded that honeycomb sandwich composites are highly suitable for use as a heliostat mirror structure.

3.4 Chapter Summary

While honeycomb sandwich composites have been broadly employed in various applications where high structural rigidity and low weight are extremely crucial, it is surprising that there is an absence of studies that rigorously investigated their suitability as the structure for heliostat mirror. Given the opportunity of reducing heliostats' cost by minimizing the total weight of the structure, and the fact that heliostats are sensitive to wind loads, there is a need for a better understanding of how honeycomb sandwich composites respond under wind effects when utilized as the structure for heliostat mirror.

In this chapter, numerical fluid-structure interaction (FSI) simulations were performed to investigate the aero-structural robustness and behaviour characteristics of honeycomb

sandwich composites when employed as a heliostat mirror support structure. The structural behaviour characteristics of the heliostat's sandwich composite panel were assessed for several loading conditions (wind velocities of 5, 10, 15, and 20 m/s) with various tilt and wind incidence angles.

From the results, it was shown that the effect of heliostat's tilt orientation on the sandwich panel's maximum deflection and stresses becomes more pronounced as wind velocity increases. At wind velocity of 5 m/s, it was seen that there is a relatively small difference in the sandwich panel's maximum recorded displacement and stresses at different tilt angles. This implies that the heliostat orientation has no significant effect on the recorded maximum deflections and stresses of the heliostat panel. For higher wind velocities, greater than 10 m/s, this effect becomes more vital and the difference in the maximum displacement and stress values at different tilt angles escalates to a maximum at wind velocity of 20 m/s.

Moreover, the wind velocity effect on the heliostat panel's structural performance for the case of 0° tilt angle was negligible. This is because of the flow uniformity (the projected area of the reflector directly facing the wind is at its minimum) that leads to a significant decrease in the wind loading effect on the panel at this tilt orientation for all wind velocities (5-20 m/s).

The study demonstrated that increasing wind incidence angle affected the recorded maximum displacement and stress results by decreasing their magnitudes at different rates. As the wind incidence angle gradually increases from 45° to 90° for all tilt angles, the wind incidence angle influence on the maximum displacement and stress values gradually increased and the values notably decreased thus reaching its minimum at $\beta = 90^\circ$. This implies that the heliostat panel at 90° wind incidence angle, regardless of any

tilt angle, is not significantly influenced by wind loadings at wind velocities of 20 m/s and below.

The study also showed that when wind strikes the heliostat structure at 0° and 45° incidence angles, the shielding effect caused by the supporting components and torque tube was clearly noticeable. When the incoming wind acted on the back surface of the reflector, the maximum displacement and stress values were slightly lower compared to the ones recorded when the flow acted on the heliostat's mirror surface.

In all of the operational conditions studied, the worst case is found to be at a tilt angle of 30° under the effect of wind flow at 0° to the heliostat surface with a velocity of 20 m/s. The wind at this orientation strikes the panel's lower edge region directly. This region is predominantly dependant on the sandwich panel's stiffness only (not fully supported by the steel attachments) for delivering the necessary rigidity and support for the reflective mirror module. This, in turn, causes an increase in the structural deflection of the panel's lower edge region, resulting in higher stresses at the lower ends of the interface between the steel attachments and the panel's back surface. According to the structural displacement distributions of the heliostat surface for the aforementioned tilt and incidence angle, the maximum resultant displacement is of 19.6 mm taking place at the lower edge of the reflector. This will not cause significantly detrimental effect on the reflector's optical performance, according to relevant optical performance standards. Simulations also indicate no structural failure is predicted for the sandwich composite under the same worst case scenario according to relevant material failure criterions. The overall result of this is that the proposed heliostat's composite structure is unlikely to experience material failure and is expected to maintain a very high optical performance when subjected to a wind of 20 m/s and below. This in turn demonstrates the suitability and feasibility of using honeycomb sandwich composites instead of conventional steel as a heliostat structure.

Chapter 4: Effect of the geometric configuration of honeycomb on the aero-structural behaviour characteristics of the sandwich composite-based heliostat

In the previous chapter the interaction between the wind and the honeycomb sandwich composite-based heliostat structure was investigated for several loading conditions at different tilt and wind incidence angles. The structural response of the heliostat's honeycomb sandwich panel showed markedly different behaviour characteristics at various operational conditions. Based on the findings of the previous chapter it was concluded that the worst case was found to be at a tilt angle of 30° under the effect of wind flow at 0° to the heliostat surface with a velocity of 20 m/s. Despite this observation, it was found that the heliostat managed to maintain its structural integrity according to relevant optical and material failure standards, demonstrating the potential for honeycomb sandwich composites to be utilized in a lightweight heliostat support structure capable of withstanding wind loads.

However, with that being said, it was mentioned earlier in Section 1.3.3 and Section 3.1 that the mechanical properties of the honeycomb core are highly dependent upon the honeycomb's cellular geometry (e.g., cell wall angle (ϕ), cell wall length (a) and cell wall thickness (t)). A simple variation in at least one of the aforementioned parameters can lead to a significant alteration in the properties of the honeycomb core. This in-turn changes the properties of the sandwich composite thus offering flexibility to the designer to customize the design as per specific requirements (Galgali, 2012).

Understanding the impact of these parameters on the performance of honeycomb cores was a source of attraction for a number of research studies (Baumgart et al., 2018; Balaji and Annamalai, 2019; Araújo et al., 2019). For instance, Ivañez et al. (2017) investigated both numerically and experimentally the effect of the variation of both cell wall length (a) and cell wall thickness (t) on the crushing behaviour of honeycomb cores. In parallel

with these studies, a number of researchers focused on studying the impact of cell wall angle (φ) on the performance of honeycomb cores. Hu et al. (2011, 2013) investigated numerically and experimentally the effect of altering the cell wall angle on the honeycomb's in-plane (parallel to the surface) mechanical properties. On the other hand, Yamashita and Gotoh (2005) studied the out-of-plane (normal to the surface) mechanical properties of honeycomb structures with changed cell wall angles. In their study, it was shown that varying the cell structures by this simple method can enhance the honeycomb's out-of-plane crushing strength to almost 1.5 times comparing to the regular hexagonal honeycomb.

In view of the above, it can be concluded that with existing production process, it is attainable to control suitably the strength of honeycomb to achieve superior mechanical properties by varying the cell's configuration. This, in turn, improves both the strength and stiffness properties of the sandwich composite-based heliostat structure. To do so, there is a need to understand the impact that each of these parameters has on the heliostat structure. In this regard, the aim of this chapter is to investigate the effect of the honeycomb's geometric configuration on the aero-structural behaviour characteristics of the sandwich composite-based heliostat.

4.1 Numerical setup

In undertaking the study, the same FSI model discussed in Chapter 3 was used. Taking the worst case operational condition ($\theta = 30^\circ$, $\beta = 0^\circ$, wind velocity = 20 m/s) as a basis, simulations were carried out for three different core thicknesses (D); 150, 300 and 450 mm. For each of these core thicknesses, the analysis considered the following variations in the honeycomb cell geometry: cell wall thicknesses (t) between 0.02 mm and 0.05 mm,

cell wall lengths (a) ranging from 5 mm to 10 mm and cell wall angles (ϕ) varying between 10° and 50° , as shown in Figure 70.

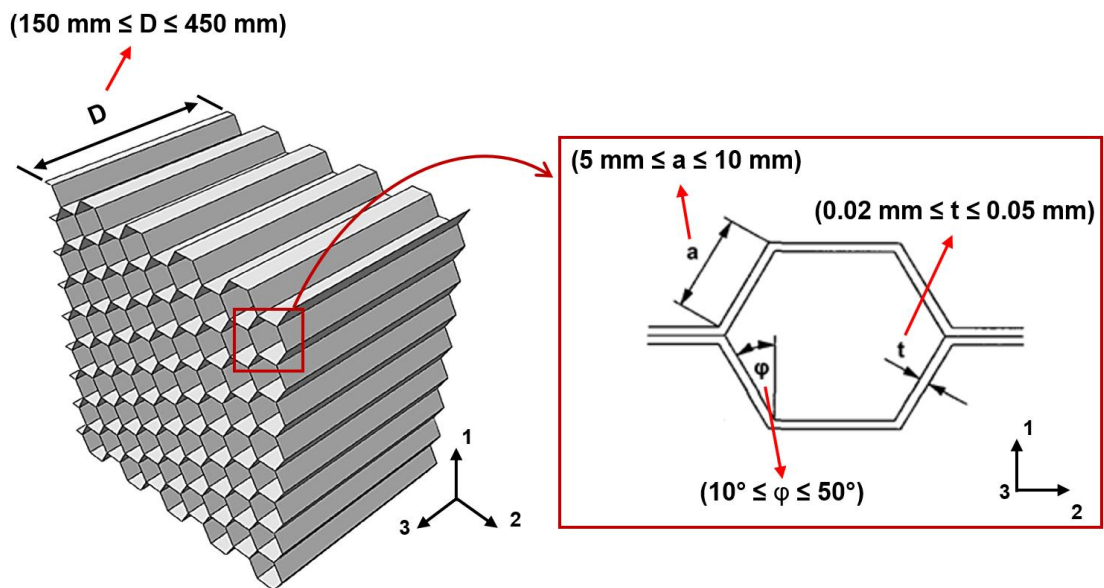
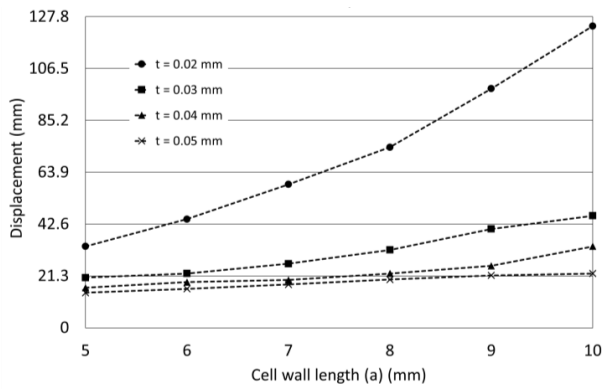


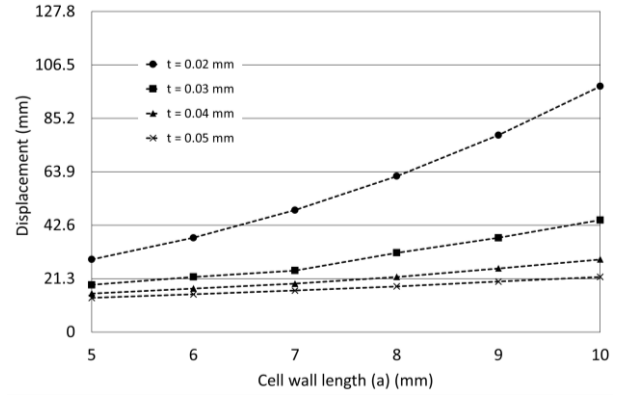
Figure 70: Geometrical parameters investigated in the study

4.2 Effect of honeycomb cell geometry on the structural behaviour of the sandwich composite-based heliostat

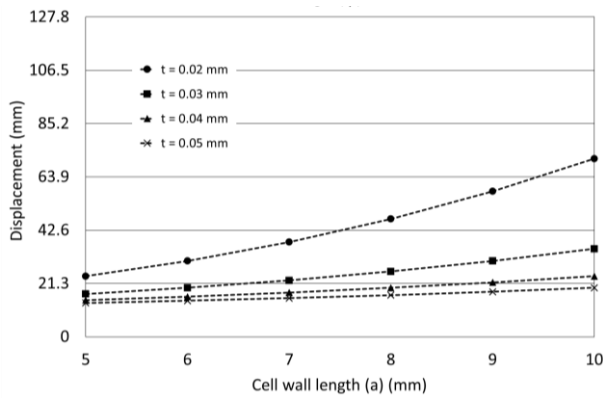
Having identified the parameters investigated in the study, it was decided initially to explore the effect of the honeycomb's cellular geometry (a , t , ϕ) on the structural behaviour characteristics of the heliostat's sandwich composite panel in detail. Figures 71 and 72 present an example of the cell geometry effect on the heliostat's maximum recorded displacement and stresses, respectively, for a core with a thickness of $D = 300$ mm.



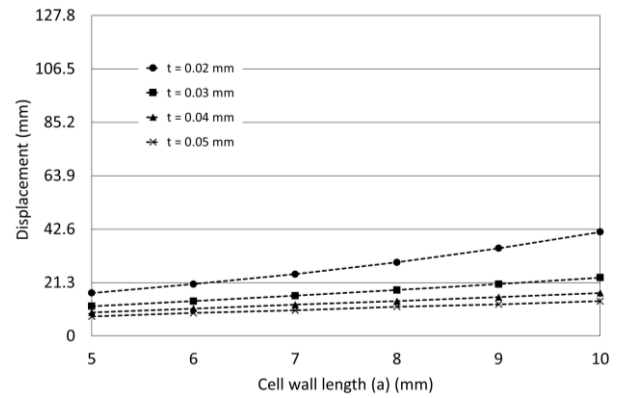
$\phi = 10^\circ$



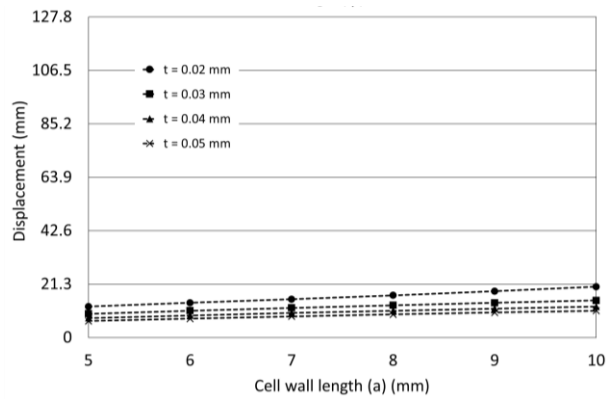
$\phi = 20^\circ$



$\phi = 30^\circ$



$\phi = 40^\circ$



$\phi = 50^\circ$

Figure 71: Cell geometry effect on the heliostat panel's maximum recorded displacement for a core with a thickness of 300 mm

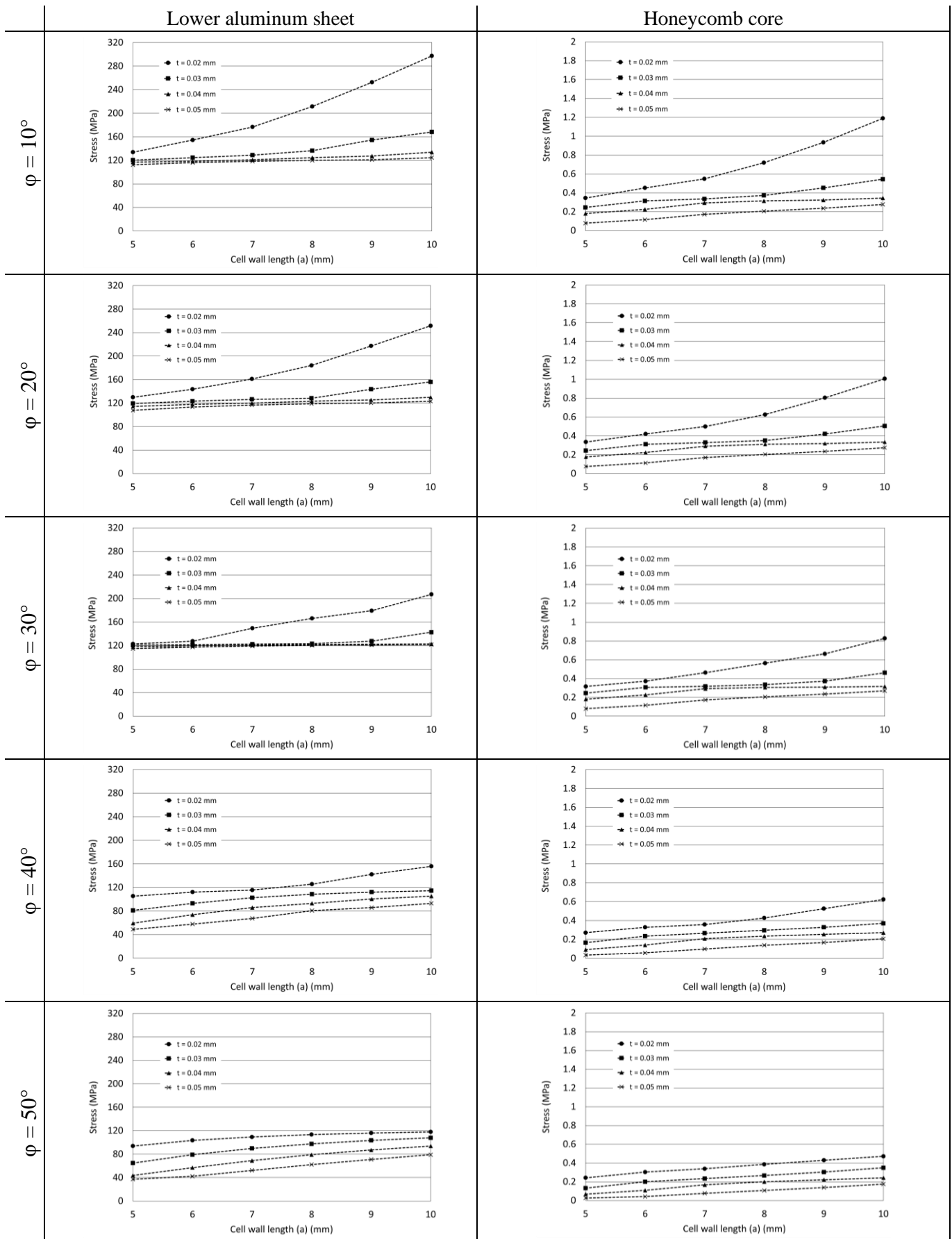


Figure 72: Cell geometry effect on the heliostat panel's maximum recorded stress for a core with a thickness of 300 mm

Starting with the case when the heliostat panel consists of a honeycomb core with cell wall angle (φ) of 10° , the panel experiences the maximum structural deformation and stress values when the honeycomb's cell wall thickness is of $t = 0.02$ mm. At this configuration ($\varphi = 10^\circ$, $t = 0.02$ mm), the resultant deformation and stresses at both the lower aluminum sheet and the aluminum honeycomb core were found to increase with the increase in the honeycomb's cell wall length (a). Exploring on the effect of cell wall length further, Figure 73 presents, for different cell wall lengths (a), the displacement distribution of the heliostat's reflective surface and stress distribution at both the lower aluminum sheet and the aluminum honeycomb core for a core with a thickness (D) of 300 mm, cell wall thickness (t) of 0.02 mm and cell wall angle (φ) of 10° . It can be observed that increasing the honeycomb's cell wall length was found to strongly affects the panel's stiffness, causing the heliostat's lower edge deflection to increase until it reaches its maximum at this configuration when the cell wall length approaches $a = 10$ mm. Similarly, and corresponding to the variation in the heliostat's structural deformation caused by changing the cell wall length, the same trend of increase was observed in the stress concentrations at both the lower aluminum sheet and the honeycomb core (Figure 73). This is due to the fact that as the honeycomb's cell wall length increases; the honeycomb cells become less dense and the area fraction of non-load-carrying cell walls increases. This results in a reduction in the Young's modulus of the honeycomb core in all directions (E_1 , E_2 , E_3), causing the heliostat panel to be less stiff and less resistant to external loads. Having said that, increasing the length of the honeycomb's cell walls, as one may expect, causes a decrease in the overall weight of the sandwich panel. This reduced weight on the supporting structure results in a decrease in the supporting steel attachments' deformation contribution to the total deformation experienced by the heliostat (Figure 74).

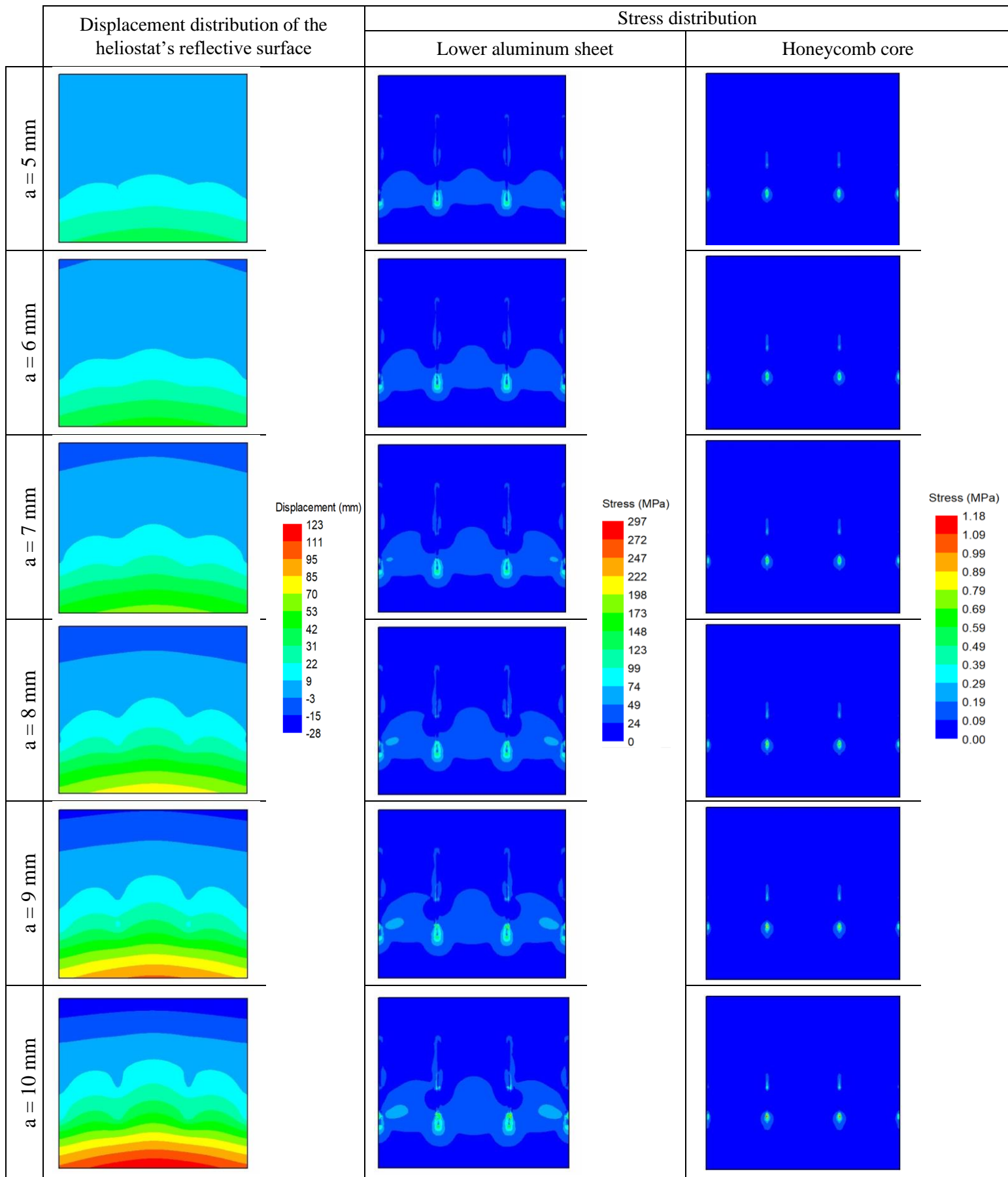


Figure 73: Displacement and stress distribution results for different cell wall lengths (a)

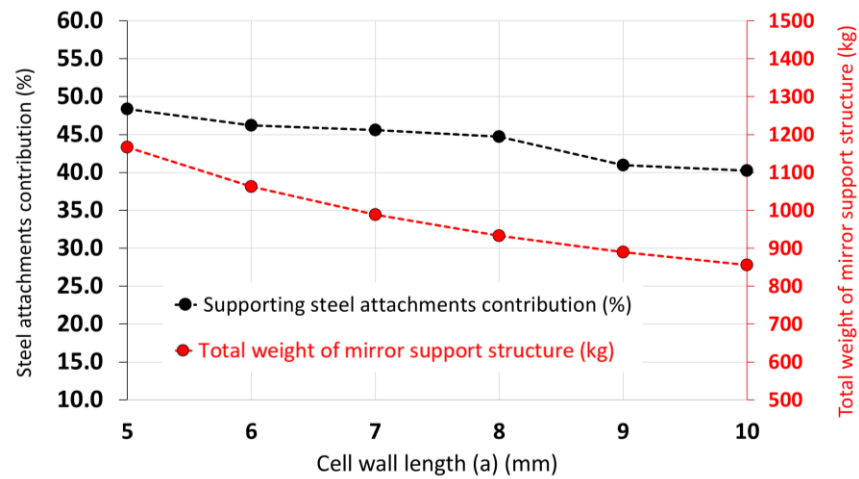
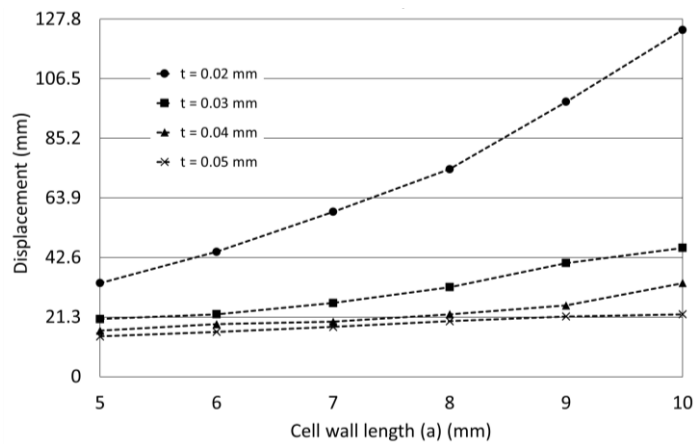


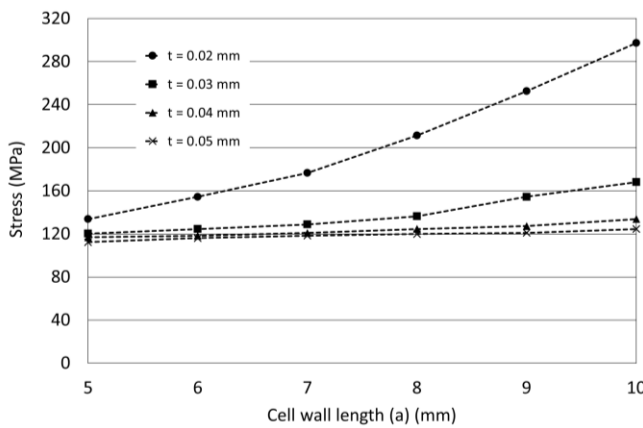
Figure 74: Supporting steel attachments' displacement contribution for different cell wall lengths (a)

As for the cell wall thickness effect on the structural behaviour characteristics of the heliostat's sandwich composite panel (Figure 75), both the displacement and stress values dramatically decrease as the honeycomb's cell wall thickness (t) increases from $t = 0.02$ mm to $t = 0.03$ mm for the same 10° cell wall angle results and all cell wall lengths. Figure 76 shows an example, for different cell wall thicknesses (t), the displacement distribution of the heliostat's reflective surface and stress distribution at both the lower aluminum sheet and the aluminum honeycomb core for a core with a thickness (D) of 300 mm, cell wall length (a) of 10 mm and cell wall angle (φ) of 40° . From the results it can be seen that increasing the honeycomb's cell wall thickness (t) causes a decrease in the structural deflection of the panel's lower edge region, resulting in lower stresses at the lower ends of the interface between the steel attachments and the panel's back surface. This can be attributed to the fact that as the honeycomb's cell walls gradually thicken, their bending resistance increases and consequently the honeycomb core becomes more resistant to local buckling and crushing, causing an increase in the heliostat panel's stiffness and resistivity to wind loads. Having said that, it was noticed that increasing the cell wall thickness results in an increase in the contribution of the supporting steel attachments to the total displacement experienced by the heliostat (Figure 77). This can be related to the

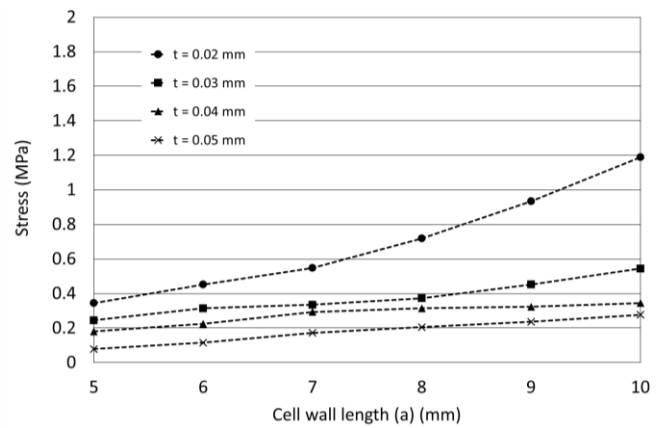
substantial increase in the overall weight of the honeycomb core with the increase in cell wall thickness, causing the supporting steel attachments to act upon this increase to maintain the deformations of the heliostat. Moreover, it is apparent from the results that a further increase in the cell wall thickness has a slight influence on the heliostat's structural performance, and as the cell wall thickness gradually increases from $t = 0.03$ mm to $t = 0.05$ mm, the displacement and stress values do slightly decrease.



(a) Displacement



(b) Stress (Lower aluminum sheet)



(c) Stress (Honeycomb core)

Figure 75: Cell wall thickness (t) effect on the heliostat panel's maximum recorded displacement and stress for a core with a thickness of 300 mm and cell wall angle (ϕ) of 10° .

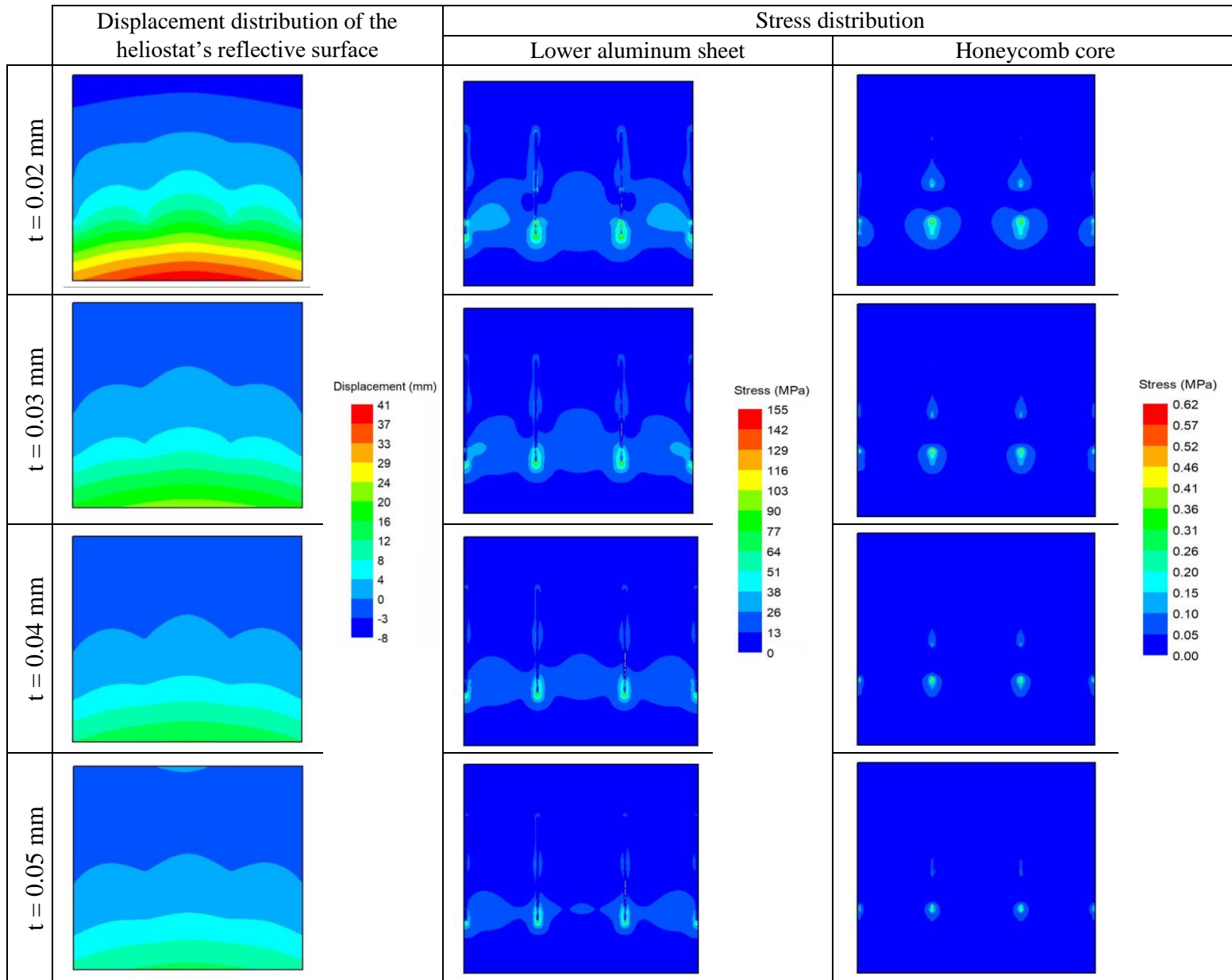


Figure 76: Displacement and stress distribution results for different cell wall thicknesses (t)

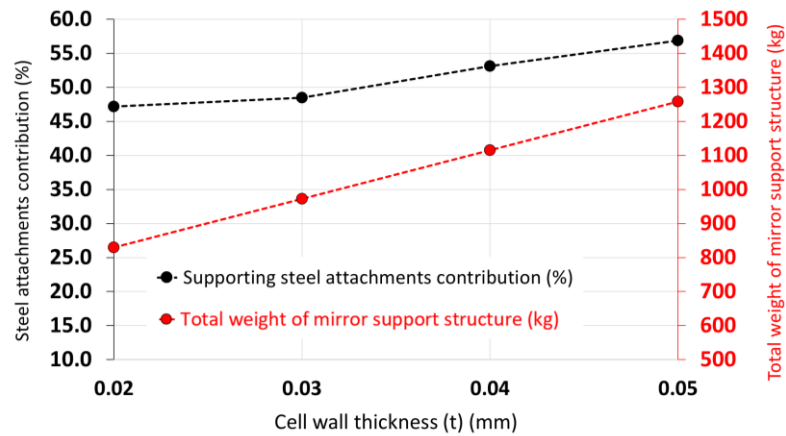
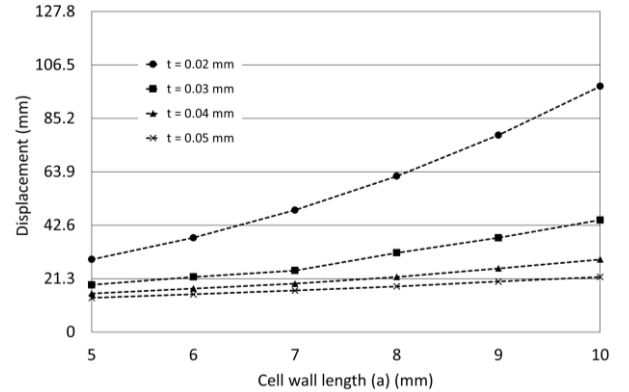
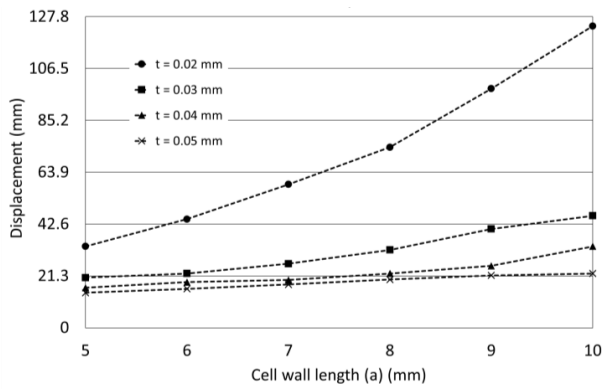


Figure 77: Supporting steel attachments' displacement contribution for different cell wall thicknesses (t)

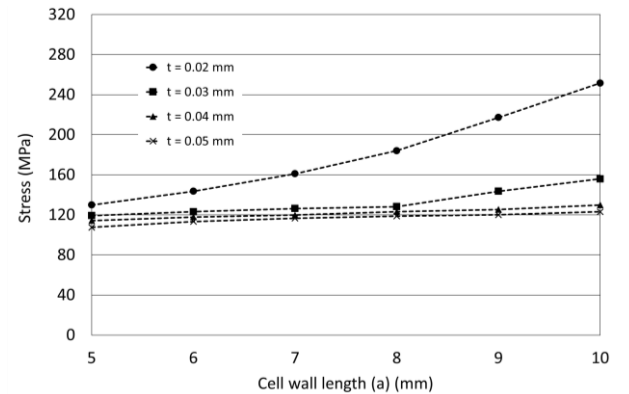
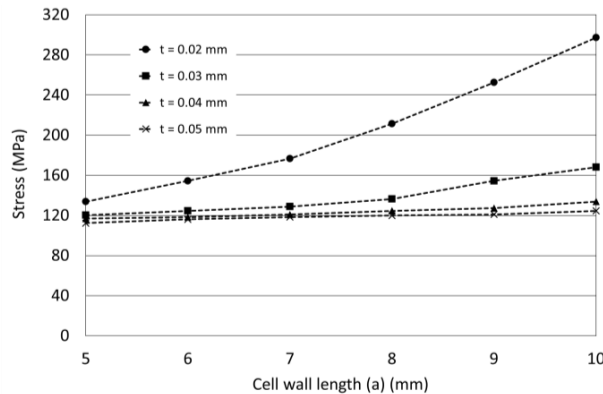
As for the cell wall angle effect (ϕ), the maximum displacement and stress results for a heliostat panel that consists of a core with $\phi = 20^\circ$ revealed the same patterns of variation seen in the 10° cell wall angle configuration but lower in magnitudes (Figure 78). This reduction carries on as the cell wall angle progressively increases until it reaches $\phi = 50^\circ$ for all cell wall lengths (as shown in Figures 71-72). Exploring on the effect of cell wall angle further, Figure 79 illustrates, for different cell wall angles (ϕ), the displacement distribution of the heliostat's reflective surface and stress distribution at both the lower aluminum sheet and the aluminum honeycomb core for a core with a thickness (D) of 300 mm, cell wall thickness (t) of 0.02 mm and cell wall length (a) of 5 mm. It can be seen that the heliostat's sandwich panel that consists of a honeycomb core with cell wall angle (ϕ) of 10° experiences the maximum structural deformation. Increasing the honeycomb's cell wall angle was found to strongly impacts the stiffness of the panel, causing the deflection at the heliostat's lower edge to decrease until it reaches its minimum when the cell wall angle reaches $\phi = 50^\circ$. Similarly, and corresponding to the change in the heliostat's structural deformation caused by altering the cell wall angle, the same trend of decrease was seen also in the stress concentrations at both the lower aluminum sheet and the honeycomb core (Figure 79). This can be attributed to the fact that as the honeycomb's cell wall angle increases; the honeycomb's cell walls become more compact and internally coherent, increasing the area fraction of load-carrying cell walls that causes the heliostat panel to be stiffer and more resistant to buckling and crushing.



$\phi = 10^\circ$

$\phi = 20^\circ$

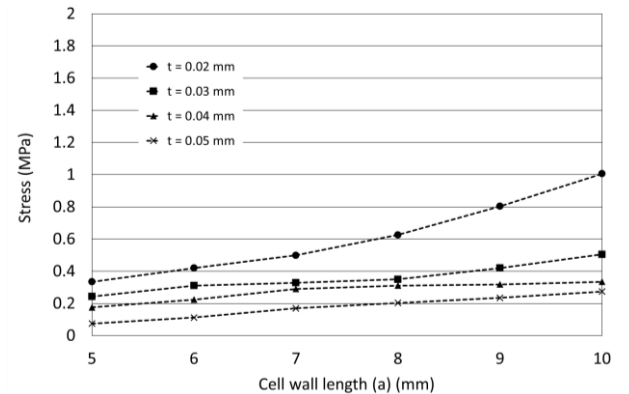
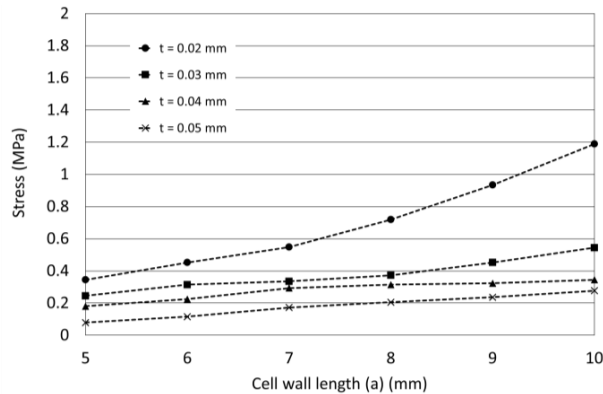
(a) Displacement



$\phi = 10^\circ$

$\phi = 20^\circ$

(b) Stress (lower aluminum sheet)



$\phi = 10^\circ$

$\phi = 20^\circ$

(c) Stress (Honeycomb core)

Figure 78: Cell wall angle effect (ϕ) on the heliostat panel's maximum recorded displacement for a core with a thickness of 300 mm

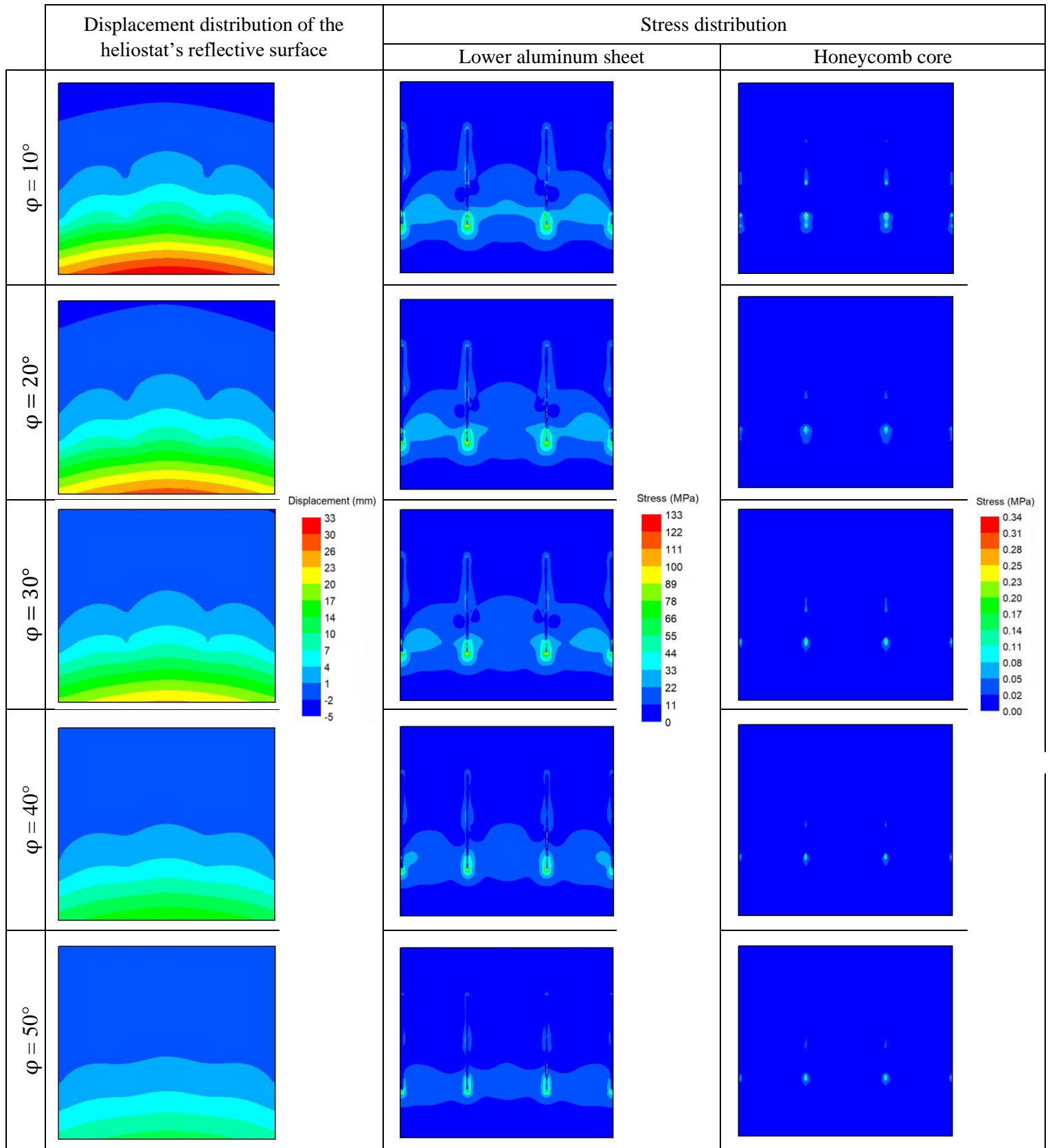


Figure 79: Displacement and stress distribution results for different cell wall angles (φ)

Despite this observation, it can be clearly noted that for very low cell wall angle ($\varphi=10^\circ$), the overall weight of the sandwich panel is high. However, with the increase in cell wall angle the overall weight decreases as a result of the increase in the void between the cell walls. Due to the reduced weight on the supporting structure, the contribution of the supporting steel attachments to the total displacement experienced by the heliostat also decreases with a similar trend and reaches its lowest value at $\varphi = 30^\circ$. Increasing the cell wall angle further, and as described previously that the honeycomb's cell walls become more compact and dense and internally coherent with the increase in cell wall angle, the sandwich panel's overall weight increases, resulting in an increase in the supporting steel attachments' deformation contribution to the total deformation experienced by the heliostat (Figure 80) to act upon this increase in weight.

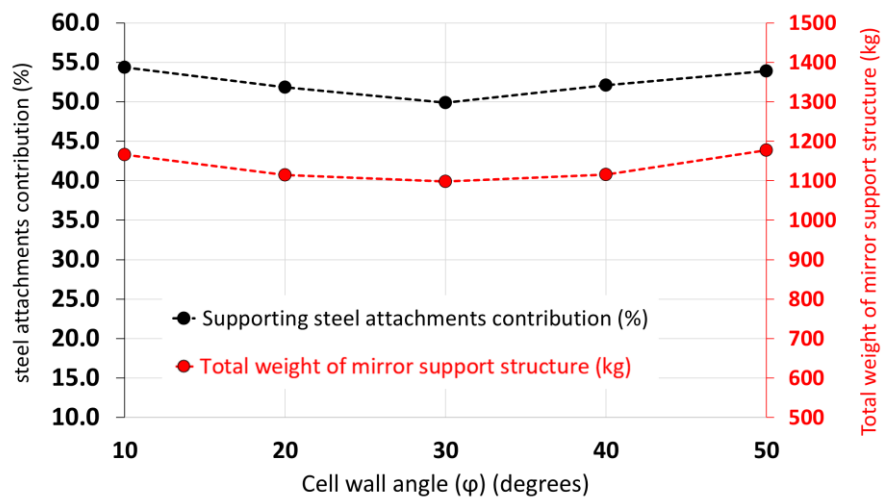


Figure 80: Supporting steel attachments' displacement contribution for different cell wall angles (φ)

4.3 Effect of honeycomb core thickness on the structural behaviour of the sandwich composite-based heliostat

Having discussed the effect of the honeycomb's cellular geometry, it was decided to examine the influence of the honeycomb core thickness (D) on the heliostat panel's structural behaviour in great detail. Figures 81 and 82 present an example of the core thickness effect on the heliostat's maximum recorded displacement and stress, respectively, for a core with honeycomb cell wall thickness of $t = 0.05$ mm.

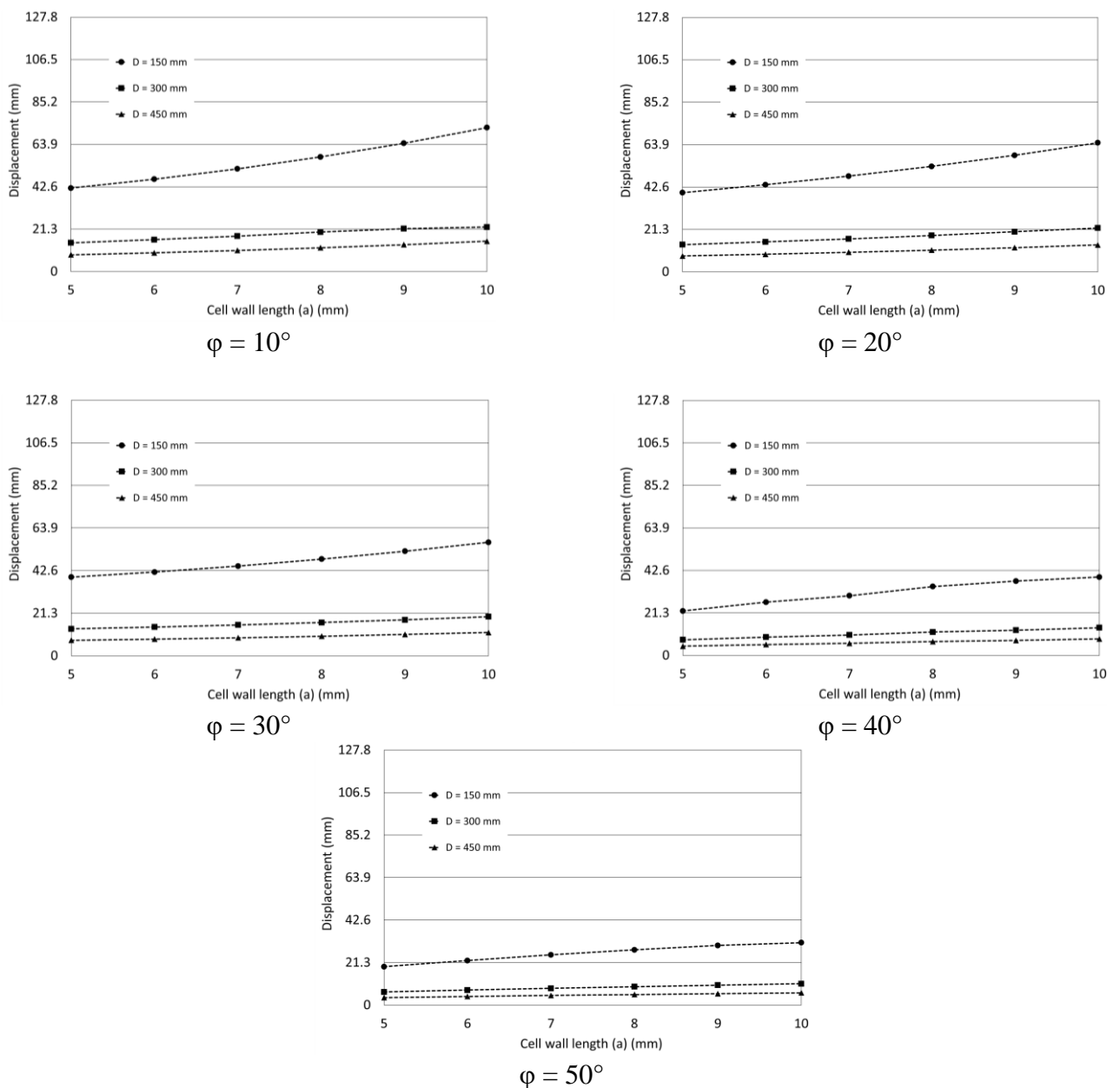


Figure 81: Core thickness effect on the heliostat panel's maximum recorded displacement at multiple cell wall angles for a core with a cell wall thickness of 0.05 mm

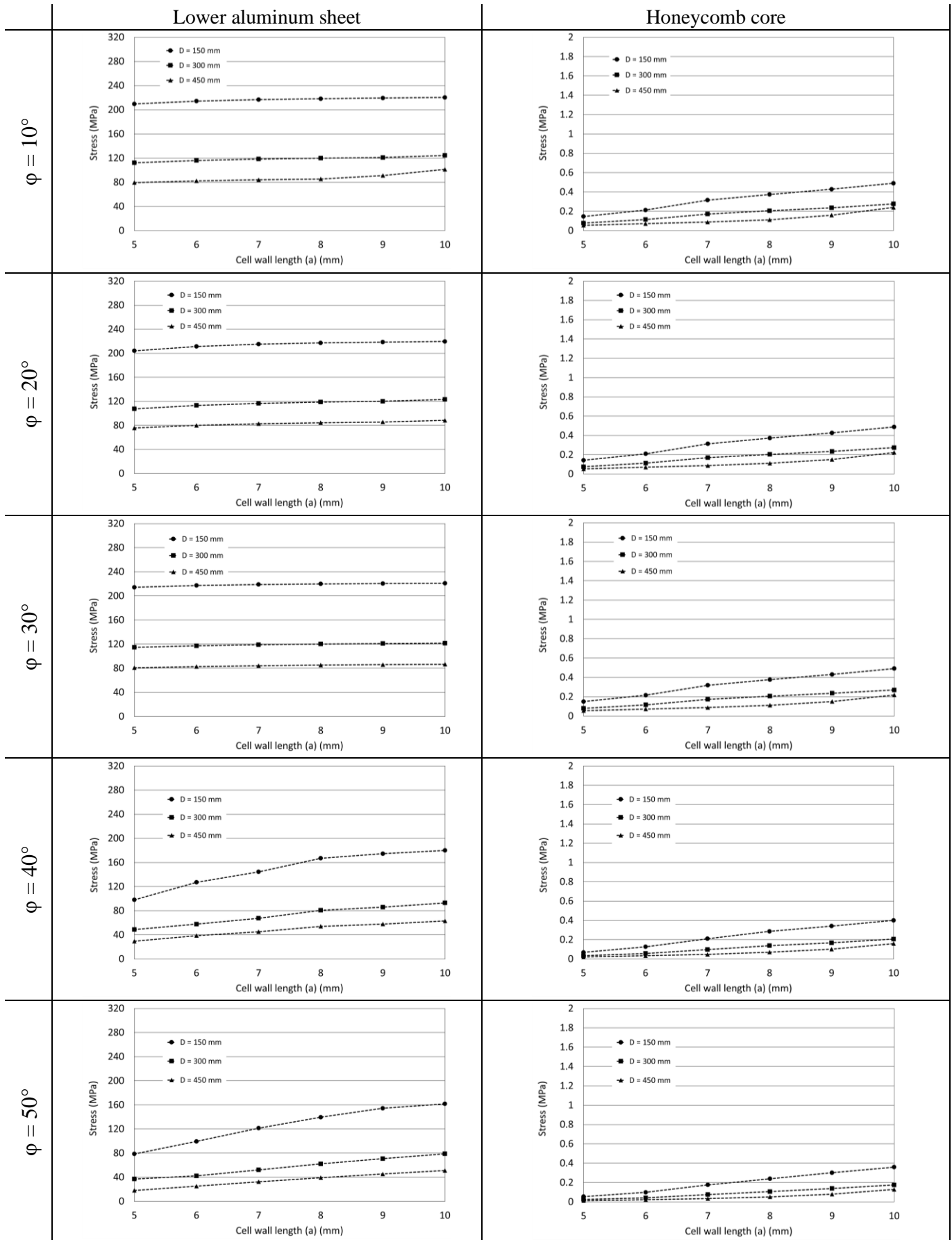


Figure 82: Core thickness effect on the heliostat panel's maximum recorded stress at multiple cell wall angles for a core with a cell wall thickness of 0.05 mm

It can be seen initially from the case when the heliostat's sandwich panel comprises of a core with cell wall angle $\varphi = 10^\circ$ that the panel experiences the maximum structural displacement and stress values when the thickness of the honeycomb core is of $D = 150$ mm. At the same honeycomb core configuration ($\varphi = 10^\circ$, $D = 150$ mm), the maximum resultant displacement and stresses at both the lower aluminum sheet and the aluminum honeycomb core were recorded when the length of the honeycomb's cell walls is of $a = 10$ mm. For the same 10° cell wall angle results and all cell wall lengths, increasing the honeycomb core thickness (D) from $D = 150$ mm to $D = 300$ mm causes a substantial decrease in both the displacement and stress values. Expanding on this, Figure 83 presents, for a core with different thicknesses but with the same cell geometry ($t = 0.05$ mm, $a = 9$ mm, $\varphi = 10^\circ$), the displacement distribution of the heliostat's reflective surface and stress distribution at both the lower aluminum sheet and the aluminum honeycomb core. It can be seen from the results that increasing the thickness of the core (D) causes a decrease in the structural deflection of the panel's lower edge region. This consequently results in a decrease in the stress concentrations at the lower ends of the interface between the panel's back surface and the steel attachments, according to Figure 83. This effect can be attributed to the fact that as the honeycomb core thickness progressively increases the stiffness and thus the resistance to deformation increases, thus resulting in lower magnitudes of deflection and stress. However, increasing the size of the core, as one may expect, causes a substantial increase in the overall weight of the sandwich panel, resulting in an effective increase in the supporting steel attachments' deformation contribution to the total deformation experienced by the heliostat (Figure 84) to act upon this increase in weight.

Furthermore, it is clear from the results that a further increase in the core thickness has a slight impact on the displacement and stress values, and as the thickness increases from $D = 300$ mm to $D = 450$ mm, the values do slightly decrease. Moreover, the recorded

maximum displacement and stress values when the panel consists of a honeycomb core with cell wall angle of $\phi = 20^\circ$ showed the same variation patterns as the 10° cell wall angle case but slightly lower. As the cell wall angle gradually increases from $\phi = 20^\circ$ until it reaches $\phi = 50^\circ$ for all cell wall lengths, the cell wall angle effect on the displacement and stress values gradually increases and the values notably decrease.

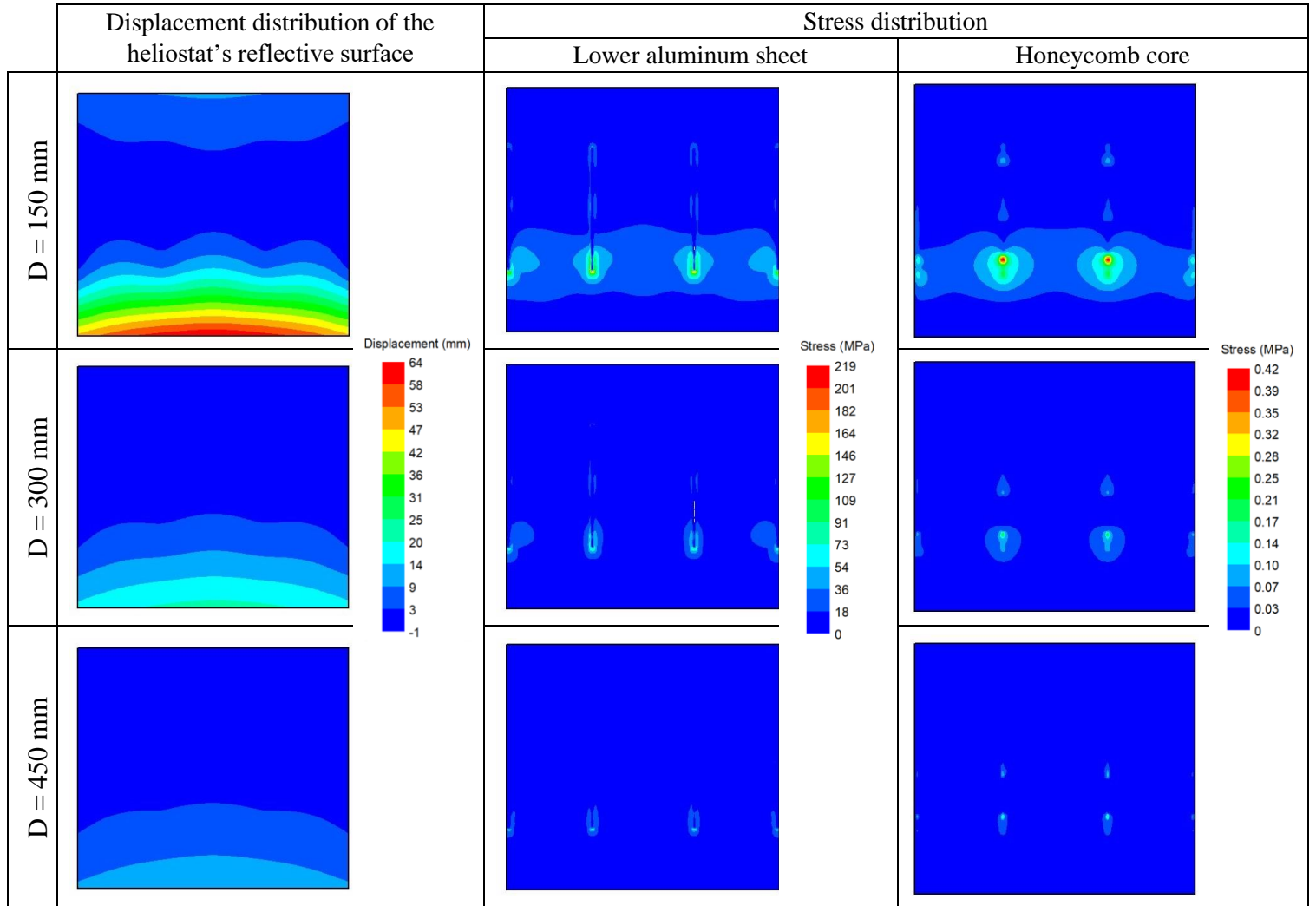


Figure 83: Displacement and stress distribution results for different core thicknesses (D)

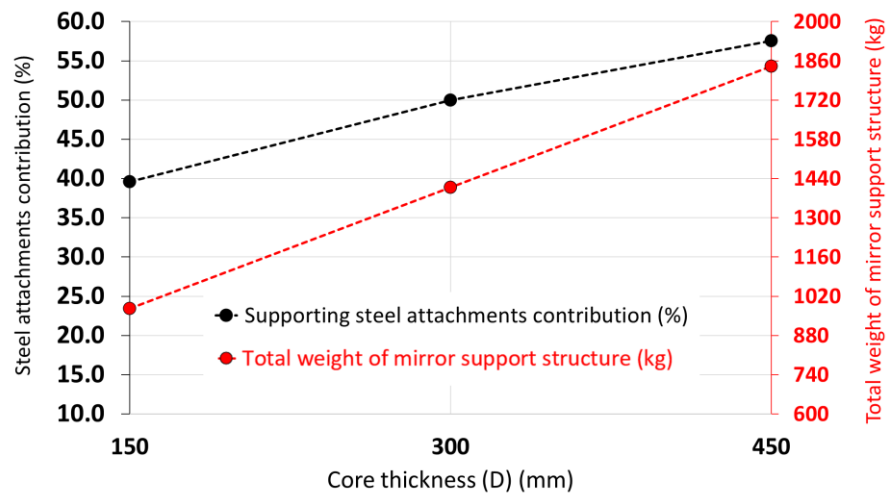


Figure 84: Supporting steel attachments' displacement contribution for different core thicknesses (D)

4.4 Chapter Summary

The mechanical properties of honeycomb sandwich composites are strongly dependent upon the honeycomb core's cellular geometry (cell wall angle (ϕ), cell wall length (a) and cell wall thickness (t)) and core thickness (D). A slight alteration in at least one of the parameters can lead to a substantial variation in the properties of the honeycomb core. This in-turn changes the properties of the sandwich composite thus providing flexibility to the designer to customize the design as per requirements. Hence, there is a necessity to understand and identify the impact that each of these parameters has on the heliostat structure, to better incorporate honeycomb sandwich panels into heliostat designs.

In this chapter, a comprehensive parametric study was performed to investigate the effect of the honeycomb's geometrical parameters on the aero-structural behaviour characteristics of the honeycomb sandwich composite-based heliostat. The study was carried out for three different core thicknesses (D) (150, 300 and 450 mm) with various honeycomb configurations. The study showed that varying the honeycomb's cellular geometry significantly affected both the strength and stiffness properties of the sandwich

composite-based heliostat structure. For instance, it was found that an increment of the cell wall thickness (t), and the cell wall angle (φ) had a substantial impact not only on the structural deformation of the heliostat panel but also on the stress concentrations at both the lower aluminum sheet and the honeycomb core. This resulted in decreasing their levels but at different rates, causing the heliostat structure to be more stiff and resistant to the aerodynamic loads imposed upon it. On the other hand, increasing the honeycomb's cell wall length (a) resulted in a decrease in the heliostat panel's stiffness and resistivity to wind loads due to the increase in the area fraction of non-load-carrying cell walls. Moreover, it was found also that increasing the honeycomb core thickness (D) strongly affected the deformation of the heliostat panel by reducing its levels. This resulted also in a decrease in the stress concentrations at both the lower aluminum sheet and the honeycomb core.

It can be concluded that, with existing production process, it is within reach to control suitably the strength of honeycomb to attain superior mechanical properties that enhances both the strength and stiffness properties of the sandwich composite-based heliostat structure by altering at least one of the honeycomb's geometrical parameters.

Chapter 5: Artificial neural network-based modelling of the honeycomb core geometry effect on the structural behaviour characteristics of the sandwich composite-based heliostat

In the previous chapter, the effect of the honeycomb's geometrical parameters on the aero-structural behaviour characteristics of the honeycomb sandwich composite-based heliostat was investigated. It was shown that altering the honeycomb's cellular geometry significantly varied both the strength and stiffness properties of the sandwich composite-based heliostat structure at different rates. These variations in the heliostat's structural response highlighted the need for a generalized model that can capture the influence of each of the honeycomb core's geometrical parameters (cell wall thickness (t), the cell wall angle (ϕ), cell wall length (a) and core thicknesses (D)) on the heliostat structure's performance (i.e. optical, material failure and weight reduction). However, accurately predicting the heliostat's structural performance based on its honeycomb core's configuration using classical analytical approaches are at best cumbersome and, at worst, unable to facilitate the predications.

In recent years, and among the various conventional modelling approaches available, artificial neural network (ANN for short) has emerged as one of the prominent tools for modelling complex non-linear relationships, particularly in situations where the development of phenomenological or conventional regression models becomes impractical or cumbersome (Lahiri and Ghanta, 2009). ANN is a biologically inspired computational technique that emulates the human brain's behaviour and learning process (Pandey et al., 2016). This approach does not require explicit knowledge of the physical phenomena under investigation (Azizi et al., 2016), but depends solely on the historic input-output dataset (example set) to learn the relationship between the data through training. With such feature, even multiple input-multiple output (MIMO) nonlinear relationships can be approximated simultaneously and effortlessly. ANN-based models

provide multiple advantages, including the possession of an outstanding generalization ability owing to which it can accurately predict outputs for a new input data set, and the capability of dealing with noisy data and uncertainties (Baughman and Liu, 1995).

Owing to their several attractive characteristics, the ANN approach has been extensively used in numerous applications in the fields of engineering, medicine, economics, meteorology, psychology and many others (Kumar et al., 2015; Kan and Song, 2016; Pandey et al., 2016; Azizi et al., 2016). Focusing on the field of composites, particularly sandwich composites, Table 2 summarizes former studies on ANN modelling of sandwich composites.

Table 2: Former studies on ANN modelling of sandwich composites

Study	Type of sandwich composite	Material		Honeycomb geometrical parameters considered in the prediction model
		Face sheets	Core	
Wong et al., 2019	Foam-cored sandwich panel	Aluminum	Bio-foam (Mycofoam)	-
Qi et al., 2013, 2014	Metallic foam-cored sandwich panel	Outer: aluminum Inner: steel	Aluminum foam	<ul style="list-style-type: none"> • Core radius of curvature • Core thickness
Mirzaei et al., 2011	Circle cellular-cored sandwich panel	Aluminum	Aluminum	<ul style="list-style-type: none"> • Cell wall thickness • Core thickness • Cellular diameter
Marzbanrad and Ebrahimi, 2011	Circle cellular-cored sandwich panel	Aluminum	Aluminum	<ul style="list-style-type: none"> • Cell wall thickness • Core thickness • Cellular diameter
Baykasoğlu and Baykasoğlu, 2016	Circle cellular-cored sandwich panel	Aluminum	Aluminum	<ul style="list-style-type: none"> • Core thickness • Cellular diameter
Qi et al., 2012	Square cellular-cored sandwich panel	Aluminum	Aluminum	<ul style="list-style-type: none"> • Cell wall thickness • Taper angle
Rodriguez-Ramirez et al., 2017, 2018	Honeycomb sandwich panel	Aluminum	Nomex	- (3D image processing of the whole panel)
Li et al., 2009	Honeycomb sandwich panel	weave carbon fabric pre-impregnated in epoxy resin	Nomex	<ul style="list-style-type: none"> • Number of face sheet plies • Core thickness
Sun et al., 2010	Honeycomb sandwich panel	Aluminum	Aluminum	<ul style="list-style-type: none"> • Cell wall thickness
Lanzi et al., 2004	Honeycomb sandwich panel	Aluminum	Aluminum	<ul style="list-style-type: none"> • Cell wall length • Cell wall thickness • Core thickness
Esfahlani et al., 2013	Honeycomb sandwich panel	Aluminum	Aluminum	<ul style="list-style-type: none"> • Cell wall length • Cell wall thickness

By concentrating on honeycomb sandwich composites, it can be observed from Table 2 that there is a scarcity of studies that attempt to establish a generalized prediction model that can capture the influence of each of the honeycomb core's geometrical parameters (cell wall thickness (t), and the cell wall angle (ϕ), cell wall length (a), core thicknesses (D)). Moreover, despite very few attempts found in literature (Lanzi et al., 2004; Sun et al., 2010; Esfahlani et al., 2013), their investigations were limited by the geometrical parameters considered and the variations in the honeycomb cell geometry.

Furthermore, given the various scientific fields that involved the use of ANN technique, the technique has only gained popularity recently in renewable energy related applications (Kalogirou, 2001; Ghritlahre and Prasad, 2018a; 2018b). For instance, Mellit et al. (2009) applied the ANN method to develop a model that considers the desired site's latitude and longitude for the estimation of the sizing parameters of stand-alone PV systems. Boukelia et al. (2016, 2017) utilized the ANN approach for parabolic trough-based power plants to predict the levelized cost of electricity of two different integrated power plants operated by a molten salt and thermic oil as primary heat transfer fluids in each type and examine the techno-economic performances. In parallel with these studies, a number of researchers have used ANN in their central tower CSP plant investigations. In their work, Moukhtar et al. (2018) used the ANN technique for modelling and simulating a complete central tower CSP plant with thermal energy storage. On the other hand, Zeghoudi and Chermitti (2014) utilized ANN technique to develop an estimation model that predicts the movements of heliostat fields of a solar tower power plant.

Given the recent developments and potential application of ANN in diverse disciplines, and in renewable energy related applications in particular, it is surprising that implementation of the ANN technique for modelling the effect of honeycomb's physical parameters on the structural performance of the honeycomb sandwich composite-based heliostat is not reported in the literature. Having a predictive model that estimates the

heliostat’s structural performance, under the worst case operational condition and based on the desired site’s maximum recorded wind speed, eradicates the need of going through the hurdles of establishing an FSI model for each of the honeycomb core’s geometrical parameters. This, in turn, runs down the implementation time and keeps off unnecessary computations. In this sense, the aim of this chapter is to establish a predictive model that predicts the performance of the honeycomb sandwich composite-based heliostat using artificial neural network (ANN) technique.

5.1 Numerical setup

In doing this, MATLAB R2018a's Neural Network Toolbox[®] was used as the platform to construct the ANN model and to evaluate its performance. The toolbox offers a broad variety of parameters for neural network development which can be chosen and implemented flexibly. The computational structure of a typical ANN, as shown in Figure 85, generally consists of three interconnected layers. The layers are described as input, hidden and output layers, with each layer consisting of at least one or multiple nodes called neurons. These neurons are tied together with weighted connections corresponding to human brain synapses (Razzak et al., 2012).

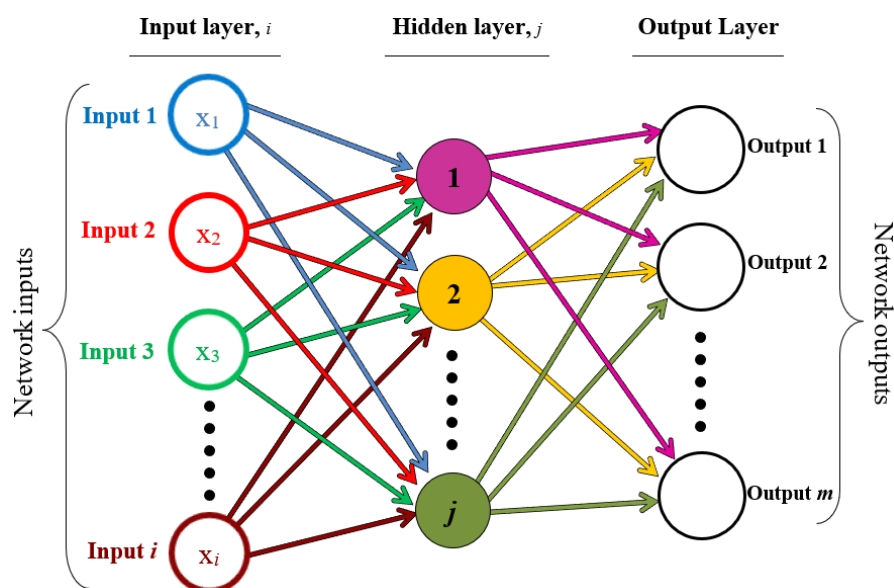


Figure 85: Schematic diagram of a typical artificial neural network

The number of neurons in the network input layer is equal to the number of inputs in the process whereas the number of output neurons equals the number of the process outputs. However, the number of hidden neurons is an adjustable parameter of which is determined by the performance and complexity of the desired network model (Lahiri and Ghanta, 2009; Azizi et al., 2016). The data from the specified source are introduced into the network's input layer and then it is propagated from there to the hidden layer and finally to the output layer. Each neuron in the hidden or output layer initially acts as a summing junction, which combines and modifies the inputs from the previous layer by means of the following equation (Eq. 21):

$$S_i = \sum_{j=1}^i x_i w_{ij} + b_j \quad (21)$$

Where S_i is the net input to neuron j in the hidden or output layer, x_i is the input to neuron j (or the previous layer's outputs), w_{ij} is the strength of the weight connection between the i th neuron and j th neuron, i is the number of neurons and b_j is the bias associated with neuron j . To establish a relationship between the input and output, the sum of bias and the previously weighted inputs must pass through a suitable transfer (activation) function to determine its output (Azizi et al., 2016). Each neuron in the hidden layer is equipped with a transfer function. Amongst the various types of transfer functions for ANNs (e.g., logarithmic sigmoid (logsig), hyperbolic tangent sigmoid (tansig), linear (purelin), radial basis (radbas)), the most popular transfer functions for a non-linear relationship are the logsig and tansig functions, which are given by Eqs. (22) and (23), respectively:

$$f(S_j) = \frac{1}{1 + e^{-S_j}} \quad (\text{logsig}) \quad (22)$$

$$f(S_j) = \frac{e^{S_j} - e^{-S_j}}{e^{S_j} + e^{-S_j}} \quad (\text{tansig}) \quad (23)$$

Where $f(S_j)$ is the output to neuron j . Both transfer functions are traditionally utilized to make the ANNs a universal function approximator given an adequate number of hidden neurons (Pandey et al., 2016). That said, based on the nature of the data, amongst these two transfer functions, one may outperform the other. In this sense, both the transfer functions are exploited in acquiring the best suited option for fitting the data.

With ANN-based models, the network establishes the relationship between data in the input and output layers by means of a process recognized as “training”. This process consists of several steps: training, testing, and sometimes validation (depending on the training algorithm selected). Based on a set of known input and output values fed to the network, the training process adjusts the weights between the neurons according to the error between the actual and predicted outputs until it learns the best relationship between the inputs and outputs (Azizi et al., 2016; Malayeri et al., 2003). Subsequently, the ANN undergoes testing and validation processes to evaluate the model’s performance on completely unseen dataset, and in order to confirm the actual predictive power of the network.

Over the years, different researchers have developed various ANN training algorithms to establish a better relationship between inputs and outputs as well as to decrease the execution time and computer storage requirements. There are several different training algorithms published in literature (e.g., Levenberg–Marquardt (LM), Bayesian regularization (BR), Scaled conjugate gradient (SCG), Broyden-Fletcher-Goldfarb-Shanno quasi-Newton (BFGS), etc.) (Plumb et al., 2005; Lahiri and Ghanta, 2009). These algorithms have a variety of different computation and storage requirements, also, no single algorithm is best suited to all locations. Among the aforementioned training algorithms, Levenberg–Marquardt (LM) and Bayesian regularization (BR) have the capability to obtain lower errors between the actual and predicted outputs than any other algorithms for functioning approximation problems (Kayri, 2016). The basic differences

between these algorithms are exhibited in how they handle the weight upgradation to reduce error and how they modify the learning rate to reduce the convergence time. LM training algorithm is very modest and forceful algorithm and is considered as one of the fastest algorithms in terms of convergence speed. However, it is suitable for moderate-sized problems in ANNs. On the other hand, BR training algorithm improves generalization and reduces the difficulty encountered in determining the optimum network architecture for large and complex neural networks. However, BR algorithm converges slower than LM algorithm (Mohd-Safar et al., 2016). In this regard, both algorithms were investigated in this study and their predictive abilities were evaluated.

Carrying on with the development of the ANN model, and considering the same geometrical variations discussed in Chapter 4 for the worst case operational condition ($\theta = 30^\circ$, $\beta = 0^\circ$) (Figure 86), the honeycomb core's physical parameters (core thickness (D), cell wall angle (φ), cell wall thickness (t), and the cell wall length (a)) were defined as input variables. Moreover, the wind velocity was considered also as an input parameter to the ANN model and was varied from 5 to 20 m/s to have a better generalized model that considers the desired site's maximum recorded wind speed.

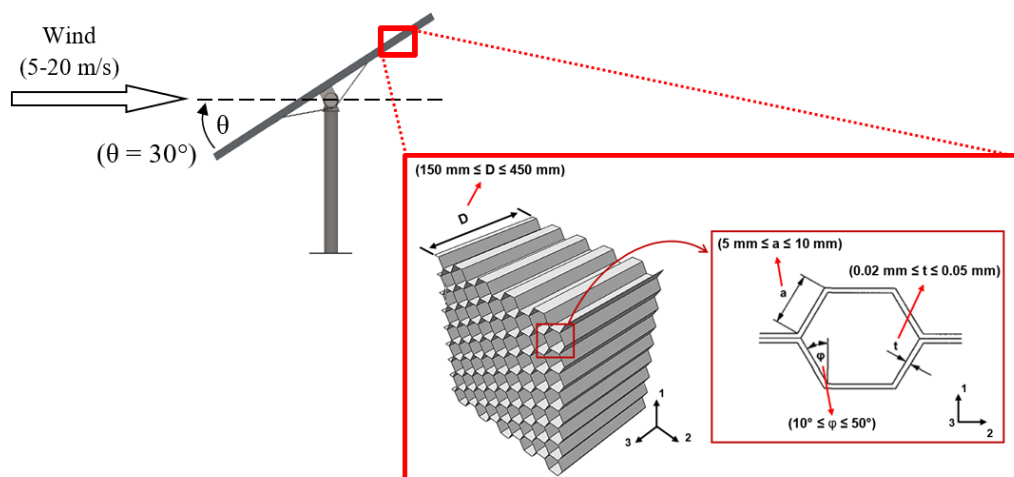


Figure 86: Configurations used for the network design input dataset

Furthermore, the ANN model's output variables that represent the heliostat's structural performance parameters were defined as: the heliostat panel's (W_{hsch}) attained weight

saving (in comparison to the support structure of the existing 148 m² steel-based ATS heliostat (W_{ATS}) that weighs around 1550 kg (Kolb et al., 2007)) calculated using Eq. (24), the reflective surface's maximum displacement, the maximum recorded stress at the heliostat panel's lower aluminum sheet, and a parameter introduced with the name "core crush index" that evaluates the performance of the honeycomb core. Core crush index is defined as the ratio of the calculated critical collapse strength of the honeycomb core ($\sigma_{collapse}$) at a specific cellular configuration to the maximum recorded stress at the core (Eq. 25).

$$\text{Weight reduction percentage (\%)} = \frac{(W_{ATS} - W_{hSCH})}{W_{ATS}} \times 100 \quad (24)$$

W_{ATS} : total weight of the ATS heliostat's mirror support structure; W_{hSCH} : total weight of the honeycomb sandwich composite-based heliostat's panel at a specific honeycomb core configuration.

$$\text{Core crush index} = \frac{\text{Critical collapse strength of honeycomb } (\sigma_{collapse})}{\text{Maximum recorded stress at the honeycomb core}} \quad (25)$$

A value greater than 1 indicates that the core is unlikely to experience material failure due to cell-wall buckling. Figure 87 summarizes the configuration of the proposed network with the defined inputs and outputs. A total of 1440 data points (Appendix G) for each output were collected based on the configurations shown in Figure 86.

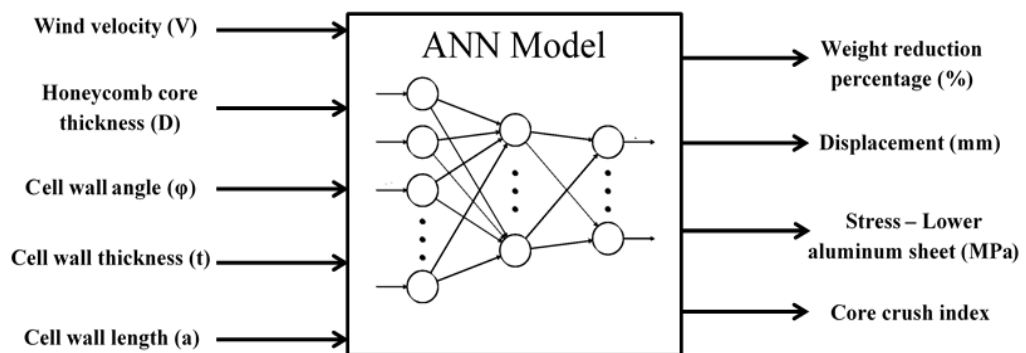


Figure 87: Inputs and outputs of the ANN model for the prediction of the structural performance of the honeycomb sandwich composite-based heliostat

Furthermore, as discussed previously, the network learns the relationship between data in the input and output layers using the training process that consists of several steps depending on the utilized training algorithm (LM or BR). When LM algorithm is activated, the training passes through three phases: training, validation and testing. The input data was randomly divided into the following three sets: 70% for training, 15% for testing, and 15% for validation. As for the BR training algorithm, it passes through only two phases: training and testing (Khalid et al., 2017). For this algorithm, the input data was randomly divided into the following sets: 70% data used for training and 30% data used for testing.

As earlier described, the number of hidden neurons is a tuneable parameter of which is normally unknown and determined by the desired ANN model's performance and complexity. For instance, having too few neurons in the hidden layer can give rise to lower predictive accuracy (i.e. the non-linear trends in the dataset cannot be captured by the network). On the other hand, having too many neurons in the hidden layer can result into various problems such as overfitting and high computational time (Pandey et al., 2016). Therefore, a trade-off needs to be found in order to determine the number of neurons in the hidden layer that provides the best prediction performance. In this study, the number of neurons in the hidden layer was estimated by varying their numbers from 3 to 101 neurons and assessing the model's performance for each set of neurons using tansig and logsig transfer functions. The most common way to evaluate the performance of an established ANN model is by calculating the mean square error (MSE) (Eq. 26) and determination coefficient (R^2) (Eq. 27) between the model predicted output and actual values, which was chosen for this study. When the MSE is at the minimum and R^2 is high, $R^2 > 0.98 \sim 0.99$, a model can be judged as very good.

$$MSE = \frac{1}{n} \sum_{i=1}^n (Y_{act,i} - Y_{pred,i})^2 \quad (26)$$

$$R^2 = 1 - \frac{\sum_{i=1}^n (Y_{act,i} - Y_{pred,i})^2}{\sum_{i=1}^n (Y_{act,i} - Y_{avg})^2} \quad (27)$$

Where n is the number of data points, Y_{act} is the cell wall length, Y_{pred} is the predicted value from the established network and Y_{avg} is the mean of the Y_{act} values. Figure 88 shows the schematic flowchart of the overall methodology of establishing the ANN model.

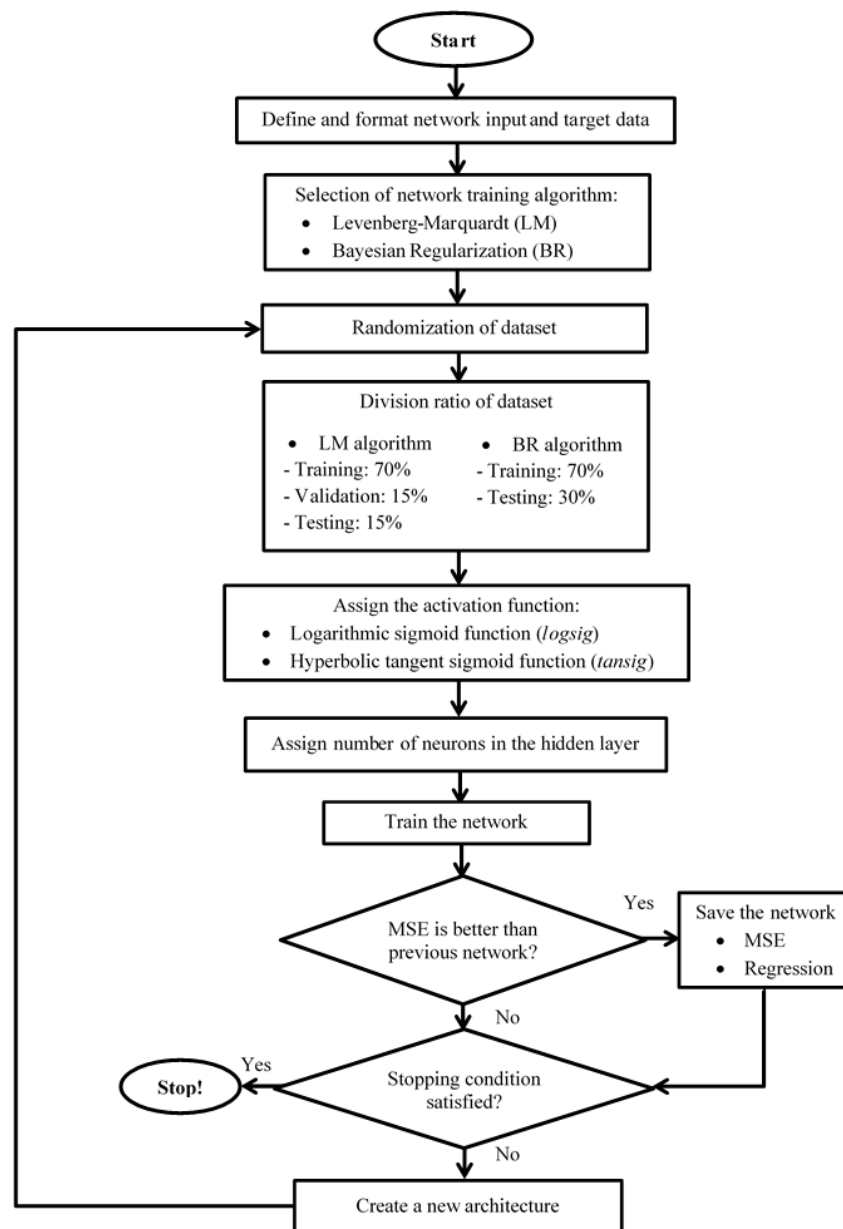
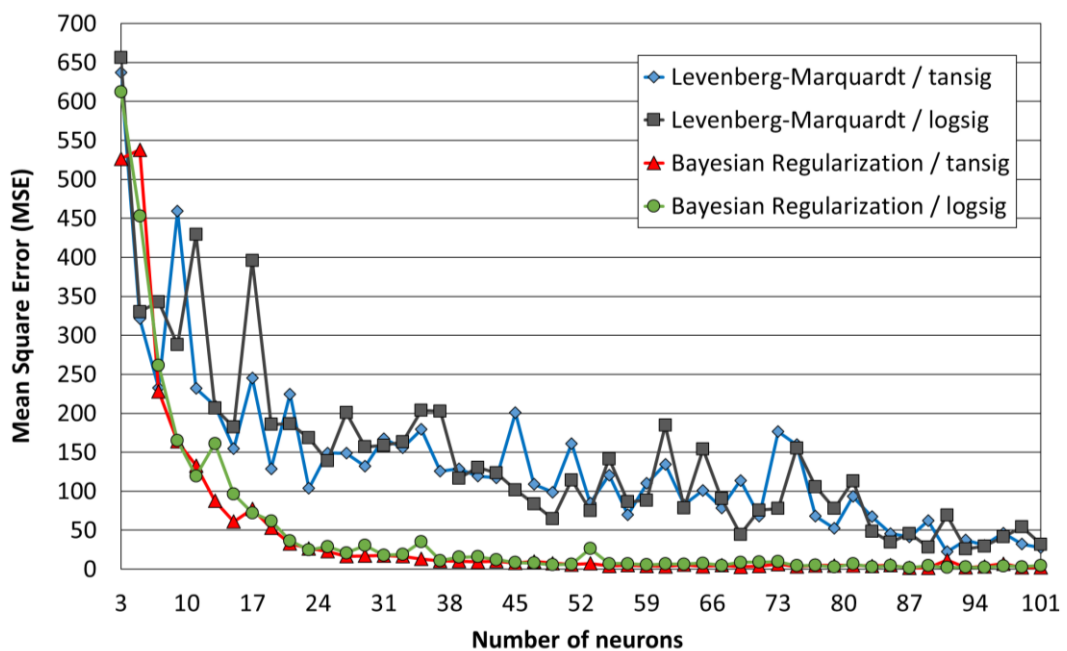


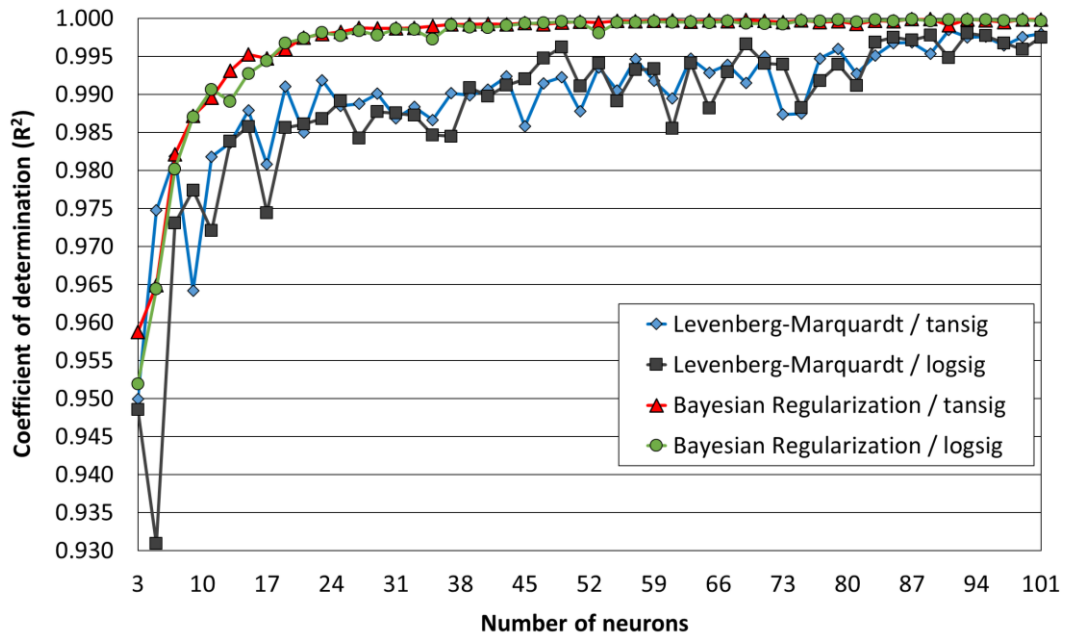
Figure 88: Flowchart of the proposed methodology

5.2 Results and discussions

Figure 89 demonstrates, for various number of neurons in the hidden layer, the mean square error (MSE) and determination coefficient (R^2) variations for the Levenberg–Marquardt (LM)- and Bayesian regularization (BR)-based ANN models using tansig and logsig transfer functions. As shown in the results, increasing the number of neurons in the hidden layer does not imply that the ANN model will have a better predictive accuracy. The best architecture for the ANN model is recognized as that which has a minimum MSE and maximum R^2 . As it can be seen, the BR training algorithm outperformed the LM algorithm. Training the network using BR algorithm resulted in lower MSE and higher R^2 values compared to the network trained using LM algorithm. Furthermore, it is also evident from the results in Figure 89 that a BR-based ANN model using tansig transfer function showed better accuracy compared to the logsig transfer function.



(a) Mean square error (MSE)



(b) Coefficient of determination (R^2)

Figure 89: Determination of optimum network architecture for different neurons in the hidden layer

Amongst all types of neural network configurations explored, the network with 89 hidden neurons, BR training algorithm and tansig transfer function demonstrated the least MSE and the highest R^2 values for all the datasets (Table 3), thus indicating a strong predictive capability. Therefore, the established model is trained with BR algorithm, with tansig as the transfer function, and constituted of 5 neurons in the input layer, 89 neurons in the hidden layer and 4 neurons in the output layer.

Table 3: ANN model performance for training, testing and all datasets

	Number of data points	Mean square error (MSE)	Coefficient of determination (R^2)
Training	1008	0.013	0.99996
Testing	432	0.6101	0.99948
Total data	1440	0.1026	0.99994

Exploring this further, Figure 90 demonstrates a normalized comparison between the predicted values from the established ANN model and the actual values for all the dataset.

From the results, it can be seen that the optimum model shows good prediction ability, thereby improving our confidence in utilizing it in further analyses.

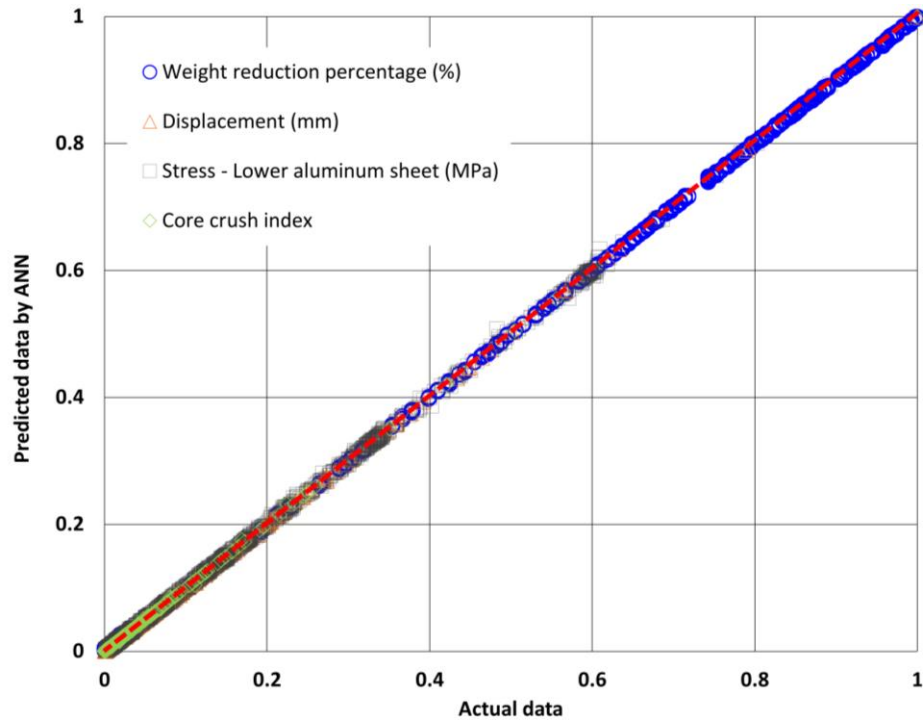


Figure 90: Predicted values from the established ANN model versus the actual values for all datasets

5.2.1 Predictive performance of the ANN model within the training dataset bounds

In order to inspect the flexibility of the established ANN model, the model was tested for its capability to predict the structural performance of the honeycomb sandwich composite-based heliostat based on an unseen dataset within the training bounds. For a heliostat panel subjected to a wind of 20 m/s and consisting of a honeycomb core with a thickness (D) of 300 mm, Figures 91 and 92 demonstrate the structural performance predictions made by the established optimum ANN model at multiple cell wall angles for unseen honeycomb cell wall thicknesses (t); 0.025, 0.035 and 0.045 mm respectively. As demonstrated in the results, the model suggests that the predictions would lie between the two limits bounding each of the investigated unseen cell wall thicknesses (t) (0.025, 0.035 and 0.045 mm), as one might expect.

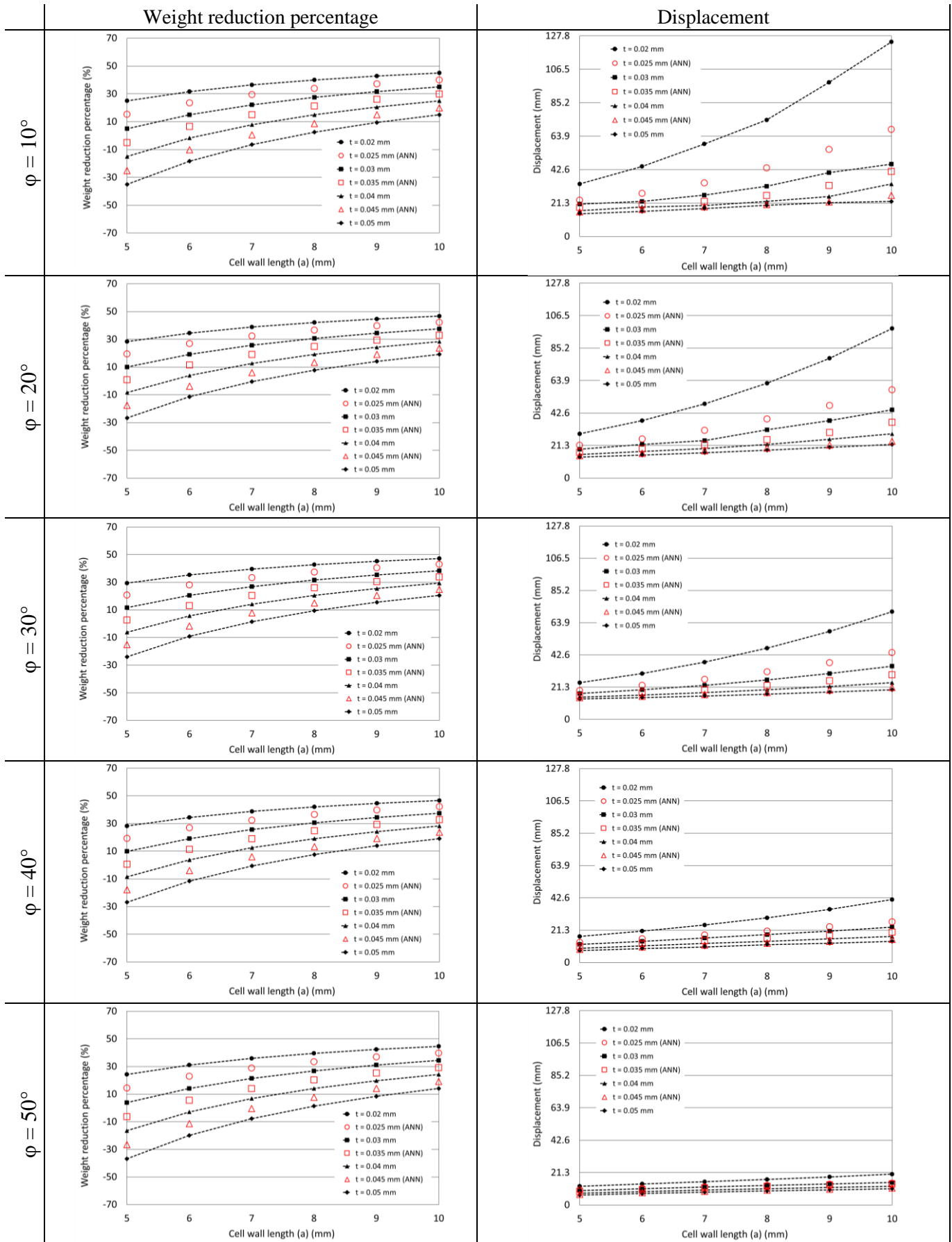


Figure 91: ANN model predictions of the heliostat's attainable weight reduction and maximum structural displacement at multiple cell wall angles for unseen cell wall thicknesses of 0.025, 0.035 and 0.045 mm

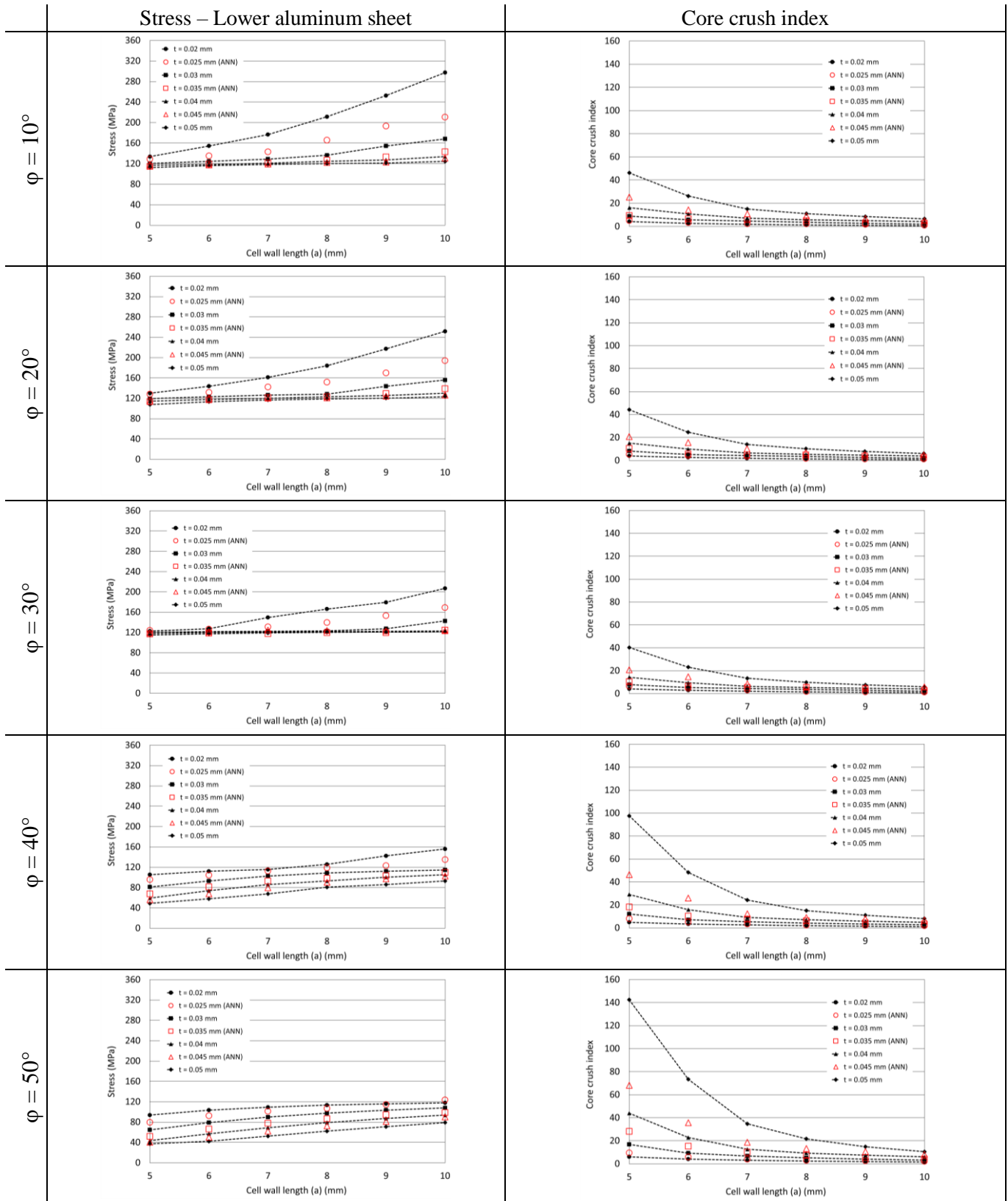


Figure 92: ANN model predictions of the heliostat's recorded maximum stress at the lower aluminium sheet and core crush index at multiple cell wall angles for unseen cell wall thicknesses of 0.025, 0.035 and 0.045 mm

5.2.2 Predictive performance of the ANN model outside the training dataset bounds

As demonstrated previously, the established ANN provided accurate predictions of the structural performance of the honeycomb sandwich composite-based heliostat within the bounds of the data it was trained. Having said that, if the ANN model is provided with inputs outside the training set's bounds, one would anticipate less accurate predictions. With a robust network, the model should be capable of delivering insights into possible outcomes that would be tremendously hard to realize by traditional approaches. Therefore, to investigate the ANN model capabilities outside the training bounds, the ANN model was utilized to predict the structural performance of the sandwich composite-based heliostat that consists of a core with honeycomb cell wall thickness of $t = 0.01$ mm. In the previous results, it could be seen that a decrease in the cell wall thickness causes an increase in the deflection of the panel, resulting in higher stresses at the interface between the steel attachments and the panel's back surface (higher stresses at the lower aluminum sheet and lower core crush index values). As the honeycomb's cell walls gradually become thinner, their bending resistance decreases and consequently the honeycomb core becomes less resistant to local buckling and crushing, causing a decrease in the heliostat panel's stiffness and resistivity to wind loads. However, this decrease in stiffness comes with a notable increase in the attained weight reduction.

Based on this, one would anticipate seeing the same behaviour characteristics for a heliostat that consists of a core with honeycomb cell wall thickness of $t = 0.01$ mm. As such, Figures 93 and 94 show, for a heliostat panel subjected to a wind of 20 m/s and consists of a honeycomb core with a thickness (D) of 300 mm, the predictions of the ANN model at multiple cell wall angles for a core with cell wall thickness (t) of 0.01 mm compared to those of cell wall thicknesses of 0.02, 0.03, 0.04 and 0.05 mm. To fully evaluate the predictive value of the ANN model, simulations were carried out using the

previously established FSI model for the same cell wall thickness ($t = 0.01$ mm) and the results were compared to the ANN model predictions. The results illustrate the behaviour one would expect, demonstrating that the ANN model can provide insights into the structural performance of the honeycomb sandwich composite-based heliostat with design parameters outside the training bounds.

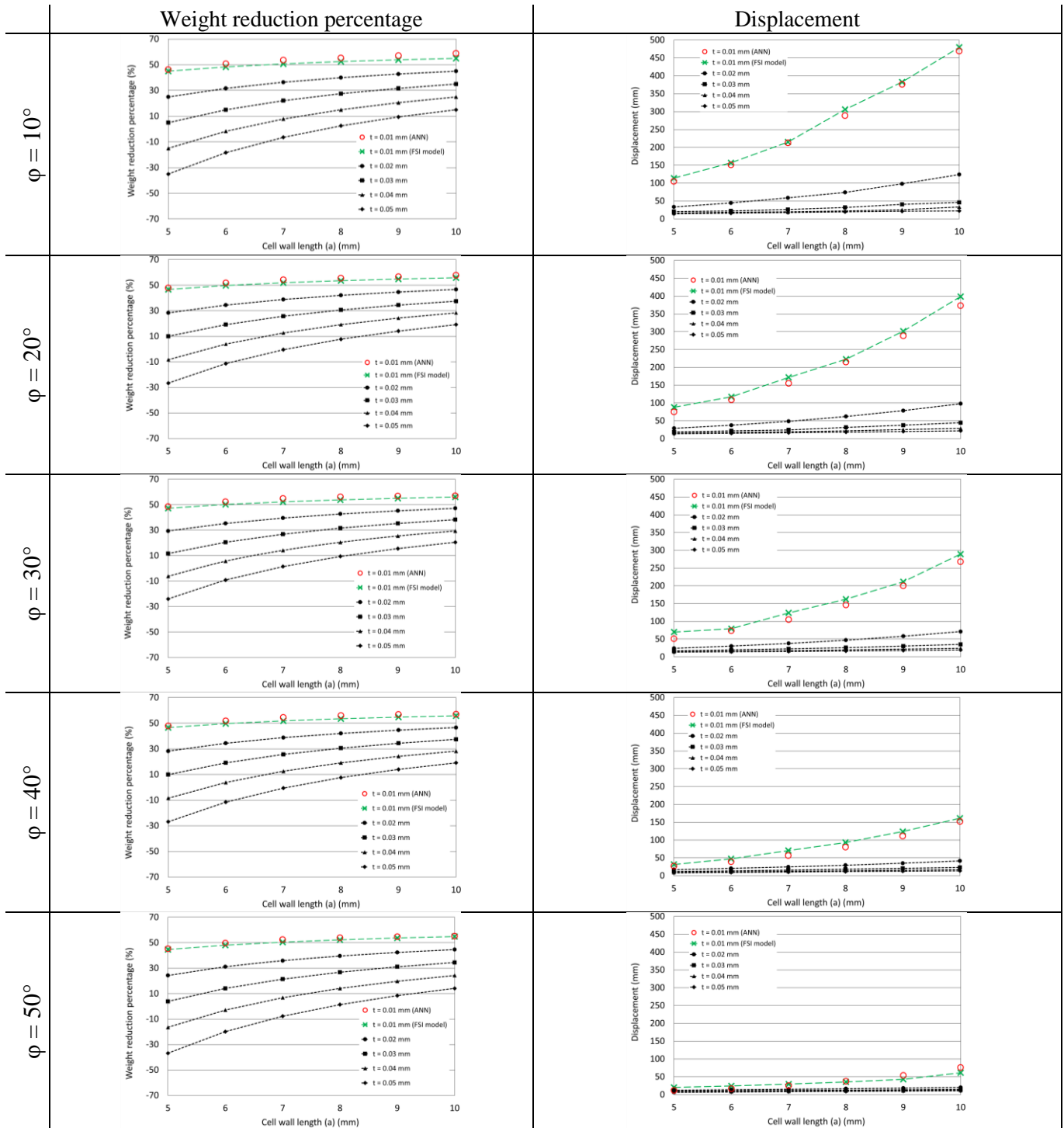


Figure 93: ANN model predictions of the heliostat's attainable weight reduction and maximum structural displacement at multiple cell wall angles for unseen cell wall thickness 0.01 mm

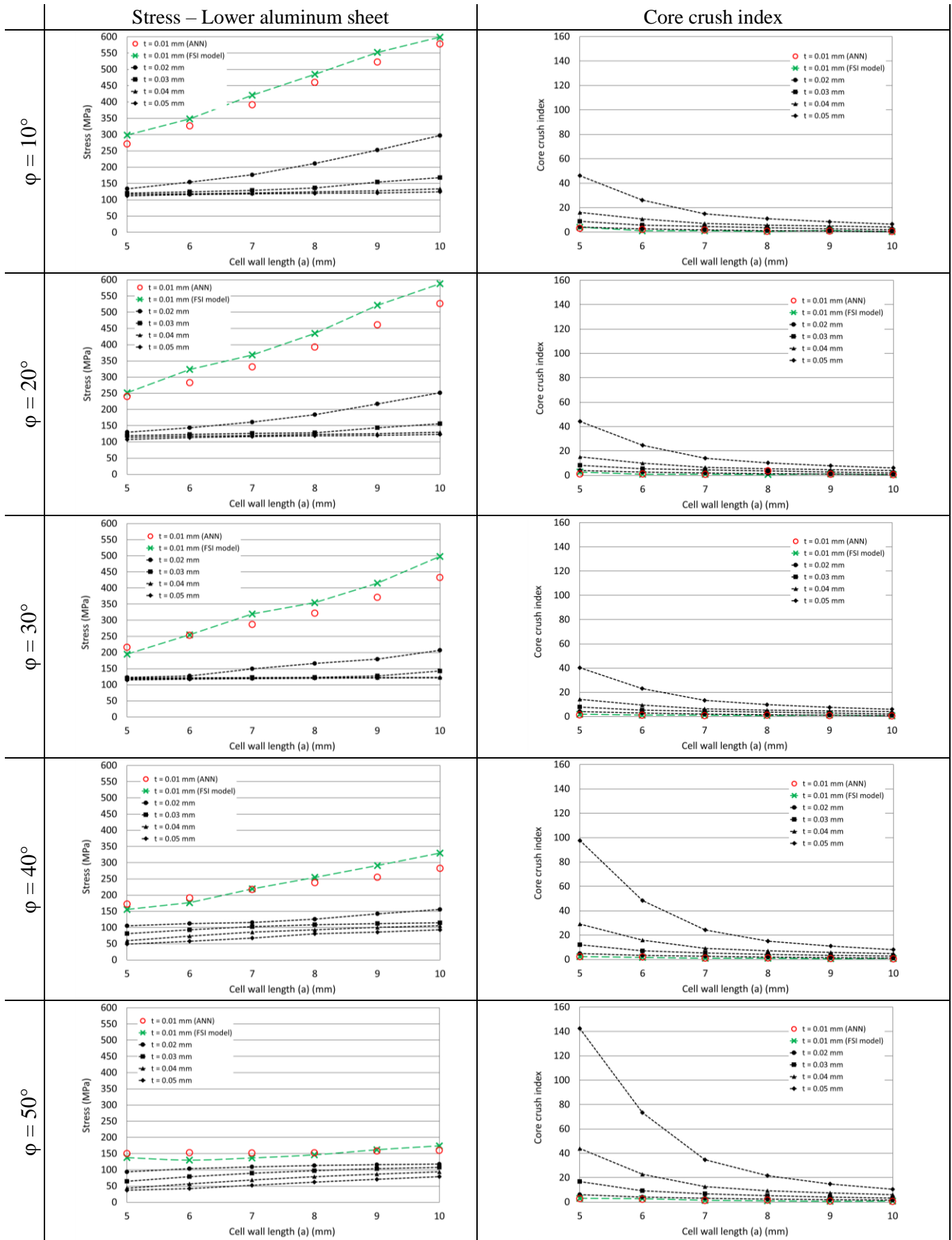


Figure 94: ANN model predictions of the heliostat’s recorded maximum stress at the lower aluminium sheet and core crush index at multiple cell wall angles for unseen cell wall thickness of 0.01 mm

5.3 Chapter Summary

The distinctions in the structural behaviour of the honeycomb sandwich composite-based heliostat with regard to the honeycomb core's physical parameters emphasised in Chapter 4 triggered the need for a generalized model that can capture the influence of each of these parameters on the heliostat structure's performance (i.e. optical, material failure and weight reduction). Given the current developments and potential application of artificial neural network (ANN) in diverse disciplines, it is surprising that implementation of the ANN technique for modelling the effect of honeycomb's physical parameters on the structural performance of honeycomb sandwich composite-based heliostats is not reported in the literature. Moreover, former studies that focused on ANN modelling of sandwich composites were limited by the geometrical parameters considered and the variations in the honeycomb cell geometry. Hence, there is a need for a comprehensive predictive model that eradicates the necessity of going through the difficulties of establishing an excessively computing-time demanding FSI model for each of the honeycomb core's geometrical parameters.

In this chapter, ANN technique was utilized to establish a novel predictive model that predicts the structural performance of the honeycomb sandwich composite-based heliostat based on its honeycomb core's physical parameters. The ANN was trained, tested and validated by a rich dataset obtained from a comprehensive parametric study carried out with various honeycomb core configurations assessed considering several loading conditions (wind velocities of 5, 10, 15, and 20 m/s). A rigorous investigation was carried out to optimally choose the training algorithm, number of neurons in the hidden layer and activation function in a network. Amongst all the neural network configurations explored, a network model with Bayesian regularization (BR) training algorithm, tansig transfer function and having 89 neurons in the hidden layer was found

to be the optimum network with the best predictive performance ($R^2=0.99994$, $MSE=0.1026$).

The results showed that the established ANN model was capable of predicting the structural performance of the honeycomb sandwich composite-based heliostat based on unseen honeycomb core configurations extremely accurately. Moreover, it was demonstrated that the established ANN model could deliver insights into the heliostat's structural performance with design parameters outside the training bounds.

Given the capability and flexibility of the ANN technique, it demonstrates a unique and novel alternative method for designing and analysing the structural performance of honeycomb sandwich composite-based heliostats. This is of great significance as accurately predicting the heliostat's structural performance based on its honeycomb core's configuration using classical analytical approaches are at best cumbersome and, at worst, unable to facilitate the predications.

Chapter 6: Particle swarm-based structural optimization of the honeycomb sandwich composite-based heliostat

Having understood the impact of the honeycomb's geometric configuration on the aerost-
structural behaviour characteristics of the sandwich composite-based heliostat, and
established a predictive model that accurately predicts the heliostat's structural
performance based on its honeycomb core's configuration and considering the desired
site's maximum recorded wind speed, attention is now turned towards the structural
optimization of the sandwich composite-based heliostat. By that we mean minimizing the
total weight of the heliostat panel while satisfying restrictive requirements concerning
both optical and material failure criteria. Determining the optimal honeycomb core
configuration, among a multitude of possible combinations, that delivers the best trade-
off between the panel's weight reduction and structural integrity is not an easy task to
achieve. The complex non-linear material behaviour, along with the large number of
design variables and performance constraints, bring about a great challenge to the
optimization procedure, especially with traditional deterministic and classical statistical-
based design of experiments methods that are generally time-consuming and inefficient
with the presence of local optima (Ajdad et al., 2019; Elsheikh and Elaziz, 2019). This
heightened the need for an accurate and powerful optimization method that overcomes
such limitations.

Because of their powerfulness and remarkable successfulness in solving complex
optimization problems efficiently where other techniques fail, nature-inspired algorithms
acquire a unique place among the many techniques for optimization. A nature-inspired
algorithm is a higher-level optimization technique comprising a heuristic approach and
iterative process in which the strategy is mostly inspired by natural phenomena (Nasir
and Tokhi, 2014). The ease of implementation and the capability of producing an
optimum and a reliable solution are the advantages as well as some of the reasons why

they have continuously received attention from researchers around the world and have been extensively utilized in countless applications. Several nature-inspired optimization techniques have come into existence over the last couple of years. Some of the well-known algorithms include genetic algorithm (GA) (Goldberg, 1989), ant colony optimization (ACO) (Dorigo and Di caro, 1999), bacterial foraging optimization (BFO) (Passino, 2002), artificial bee colony (ABC) (Karaboga and Basturk, 2007) and particle swarm optimization (PSO) (Eberhart and Kennedy, 1995).

Among the diverse nature-inspired optimization techniques available nowadays, particle swarm optimization (PSO) algorithm stood out distinctively as one of the well-known, most promising and effective optimization techniques in solving highly constrained non-linear and non-convex optimization problems (Assarzadeh and Naghsh-Nilchi, 2015). Introduced by Eberhart and Kennedy (1995), the PSO algorithm is based on the cooperative behaviour among species such as bird flocking and fish schooling. The positions of points (particles) in the design space record the potential solutions of an optimization problem. Each particle updates its location according to its own best position and the entire swarm's best position at each generation (Tao et al., 2017). PSO has many merits over other optimization techniques, such as the fewer number of parameters to adjust unlike many other competing techniques, the low computational time and the flexibility to combine with other optimization techniques to form hybrid tools. Added also, the PSO algorithm does not depend on the initial solution to start its iteration process (AlRashidi and El-Hawary, 2009; Hasaniien, 2010).

Because of its implementation simplicity and fast searching speed, the PSO algorithm has been widely used in various engineering applications (Hasaniien, 2010; Li and Chandrashekhara, 2015; Liu et al., 2016; Tao et al., 2017). Focusing on the field of composites, with emphasis on honeycomb sandwich composites, Table 4 summarizes former studies on the optimization of honeycomb sandwich composites.

Table 4: Former studies on the optimization of sandwich composites

Study	Type of sandwich composite	Material		Honeycomb geometrical parameters considered in the optimization	Optimization algorithm
		Face sheets	Core		
Vinson, 1986	Honeycomb sandwich panel	Multiple	Multiple	<ul style="list-style-type: none"> Cell wall thickness Cell wall length Core thickness 	- (Analytical)
Ding, 1989	Honeycomb sandwich panel	Aluminum	PVC	<ul style="list-style-type: none"> Cell wall thickness Cell wall length Core thickness 	- (Analytical)
Hou et al., 2007	Honeycomb sandwich panel	Aluminum	Aluminum	<ul style="list-style-type: none"> Cell wall thickness Cell wall length 	Nonlinear multivariable optimization algorithm
Qiao, 2008	Honeycomb sandwich panel	Fiber-reinforced plastic	Fiber-reinforced plastic	<ul style="list-style-type: none"> Cell wall thickness Cell wall length Cell wall angle 	Sequential quadratic programming
Caccese et al., 2013	Honeycomb sandwich panel	-	-	<ul style="list-style-type: none"> Core thickness 	GA
Boudjemai et al., 2014	Honeycomb sandwich panel	Aluminum	Aluminum	<ul style="list-style-type: none"> Core thickness 	GA, Gravitational search algorithm
He et al., 2016	Honeycomb sandwich panel	Aluminum	Aluminum	<ul style="list-style-type: none"> Cell wall thickness Cell wall length 	Optimal latin hypercube design of experiments
Sun et al., 2010	Honeycomb sandwich panel	Aluminum	Aluminum	<ul style="list-style-type: none"> Cell wall thickness 	PSO
Yin et al., 2011	Honeycomb sandwich panel	Aluminum	Aluminum	<ul style="list-style-type: none"> Cell wall thickness Cell wall length Cell wall angle 	PSO
Ebrahimi and Vahdatazad, 2015	honeycomb sandwich cylindrical column	Aluminum	Aluminum	<ul style="list-style-type: none"> Cell wall thickness Core thickness 	PSO
He and Ma, 2015	Reinforced honeycomb sandwich panel	Aluminum	Aluminum	<ul style="list-style-type: none"> Cell wall thickness Cell wall length 	PSO
He et al., 2015	Honeycomb sandwich panel	Aluminum	Aluminum	<ul style="list-style-type: none"> Cell wall thickness Cell wall length 	PSO
Xie et al., 2018	Honeycomb sandwich panel	Aluminum	Aluminum	<ul style="list-style-type: none"> Cell wall thickness Cell wall length 	PSO

Despite the very few attempts found in literature that utilized PSO into their honeycomb sandwich composite investigations (Sun et al., 2010; Yin et al., 2011; Ebrahimi and Vahdatazad, 2015; He and Ma, 2015; He et al., 2015; Xie et al., 2018), it is surprising that these former studies did not consider all the four honeycomb core's physical parameters (core thickness (D), cell wall angle (ϕ), cell wall thickness (t), and the cell wall length (a)) in their optimization problems. Considering the impact that each of these parameters has on the performance of honeycomb cores, increasing the number of design variables brings new challenges and complexity to the design and optimization of honeycomb sandwich composites.

In the renewable energy investigations, the PSO method became a very attractive algorithm recently in the field of solar energy related applications, CSP technologies in particular. For instance, Ajdad et al. (2019) applied the PSO method in the optical-geometric optimization of linear Fresnel collectors. On the other hand, Cheng et al. (2015) developed an optimization model on optical performance of parabolic trough solar collector systems based on the PSO algorithm and the Monte Carlo ray-tracing method. Focusing on central tower CSP systems, Li et al. (2017, 2018) focused on determining the maximum potential daily energy collection of a heliostat via optimizing the field layout using PSO. Farges et al. (2018), on the other hand, utilized PSO algorithm to optimize the performance of solar central tower considering the following design parameters: tower height and the width, height and tilt angle of the receiver. The obtained results revealed that the collected thermal energy increased by 23.5%, and the heliostat field optical efficiency was enhanced by 9%. In their work, Piroozmand and Boroushaki (2016) investigated the optimal design and layout of a multiple solar central tower system via applying PSO method to overcome the issue of impairing the optical efficiency due to shading effects. The obtained results showed that by using PSO algorithm, the multiple

solar central tower system's optical performance was improved, and the annual efficiency reached 54.58%.

In view of the above, it can be highlighted that the previous studies that incorporated nature-inspired optimization techniques, PSO in particular, in their central tower CSP systems' investigations mainly focused on optimizing the heliostat field layout and aiming strategy. Given the recent developments and potential application of PSO in diverse disciplines, and particularly in central tower CSP systems, it appears that the application of PSO method for structural optimization of honeycomb sandwich composite-based heliostats has not been studied yet. In this regard, this chapter investigates the implementation of PSO algorithm for determining the optimum honeycomb core configuration leading to minimum self-weight of the heliostat's sandwich composite panel while satisfying the structural performance requirements (i.e. optical and material failure). Coupled with the previously established ANN predictive model in Chapter 5, the proposed integrated ANN-PSO approach will provide a useful, flexible and time-efficient tool for heliostat designers to optimize the structural performance of honeycomb sandwich composite-based heliostats as per specified requirements (i.e. the chosen site's maximum design wind velocity and optical and material failure limits).

6.1 Numerical setup

In undertaking this investigation, MATLAB R2018a was used as the platform to implement the PSO algorithm. As described earlier, PSO algorithm emulates the cooperative behaviour among species such as flocks of birds and schools of fishes. Potential solutions of an optimization problem are regarded as points (particles) in the design space. Each particle (i) possesses two characteristic components: position (x^i) and velocity (v^i). The particle's position is the candidate solution whereas the velocity

determines the updating direction of the particle. These particles in the swarm proceed through the feasible solution space to explore optimal solutions. Each particle updates its location according to its own best position ($pbest_k^i$) and the entire swarm's best position ($gbest_k$) at each generation (iteration) (k). The velocity and position of a particle is updated based on the following equations (Eqs. 28 and 29):

$$v_{k+1}^i = \omega v_k^i + c_1 rand_1 (pbest_k^i - x_k^i) + c_2 rand_2 (gbest_k - x_k^i) \quad (28)$$

$$x_{k+1}^i = x_k^i + v_{k+1}^i \quad (29)$$

Where v_k^i and x_k^i are the velocity and position of the i^{th} particle in k^{th} generation, respectively. c_1 and c_2 are acceleration constants (defined by $c_1 + c_2 > 4$ (Ajdad et al., 2019)) which determine the cognitive and the social learning rates, respectively, ω is an inertia weight used to improve the convergence speed and $rand_1$ and $rand_2$ are two random numbers comprise within the range of 0 and 1.

For selecting the values of acceleration constants c_1 (cognitive learning parameter) and c_2 (social scaling parameter), it was assumed that the cognitive behaviour of each particle cannot be privileged compared to the social (collective) behaviour. Hence, no difference can be made between the two constants c_1 and c_2 . In this study and based on the restriction: $c_1 + c_2 > 4$ (Ajdad et al., 2019), a value of $c_1 = c_2 = 2.05$ have been selected. As for determining the inertia weight (ω), the best suggested approach is by having a dynamical inertia weight (Eq. 30) according to the number of iterations (Hasanien, 2010; Ajdad et al., 2019). At the start of the search procedure, each particle must be more flexible with respect to the group's global tendency. As the search procedure converges to the optimal solution, this flexibility must be reduced progressively. In this regard, it is crucial to have a varying ω to achieve the best swarm performance. The dynamic inertia weight (ω) is given by Eq. (30):

$$\omega(iter) = \frac{(iter_{max} - iter)}{iter_{max}} \times (\omega_{max} - \omega_{min}) + \omega_{min} \quad (30)$$

Where $iter$ represents the current generation, $iter_{max}$ is the maximum generation number and ω_{max} and ω_{min} are respectively the maximum and minimum values of the inertia weight, which can be set as 0.9 and 0.4 respectively as suggested by previous PSO investigations (Sharma and Siddhartha, 2012; Liu et al., 2016; Ajdad et al., 2019).

6.1.1 Optimization problem formulation (objective function, decision variables and restrictions)

6.1.1.1 Objective function

For this optimization problem, the main objective function is the total weight of the heliostat's sandwich composite panel which is intended to be as light as possible; lighter than that of the existing 148 m² steel-based ATS heliostat's mirror support structure (approximately 1550 kg as reported by Kolb et al. (2007)). Hence, the objective function can be formulated as follows:

Maximize weight reduction percentage (%)

$$= \text{Maximize} \frac{(W_{ATS} - W_{hsch})}{W_{ATS}} \times 100 \quad (31)$$

Where W_{ATS} is the total weight of the ATS heliostat's mirror support structure and W_{hsch} is the total weight of the honeycomb sandwich composite-based heliostat's panel at a specific honeycomb core configuration.

6.1.1.2 Decision variables

The optimization procedure consists of searching for the various geometrical parameters of the sandwich composite-based heliostat's panel. Therefore, the honeycomb core's physical parameters (core thickness (D), cell wall angle (ϕ), cell wall thickness (t), and

the cell wall length (a) were defined as design variables, and their ranges are illustrated in Figure 95. The wind velocity, on the other hand, was not defined as a design variable and was considered a flexible input parameter that is set by the user, depending on the requirements associated with the desired site's maximum recorded wind speed.

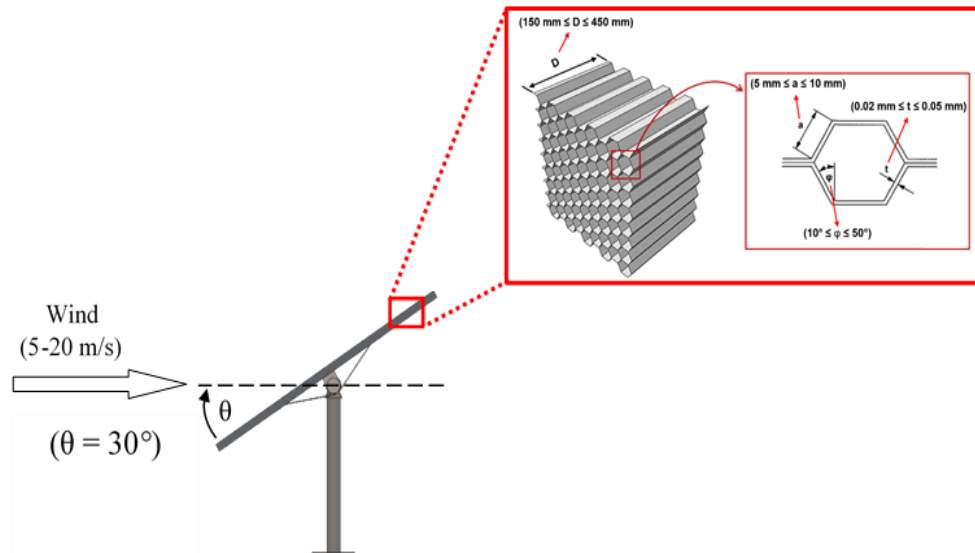


Figure 95: Design variables of optimization study with their search ranges

6.1.1.3 Constraints

In order to accomplish the investigation objective, which is to determine the optimum honeycomb core configuration leading to minimum self-weight, the heliostat structure must satisfy restrictive requirements (constraints) concerning optical, material failure and weight criteria. For the optical criteria, the structure should be able to keep its deformation below 21.3 mm (derived earlier from Björkman's (2014) approach of calculating the maximum allowable displacement). As for the material failure criteria, the two highly stressed components of the sandwich panel, as discussed previously in Section 3.3.2, that have a higher probability of experiencing material failure are the lower aluminum sheet and the aluminum honeycomb core. For the lower aluminum sheet, the stresses imposed upon it should not exceed the yield strength of the material ($\sigma_y = 280$ MPa) so that the face yielding failure mode does not occur. As for the honeycomb core,

the ratio of the calculated critical collapse strength of the honeycomb core at a specific cellular configuration to the maximum recorded stress at the core (defined earlier as core crush index) should be greater than 1. It is important to highlight that the aforementioned requirements are the minimum conditions necessary for a reliable operation of a heliostat. These constraints can be altered for an enhanced structural performance depending on the heliostat designer's needs.

6.1.2 ANN-PSO optimization procedure

Figure 96 illustrates a flowchart of the PSO algorithm with the heliostat structural performance ANN model. This ANN-PSO approach involves the following major steps: (1) Set the PSO parameters' values (e.g. Number of particles, maximum number of iterations, etc.) and initialize randomly the swarm particles' position and velocity in the population; (2) Evaluate each particle's fitness, using an objective function as outputs from the ANN model run with inputs of the honeycomb core's physical parameters (i.e., values of particles' position); (3) Update and record the local best ($pbest_k^i$) and the global best ($gbest_k$) values while comparing the currently calculated fitness values with the previous records; (4) Update the velocity and position of each swarm particle using Eqs. (24) and (25), respectively; (5) Check the stopping criteria, so that the optimization process can be repeated until the desired value of the objective function is reached with an accepted deviation or unchanged or the number of iterations reaches the predefined maximum number of iterations ($iter_{max}$). As the PSO algorithm arrives at the imposed termination criteria, the final recorded global best position over all iterations leads to the optimization problem's solution.

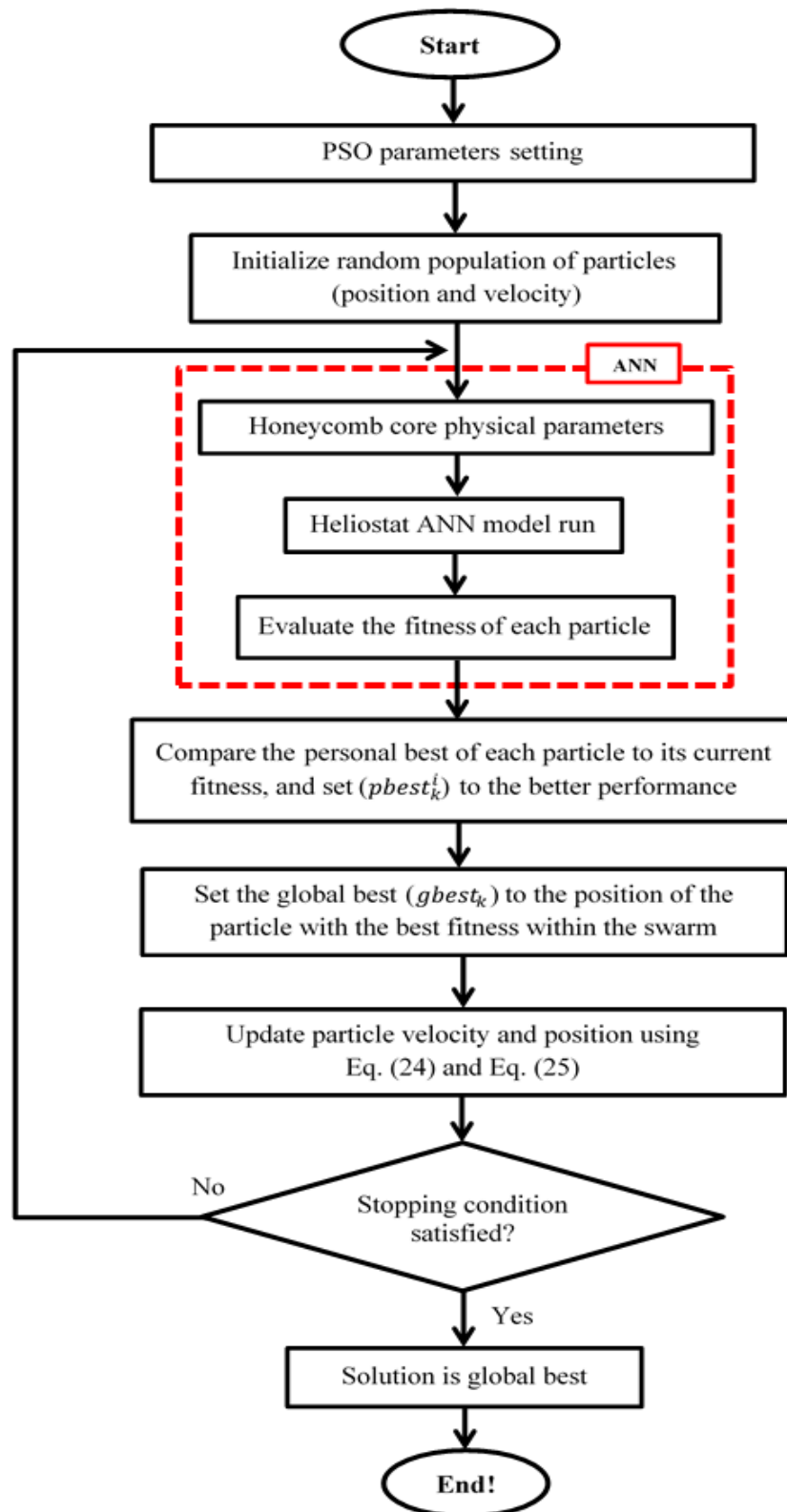


Figure 96: Flowchart of the ANN-PSO methodology

In undertaking the optimization process, the swarm size (number of particles) was varied from 5 to 60 particles. The number of particles is an adjustable parameter of which is

normally unknown and determined by the algorithm's convergence performance and processing time. For small numbers of particles, the swarm will fall effortlessly into local optima without being able to leave later to find better results. On the other hand, having too many particles might result in better convergence towards a more global optimum (particles gather more information to have a further global view regarding the search space) but will result in high computational time. In this regard, the swarm size was varied to analyse and find the suitable number of particles that delivers the best performance for convergence and processing time. Moreover, the number of iterations was set sufficiently high ($iter_{max}= 100$) to ensure a good convergence to the optimum solution with no or very little improvement. Table 5 summarizes all the PSO parameters used in this study.

Table 5: PSO algorithm characteristics

PSO parameters	
Number of particles	5 – 60
Cognitive learning parameter (c_1)	2.05
Social scaling parameter (c_2)	2.05
Maximum inertia weight (ω_{max})	0.9
Minimum inertia weight (ω_{min})	0.4
Number of iterations ($iter_{max}$)	100

To demonstrate the feasibility of the proposed approach for this system, two additional case scenarios are considered and are summarized in Table 6. In the second case, it was assumed that the targeted heliostat is also subjected to a wind of 20 m/s but the design requirements are altered for more enhanced structural performance, unlike the first case where the design requirements are the minimum conditions necessary for a reliable operation of a heliostat. As for the third case, the design wind speed was reduced to 5 m/s, with minimum design requirements similar to the first case.

Table 6: Description of the three cases to be optimized

		Configuration 1	Configuration 2	Configuration 3
Design variables	Chosen site's maximum design wind velocity (m/s)	20	20	5
	core thickness (D) (mm)	To be optimized	To be optimized	To be optimized
	cell wall angle (ϕ) (degree)	To be optimized	To be optimized	To be optimized
	cell wall thickness (t) (mm)	To be optimized	To be optimized	To be optimized
	cell wall length (a) (mm)	To be optimized	To be optimized	To be optimized
Design requirements	Maximum allowable structural deformation (mm)	21.3	10	21.3
	Maximum allowable stress at lower aluminium sheet (MPa)	280	100	280
	Minimum allowable core crush index	1	5	1

6.2 Results and discussions

As discussed earlier, the swarm size is an adjustable parameter of which is normally unknown and determined by the algorithm's performance. In this regard, and having set up the optimization scheme, the effect of the swarm size (number of particles) on the optimization performance was investigated to find the suitable number of particles that delivers the best performance for convergence and processing time. Figure 97 demonstrates for the first case scenario (configuration 1) the objective function evolution (weight reduction percentage) as a function of the number of iterations realized for various swarm sizes. According to the results, the most compelling remark is that increasing the size of the swarm improves the quality of the optimum obtained. However, the optimum improvement according to the swarm size remains constant from 40 particles. In this sense, a swarm size of 40 particles was selected for the optimization study.

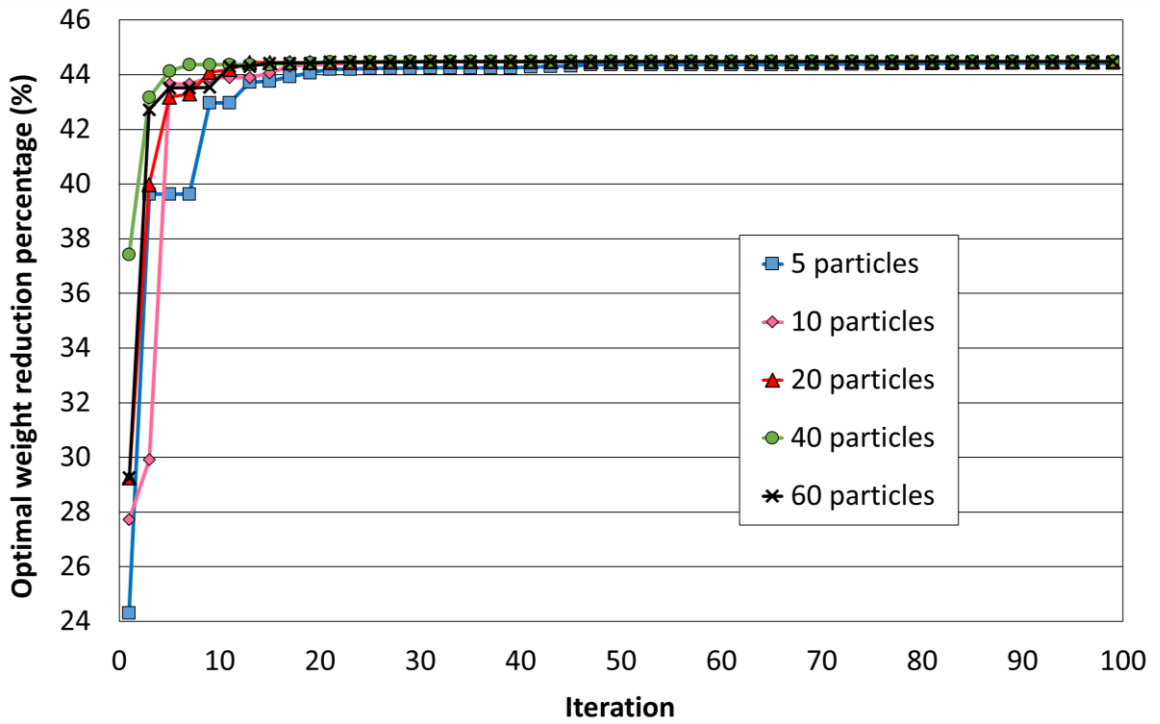


Figure 97: Objective function evolution (weight reduction percentage) according to the number of iterations performed for various swarm sizes (case of configuration 1)

Having identified the swarm size, attention was focused on evaluating the effectiveness of the established PSO algorithm. This evaluation was based on the comparison between results attained by the PSO approach and those attained by scanning of all the search space defined by the variables to be optimized. It should be noted that the high number of parameters to optimize, the dependence between them and the existence of several local optima makes the optimization procedure extremely complex. With the latter approach (search space scanning), the optimization operation becomes very expensive in computing time, since no automated algorithm can locate a global optimum between numerous local optima prior to scanning all the domains. In undertaking the evaluation, the algorithm was applied to the first case scenario (configuration 1), where the targeted heliostat is subjected to a wind of 20 m/s and the design requirements are as follows: maximum allowable structural deformation = 21.3 mm, maximum allowable stress at lower aluminium sheet = 280 MPa and minimum allowable core crush index = 1.

Starting with the search space scanning method, Figures 98, 100 and 102 visualize the relationship between the honeycomb cellular configuration and the heliostat surface's maximum recorded displacement, lower aluminum sheet's maximum recorded stress and core crush index for the three core thicknesses (D); 150, 300 and 450 mm respectively. The area bounded in red shows the zone where the criterion for each of the aforementioned requirements is met.

Starting with the case when the heliostat panel consists of a honeycomb core with a thickness of $D = 150$ mm (Figure 98), one can see from the plots that for the range of cell wall angles between $\varphi = 10^\circ$ and $\varphi = 40^\circ$ the heliostat panel was not able to cope with the aerodynamic loads imposed upon it and the deformations exceeded the allowable threshold for all cell wall length and cell wall thickness configurations. As the honeycomb's cell wall angle (φ) changes to $\varphi = 50^\circ$ for the same 150 mm core thickness results, only few honeycomb configurations have satisfied the optical criteria, with a minimum deformation of 19.27 mm recorded when the honeycomb's cell wall thickness (t) and length (a) are of 0.05 mm and 5 mm respectively. At this configuration ($\varphi = 50^\circ$, $t = 0.05$ mm, $a = 5$ mm), the maximum recorded stress at the lower aluminum sheet (78.73 MPa) and the core crush index (67.2) are found to be within the permissible material failure limits. With both optical and structural strength requirements being satisfied, it can be observed from Figure 99, which illustrates the influence of honeycomb cellular configuration on the attained weight reduction for a heliostat panel with the same core thickness ($D = 150$ mm), that a weight reduction of approximately 14.07% is achieved with this core configuration.

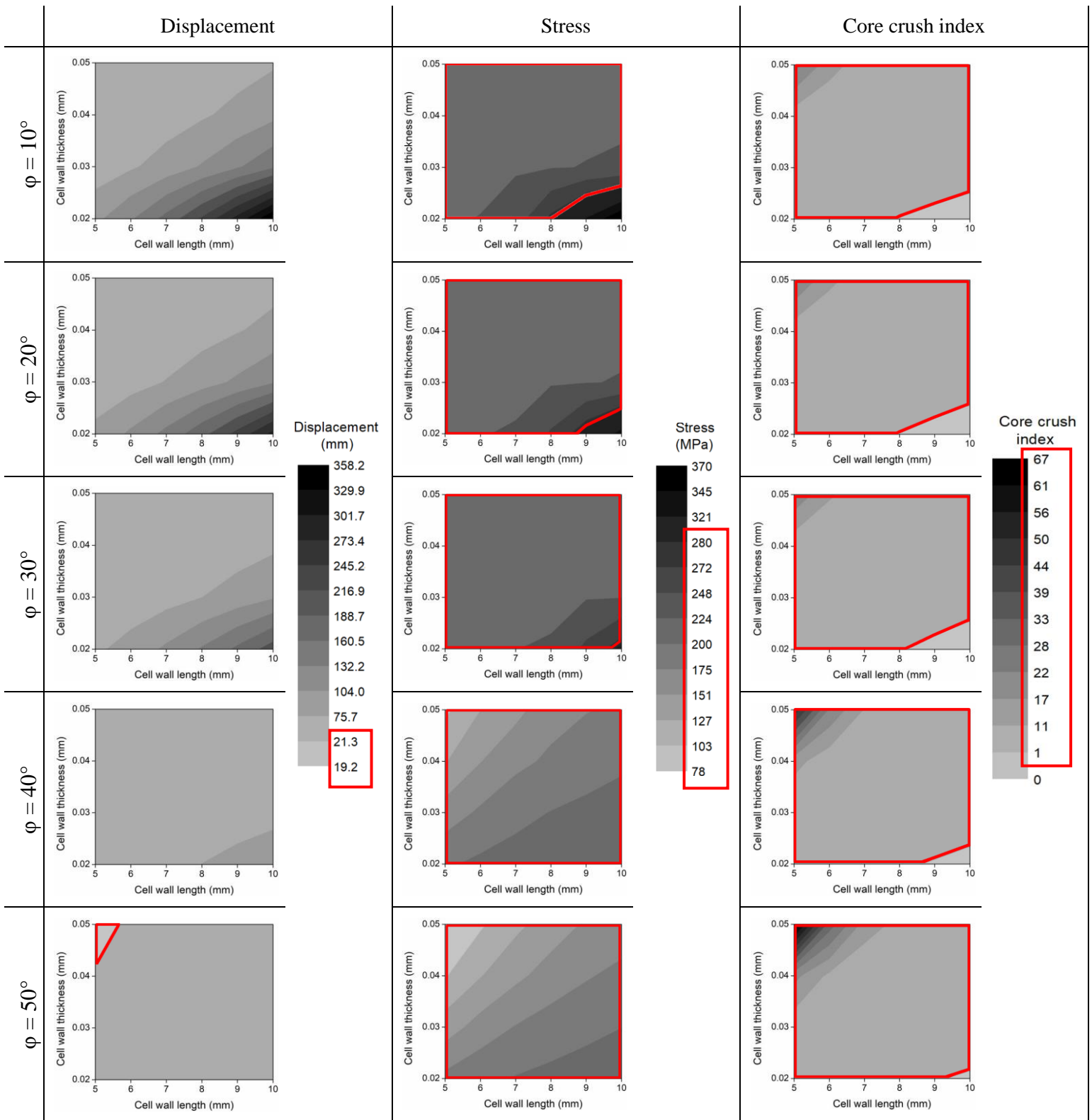


Figure 98: Effect of honeycomb cellular configuration on the heliostat surface's maximum recorded displacement, lower aluminum sheet's maximum recorded stress and core crush index for a core with a thickness of 150 mm

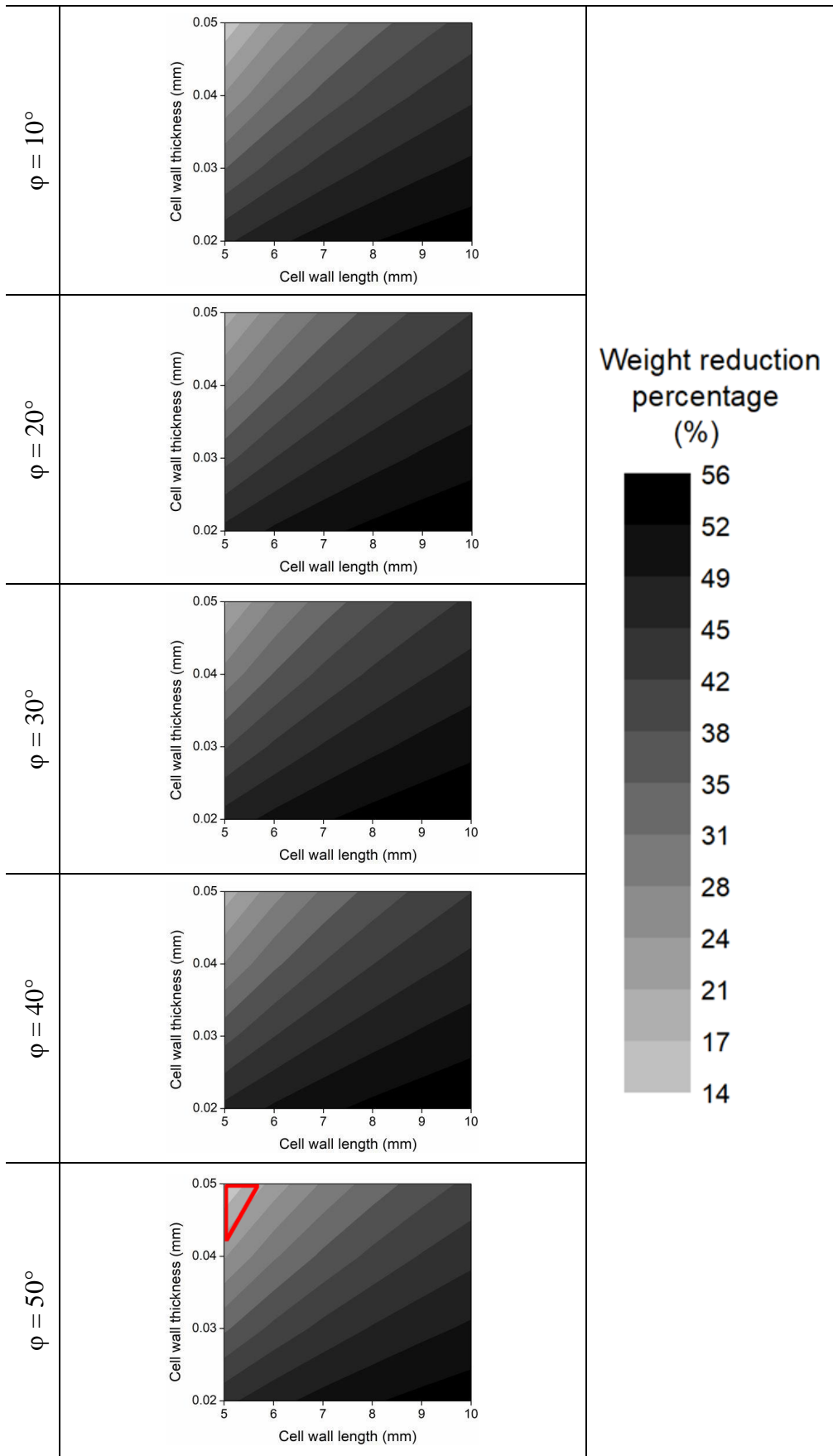


Figure 99: Effect of honeycomb cellular configuration on the mirror support structure's attainable weight reduction for a core with a thickness of 150 mm

Moving to the case when the heliostat panel consists of a honeycomb core with a thickness of $D = 300$ mm (Figure 100), it can be observed from the plots associated with the displacement results that the zone where the maximum deformations are within the allowable threshold increases with the increase in cell wall angle (ϕ). Once the cell wall angle reaches 50° for the same 300 mm core thickness results, the area bounded in red covers the entire plot, indicating that the heliostat panel is expected to maintain a very high optical performance for all cell wall lengths and cell wall thicknesses. As for the effect of varying the honeycomb's cellular geometry on the maximum stress at the heliostat panel's lower aluminum sheet, the stress values for all cell wall angles are found to be below the material failure limit, except when the panel consists of a core with cell wall angle of $\phi = 10^\circ$, cell wall length of $a = 10$ mm and cell wall thickness of $t = 0.02$ mm and the maximum recorded stress was found to be approximately 297.25 MPa. For the core crush index results, the red-bounded area that highlights the honeycomb's cellular configurations where the core crush index is greater than 1 gradually increases with the increase in cell wall angle (ϕ). At a cell wall angle of 40° and onwards, the core crush index values demonstrate that the core is unlikely to experience material failure for all cell wall lengths and cell wall thicknesses. Figure 101 shows the impact of honeycomb cellular configuration on the achieved weight reduction for a heliostat panel with the same core thickness ($D = 300$ mm). The area bounded in red indicates the zone where all the requirements (i.e. optical, material failure and weight reduction) are satisfied. From these results it is clear that the configuration that gives most desirable trade-off between the heliostat panel's structural integrity and attained weight reduction is when the panel consists of a honeycomb core with cell wall angle of $\phi = 50^\circ$, cell wall length of $a = 10$ mm and cell wall thickness of $t = 0.02$ mm, with a maximum displacement of 20.3 mm, a maximum stress of 117.83 MPa, a core crush index value of 1.57, and an achieved weight reduction of approximately 44%.

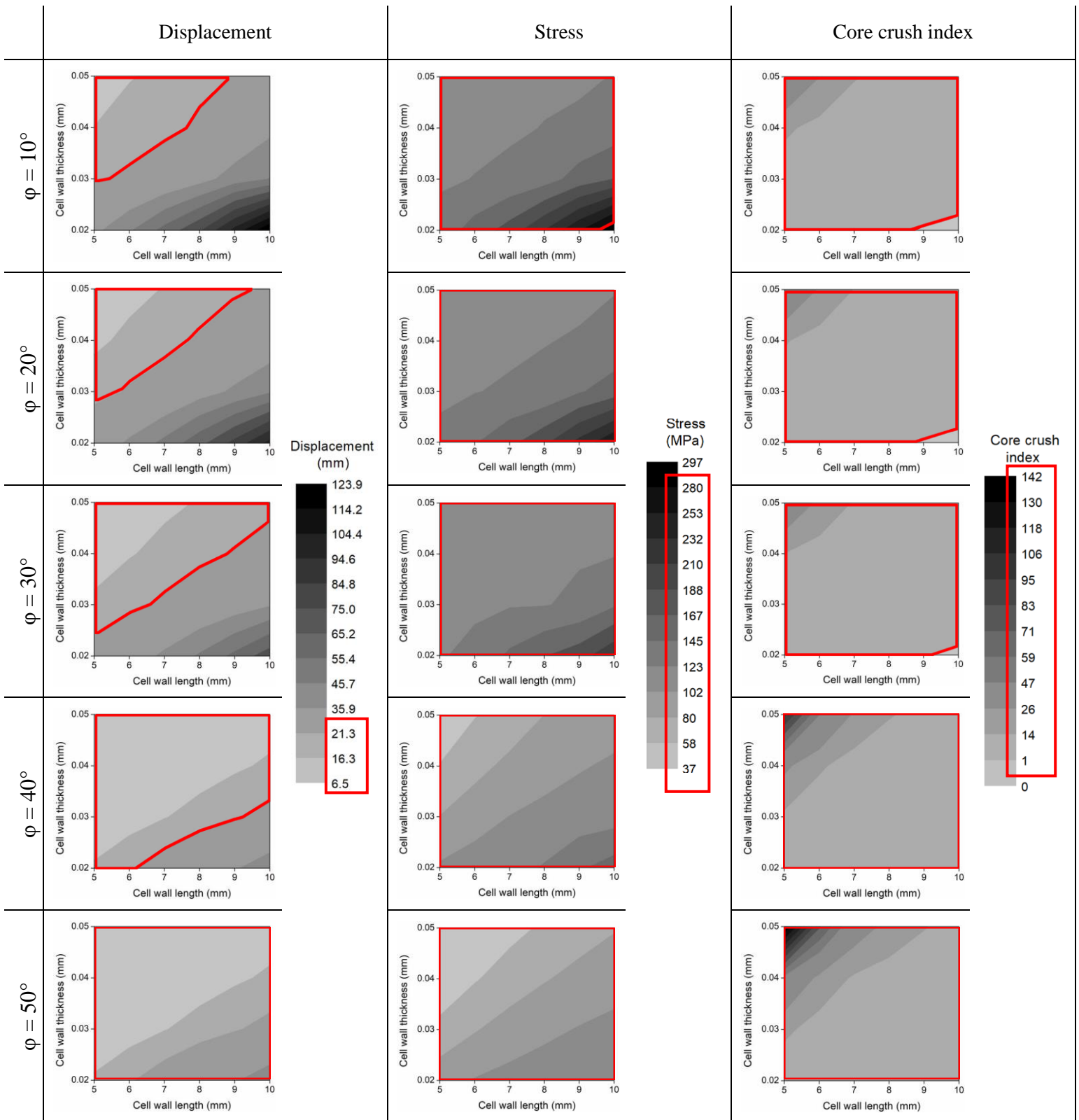


Figure 100: Effect of honeycomb cellular configuration on the heliostat surface's maximum recorded displacement, lower aluminum sheet's maximum recorded stress and core crush index for a core with a thickness of 300 mm

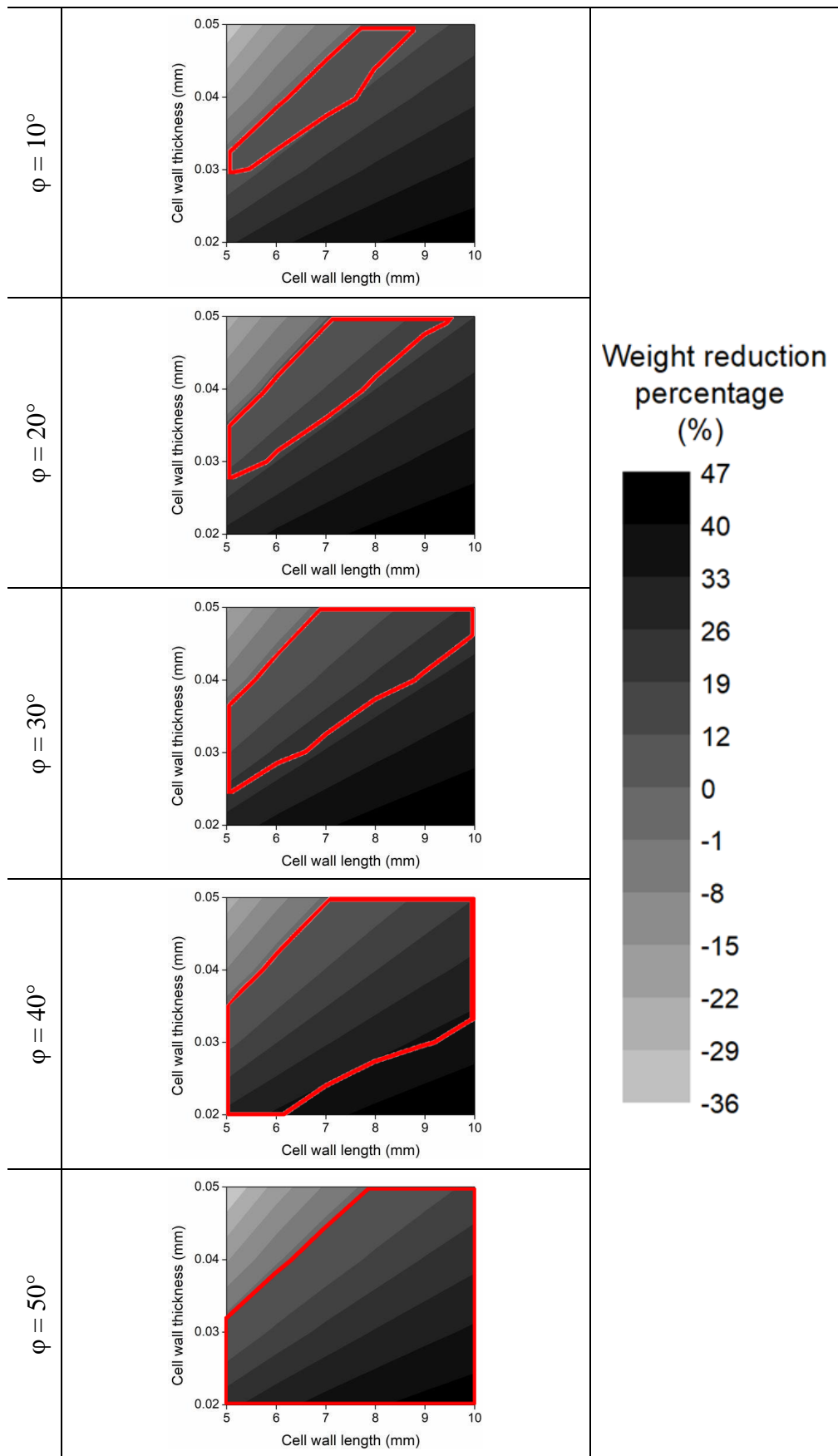


Figure 101: Effect of honeycomb cellular configuration on the mirror support structure's attainable weight reduction for a core with a thickness of 300 mm

For the case when the heliostat panel consists of a honeycomb core with a thickness of $D = 450$ mm (Figure 102), the plots related to displacement results illustrate the gradual increase in the red-bounded zone (the zone where the optical requirement is met) with the increase in cell wall angle (φ). As φ approaches 50° , the maximum displacement values illustrate that the panel is expected to maintain a very high optical performance for all cell wall lengths and cell wall thicknesses. Moving to the effect of altering the honeycomb's cellular geometry on the maximum stress at the heliostat panel's lower aluminum sheet, the zone bounded in red covers the entire plot for all cell wall angles, demonstrating that the stress values are below the yield strength of the material ($\sigma_y = 280$ MPa) and the lower aluminum sheet is unlikely to experience material failure for all cell wall length and cell wall thickness configurations. As for the core crush index results, and similar to the 300 mm core thickness case, the red-bounded area (the area where the core crush index is greater than 1) increases with the gradual increase in φ . For the cell wall angles $\varphi = 40^\circ$ and $\varphi = 50^\circ$, the core crush index results show that the heliostat panel's core is unlikely to experience material failure for all the honeycomb's cellular configurations. Figure 103 presents the influence of honeycomb cellular configuration on the attained weight reduction for a heliostat panel with the same core thickness ($D = 450$ mm). With all the requirements being satisfied (i.e. optical, material failure and weight reduction), as indicated by the red-bounded area, one can observe from Figure 103 that a heliostat panel with a core configuration of $\varphi = 50^\circ$, $a = 10$ mm and $t = 0.02$ mm provides the most reasonable trade-off between the panel's structural integrity and weight reduction percentage, with a maximum displacement of 12.21 mm, a maximum stress of 83.1 MPa, a core crush index value of 4.13, and an attained weight reduction of approximately 34.45%.

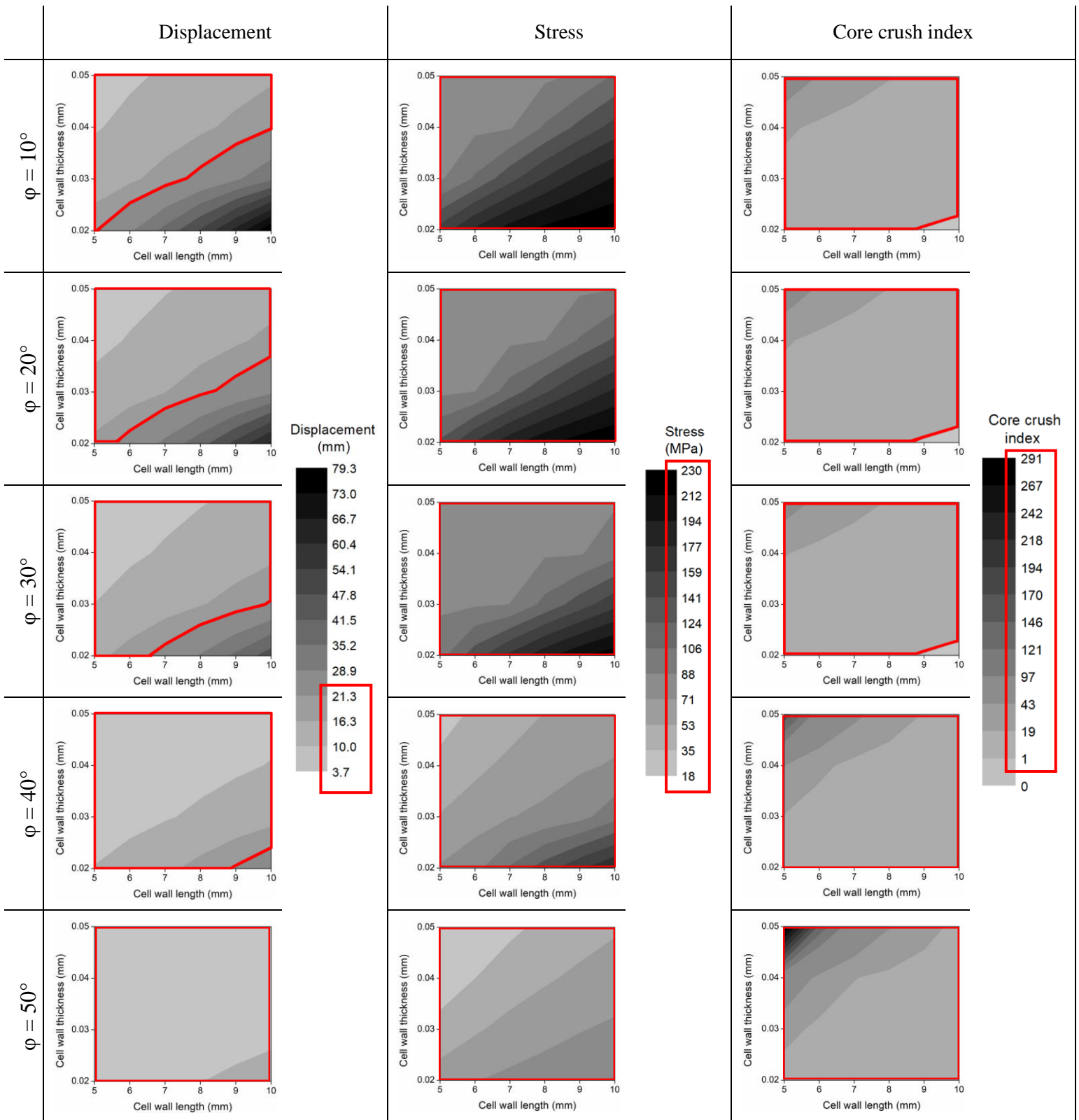


Figure 102: Effect of honeycomb cellular configuration on the heliostat surface's maximum recorded displacement, lower aluminum sheet's maximum recorded stress and core crush index for a core with a thickness of 450 mm

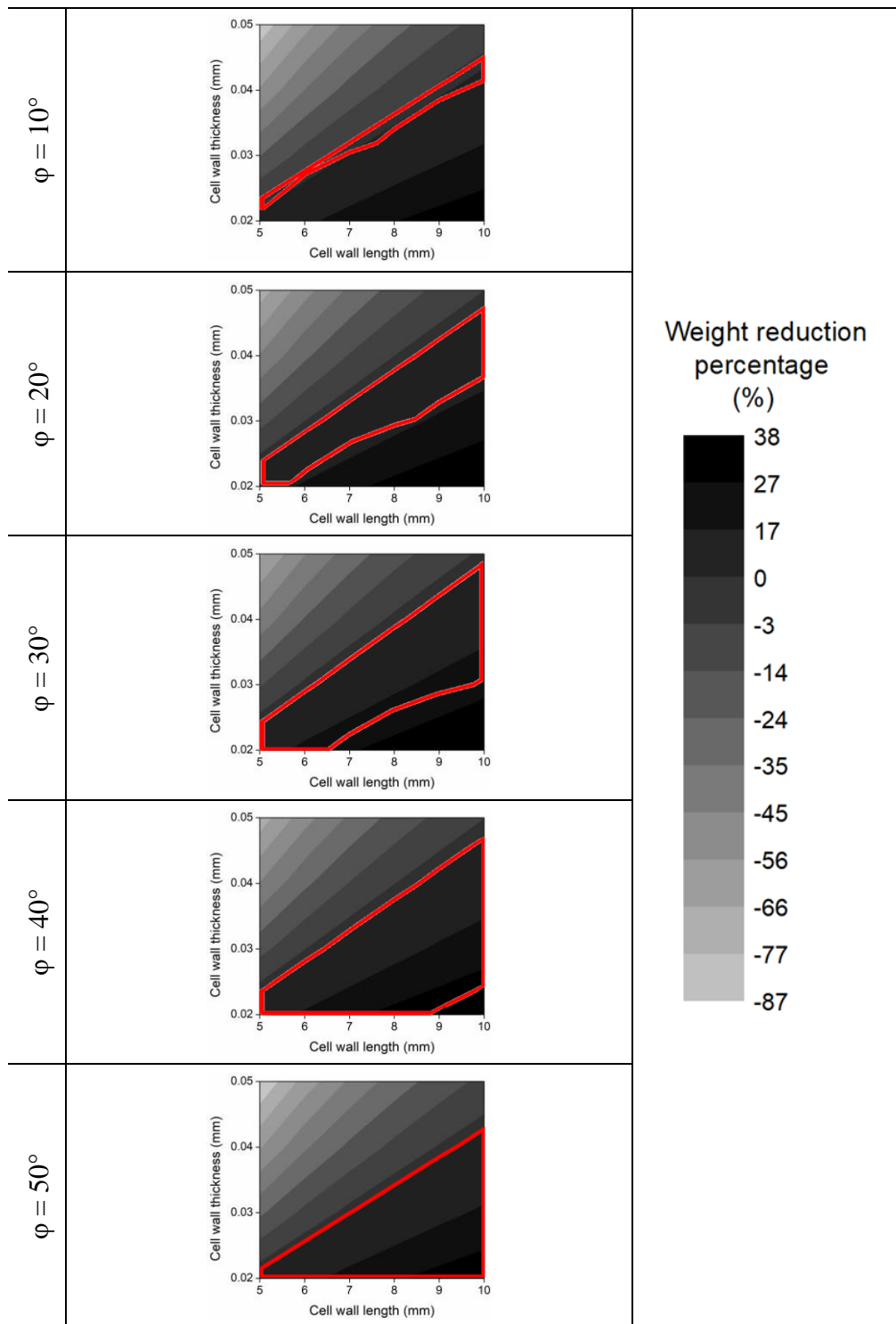


Figure 103: Effect of honeycomb cellular configuration on the mirror support structure's attainable weight reduction for a core with a thickness of 450 mm

From these results, it can be concluded that among the various honeycomb core configurations investigated earlier using the search space scanning method, one stood out distinctively in terms of providing the most desirable trade-off between the heliostat

panel's structural integrity and attained weight saving (~ 44% weight reduction percentage). This configuration is when the heliostat panel consists of a honeycomb core with a thickness of 300 mm, cell wall angle of 50°, cell wall length of 10 mm and cell wall thickness of 0.02 mm.

For the values acquired by the ANN-PSO approach, Figure 104 demonstrates the evolution of the honeycomb core's physical parameters (core thickness (D), cell wall angle (ϕ), cell wall thickness (t), and the cell wall length (a)) and the weight reduction percentage along the iterative procedure.

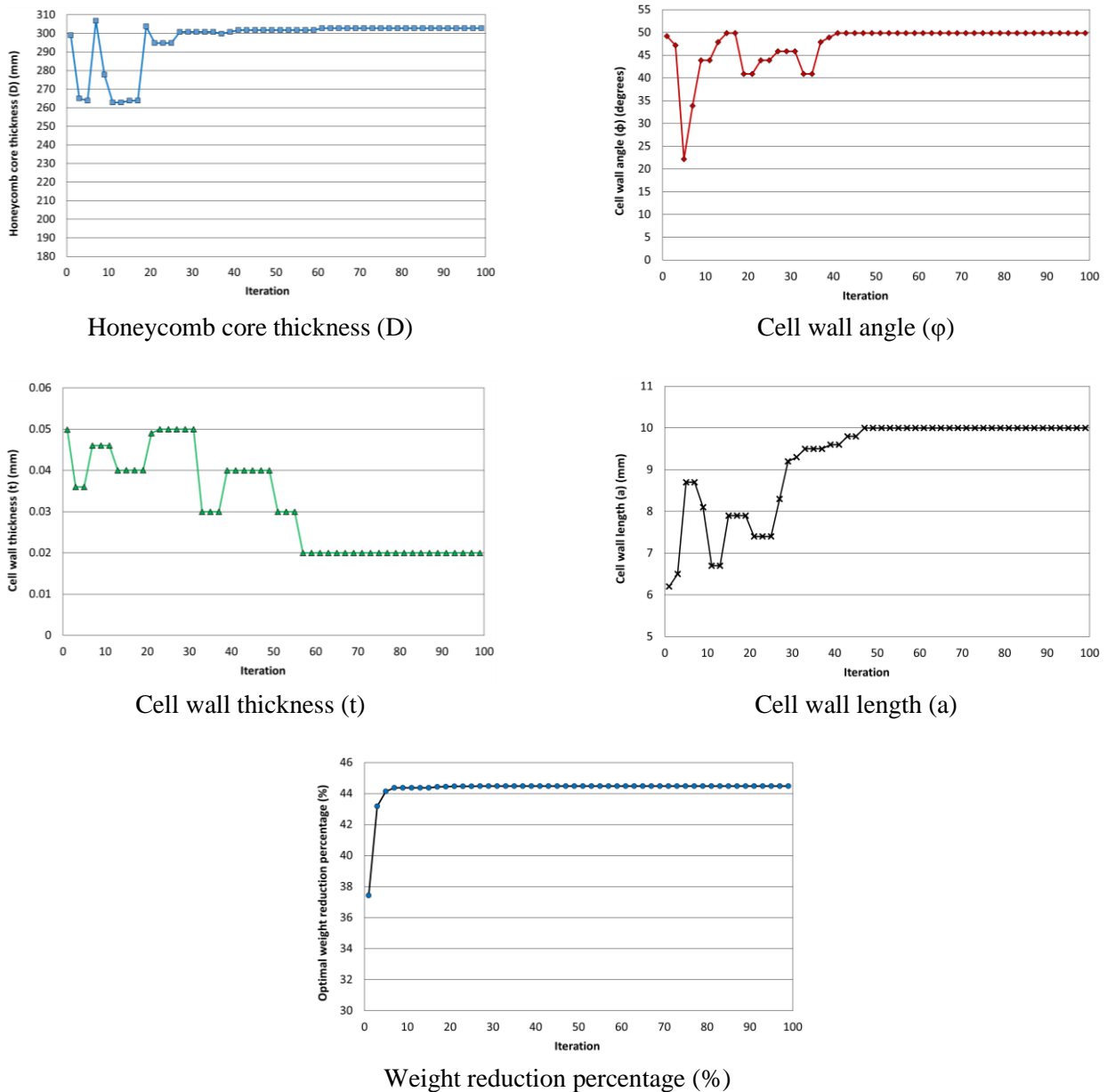


Figure 104: Evolution of the optimum along the iterative procedure (case of configuration 1)

It can be observed that the honeycomb core thickness, the cell wall angle, the cell wall thickness, and the cell wall length converge to constant values after 60 iterations, to finally reach the optimum ($D = 302.91$ mm, $\phi = 50^\circ$, $t = 0.02$ mm, $a = 10$ mm) that corresponds to a maximum weight reduction percentage of 44.47%, a maximum panel displacement of 19.6 mm, a maximum stress at the lower aluminum sheet of 116.33 MPa and a core crush index value of 1.99. From this, it can be noted that the PSO optimization results are in good agreement with the results attained by scanning of all the search space, proving the reliability of the approach and the selected PSO parameters. However, this cannot be retained as a comparison between the two approaches since the computing time consumed by using the scanning method is far from ideal. Besides, a slight change in the structural performance requirements (constraints) can lead to a superficial adjustment in the optimal solution, necessitating the need of going through the hurdles of scanning of all the search space defined by the variables to be optimized again. Also, the scanning approach cannot be used for a higher number of parameters. For instance, if the method in the aforementioned case requires a scan resolution of 1% of the definition interval of each parameter, the number of simulations required to scan all the calculation domains is $100 \times 100 \times 100 \times 100 = 1 \times 10^8$. Whereas, via the PSO approach, the number of simulations performed is: Number of particles \times Number of iterations = $40 \times 100 = 4000$ simulations only. This demonstrates that such limitations can be avoided by utilizing the ANN-PSO approach, making this approach very attractive in terms of computational time and the capability of producing an optimum and a reliable solution.

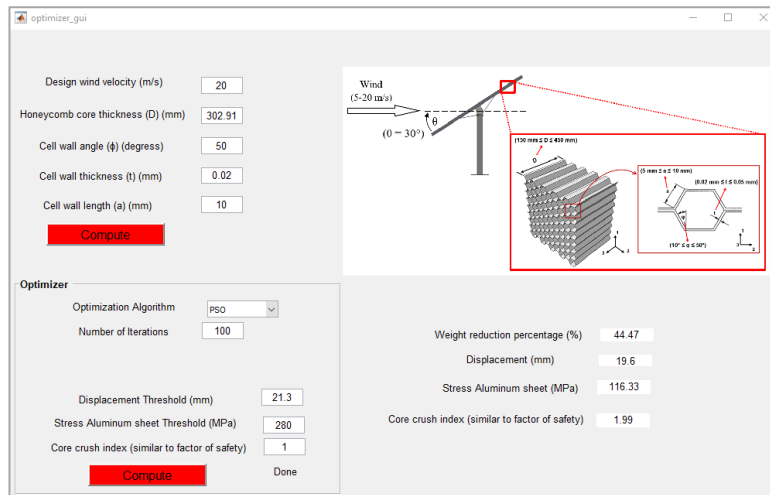
In what follows, the ANN-PSO approach was applied to the remaining two cases illustrated previously in Table 6 and the optimization results are summarized in Table 7. Starting with the second scenario (configuration 2), it was observed that changing the design requirements to attain less panel deflection and stresses at both the lower aluminum sheet and the honeycomb core results in an increase in the honeycomb core

thickness to compensate those changes. However, this increase came with a decrease in the attained weight reduction. As for the third case scenario (configuration 3), one can observe that the reduction in the design wind speed requirement affected the optimal solution. A heliostat panel with a reduced core thickness ($D = 150$ mm) and with the following configurations: $t = 0.02$ mm, $a = 10$ mm, $\varphi = 47.92^\circ$ satisfies all the requirements (i.e. optical and material failure), with an achieved weight saving of approximately 55.23%.

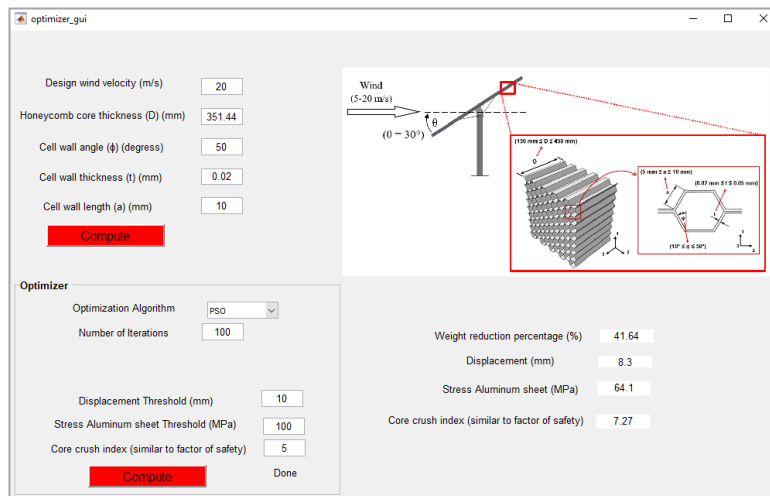
Table 7: PSO optimization results of the three cases

		Configuration 1	Configuration 2	Configuration 3
Design requirements	Chosen site's maximum design wind velocity (m/s)	20 m/s	20 m/s	10 m/s
	Maximum allowable structural deformation (mm)	21.3 mm	10 mm	21.3 mm
	Maximum allowable stress at lower aluminium sheet (MPa)	280 MPa	100 MPa	280 MPa
	Minimum allowable core crush index	1	5	1
Optimized honeycomb core parameters	core thickness (D) (mm)	302.91	351.44	150
	cell wall angle (φ) (degree)	50	50	47.92
	cell wall thickness (t) (mm)	0.02	0.02	0.02
	cell wall length (a) (mm)	10	10	10
Structural performance	Optimized weight reduction percentage (%)	44.47	41.64	55.23
	Panel displacement	19.6	8.3	19.6
	Stress – Aluminum sheet	116.33	64.1	49.31
	Core crush index	1.99	7.35	3.25

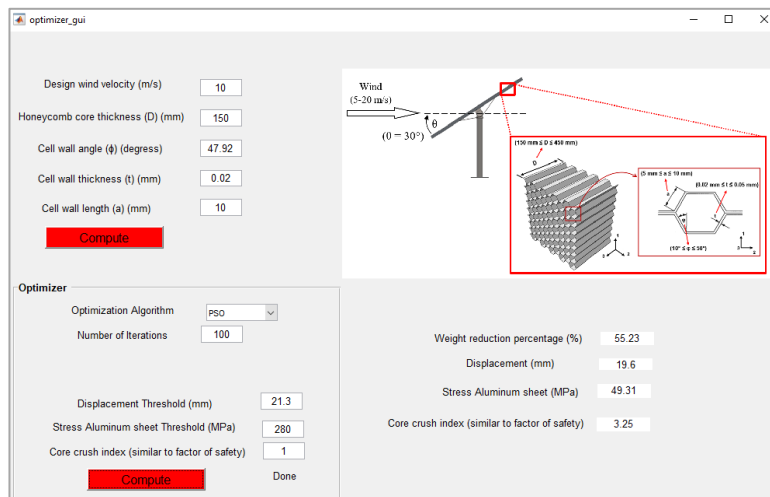
Having established the ANN-PSO model to be both robust and efficient, a graphical user interface (GUI) has been created using the GUI developer (GUIDE) in the MATLAB software (Figure 105). This GUI encompasses the study in the form of a user-friendly and time-efficient tool that allows heliostat designers to predict and optimize the structural performance of honeycomb sandwich composite-based heliostats as per desired requirements.



(a) Configuration 1



(b) Configuration 2



(c) Configuration 3

Figure 105: Screenshots of the established GUI for the three case scenarios

6.3 Chapter Summary

Considering the impact that each of the honeycomb core's physical parameters (core thickness (D), cell wall angle (ϕ), cell wall thickness (t), and the cell wall length (a)) has on the performance of honeycomb cores, identifying the ideal configuration, among a crowd of conceivable combinations, that provides the best trade-off between the heliostat panel's weight reduction and structural integrity is very challenging due to the complex non-linear material behaviour, along with the large number of design variables and performance constraints. Given the recent developments and potential application of particle swarm optimization (PSO) algorithm in diverse disciplines, and particularly in central tower CSP systems, it appears that the application of PSO method for structural optimization of honeycomb sandwich composite-based heliostats has not been studied yet. Former studies mainly focused on optimizing the heliostat field layout and aiming strategy. Moreover, previous studies that focused on the optimization of honeycomb sandwich composites utilizing PSO did not consider all the four honeycomb core's physical parameters in their optimization problems.

This chapter investigated the utilization of particle swarm optimization (PSO) algorithm to establish a novel prediction-optimization model that predicts and optimizes the structural performance of honeycomb sandwich composite-based heliostats. The proposed model couples the artificial neural network (ANN) predictive model, which was established earlier on in Chapter 5, with the PSO algorithm for determining the optimum honeycomb core configuration leading to minimum self-weight of the heliostat's sandwich composite panel while satisfying the structural performance requirements (i.e. optical and material failure).

A rigorous investigation was carried out to optimally choose the suitable swarm size (number of particles) that delivers the best performance for convergence and processing

time. It was found that increasing the size of the swarm greater than 40 particles does not further improve the quality of the optimum obtained. In this sense, a swarm size of 40 particles was selected for the optimization study. The optimization process was carried out for three case scenarios, each with different design requirements, to demonstrate the feasibility of the proposed approach for this system.

The results showed that the proposed integrated ANN-PSO approach, which was later encompassed as a user-friendly graphical user interface (GUI), provides a useful, flexible and time-efficient tool for heliostat designers to predict and optimize the structural performance of honeycomb sandwich composite-based heliostats as per desired requirements.

Chapter 7: Conclusion and Recommendations

Central tower CSP systems offer a promising option for electricity generation. However, the widespread implementation of these systems is limited by cost. Heliostats contribute almost 50% to the plant's cost and are thus the most significant capital element in central tower CSP systems. For both large and small-sized heliostats, the drive elements prove the largest cost element in these systems. This research concentrated on large-sized heliostats, which require high-torque drives due to the heavyweight mirror support structure usually constructed from steel. A promising opportunity arises for reducing the cost of heliostats by reducing the mirror support structure's total weight. Given the fact that honeycomb sandwich composites with their lightweight and high flexural stiffness have been widely employed over the past decades in many applications; this work investigated the suitability of the use of these materials as the structure for heliostat mirror.

At first, an investigation of the airflow characteristics and the aerodynamic forces and moments acting on a heliostat was carried out. A computational fluid dynamics (CFD) analysis was utilized to examine the effect of wind incidence angles on a heliostat operating at varying tilt angles, to better characterise the aerodynamic loading of these structures. The numerical model's accuracy was verified by comparing the computation predictions of the heliostat's drag, lift, base overturning moment and hinge moment coefficients with both experimental measurements and numerical results from previously published work. The study demonstrated that, for a 0° wind incidence angle, the drag and base overturning moment coefficients decrease as the tilt angle alters from vertical to horizontal. The lift and hinge moment coefficients, on the other hand, showed an asymmetric behaviour about the 0° tilt angle with maximum values occurring at tilt angles of 30° and -30° . Increasing wind incidence angle affected the wind loading coefficients by decreasing their magnitudes at different rates. Moreover, a subsequent non-linear

regression analysis delivered a correlation for each of the coefficients based on the heliostat's tilt and wind incidence angle was developed. In summary, it was shown that the aerodynamic coefficients (i.e. lift, drag, hinge moment and base overturning moment coefficients) vary strongly with respect to the wind incidence angle and it is crucial to consider this variation when examining the performance of heliostat systems in order to avoid any structural deformations that can lead to potential mechanical failure.

Taking the wind incidence effect into consideration, numerical fluid-structure interaction (FSI) simulations were performed to examine and understand the structural behaviour characteristics of honeycomb sandwich composites under wind-loaded conditions when utilized as a heliostat mirror support structure. Several loading conditions were assessed for various tilt and wind incidence angles, with the worst case found to be at a tilt angle of 30° under the effect of wind flow at 0° to the heliostat surface with a speed of 20 m/s. The maximum reflective surface displacement and the maximum stress at the heliostat panel's lower aluminum sheet and honeycomb core were found to be within the allowable limits, according to relevant optical and material failure standards. This indicated the proposed heliostat's honeycomb composite structure is expected to operate efficiently at a wind speed of 20 m/s and below.

Given that the mechanical properties of honeycomb core-based sandwich composites are highly dependent upon the honeycomb's geometric configuration (e.g., cell wall angle (ϕ), cell wall length (a), cell wall thickness (t)) and the core thickness (D), the study delivered an understanding on the impact that each of these parameters has on the proposed heliostat structure's aero-structural behaviour characteristics. The study showed that increasing the honeycomb's cell wall length (a) caused a substantial increase in the heliostat's deflection and the stress concentrations at both the lower aluminum sheet and the honeycomb core. Due to an increase in the area fraction of non-load-carrying cell walls, there was a noticeable reduction in the Young's modulus of the honeycomb core,

leading to the heliostat panel being less stiff and resistant to wind loads. The study also showed that an increase in the cell wall thickness (t) and the cell wall angle (ϕ) had a significant effect on both the structural deformation of the heliostat panel and the stress concentrations at both the lower aluminum sheet and the honeycomb core. This resulted in decreasing their levels at different rates, thus improving the heliostat panel's stiffness and resistivity to wind loads. Moreover, it was demonstrated that the deformation of the heliostat panel was strongly affected by the increase in the honeycomb core thickness (D). The observed decrease in the deformation levels was due to an increase in the panel's stiffness that results in an increase in the panel's resistance to deformation. This in turn resulted in lowering the magnitudes of both deflection and stress.

These variations in the heliostat's structural response highlighted the need for a generalized model that can capture the influence of each of the honeycomb core's geometrical parameters on the heliostat structure's performance (i.e. optical, material failure and weight reduction). Having a predictive model that estimates the heliostat's structural performance, under the worst-case operational condition and based on the desired site's maximum recorded wind speed, eradicates the need of going through the hurdles of establishing an FSI model for each of the honeycomb core's geometrical parameters. This, in turn, runs down the implementation time and keeps off unnecessary computations. In this sense, and given that this approach is one of the prominent tools for modelling complex non-linear relationships, particularly in situations where the development of phenomenological or conventional regression models becomes impractical or cumbersome, artificial neural network (ANN) technique was utilized to establish a novel predictive model that predicts the structural performance of the honeycomb sandwich composite-based heliostat based on its honeycomb core's physical parameters.

The results showed that the established ANN model was capable of predicting the structural performance of the honeycomb sandwich composite-based heliostat based on unseen honeycomb core configurations extremely accurately. Moreover, it was illustrated that the established ANN model could deliver insights into the heliostat's structural performance with design parameters outside the training bounds. Given the capability and flexibility of the ANN technique, it demonstrates a unique and novel alternative method to designing and analysing the structural performance of honeycomb sandwich composite-based heliostats. This is of particular significance as accurately predicting the heliostat's structural performance based on its honeycomb core's configuration using classical analytical approaches are at best cumbersome and, at worst, unable to facilitate the predications.

Having understood the impact of the honeycomb's geometric configuration on the aero-structural behaviour characteristics of the sandwich composite-based heliostat, and established a predictive model that accurately predicts the heliostat's structural performance based on its honeycomb core's configuration and considers the desired site's maximum recorded wind speed, a rigorous investigation was carried out on the utilization of particle swarm optimization (PSO) algorithm to establish a novel prediction-optimization model that predicts and optimizes the structural performance of honeycomb sandwich composite-based heliostats. The model couples the ANN predictive model with the PSO algorithm for determining the optimum honeycomb core configuration leading to minimum self-weight of the heliostat's sandwich composite panel while satisfying the structural performance requirements (i.e. optical and material failure). It was shown that the proposed integrated ANN-PSO model, which was encompassed as a user-friendly graphical user interface (GUI), delivers a useful, flexible and time-efficient tool for heliostat designers to predict and optimize the structural performance of honeycomb sandwich composite-based heliostats as per desired requirements.

7.1 Recommendations for future work

Despite proving the potential of honeycomb sandwich composites in developing a stiff lightweight heliostat support structure that can withstand wind loads, some other important factors have been partly discussed in the study and are worthwhile to be investigated further in future work to improve our understanding on the utilization of sandwich composites in the design of heliostats.

In determining the flow behaviour and aerodynamic forces on the heliostat the study was carried out for wind incidence angles between 0° to 90° with an angular resolution of 11.25° and tilt angles between 90° and -90° with an angular resolution of 30° . To better characterise the aerodynamic loading of these structures, a more detailed numerical investigation is crucial, using smaller incremental tilt and wind incidence angles.

Furthermore, the study was carried out for a single isolated heliostat. Although, as previously discussed, investigating the aerodynamic loads acting on a stand-alone heliostat serves as an upper design limit, configurations of a stand-alone system and an array of heliostats are different with an expected difference in the wind flow field around the heliostats and thus the wind loads. Therefore, further analysis can be carried out to investigate the wind loading and wind incidence effect on an array of heliostats and relate those loads to the flow field characteristics around them.

The study investigated the use of aluminum honeycomb-shaped configuration as a core for the proposed heliostat structure. Other cellular configurations (square, circle, diamond, kagome, etc.) with different material combinations can be investigated to identify the properties that have the major influence on the heliostat's rigidity and to obtain the optimum cellular configuration and material combination with high performance while reducing the structural weight.

Moreover, the heliostat structural optimization was carried out using PSO algorithm. A comparative assessment of the ANN-PSO model with other nature-inspired optimization algorithms can be carried out, aiming to further run down the implementation and computational time and to improve the convergence towards the optimal solution.

References

- Abbadi, A., Koutsawa, Y., Carmasol, A., Belouettar, S., Azari, Z., 2009. Experimental and numerical characterization of honeycomb sandwich composite panels. *Simulation Modelling Practice and Theory*, 17(10), 1533-1547.
- Abengoa, 2012. ABENGOA Annual Report 2012. Available from <http://www.abengoa.com/export/sites/abengoa_corp/resources/pdf/en/gobierno_corporativo/informes_anuales/2012/2012_Volume1_AR.pdf>
- Ajdad, H., Baba, Y. F., Al Mers, A., Merroun, O., Bouatem, A., Boutammachte, N., 2019. Particle swarm optimization algorithm for optical-geometric optimization of linear Fresnel solar concentrators. *Renewable Energy*, 130, 992-1001.
- Aldaz, L., Burisch, M., Zaversky, F., Sánchez, M., Villasante, C., Olasolo, D., 2018. Heliostat structural optimization: A study of wind load effects with CFD-FEM methods. *AIP Conference Proceedings*, 2033(1), 210001.
- Al-Qubaisi, E. M., Al-Ameri, M. A., Al-Obaidi, A. A., Rabia, M. F., El-Chaar, L., Lamont, L. A., 2009. Microcontroller based dust cleaning system for a standalone photovoltaic system. *International Conference on Electric Power and Energy Conversion Systems (EPECS)*, 1-6.
- AlRashidi, M. R., El-Hawary, M. E., 2009. A survey of particle swarm optimization applications in electric power systems. *IEEE Transactions on Evolutionary Computation*, 13(4), 913-918.
- ANSYS Inc. 2015. *FLUENT user's guide*, ANSYS, Canonsburg.
- Araújo, H., Leite, M., Ribeiro, A. R., Deus, A. M., Reis, L., Vaz, M. F., 2019. The effect of geometry on the flexural properties of cellular core structures. *Proceedings of the*

Institution of Mechanical Engineers, Part L: Journal of Materials: Design and Applications, 233(3), 338–347.

Assarzadeh, Z., Naghsh-Nilchi, A. R., 2015. Chaotic particle swarm optimization with mutation for classification. *Journal of Medical Signals and Sensors*, 5(1), 12-20.

Aydincak, İ., Kayran, A., 2009. An approach for the evaluation of effective elastic properties of honeycomb cores by finite element analysis of sandwich panels. *Journal of Sandwich Structures & Materials*, 11(5), 385-408.

Ayub, M. Y., Ahmer, Z., Khan, S. R., Shah, M. A., 2011. Mechanical behavior characterization of aluminum based honey comb structure by optimized modeling and numerical simulations. *Journal of Space Technology*, 1(1), 26-33.

Azizi, S., Awad, M. M., Ahmadloo, E., 2016. Prediction of water holdup in vertical and inclined oil–water two-phase flow using artificial neural network. *International Journal of Multiphase Flow*, 80, 181-187.

Balaji, G., Annamalai, K., 2019. Numerical investigation of honeycomb filled crash box for the effect of honeycomb's physical parameters on crashworthiness constants. *International journal of crashworthiness*, 24(2), 184-198.

Balz, M., Göcke, V., Keck, T., von Reeken, F., Weinrebe, G., Wöhrbach, M., 2015. Stellio – Development, construction and testing of a smart heliostat, *SolarPACES 2015 conference*, Cape Town, South Africa

Baughman, D. R., Liu, Y. A., 1995. *Neural networks in bioprocessing and chemical engineering*. Academic press, New York, USA.

Baumgart, C., Halle, T., Weigelt, C., Krüger, L., Aneziris, C. G., 2018. Effect of honeycomb cell geometry on compressive properties: Finite element analysis and experimental verification. *Science and Technology of Materials*, 30(1), 35-42.

Baykasoğlu, A., Baykasoğlu, C. (2016). Multiple objective crashworthiness optimization of circular tubes with functionally graded thickness via artificial neural networks and genetic algorithms. *Proceedings of the Institution of Mechanical Engineers, Part C: Journal of Mechanical Engineering Science*, 231(11), 2005-2016.

Behar, O., Khellaf, A., Mohammedi, K., 2013. A review of studies on central receiver solar thermal power plants. *Renewable and Sustainable Energy Reviews*, 23, 12-39.

Bender, W., 2013. *Final technical progress report: Development of low-cost suspension heliostat*. National Renewable Energy Laboratory (NREL), Golden, Colorado, Report No. NREL/SR-5200-57611.

Bendjebbas, H., Abdellah-ElHadj, A., Abbas, M., 2016. Full-scale, wind tunnel and CFD analysis methods of wind loads on heliostats: A review. *Renewable and Sustainable Energy Reviews*, 54, 452-472.

Birman, V., Kardomateas, G. A., 2018. Review of current trends in research and applications of sandwich structures. *Composites Part B: Engineering*, 142, 221-240.

Björkman, N., 2014. Heliostat design. Master Thesis, Department of Industrial Engineering and Management, KTH Royal Institute of Technology, Stockholm, Sweden.

Boudjemai, A., Zafrane, A., Hocine, R., 2014. Hexagonal honeycomb sandwich plate optimization using gravitational search algorithm. *International Journal of Mechanical, Aerospace, Industrial and Mechatronics Engineering*, 8(6), 1148-1153.

Boukelia, T. E., Arslan, O., Mecibah, M. S., 2016. ANN-based optimization of a parabolic trough solar thermal power plant. *Applied Thermal Engineering*, 107, 1210-1218.

Boukelia, T. E., Arslan, O., Mecibah, M. S., 2017. Potential assessment of a parabolic trough solar thermal power plant considering hourly analysis: ANN-based approach. *Renewable Energy*, 105, 324-333.

- Caccese, V., Ferguson, J. R., Edgecomb, M. A., 2013. Optimal design of honeycomb material used to mitigate head impact. *Composite Structures*, 100, 404-412.
- Castellon, J. (2012). Cellular Ceramics: Reinforced Brick Construction in the Digital Age. *Interceram*, 61(5), 277-282.
- Cermak, J. E., Peterka, J. A., Kareem, A., 1978. *Heliostat field-array wind-tunnel test. Report Number CER78-79JEC-JAPAK2*. McDonnell Douglas Astronautics Company, California, USA.
- Cheng, S., Qiao, P., Chen, F., 2016. Numerical analysis of I-Lam honeycomb sandwich panels for collision protection of reinforced concrete beams. *Journal of Sandwich Structures and Materials*, 1, 1-26.
- Cheng, Z. D., He, Y. L., Du, B. C., Wang, K., Liang, Q., 2015. Geometric optimization on optical performance of parabolic trough solar collector systems using particle swarm optimization algorithm. *Applied Energy*, 148, 282-293.
- Coventry, J., Pye, J., 2014. Heliostat cost reduction - where to now? *Energy Procedia*, 49, 60-70.
- Ding, Y. (1989). Optimum design of honeycomb sandwich constructions with buckling constraints. *Computers & Structures*, 33(6), 1355-1364.
- Diver, R. B., Grossman, J. W., 1998. *Sandwich construction solar structural facets*. Sandia National Laboratories, Albuquerque, New Mexico, Report Number SAND98-2845C.
- Dorian, J. P., Franssen, H. T., Simbeck, D. R., 2006. Global challenges in energy. *Energy Policy*, 34(15), 1984-1991.
- Dorigo, M., Di Caro, G., 1999. Ant colony optimization: A new meta-heuristic. *IEEE Congress on Evolutionary Computation (CEC)*, 2, 1470-1477.

- Ebrahimi, S., Vahdatazad, N., 2015. Multiobjective optimization and sensitivity analysis of honeycomb sandwich cylindrical columns under axial crushing loads. *Thin-Walled Structures*, 88, 90-104.
- Elsheikh, A. H., Elaziz, M. A., 2019. Review on applications of particle swarm optimization in solar energy systems. *International Journal of Environmental Science and Technology*, 16, 1159-1170.
- Emes, M. J., Arjomandi, M., Ghanadi, F., Kelso, R. M., 2017. Effect of turbulence characteristics in the atmospheric surface layer on the peak wind loads on heliostats in stow position. *Solar Energy*, 157, 284-297.
- Esfahlani, S. S., Shirvani, H., Shirvani, A., Nwaubani, S., Mebrahtu, H., Chirwa, C., 2013. Hexagonal honeycomb cell optimisation by way of meta-model techniques. *International Journal of Crashworthiness*, 18(3), 264-275.
- eSolar®, 2014. Commercial readiness of eSolar next generation heliostat, Las Vegas, USA (cited 2016, June 11). Available from <<http://www.esolar.com/wp-content/uploads/2014/08/SolarPaces-Presentation-Commercial-Readiness-of-eSolar-Next-Generation-Heliostat.pdf>>.
- Farges, O., Bézian, J. J., El Hafi, M., 2018. Global optimization of solar power tower systems using a Monte Carlo algorithm: Application to a redesign of the PS10 solar thermal power plant. *Renewable Energy*, 119, 345-353.
- Foster, R., Ghassemi, M., Cota, A., 2010. *Solar energy: Renewable energy and the environment*. Boca Raton: CRC Press.
- Galgalikar, R., 2012. *Design automation and optimization of honeycomb structures for maximum sound transmission loss*, Master's thesis, Clemson University, South Carolina, United States of America.

Galletti, G. G., Vinquist, C., Es-Said, O. S., 2008. Theoretical design and analysis of a honeycomb panel sandwich structure loaded in pure bending. *Engineering Failure Analysis*, 15(5), 555-562.

Ghanadi, F., Yu, J., Emes, M., Arjomandi, M., Kelso, R., 2017a. Numerical investigation of wind loads on an operating heliostat. *AIP Conference Proceedings* 1850 (1), 130003.

Ghanadi, F., Emes, M., Yu, J., Arjomandi, M., Kelso, R., 2017b. Investigation of the atmospheric boundary layer characteristics on gust factor for the calculation of wind load. *AIP Conference Proceedings*, 1850(1), 130002.

Ghritlahre, H. K., Prasad, R. K., 2018a. Exergetic performance prediction of a roughened solar air heater using artificial neural network. *Journal of Mechanical Engineering*, 64(3), 195-206.

Ghritlahre, H. K., Prasad, R. K., 2018b. Investigation of thermal performance of unidirectional flow porous bed solar air heater using MLP, GRNN, and RBF models of ANN technique. *Thermal Science and Engineering Progress*, 6, 226-235.

Gibson, L. J., Ashby, M. F., 1997. Cellular solids: Structure and properties. 2nd Edition, Cambridge University Press, Cambridge.

Goldberg, D. E., 1989. *Genetic algorithms in search, optimization and machine learning*. Addison Wesley Longman Publishing Co., Inc., New York, USA.

Google, 2011. *RE<C: Heliostat Wind Tunnel Experiments* <http://www.google.org/pdfs/google_heliostat_wind_tunnel.pdf>. (accessed 15th August, 2017).

Goswami, D. Y., 2015. *Principles of solar engineering*. (3rd edition), CRC Press, New York, USA.

Haghpanah, B., Papadopoulos, J., Mousanezhad, D., Nayeb-Hashemi, H., Vaziri, A., 2014. Buckling of regular, chiral and hierarchical honeycombs under a general macroscopic stress state. *Proceedings of the Royal Society A*, 470, 20130856.

Hasanien, H. M., 2010. Particle swarm design optimization of transverse flux linear motor for weight reduction and improvement of thrust force. *IEEE Transactions on Industrial Electronics*, 58(9), 4048-4056.

He, Q., Ma, D. W., 2015. Parametric study and multi-objective crashworthiness optimisation of reinforced hexagonal honeycomb under dynamic loadings. *International Journal of Crashworthiness*, 20(5), 495-509.

He, Q., Ma, D., Zhang, Z., Yao, L., 2015. Mean compressive stress constitutive equation and crashworthiness optimization design of three novel honeycombs under axial compression. *International Journal of Mechanical Sciences*, 99, 274-287.

He, Q., Ma, D., Zhang, Z., Yao, L., 2016. Crushing analysis and crashworthiness optimization design of reinforced regular hexagon honeycomb sandwich panel. *Science and Engineering of Composite Materials*, 23(6), 625-639.

Heimbs, S., Vogt, D., Hartnack, R., Schlattmann, J., Maier, M., 2008. Numerical simulation of aircraft interior components under crash loads. *International Journal of Crashworthiness*, 13(5), 511-521.

Hexcel, 1999. HexWeb™ Honeycomb Attributes and Properties: A comprehensive guide to standard Hexcel honeycomb materials, configurations, and mechanical properties.

Hexcel Composite. Available from <http://www.hexcel.com/user_area/uploads/Honeycomb_Attributes_and_Properties.pdf>.

- Hou, S., Li, Q., Long, S., Yang, X., Li, W., 2007. Design optimization of regular hexagonal thin-walled columns with crashworthiness criteria. *Finite elements in Analysis and Design*, 43(6-7), 555-565.
- Hu, L. L., You, F. F., Yu, T. X., 2011. Crushing strength of honeycombs with various cell wall angles. *Materials Research Innovations*, 15(sup1), s155-s157.
- Hu, L., You, F., Yu, T., 2013. Effect of cell-wall angle on the in-plane crushing behaviour of hexagonal honeycombs. *Materials and Design*, 46, 511-523.
- Hutchins, N., Chauhan, K., Marusic, I., Monty, J., Klewicki, J., 2012. Towards Reconciling the Large-Scale Structure of Turbulent Boundary Layers in the Atmosphere and Laboratory, *Boundary-Layer Meteorology* 145(2), 273-306
- Ivañez, I., Fernandez-Cañadas, L. M., Sanchez-Saez, S., 2017. Compressive deformation and energy-absorption capability of aluminium honeycomb core. *Composite Structures*, 174, 123-133.
- Jen, Y. M., Chang, L. Y., 2009. Effect of thickness of face sheet on the bending fatigue strength of aluminum honeycomb sandwich beams. *Engineering Failure Analysis*, 16(4), 1282-1293.
- Jubayer, C. M., Hangan, H., 2014. Numerical simulation of wind effects on a stand-alone ground mounted photovoltaic (PV) system. *Journal of Wind Engineering and Industrial Aerodynamics*, 134, 56-64.
- Kalogirou, S. A., 2001. Artificial neural networks in renewable energy systems applications: A review. *Renewable and Sustainable Energy Reviews*, 5(4), 373-401.
- Kan, C. W., Song, L. J., 2016. An artificial neural network model for prediction of colour properties of knitted fabrics induced by laser engraving. *Neural Processing Letters*, 44, 639-650.

- Karaboga, D., Basturk, B., 2007. A powerful and efficient algorithm for numerical function optimization: Artificial bee colony (ABC) algorithm. *Journal of Global Optimization*, 39, 459-471.
- Kayri, M., 2016. Predictive abilities of Bayesian regularization and Levenberg–Marquardt algorithms in artificial neural networks: A comparative empirical study on social data. *Mathematical and Computational Applications*, 21(2), 20.
- Kennedy, J., Eberhart, R., 1995. Particle swarm optimization. *IEEE International Conference on Neural Networks (ICNN)*, 4, 1942-1948.
- Khalid, A., Latif, M. A., Adnan, M., 2017. An approach to estimate the duration of software project through machine learning techniques. *Gomal University Journal of Research*, 33(1), 47-59.
- Kolb, G., Jones, S., Donnelly, M., Gorman, D., Thomas, R., Davenport, R., Lumia, R., 2007. *Heliostat cost reduction study*. Sandia National Laboratories, Albuquerque, New Mexico, Report number SAND2007-3293.
- Kolb, G. J., Ho, C. H., Mancini, T. R., Gary, J. A., 2011. *Power tower technology roadmap and cost reduction plan*. Sandia National Laboratories, Albuquerque, New Mexico, Report No. SAND2011-2419.
- Kosmadakis, G., Karellas, S., Kakaras, E., 2013. Renewable and conventional electricity generation systems: Technologies and diversity of energy systems. *Renewable Energy Governance*, 23, 9-30.
- Kumar, R., Aggarwal, R. K., Sharma, J. D., 2015. Comparison of regression and artificial neural network models for estimation of global solar radiations. *Renewable and Sustainable Energy Reviews*, 52, 1294-1299.

- Lahiri, S. K., Ghanta, K. C., 2009. Artificial neural network model with the parameter tuning assisted by a differential evolution technique: The study of the hold up of the slurry flow in a pipeline. *Chemical Industry and Chemical Engineering Quarterly*, 15(2), 103-117.
- Lande, P. R., Patil, R. V., 2015. Analysis of bumper beam in frontal collision. *International Journal of Innovative Research in Science*, 4, 2807-2810.
- Lanzi, L., Bisagni, C., Ricci, S., 2004. Neural network systems to reproduce crash behavior of structural components. *Computers & Structures*, 82(1), 93-108.
- Lee, K., Huque, Z., Kommalapati, R., Han, S. E., 2017. Fluid-structure interaction analysis of NREL phase VI wind turbine: Aerodynamic force evaluation and structural analysis using FSI analysis. *Renewable Energy*, 113, 512-531.
- Lewis, N. S., Nocera, D. G., 2006. Powering the planet: Chemical challenges in solar energy utilization. *Proceedings of the National Academy of Sciences*, 103(43), 15729-15735.
- Li, C., Zhai, R., Yang, Y., 2017. Optimization of a heliostat field layout on annual basis using a hybrid algorithm combining particle swarm optimization algorithm and genetic algorithm. *Energies*, 10(11), 1924.
- Li, C., Zhai, R., Liu, H., Yang, Y., Wu, H., 2018. Optimization of a heliostat field layout using hybrid PSO-GA algorithm. *Applied Thermal Engineering*, 128, 33-41.
- Li, H., Chandrashekhara, K., 2015. Particle swarm-based structural optimization of laminated composite hydrokinetic turbine blades. *Engineering Optimization*, 47(9), 1191-1207.
- Li, J., Chen, X., Wang, H., 2009. Comparison of artificial neural networks with response surface models in characterizing the impact damage resistance of sandwich airframe

structures. *2009 Second International Symposium on Computational Intelligence and Design*, 2, 210-215.

Liedke, P., Pfahl, A., Vásquez-Arango, J. F., Hölle, E., 2018. 3rd generation rim drive heliostat with monolithic sandwich panel. *AIP Conference Proceedings*, 2033(1), 040021.

Lin, C. -K., Dai, C. -Y., Wu, J. -C., 2013. Analysis of structural deformation and deformation-induced solar radiation misalignment in a tracking photovoltaic system. *Renewable Energy*, 59, 65-74.

Liu, Z., Lu, J., Zhu, P., 2016. Lightweight design of automotive composite bumper system using modified particle swarm optimizer. *Composite Structures*, 140, 630-643.

Lovegrove, K., Stein, W., 2012. *Concentrating solar power technology: Principles, developments and applications*. Woodhead Publishing Limited, Cambridge, UK.

MacPhee, D., Beyene, A., 2013. Fluid-structure interaction of a morphing symmetrical wind turbine blade subjected to variable load. *International Journal of Energy Research*, 37(1), 69-79.

Mahendran, P., 2016. *Building integrated solar concentrators for façade applications*, Doctoral dissertation, Auckland University of Technology, Auckland, New Zealand.

Malayeri, M. R., Müller-Steinhagen, H., Smith, J. M., 2003. Neural network analysis of void fraction in air/water two-phase flows at elevated temperatures. *Chemical Engineering and Processing: Process Intensification*, 42(8-9), 587-597.

Mammar, M., Djouimaa, S., Hamidat, A., Bahria, S., El Ganaoui, M., 2017. Wind effect on full-scale design of heliostat with torque tube. *Mechanics & Industry*, 18(3), 312.

Mancini, T. R., 2000. *Catalog of solar heliostats*. *SolarPACES Report No. III-1/00*.

- Marais, M. D., Craig, K. J., Meyer, J. P., 2015. Computational flow optimization of heliostat aspect ratio for wind direction and elevation angle. *Energy Procedia*, 69, 148-157.
- Marzbanrad, J., Ebrahimi, M. R., 2011. Multi-objective optimization of aluminum hollow tubes for vehicle crash energy absorption using a genetic algorithm and neural networks. *Thin-Walled Structures*, 49(12), 1605-1615.
- Mellit, A., Kalogirou, S. A., Hontoria, L., Shaari, S., 2009. Artificial intelligence techniques for sizing photovoltaic systems: A review. *Renewable and Sustainable Energy Reviews*, 13(2), 406-419.
- Mirzaei, M., Shakeri, M., Sadighi, M., Akbarshahi, H., 2011. Crashworthiness design for cylindrical tube using neural network and genetic algorithm. *Procedia Engineering*, 14, 3346-3353.
- Mohd-Safar, N. Z., Ndzi, D., Sanders, D., Noor, H. M., Kamarudin, L. M., 2016. Integration of fuzzy c-means and artificial neural network for short-term localized rainfall forecasting in tropical climate. *Proceedings of SAI Intelligent Systems Conference*, 499-516.
- Moukhtar, I., A. Elbaset, A., Z. El Dein, A., Qudaih, Y., Blagin, E., Uglanov, D., Mitani, Y., 2018. Electric power regulation and modeling of a central tower receiver power plant based on artificial neural network technique. *Journal of Renewable and Sustainable Energy*, 10(4), 1-20.
- Nasir, A. N. K., Tokhi, M. O., 2014. A novel hybrid bacteria-chemotaxis spiral-dynamic algorithm with application to modelling of flexible systems. *Engineering Applications of Artificial Intelligence*, 33, 31-46.

- Nast, E., 1997. On Honeycomb-Type Core Moduli. *Presented at the Collection of Technical Papers-AIAA/ASME/ASCE/AHS/ ASC Structures, Structural Dynamics and Materials Conference, 2*, 1035-1044.
- Nayak, S. K., 2012. *Design optimization of honeycomb sandwich panels for blast load mitigation*, Doctoral dissertation, The Pennsylvania State University, United States. OECD Publication, France.
- Paik, J. K., Thayamballi, A. K., Kim, G. S., 1999. The strength characteristics of aluminum honeycomb sandwich panels. *Thin-walled structures*, 35(3), 205-231.
- Pandey, D. S., Das, S., Pan, I., Leahy, J. J., Kwapinski, W., 2016. Artificial neural network based modelling approach for municipal solid waste gasification in a fluidized bed reactor. *Waste Management*, 58, 202-213.
- Passino, K. M., 2002. Biomimicry of bacterial foraging for distributed optimization and control. *IEEE Control Systems Magazine*, 22(3), 52-67.
- Peterka, J. A., Derickson, R. G., 1992. *Wind load design methods for ground-based heliostats and parabolic dish collectors. Report number SAND92-7009*. Sandia National Laboratories, Albuquerque, NM (United States).
- Peterka, J. A., Hosoya, N., Bienkiewicz, B., Cermak, J. E., 1986. *Wind load reduction for heliostats. Report SERI/STR-253-2859*. Solar Energy Research Institute, Golden, Colorado, USA.
- Pfahl, A., 2014. Survey of heliostat concepts for cost reduction. *Journal of Solar Energy Engineering*, 136(1), 014501.
- Pfahl, A., Uhlemann, H., 2011. Wind loads on heliostats and photovoltaic trackers at various Reynolds numbers. *Journal of Wind Engineering and Industrial Aerodynamics*, 99(9), 964-968.

- Pfahl, A., Buselmeier, M., Zschke, M., 2011. Wind loads on heliostats and photovoltaic trackers of various aspect ratios. *Solar Energy*, 85(9), 2185-2201.
- Pfahl, A., Coventry, J., Röger, M., Wolfertstetter, F., Vásquez-Arango, J. F., Gross, F., Arjomandi, M., Schwarzbözl, P., Geiger, M., Liedke, P., 2017. Progress in heliostat development. *Solar Energy*, 152, 3-37.
- Philibert, C., 2011. *Solar energy perspectives*. International Energy Agency (IEA),
- Philibert, C., 2014. *Technology roadmap: Solar thermal electricity*. International Energy Agency (IEA), OECD Publication, France.
- Piroozmand, P., Boroushaki, M., 2016. A computational method for optimal design of the multi-tower heliostat field considering heliostats interactions. *Energy*, 106, 240-252.
- Plumb, A. P., Rowe, R. C., York, P., Brown, M., 2005. Optimisation of the predictive ability of artificial neural network (ANN) models: A comparison of three ANN programs and four classes of training algorithm. *European Journal of Pharmaceutical Sciences*, 25(4-5), 395-405.
- Qi, C., Yang, S., Dong, F., 2012. Crushing analysis and multiobjective crashworthiness optimization of tapered square tubes under oblique impact loading. *Thin-Walled Structures*, 59, 103-119.
- Qi, C., Yang, S., Yang, L. J., Wei, Z. Y., Lu, Z. H., 2013. Blast resistance and multi-objective optimization of aluminum foam-cored sandwich panels. *Composite Structures*, 105, 45-57.
- Qi, C., Yang, S., Yang, L. J., Han, S. H., Lu, Z. H., 2014. Dynamic response and optimal design of curved metallic sandwich panels under blast loading. *The Scientific World Journal*, 1-14.

- Qiao, P., Fan, W., Davalos, J. F., Zou, G., 2008. Optimization of transverse shear moduli for composite honeycomb cores. *Composite Structures*, 85(3), 265-274.
- Rafiee, R., Tahani, M., Moradi, M., 2016. Simulation of aeroelastic behavior in a composite wind turbine blade. *Journal of Wind Engineering and Industrial Aerodynamics*, 151, 60-69.
- Razzak, S. A., Rahman, S. M., Hossain, M. M., Zhu, J., 2012. Investigation of artificial neural network methodology for modeling of a liquid–solid circulating fluidized bed riser. *Powder Technology*, 229, 71-77.
- Ricklin, P., Slack, M., Rogers, D., Huibregtse, R., 2014. Commercial readiness of eSolar next generation heliostat. *Energy Procedia*, 49, 201-208.
- Rodriguez-Ramirez, J. D. D., Castanié, B., Bouvet, C., 2017. Analysis of nonlinear behavior on honeycomb cores. *21st International Conference on Composite Materials (ICCM 21)*, hal-02177061.
- Rodriguez-Ramirez, J. D. D., Castanie, B., Bouvet, C., 2018. Experimental and numerical analysis of the shear nonlinear behaviour of Nomex honeycomb core: Application to insert sizing. *Composite Structures*, 193, 121-139.
- Rumsey-Hill, N., Pottas, J., Coventry, J. (2019). Design of efficient stamped mirror facets using topography optimisation. *AIP Conference Proceedings*, 2126(1), 030048.
- Sadowski, T., Bęc, J., 2011. Effective properties for sandwich plates with aluminium foil honeycomb core and polymer foam filling – Static and dynamic response. *Computational Materials Science*, 50(4), 1269-1275.
- Schwingshackl, C. W., Aglietti, G. S., Cunningham, P. R., 2006. Determination of honeycomb material properties: Existing theories and an alternative dynamic approach. *Journal of Aerospace Engineering*, 19(3), 177-183.

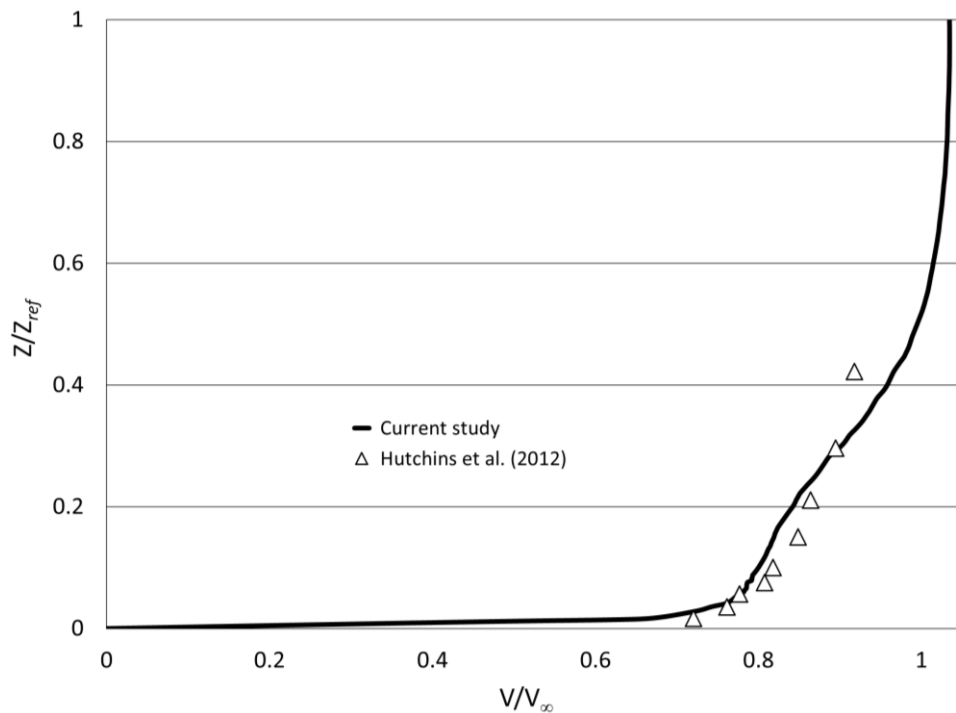
- Sharma, N., Siddhartha, V., 2012. Stochastic techniques used for optimization in solar systems: A review. *Renewable and Sustainable Energy Reviews*, 16(3), 1399-1411.
- Simiu, E., Scanlan, R. H., 1996. *Wind Effects on Structures: Fundamentals and Applications to Design*, third ed. John Wiley & Sons Wiley, New York.
- Sorohan, Ş., Constantinescu, D. M., Sandu, M., Sandu, A. G., 2016. Assessment of effective elastic properties of honeycomb cores by modal finite element analyses. *Proceedings of the European Automotive Congress EAEC-ESFA 2015*, 443-454.
- Staal, R. A., Mallinson, G. D., Jayaraman, K., Horrigan, D. P. W., 2009. Predicting failure loads of impact damaged honeycomb sandwich panels. *Journal of Sandwich Structures & Materials*, 11(2-3), 213-244.
- Strachan, J. W., Houser, R. M., 1993. Testing and Evaluation of Large-Area Heliostats for Solar Thermal Applications. Albuquerque (NM), SANDIA Labs: SAND92-1381. Available from <http://energy.sandia.gov/wp-content/gallery/uploads/SAND92_1381_heliostat_testing.pdf>.
- Sun, G., Li, G., Stone, M., & Li, Q. (2010). A two-stage multi-fidelity optimization procedure for honeycomb-type cellular materials. *Computational Materials Science*, 49(3), 500-511.
- Tao, W., Liu, Z., Zhu, P., Zhu, C., Chen, W., 2017. Multi-scale design of three dimensional woven composite automobile fender using modified particle swarm optimization algorithm. *Composite Structures*, 181, 73-83.
- Téllez, F., Burisch, M., Villasente, C., Sánchez, M., Sansom, C., Kirby, P., Turner, P., Caliot, C., Ferriere, A., Bonanos, C. A., Papanicolas, C., Montenon, A., Monterreal, R., Fernández, J., 2014. *State of the art in heliostats and definition of specifications: Survey for a low cost heliostat development. STAGE-STE Project Report.*

- Tiba, C., Reis, R., Costa, J., Azevedo, V., Abreu, J., Alves, M., Guimarães, D., Porto, M., 2014. Siting study of solar thermoelectric plants in the state of Minas Gerais. *Journal of Geographic Information System*, 6, 423-439.
- Totten, G. E., Tiryakioglu, M., Kessler, O., 2018. Encyclopedia of Aluminum and Its Alloys. 1st Edition, CRC Press.
- Upreti, S., Singh, V. K., Kamal, S. K., Jain, A., Dixit, A., 2019. Modelling and analysis of honeycomb sandwich structure using finite element method. *Materials Today: Proceedings*.
- Uzair, M., 2018. *Wind induced heat losses from solar dish-receiver systems*, Doctoral dissertation, Auckland University of Technology, Auckland, New Zealand.
- Uzair, M., Anderson, T. N., Nates, R. J., 2017. The impact of the parabolic dish concentrator on the wind induced heat loss from its receiver. *Solar Energy*, 151, 95-101.
- Vast Solar, 2017. <<http://www.vastsolar.com/>> (accessed April 2017).
- Vinson, J. R., 1986. Optimum design of composite honeycomb sandwich panels subjected to uniaxial compression. *AIAA Journal*, 24(10), 1690-1696.
- von Reeken, F., Weinrebe, G., Balz, M., 2016. Special stiffness requirements of heliostats for regions with high operational wind speeds. *SolarPACES 2016 conference*, Abu Dhabi, UAE.
- Wang, L., Quant, R., Kolios, A., 2016. Fluid structure interaction modelling of horizontal-axis wind turbine blades based on CFD and FEA. *Journal of Wind Engineering and Industrial Aerodynamics*, 158, 11-25.
- Wong, Y. J., Arumugasamy, S. K., Mustapha, K. B., 2019. Development of a computational predictive model for the nonlinear in-plane compressive response of sandwich panels with bio-foam. *Composite Structures*, 212, 423-433.

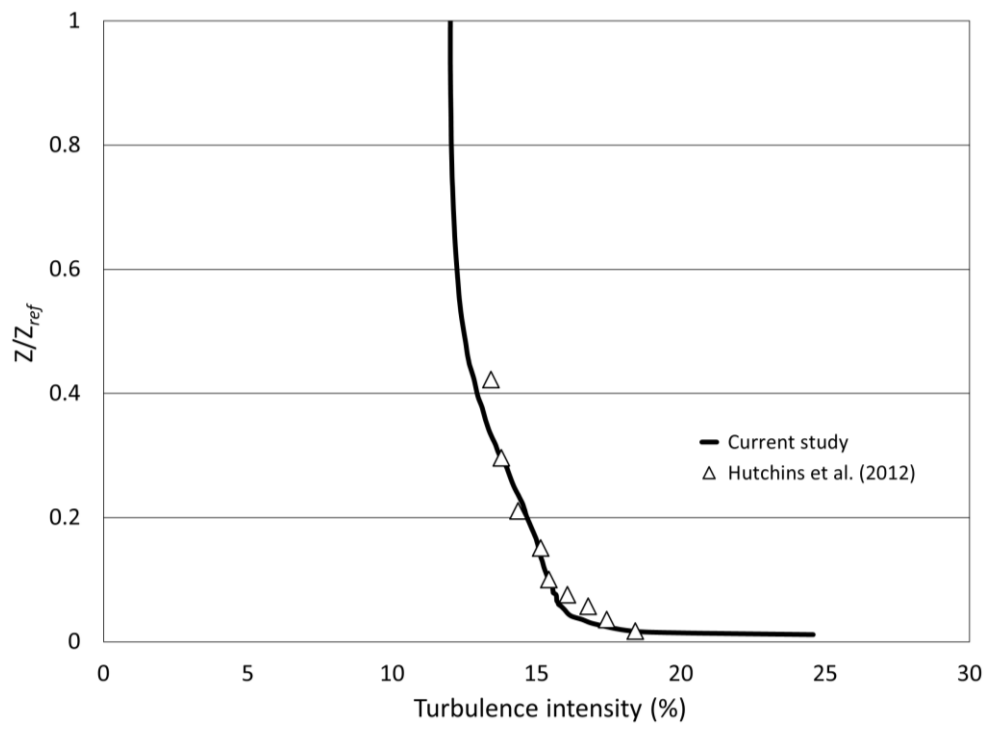
- Wu, Z., Gong, B., Wang, Z., Li, Z. Zang, C., 2010. An experimental and numerical study of the gap effect on wind load on heliostat. *Renewable Energy*, 35(4), 797-806.
- Xie, S., Li, H., Yang, C., Yao, S., 2018. Crashworthiness optimisation of a composite energy-absorbing structure for subway vehicles based on hybrid particle swarm optimisation. *Structural and Multidisciplinary Optimization*, 58, 2291-2308.
- Yamashita, M., Gotoh, M., 2005. Impact behavior of honeycomb structures with various cell specifications—numerical simulation and experiment. *International Journal of Impact Engineering*, 32, 618-630.
- Yin, H., Wen, G., Gan, N., 2011. Crashworthiness design for honeycomb structures under axial dynamic loading. *International Journal of Computational Methods*, 8(4), 863-877.
- Zeghoudi, A., Chermitti, A., 2014. Estimation of the solar power tower heliostat position using neural network. *International Journal of Computer Applications*, 94(4), 41-46.
- Zenkert, D., 1997. The handbook of sandwich construction. EMAS Ltd., West Midlands.
- Zhang, H. L., Baeyens, J., Degève, J., Cacères, G., 2013. Concentrated solar power plants: Review and design methodology. *Renewable and Sustainable Energy Reviews*, 22, 466-481.
- Zhang, Z., Liu, S., Tang, Z., 2011. Comparisons of honeycomb sandwich and foam-filled cylindrical columns under axial crushing loads. *Thin-Walled Structures*, 49(9), 1071-1079.
- Zhu, G., Wendelin, T., Wagner, M. J., Kutscher, C., 2014. History, current state, and future of linear Fresnel concentrating solar collectors. *Solar Energy*, 103, 639-652.

Appendix A: Wind profile development

As noted, the computational domain was extended upstream from the heliostat in order to allow the boundary layer to develop. To assure the inlet wind profile is in fact developed by the time it reaches the heliostat, Figure 106 demonstrates the incident velocity and turbulence intensity profiles compared with field experiment velocity data collected by Hutchins et al. (2012) in a real atmospheric boundary layer. Velocity and vertical distance are normalized by the free stream velocity (V_∞) and the height of the domain (Z_{ref}), respectively. The obtained velocity and turbulence intensity profiles, demonstrate that the upstream extension of the computational domain was sufficient to allow the boundary layer to develop, with a turbulence intensity (I_u) of 14.6% measured at 10 meters above ground. Furthermore, this value falls within the range of turbulence intensities usually measured near the ground for an open field environment; between 11% for flat desert terrain and 17% for open country with isolated trees and buildings (Peterka and Derickson, 1992; Simiu and Scanlan, 1996).



(a) Velocity profile



(b) Turbulence intensity profile

Figure 106: Incident velocity and turbulence intensity profiles

Appendix B: CFD mesh sensitivity analysis

Achieving good results from the CFD simulation requires investigating the effect of grid sizes on the numerical results. In this regard, mesh sensitivity test was performed to determine how the mesh quality impacts the numerical output. Different grid sizes were tested to check their effects on the drag force coefficient experienced by the heliostat structure.

Figure 107 demonstrates the variation of drag coefficient experienced by the heliostat at various grid sizes. Fine grid elements were employed near the heliostat and in its wake region and the regions away from the heliostat were meshed with larger grid sizes (Figure 108). After carrying out mesh independence tests with different grid sizes, high-quality mesh was selected with grid size of approximately 13 million elements being used to perform a steady state simulation of the flow around the heliostat.

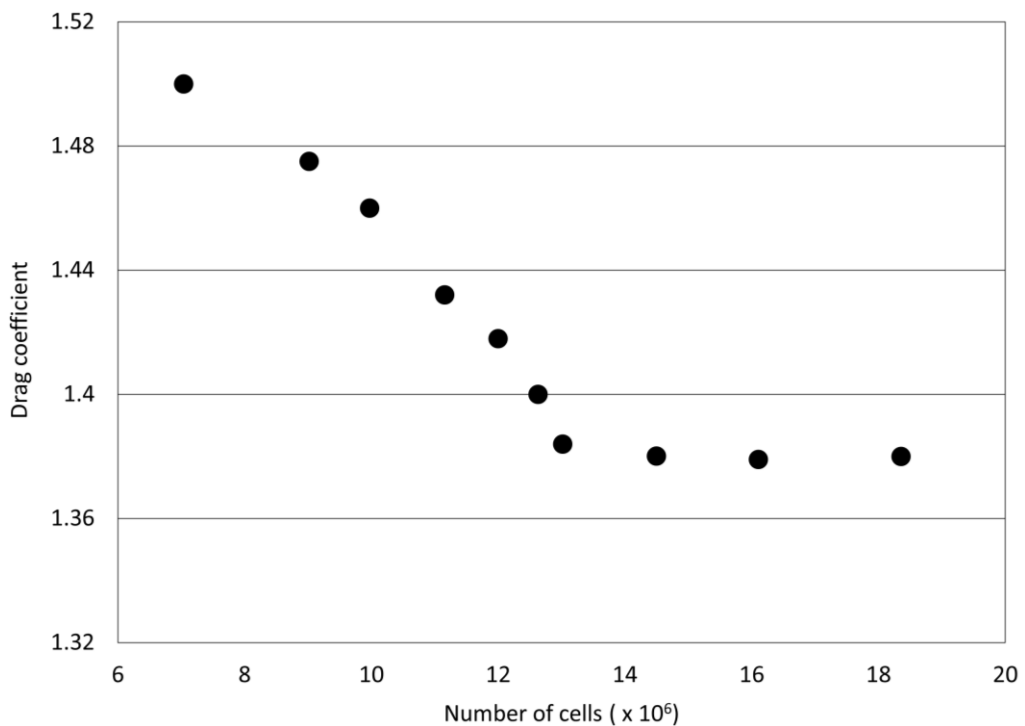


Figure 107: Grid independency test

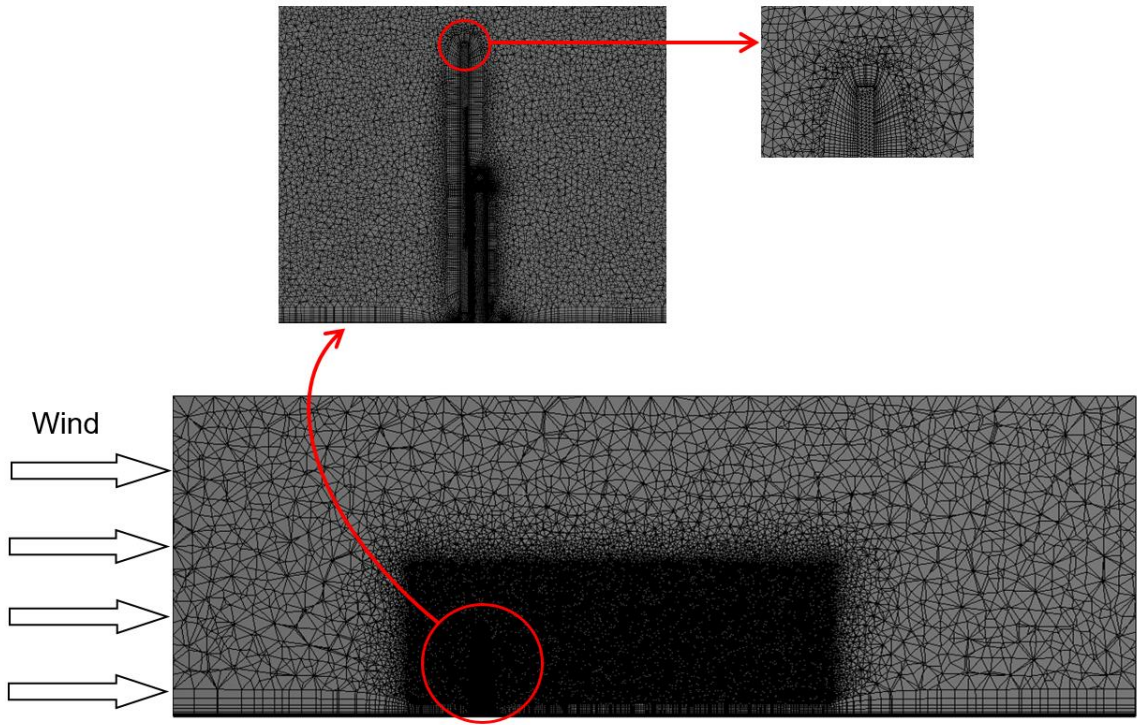


Figure 108: Mesh around the heliostat

Appendix C: Size selection analysis of the heliostat supporting steel attachments

Determining a proper size for the sandwich panel's supporting steel attachments that minimizes the overall weight of the mirror support structure (in comparison to the support structure of the existing 148 m² steel-based ATS heliostat that weighs around 1550 kg (Kolb et al., 2007)) while maintaining its structural integrity requires investigating the effect of attachment sizes on the heliostat panel's structural behaviour. Different attachment sizes were tested (Figure 109) to check their effects on the heliostat surface's maximum recorded displacement when the structure is tilted at an angle of 30° and experiencing wind at 0° incidence angle with a velocity of 20 m/s.

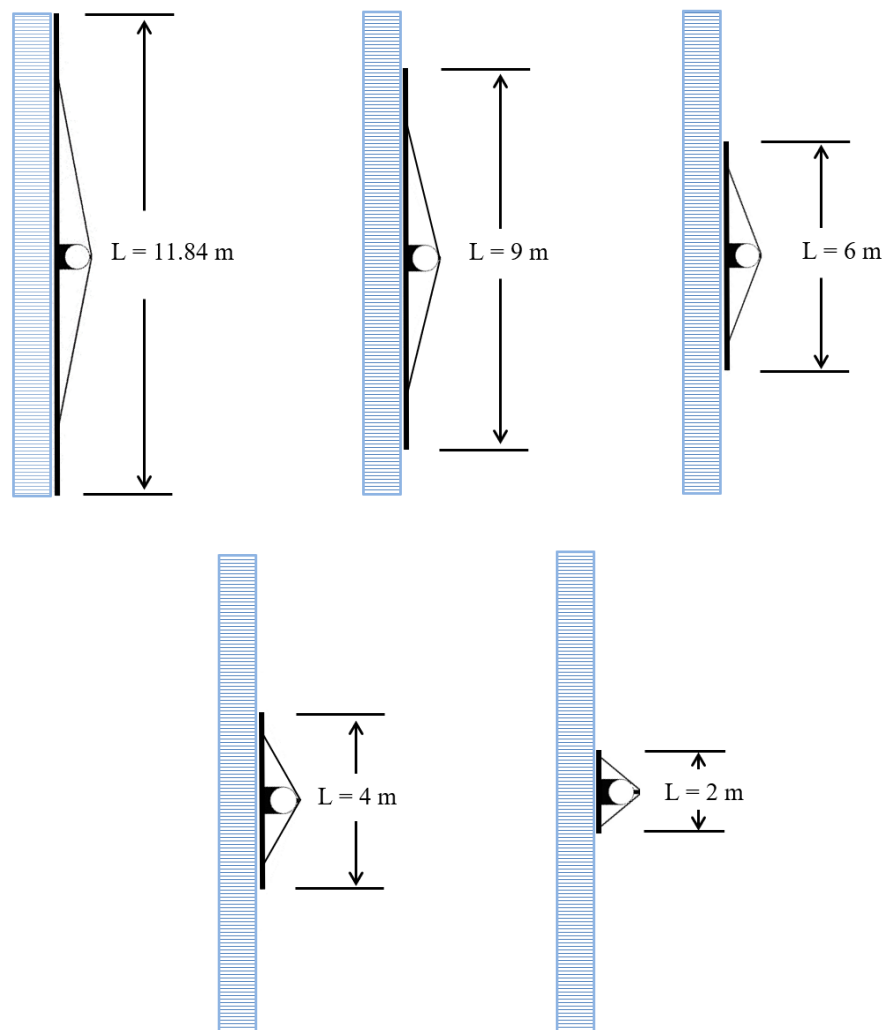


Figure 109: Attachment sizes investigated in the study

Figure 110 demonstrates the displacement and weight reduction percentage variations at various attachment sizes. As one may expect, increasing the size of the attachment reduces the recorded maximum displacement values significantly. However, this improvement comes with a major decrease in the attained weight reduction. For reliable operation of a heliostat, the structure should be able to keep its deformation below 21.3 mm (as derived from Björkman’s (2014) approach of calculating the maximum allowable displacement) such that the acceptance angle loss of its reflective surface resides within tolerable limits. From the results, it is clear that the most desirable trade-off between the heliostat panel’s structural deformation and attained weight reduction is when the panel is supported by attachments with a length of around 6 m, hence the 6 m attachment size was selected for further FSI analysis.

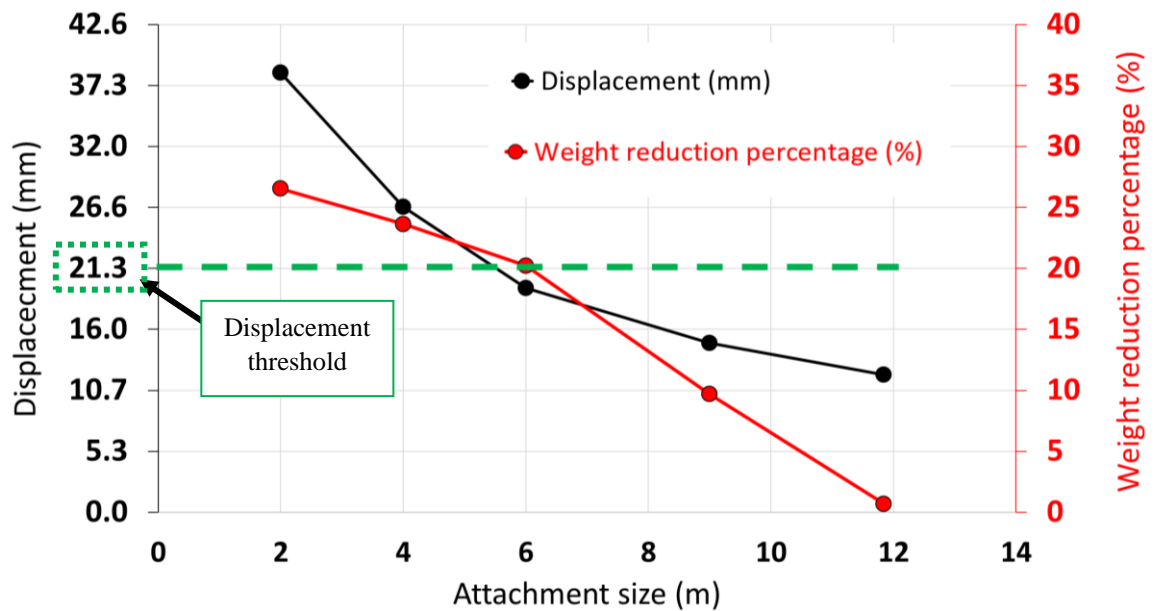


Figure 110: Displacement and weight reduction percentage variations with attachment size

Appendix D: FEA mesh sensitivity analysis

Reducing any numerical instabilities when importing the aerodynamic loads from the CFD solver to the FEA model of the sandwich composite-based heliostat requires investigating the effect of grid sizes on the FEA numerical results. In this sense, and similar to the CFD model, mesh sensitivity test was carried out to determine how the mesh quality affect the numerical output of the FEA model, and to ensure that the stress field around the steel attachment points is not singular. Different grid sizes were tested to check their effects on the heliostat's recorded stress at a specified point shown in Figure 111 when the structure is tilted at an angle of 30° and experiencing wind at 0° incidence angle with a velocity of 20 m/s.

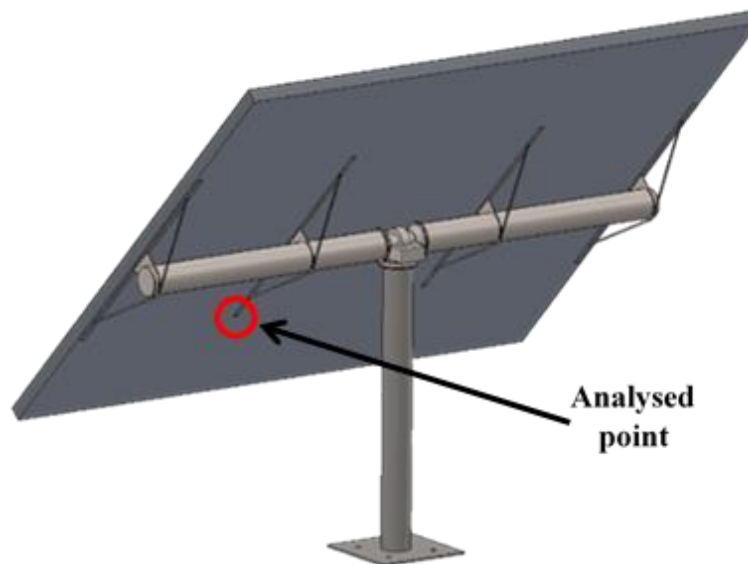
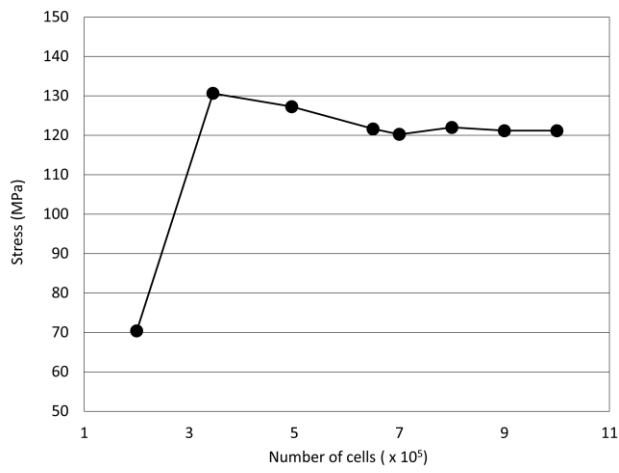
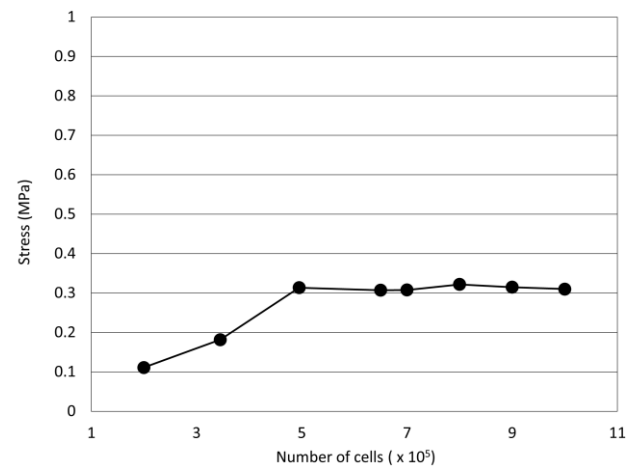


Figure 111: Point analysed in the grid independency test

Figure 112 demonstrates the stress variations at various grid sizes. It can be seen that there is no significant change in the results with the increase in grid size after 650,000 elements, hence the 650,000 elements model (Figure 113) was selected for further FEA analysis.



(a) Lower aluminum sheet



(b) Honeycomb core

Figure 112: FEA grid independency test

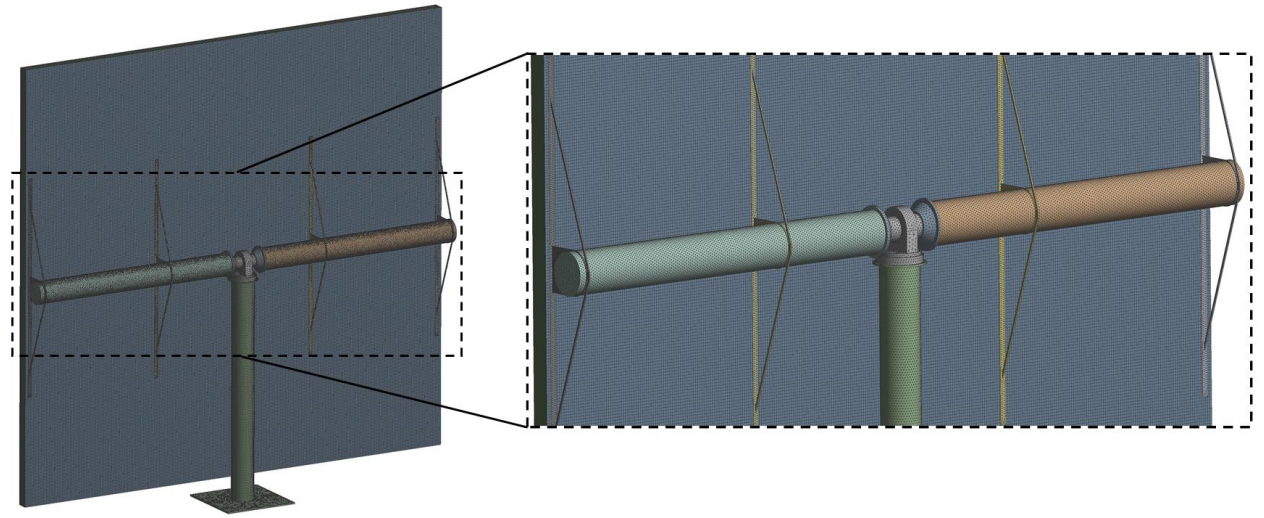


Figure 113: FEA model of the heliostat structure

Appendix E: Equations used for calculating the mechanical properties of the sandwich composite's honeycomb core

Nomenclature			
t	Cell wall thickness	E_3	Young's modulus of the honeycomb core in direction 3
a	Cell wall length	ν_{12}	Poisson's ratio of the honeycomb core in plane 1–2
φ	Cell wall angle	ν_{23}	Poisson's ratio of the honeycomb core in plane 2–3
E	Young's modulus of the honeycomb's solid material	ν_{13}	Poisson's ratio of the honeycomb core in plane 1–3
v	Poisson's ratio of the honeycomb's solid material	G_{12}	Shear modulus of the honeycomb core in plane 1–2
G	Shear modulus of the honeycomb's solid material	G_{23}	Shear modulus of the honeycomb core in plane 2–3
ρ	Density of the honeycomb's constituent material	G_{13}	Shear modulus of the honeycomb core in plane 1–3
E_1	Young's modulus of the honeycomb core in direction 1	$\rho_{\text{honeycomb}}$	Density of the honeycomb core
E_2	Young's modulus of the honeycomb core in direction 2		

$$E_1 = \frac{t^3(1+\sin \varphi)}{12 a^3 \cos^3 \varphi \left[\frac{\cos \varphi}{3} - \frac{1+\cos \varphi}{8} \right] (1-\nu^2)} E \quad (9)$$

$$E_2 = \frac{t^3 \cos \varphi}{(1+\sin \varphi) a^3 \sin^2 \varphi (1-\nu^2)} E \quad (10)$$

$$E_3 = \frac{2 t}{a \cos \varphi (1+\sin \varphi)} E \quad (11)$$

$$G_{12} = \frac{t^3(1+\sin \varphi)}{a^3 (1-\nu^2) \cos \varphi (6.25-6 \sin \varphi)} E \quad (12)$$

$$G_{23} = \frac{10 t}{9 a \cos^3 \varphi (1+\sin \varphi)} G \quad (13)$$

$$G_{13} = \frac{2 t}{a \cos \varphi (1+\sin \varphi)} G \quad (14)$$

$$\nu_{12} = \frac{\cos^2 \varphi}{\sin \varphi (1+\sin \varphi)} \quad (15)$$

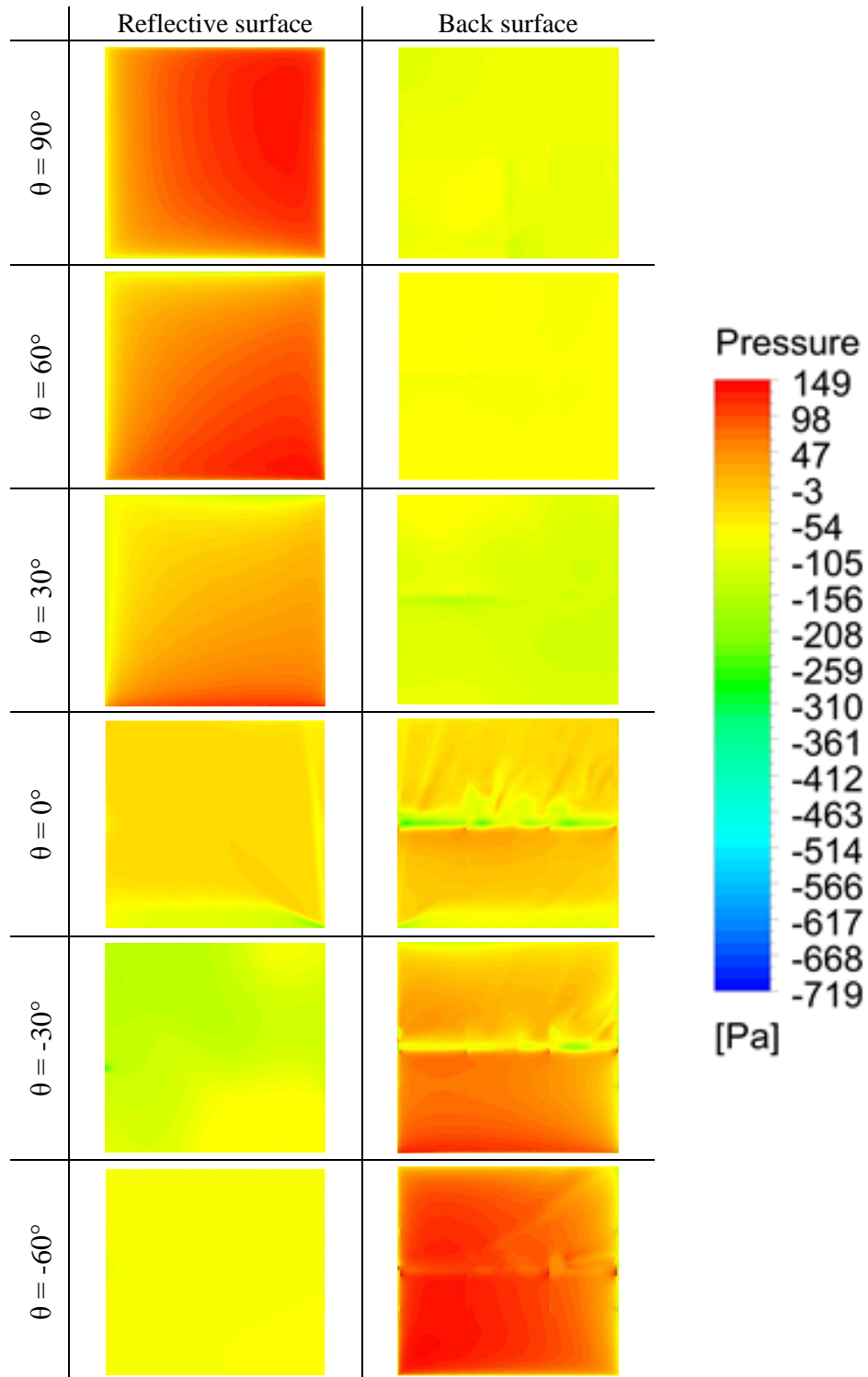
$$\nu_{23} = \frac{t^2 \cos^2 \varphi}{2 a^2 \sin^2 \varphi (1-\nu^2)} \nu \quad (16)$$

$$V_{13} = \frac{t^2 (1+\sin \varphi)^2}{24 a^2 \cos \varphi \left[\frac{\cos \varphi - 1 + \cos \varphi}{3} \frac{1 + \cos \varphi}{8} \right]} * \frac{v}{(1-v^2)} \quad (17)$$

$$\rho_{\text{honeycomb}} = \frac{3 t}{2 a \cos \varphi (1 + \sin \varphi)} \rho \quad (18)$$

Appendix F: FSI results for wind flow at $\beta = 22.5^\circ$ and $\beta = 67.5^\circ$ to the heliostat surface

- **Pressure distribution**



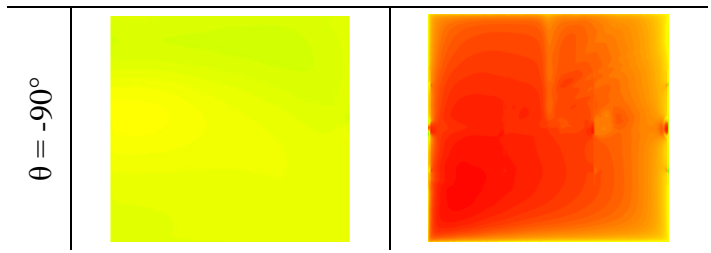
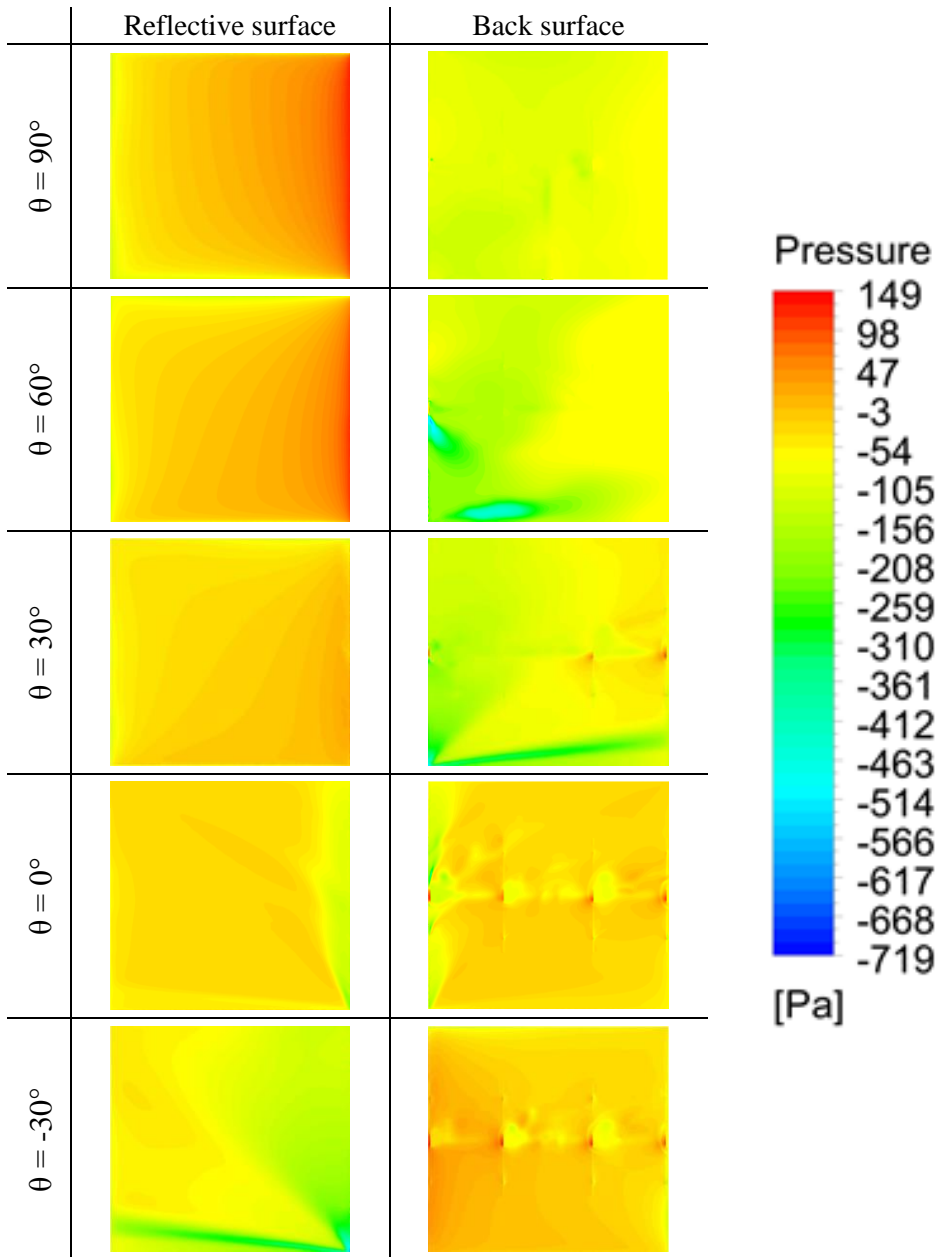


Figure 114: Pressure distribution on the heliostat at wind velocity of 15 m/s approaching at 22.5° incidence angle



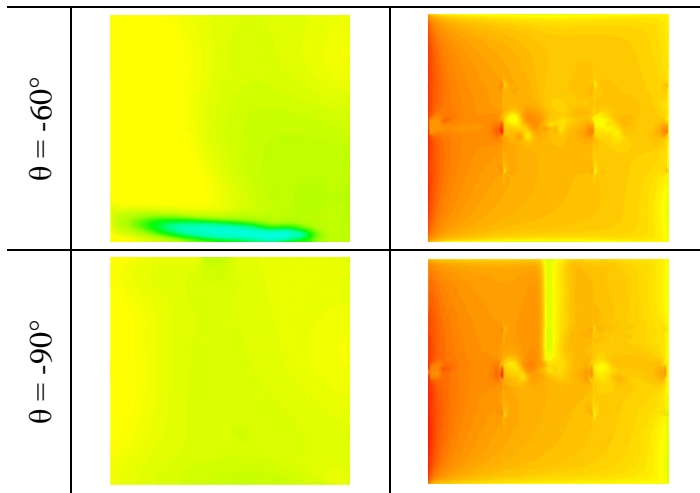
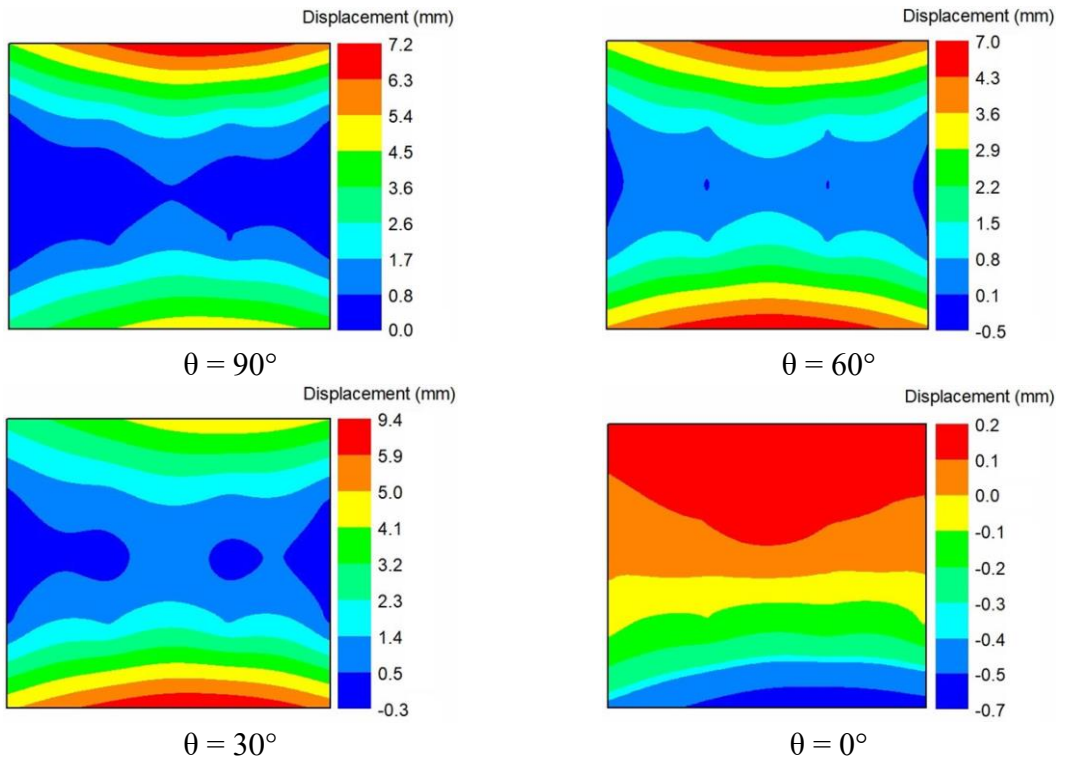


Figure 115: Pressure distribution on the heliostat at wind velocity of 15 m/s approaching at 67.5° incidence angle

• **Deflections**



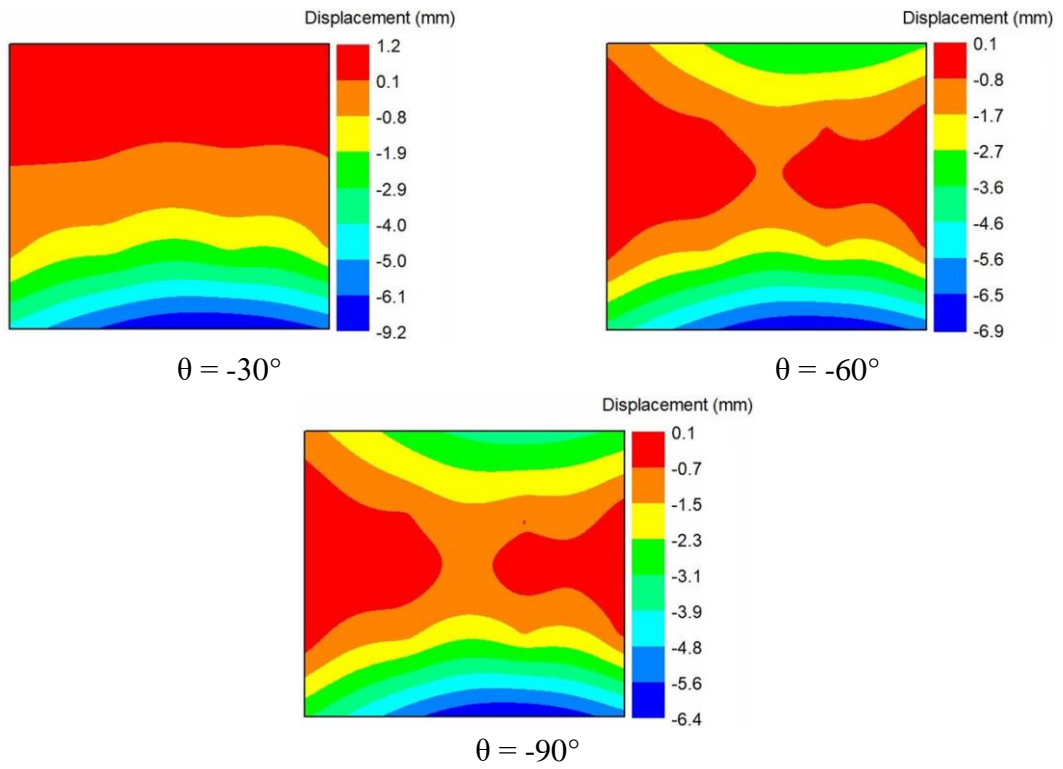
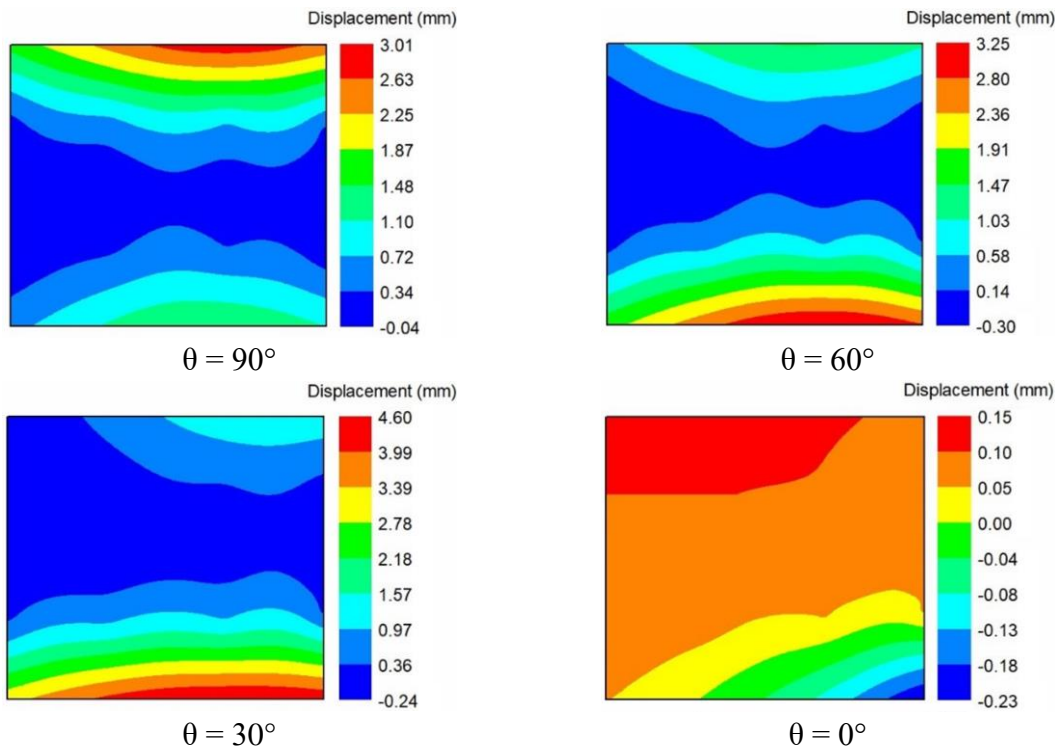


Figure 116: Displacement distribution of the heliostat surface for different tilt angles (θ) at wind velocity of 15 m/s approaching at 22.5° incidence angle (β)



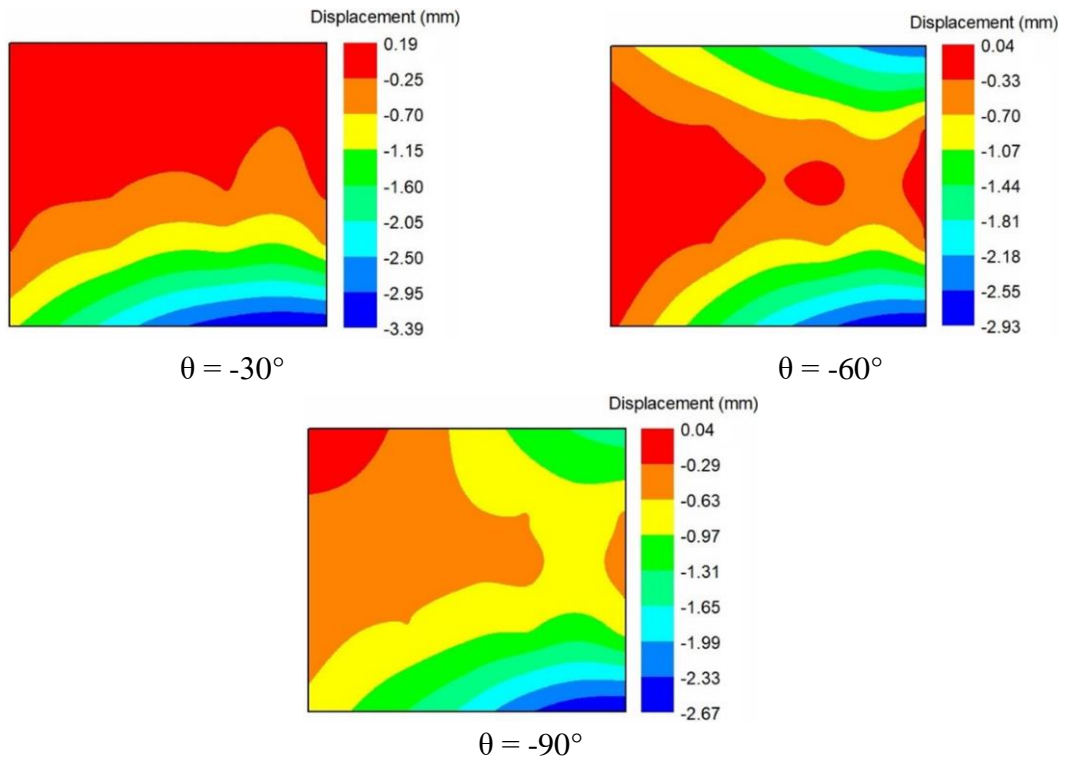


Figure 117: Displacement distribution of the heliostat surface for different tilt angles (θ) at wind velocity of 15 m/s approaching at 67.5° incidence angle (β)

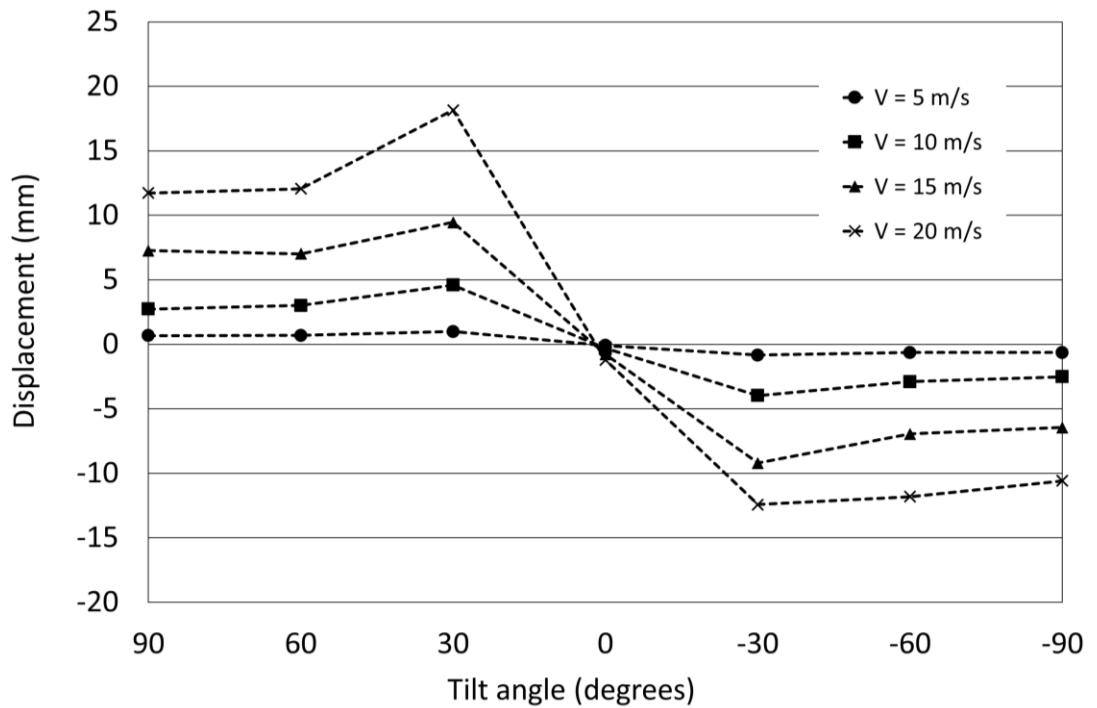


Figure 118: Wind velocity and tilt angle effects on the heliostat surface's maximum recorded displacement for 22.5° wind incidence angle

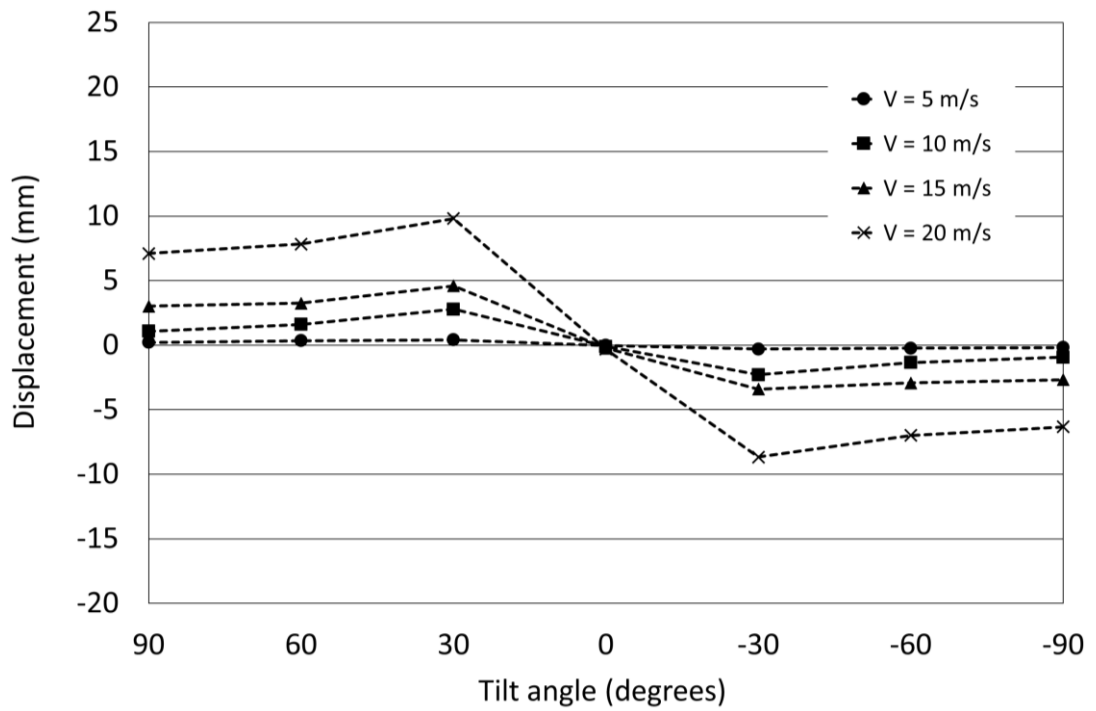
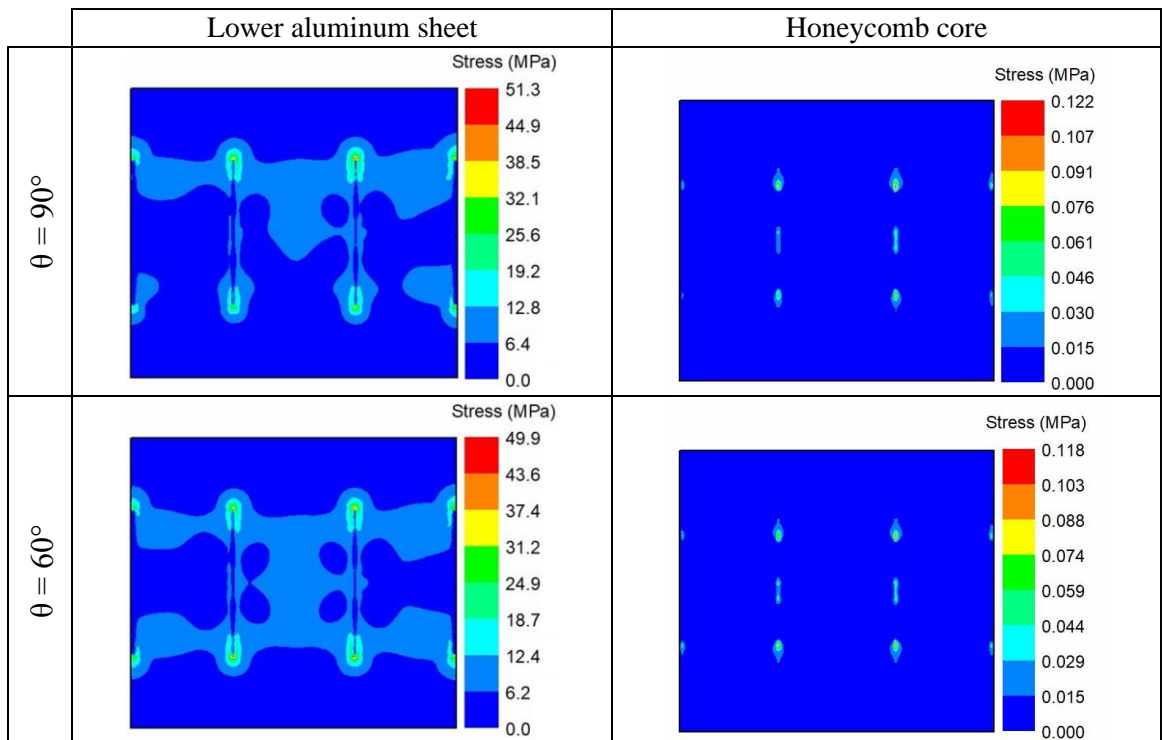


Figure 119: Wind velocity and tilt angle effects on the heliostat surface's maximum recorded displacement for 67.5° wind incidence angle

• **Stress distributions**



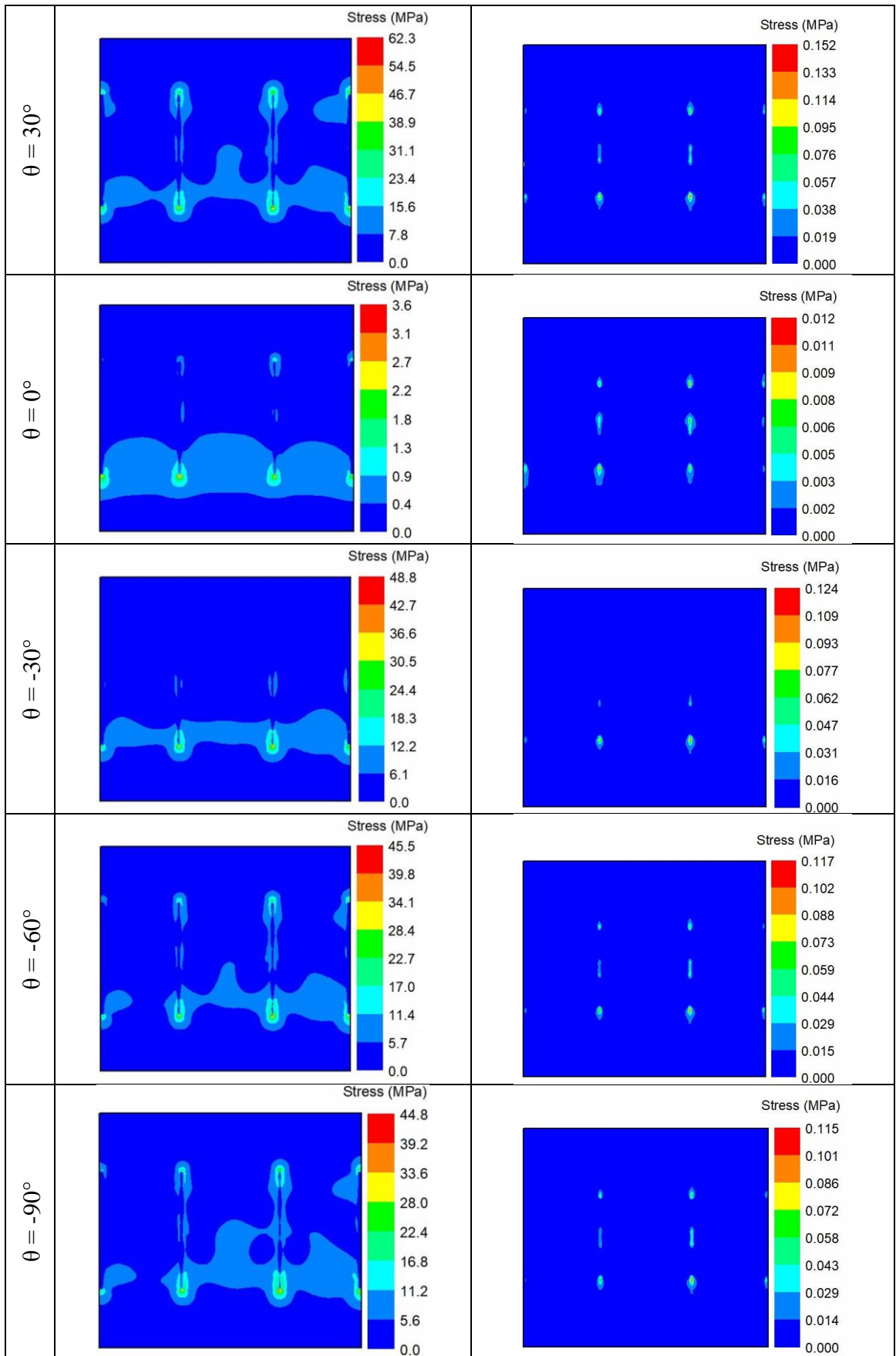
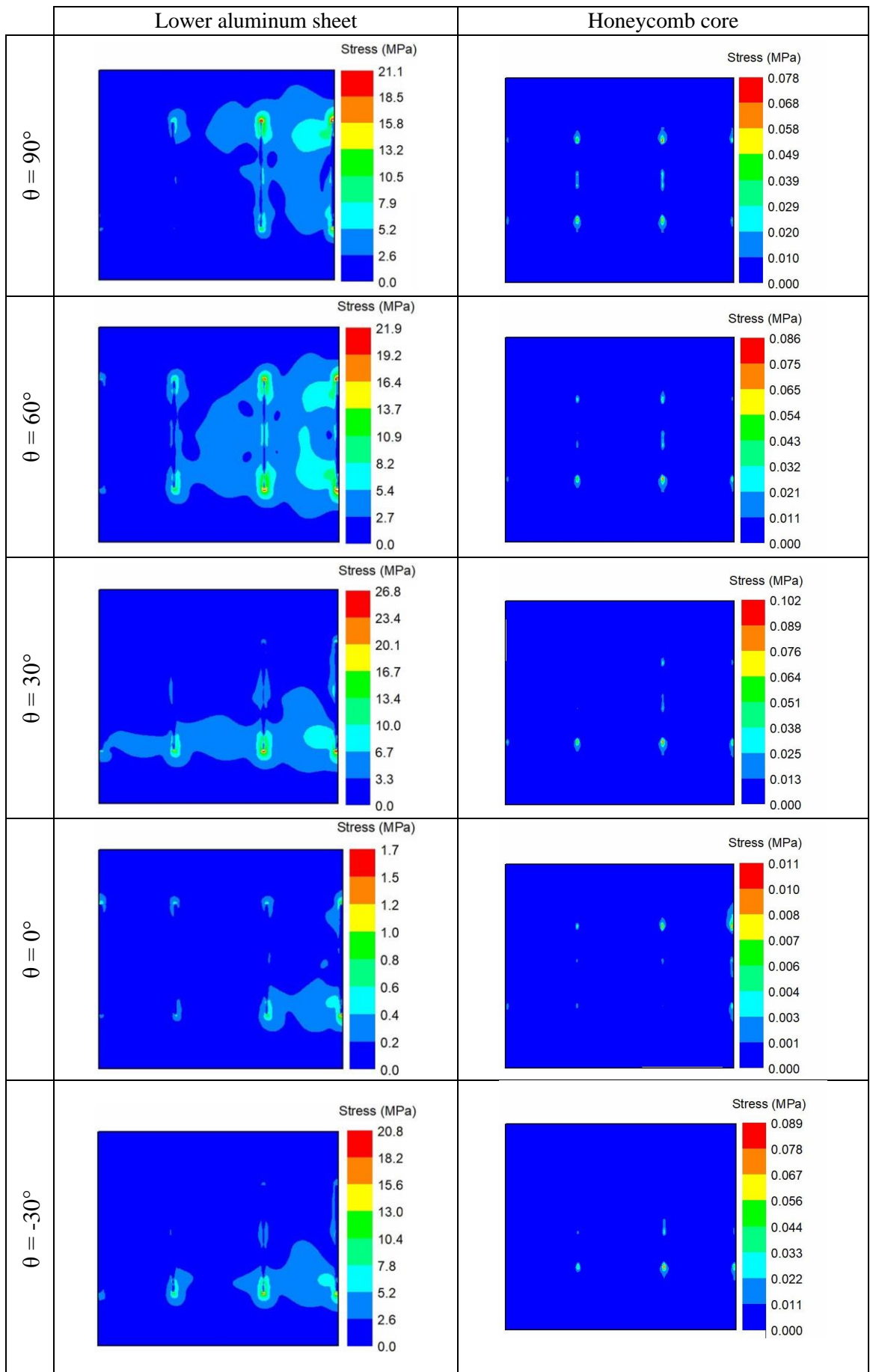


Figure 120: Stress distribution of the heliostat surface for different tilt angles at wind velocity of 15 m/s approaching at 22.5° incidence angle



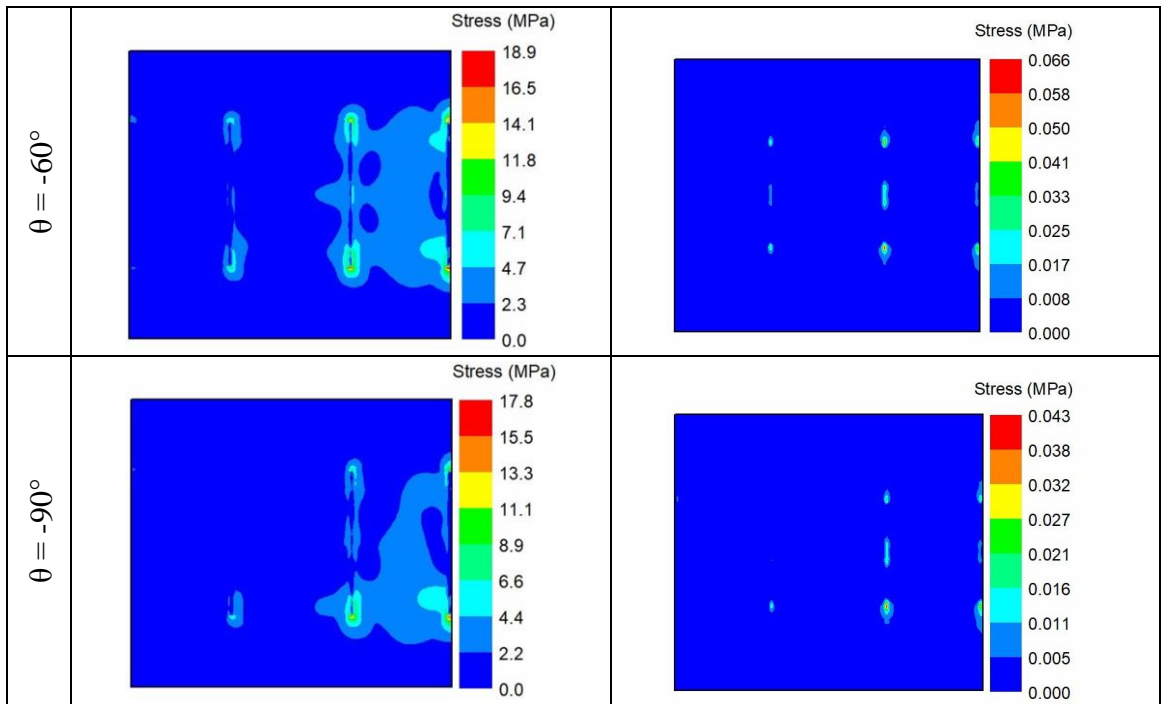
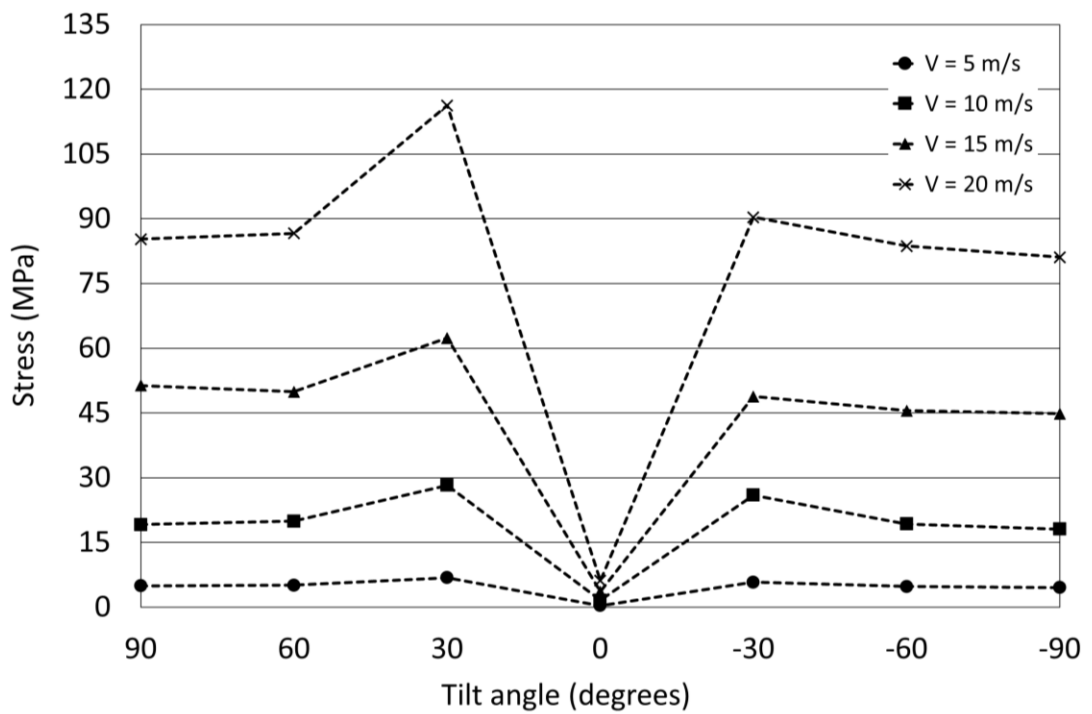
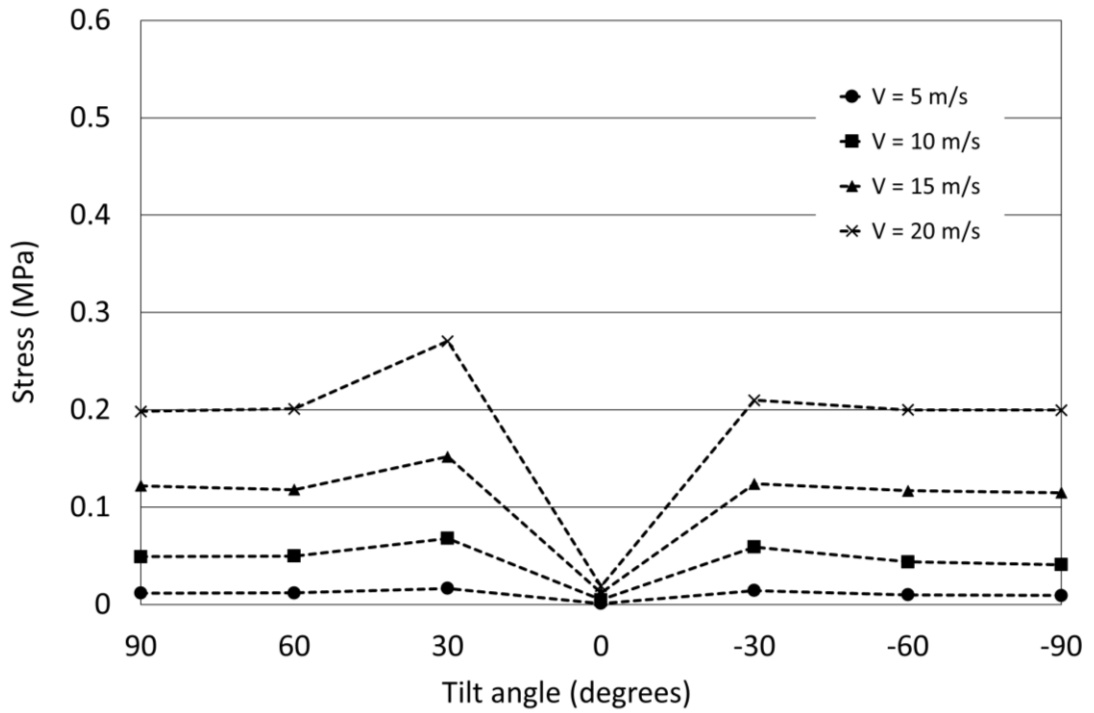


Figure 121: Stress distribution of the heliostat surface for different tilt angles at wind velocity of 15 m/s approaching at 67.5° incidence angle

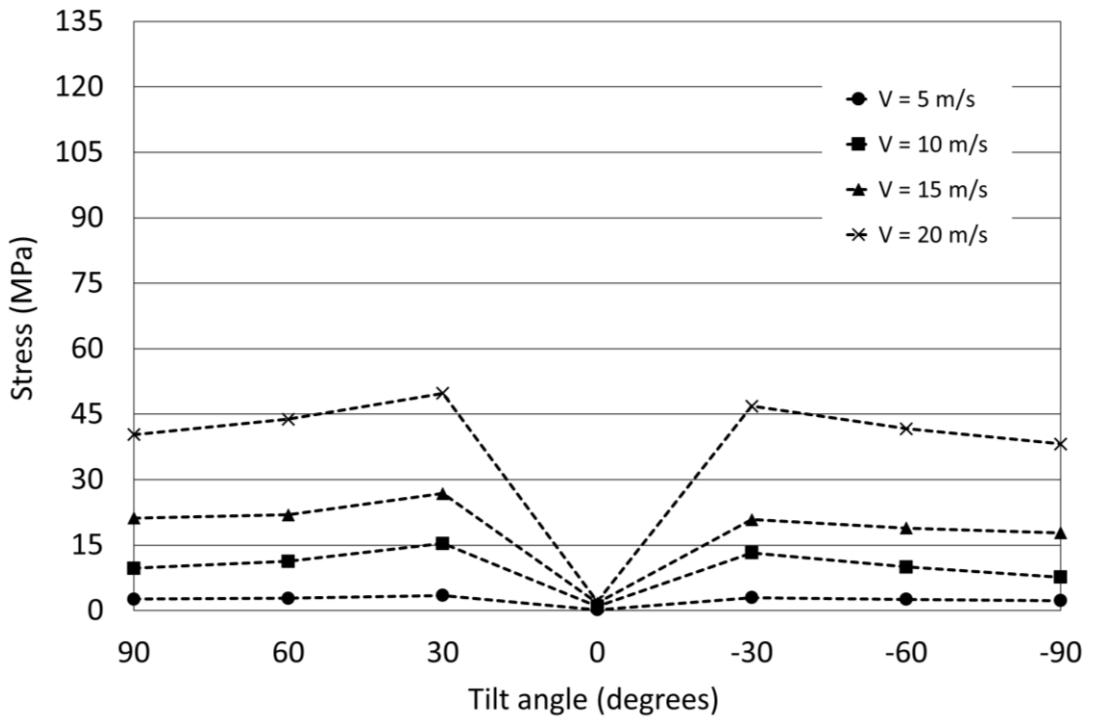


(a) Lower aluminum sheet

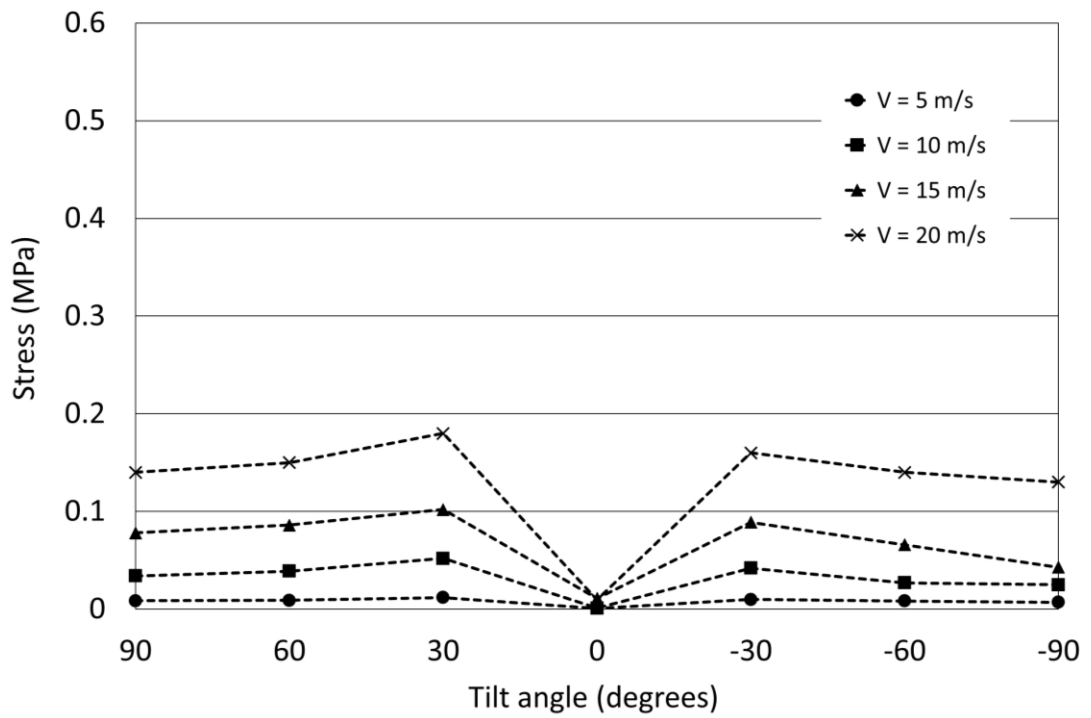


(b) Honeycomb core

Figure 122: Wind velocity and tilt angle effects on the heliostat's maximum recorded stress for 22.5° wind incidence angle



(a) Lower aluminum sheet



(b) Honeycomb core

Figure 123: Wind velocity and tilt angle effects on the heliostat's maximum recorded stress for 67.5° wind incidence angle

Appendix G: Dataset used in establishing the ANN model

Input data					Output data			
Wind velocity (m/s)	Honeycomb core thickness (D) (mm)	Cell wall angle (ϕ) (degrees)	Cell wall thickness (t) (mm)	Cell wall length (a) (mm)	Weight reduction percentage (%)	Displacement (mm)	Stress Aluminum sheet (MPa)	Core crush index
5	150	10	0.02	5	44.99531869	5.9737	13.717	41.09343831
5	150	10	0.02	6	48.33007099	7.9695	13.843	29.88751008
5	150	10	0.02	7	50.71203508	10.522	14.534	23.04224501
5	150	10	0.02	8	52.49850815	13.692	17.141	15.58707485
5	150	10	0.02	9	53.88798935	17.548	19.89	10.97212289
5	150	10	0.02	10	54.99956917	22.13	22.752	7.985279272
5	150	10	0.03	5	34.98893976	3.6871	13.466	79.38369194
5	150	10	0.03	6	39.99319024	4.4615	13.569	53.04304773
5	150	10	0.03	7	43.56613638	5.4181	13.668	43.82123175
5	150	10	0.03	8	46.24585241	6.5808	13.763	36.26562738
5	150	10	0.03	9	48.33007099	7.9695	13.843	29.88751008
5	150	10	0.03	10	49.99744714	9.6055	13.902	24.22743238
5	150	10	0.04	5	24.9897114	2.9386	13.244	142.2486923
5	150	10	0.04	6	31.6580071	3.3604	13.4	95.14588845
5	150	10	0.04	7	36.4202441	3.8647	13.493	63.47001005
5	150	10	0.04	8	39.99319024	4.4615	13.569	53.04304773
5	150	10	0.04	9	42.77215263	5.1611	13.644	46.5995517
5	150	10	0.04	10	44.99531869	5.9737	13.717	41.09343831
5	150	10	0.05	5	14.98405268	2.586	12.911	402.3375801
5	150	10	0.05	6	23.3178147	2.8622	13.194	230.8277163
5	150	10	0.05	7	29.27233911	3.1823	13.349	133.5777516
5	150	10	0.05	8	33.74144761	3.5518	13.441	98.52534842
5	150	10	0.05	9	37.21423427	3.977	13.51	76.47842109
5	150	10	0.05	10	39.99319024	4.4615	13.569	60.19731198
5	150	20	0.02	5	46.66551777	5.1879	13.658	37.82585535
5	150	20	0.02	6	49.72190571	6.7342	13.785	27.50789962
5	150	20	0.02	7	51.90503627	8.6953	13.889	22.09953903
5	150	20	0.02	8	53.54238258	11.105	15.46	15.83928353
5	150	20	0.02	9	54.81587916	14.019	17.836	11.21430154
5	150	20	0.02	10	55.83467514	17.473	20.317	8.195856669
5	150	20	0.03	5	37.49636684	3.3776	13.407	73.077308
5	150	20	0.03	6	42.08094552	3.9998	13.525	48.7734285
5	150	20	0.03	7	45.35563815	4.7542	13.614	40.32255579
5	150	20	0.03	8	47.81166084	5.6616	13.702	33.38632283
5	150	20	0.03	9	49.72190571	6.7342	13.785	27.50789962
5	150	20	0.03	10	51.25009646	7.9932	13.858	22.27554632
5	150	20	0.04	5	28.32707444	2.7628	13.09	131.9082792
5	150	20	0.04	6	34.44235815	3.1136	13.323	87.7075628

5	150	20	0.04	7	38.80624646	3.5229	13.445	58.37952105
5	150	20	0.04	8	42.08094552	3.9998	13.525	48.7734285
5	150	20	0.04	9	44.62793225	4.5531	13.593	42.86989101
5	150	20	0.04	10	46.66551777	5.1879	13.658	37.82585535
5	150	20	0.05	5	19.15736406	2.4538	12.574	378.6354489
5	150	20	0.05	6	26.79664592	2.6984	13.018	214.4195667
5	150	20	0.05	7	32.25603169	2.9671	13.25	123.3420695
5	150	20	0.05	8	36.35022378	3.2692	13.379	90.71939672
5	150	20	0.05	9	39.53395879	3.6119	13.462	70.34430171
5	150	20	0.05	10	42.08094552	3.9998	13.525	55.35182116
5	150	30	0.02	5	47.20127707	4.3406	13.665	36.70368912
5	150	30	0.02	6	50.16836643	5.4085	13.734	26.80468119
5	150	30	0.02	7	52.28772056	6.7374	13.809	21.57920551
5	150	30	0.02	8	53.87723134	8.3555	13.873	17.13634213
5	150	30	0.02	9	55.11352179	10.29	15.629	12.42458781
5	150	30	0.02	10	56.10255157	12.568	17.638	9.165329547
5	150	30	0.03	5	38.30000257	3.0621	13.56	70.14519847
5	150	30	0.03	6	42.75063661	3.504	13.607	47.06539004
5	150	30	0.03	7	45.92966459	4.0371	13.643	39.06316306
5	150	30	0.03	8	48.31393719	4.6691	13.685	32.4527301
5	150	30	0.03	9	50.16836643	5.4085	13.734	26.80468119
5	150	30	0.03	10	51.65191111	6.2637	13.785	21.7403053
5	150	30	0.04	5	29.40094655	2.6285	13.414	124.9674441
5	150	30	0.04	6	35.32974947	2.8734	13.521	83.9022768
5	150	30	0.04	7	39.57161505	3.1644	13.575	56.13386992
5	150	30	0.04	8	42.75063661	3.504	13.607	47.06539004
5	150	30	0.04	9	45.2232175	3.8949	13.634	41.49424764
5	150	30	0.04	10	47.20127707	4.3406	13.665	36.70368912
5	150	30	0.05	5	20.49488142	2.4273	13.199	350.1847155
5	150	30	0.05	6	27.91553063	2.5848	13.382	202.5028518
5	150	30	0.05	7	33.21415711	2.77	13.487	117.6400606
5	150	30	0.05	8	37.18734246	2.9841	13.547	86.98095355
5	150	30	0.05	9	40.27806214	3.2284	13.583	67.68404356
5	150	30	0.05	10	42.75063661	3.504	13.607	53.41340833
5	150	40	0.02	5	46.62707701	3.1028	12.397	41.76714331
5	150	40	0.02	6	49.68986959	3.732	12.9	29.46117059
5	150	40	0.02	7	51.87757858	4.4399	13.154	23.38685716
5	150	40	0.02	8	53.51835871	5.2806	13.362	18.36745832
5	150	40	0.02	9	54.7945239	6.2815	13.555	14.78923395
5	150	40	0.02	10	55.81544833	7.4408	13.707	12.17550632
5	150	40	0.03	5	37.43869926	2.1614	10.301	95.32575871
5	150	40	0.03	6	42.03289135	2.5253	11.389	58.05110271
5	150	40	0.03	7	45.31445162	2.9178	12.19	45.1341845
5	150	40	0.03	8	47.77562503	3.316	12.649	36.24698323

5	150	40	0.03	9	49.68986959	3.732	12.9	29.46117059
5	150	40	0.03	10	51.22126267	4.1906	13.076	23.66080504
5	150	40	0.04	5	28.24990997	1.678	7.9851	216.7239213
5	150	40	0.04	6	34.37805443	1.9795	9.5654	122.4366513
5	150	40	0.04	7	38.75132466	2.2758	10.76	73.11131086
5	150	40	0.04	8	42.03289135	2.5253	11.389	58.05110271
5	150	40	0.04	9	44.58521529	2.817	12.014	48.61335298
5	150	40	0.04	10	46.62707701	3.1028	12.397	41.76714331
5	150	40	0.05	5	19.06090848	1.3769	6.0342	790.7706371
5	150	40	0.05	6	26.71948145	1.647	7.8245	357.5424356
5	150	40	0.05	7	32.1852976	1.8464	8.8953	184.1374045
5	150	40	0.05	8	36.29015767	2.1304	10.286	118.264063
5	150	40	0.05	9	39.48056099	2.2992	10.748	88.3052164
5	150	40	0.05	10	42.03289135	2.5253	11.389	65.88083623
5	150	50	0.02	5	44.63176475	2.2571	11.623	49.39468453
5	150	50	0.02	6	48.02711045	2.5103	12.382	34.03266742
5	150	50	0.02	7	50.45235737	2.7557	12.784	26.68148633
5	150	50	0.02	8	52.27129096	3.0237	13.058	20.83967522
5	150	50	0.02	9	53.6860178	3.3119	13.216	16.81869331
5	150	50	0.02	10	54.81779541	3.6314	13.331	13.88077757
5	150	50	0.03	5	34.44878852	1.7488	8.8704	122.7420956
5	150	50	0.03	6	39.53874942	1.9779	10.308	71.11623184
5	150	50	0.03	7	43.1766166	2.1715	11.282	54.07173318
5	150	50	0.03	8	45.90501698	2.3423	11.919	42.65159925
5	150	50	0.03	9	48.02711045	2.5103	12.382	34.03266742
5	150	50	0.03	10	49.72478008	2.6751	12.687	27.03912101
5	150	50	0.04	5	24.256649	1.4179	6.4335	298.2544858
5	150	50	0.04	6	31.05355214	1.6277	8.018	161.9554649
5	150	50	0.04	7	35.90088225	1.8136	9.3059	93.73149434
5	150	50	0.04	8	39.53874942	1.9779	10.308	71.11623184
5	150	50	0.04	9	42.3682031	2.1224	11.052	58.59349559
5	150	50	0.04	10	44.63176475	2.2571	11.623	49.39468453
5	150	50	0.05	5	14.07093986	1.1887	4.8462	1091.731854
5	150	50	0.05	6	22.55903081	1.3784	6.1237	506.5442186
5	150	50	0.05	7	28.62287155	1.554	7.4734	243.0140982
5	150	50	0.05	8	33.17557488	1.7084	8.5954	156.920724
5	150	50	0.05	9	36.70929575	1.8464	9.5154	110.5946319
5	150	50	0.05	10	39.53874942	1.9779	10.308	80.70814515
5	300	10	0.02	5	24.9897114	2.0221	7.4075	76.09567239
5	300	10	0.02	6	31.6580071	2.6999	8.4406	49.01698955
5	300	10	0.02	7	36.4202441	3.5653	10.536	31.78587594
5	300	10	0.02	8	39.99369824	4.6398	12.749	20.95678485
5	300	10	0.02	9	42.77215263	5.9473	15.055	14.49588338
5	300	10	0.02	10	44.99537013	7.5089	17.441	10.41689548

5	300	10	0.03	5	4.97839395	1.2453	7.2181	148.0972549
5	300	10	0.03	6	14.98405268	1.5082	7.3081	98.48539492
5	300	10	0.03	7	22.12819589	1.8334	7.3784	81.17594541
5	300	10	0.03	8	27.48469571	2.2284	7.7687	64.24805047
5	300	10	0.03	9	31.6580071	2.6999	8.4406	49.01698955
5	300	10	0.03	10	34.98893976	3.2546	9.8232	34.28717373
5	300	10	0.04	5	-15.0329235	0.99123	7.0121	268.6701104
5	300	10	0.04	6	-1.689901744	1.1345	7.1555	178.1783111
5	300	10	0.04	7	7.833479088	1.3055	7.2435	118.2302541
5	300	10	0.04	8	14.98405268	1.5082	7.3081	98.48539492
5	300	10	0.04	9	20.53989403	1.746	7.3624	86.35829124
5	300	10	0.04	10	24.9897114	2.0221	7.4075	76.09567239
5	300	10	0.05	5	-35.03781059	0.87065	6.7445	770.1950473
5	300	10	0.05	6	-18.36385617	0.96526	6.9697	436.9687201
5	300	10	0.05	7	-6.454807346	1.0741	7.1074	250.8835027
5	300	10	0.05	8	2.476979268	1.1994	7.1951	184.052926
5	300	10	0.05	9	9.421780956	1.3436	7.2582	142.3525762
5	300	10	0.05	10	14.98405268	1.5082	7.3081	111.768767
5	300	20	0.02	5	28.32707444	1.7506	7.3715	70.08417994
5	300	20	0.02	6	34.44235815	2.2754	7.8816	48.11160123
5	300	20	0.02	7	38.80624646	2.9417	9.098	33.73713977
5	300	20	0.02	8	42.08099696	3.7611	10.978	22.30600505
5	300	20	0.02	9	44.62793225	4.7537	12.952	15.44304217
5	300	20	0.02	10	46.66551777	5.9342	15	11.10101466
5	300	20	0.03	5	9.987653686	1.1386	7.1542	136.9471735
5	300	20	0.03	6	19.15736406	1.3484	7.2662	90.78481469
5	300	20	0.03	7	25.70991306	1.6037	7.34	74.78900198
5	300	20	0.03	8	30.61628685	1.9113	7.3996	61.82217896
5	300	20	0.03	9	34.44235815	2.2754	7.8816	48.11160123
5	300	20	0.03	10	37.49678481	2.7031	8.4928	36.34779118
5	300	20	0.04	5	-8.351767066	0.93063	6.8607	251.6768515
5	300	20	0.04	6	3.87880035	1.0495	7.0715	165.2446948
5	300	20	0.04	7	12.61124543	1.1875	7.1904	109.1611956
5	300	20	0.04	8	19.15736406	1.3484	7.2662	90.78481469
5	300	20	0.04	9	24.25021863	1.5355	7.3239	79.56559053
5	300	20	0.04	10	28.32707444	1.7506	7.3715	70.08417994
5	300	20	0.05	5	-26.68475745	0.82484	6.4552	737.5390592
5	300	20	0.05	6	-11.40619373	0.90868	6.8001	410.4813047
5	300	20	0.05	7	-0.487422192	0.99998	7.0028	233.375567
5	300	20	0.05	8	7.698441278	1.102	7.1254	170.3391822
5	300	20	0.05	9	14.06450949	1.2176	7.207	131.3965575
5	300	20	0.05	10	19.15736406	1.3484	7.2662	103.0295589
5	300	30	0.02	5	29.40094655	1.464	7.3567	68.17675205
5	300	30	0.02	6	35.32974947	1.8301	7.4091	49.68693788

5	300	30	0.02	7	39.57161505	2.2879	8.2339	36.19029244
5	300	30	0.02	8	42.75063661	2.8471	9.1092	26.09806288
5	300	30	0.02	9	45.2232175	3.5169	10.69	18.16500308
5	300	30	0.02	10	47.20127707	4.307	12.342	13.09820795
5	300	30	0.03	5	11.59524667	1.031	7.2278	131.5986733
5	300	30	0.03	6	20.49488142	1.1799	7.2938	87.80317012
5	300	30	0.03	7	26.85451927	1.3607	7.3378	72.62922588
5	300	30	0.03	8	31.62585524	1.5764	7.3749	60.21988249
5	300	30	0.03	9	35.32974947	1.8301	7.4091	49.68693788
5	300	30	0.03	10	38.30000257	2.1245	7.8971	37.94938757
5	300	30	0.04	5	-6.204022841	0.8843	7.066	237.2365263
5	300	30	0.04	6	5.660013375	0.96736	7.1777	158.051003
5	300	30	0.04	7	14.14167395	1.0654	7.2478	105.1377362
5	300	30	0.04	8	20.49488142	1.1799	7.2938	87.80317012
5	300	30	0.04	9	25.43983744	1.3123	7.3278	77.20360441
5	300	30	0.04	10	29.40094655	1.464	7.3567	68.17675205
5	300	30	0.05	5	-24.00972272	0.8146	6.8878	671.0543366
5	300	30	0.05	6	-9.174854674	0.86934	7.0367	385.1085258
5	300	30	0.05	7	1.422398272	0.93243	7.1393	222.2362833
5	300	30	0.05	8	9.37033798	1.0047	7.2096	163.4391614
5	300	30	0.05	9	15.54992541	1.087	7.2585	126.6587261
5	300	30	0.05	10	20.49488142	1.1799	7.2938	99.64576039
5	300	40	0.02	5	28.24990997	1.0363	6.313	82.01921046
5	300	40	0.02	6	34.37805443	1.2513	6.7206	56.54987658
5	300	40	0.02	7	38.75132466	1.4923	6.9281	44.40333123
5	300	40	0.02	8	42.03289778	1.7779	7.0882	34.62458425
5	300	40	0.02	9	44.58521529	2.1171	7.8702	25.47178803
5	300	40	0.02	10	46.62707701	2.5096	8.5363	19.55058574
5	300	40	0.03	5	9.871906991	0.71888	4.862	201.964344
5	300	40	0.03	6	19.06090848	0.83979	5.573	118.6334127
5	300	40	0.03	7	25.62631823	0.97295	6.15	89.46109091
5	300	40	0.03	8	30.54555275	1.1092	6.5122	70.40448557
5	300	40	0.03	9	34.37805443	1.2513	6.7206	56.54987658
5	300	40	0.03	10	37.43869926	1.4075	6.867	45.05441775
5	300	40	0.04	5	-8.506095993	0.56636	3.5601	486.0993185
5	300	40	0.04	6	3.750192911	0.6601	4.4203	264.9493348
5	300	40	0.04	7	12.50192911	0.75576	5.1443	152.9222061
5	300	40	0.04	8	19.06090848	0.83979	5.573	118.6334127
5	300	40	0.04	9	24.1666238	0.93857	6.0187	97.03770295
5	300	40	0.04	10	28.24990997	1.0363	6.313	82.01921046
5	300	40	0.05	5	-26.8776686	0.47366	2.9037	1643.306188
5	300	40	0.05	6	-11.56695303	0.55567	3.4672	806.8732082
5	300	40	0.05	7	-0.628890375	0.61884	4.0486	404.5737921
5	300	40	0.05	8	7.576264211	0.70738	4.8388	251.3978986

5	300	40	0.05	9	13.95519317	0.76444	5.1471	184.3959639
5	300	40	0.05	10	19.06090848	0.83979	5.573	134.6342802
5	300	50	0.02	5	24.256649	0.74379	5.6252	102.0611566
5	300	50	0.02	6	31.05355214	0.83483	6.208	67.87894458
5	300	50	0.02	7	35.90088225	0.92159	6.5495	52.07971925
5	300	50	0.02	8	39.53874942	1.0152	6.7995	40.02124848
5	300	50	0.02	9	42.3682031	1.1143	6.9527	31.96971691
5	300	50	0.02	10	44.63176475	1.2238	7.0652	26.19099895
5	300	50	0.03	5	3.885230722	0.56992	3.8827	280.4160725
5	300	50	0.03	6	14.07093986	0.64554	4.7358	154.792457
5	300	50	0.03	7	21.35012089	0.71319	5.3818	113.3519071
5	300	50	0.03	8	26.80307629	0.7744	5.8454	86.96828471
5	300	50	0.03	9	31.05355214	0.83483	6.208	67.87894458
5	300	50	0.03	10	34.44878852	0.89346	6.4642	53.06848925
5	300	50	0.04	5	-16.48618756	0.46742	2.6187	732.7377074
5	300	50	0.04	6	-2.905242039	0.53162	3.4187	379.8399736
5	300	50	0.04	7	6.798189207	0.59071	4.1303	211.1846387
5	300	50	0.04	8	14.07093986	0.64554	4.7358	154.792457
5	300	50	0.04	9	19.72966716	0.69579	5.2233	123.9781964
5	300	50	0.04	10	24.256649	0.74379	5.6252	102.0611566
5	300	50	0.05	5	-36.85760584	0.39649	2.2392	2362.786224
5	300	50	0.05	6	-19.88142394	0.45524	2.5513	1215.82128
5	300	50	0.05	7	-7.753742476	0.5087	3.1349	579.3299823
5	300	50	0.05	8	1.338803436	0.55683	3.7293	361.6754863
5	300	50	0.05	9	8.412212562	0.60147	4.2527	247.4550664
5	300	50	0.05	10	14.07093986	0.64554	4.7358	175.6703324
5	450	10	0.02	5	4.97839395	1.2946	8.8392	63.77032913
5	450	10	0.02	6	14.98405268	1.7475	10.646	38.86274676
5	450	10	0.02	7	22.12819589	2.324	11.84	28.2851342
5	450	10	0.02	8	27.48469571	3.0381	12.492	21.38793228
5	450	10	0.02	9	31.6580071	3.906	12.774	17.08435293
5	450	10	0.02	10	34.98893976	4.9408	13.398	13.56031303
5	450	10	0.03	5	-25.03215186	0.77365	5.3493	199.8356412
5	450	10	0.03	6	-10.03009414	0.95011	6.5173	110.435474
5	450	10	0.03	7	0.689335871	1.1682	8.1104	73.84945201
5	450	10	0.03	8	8.727300787	1.4327	9.5081	52.49459194
5	450	10	0.03	9	14.98405268	1.7475	10.646	38.86274676
5	450	10	0.03	10	19.98688204	2.1172	11.508	29.26744569
5	450	10	0.04	5	-55.04912804	0.60341	5.1671	364.6032941
5	450	10	0.04	6	-35.03781059	0.69937	5.291	240.9667181
5	450	10	0.04	7	-20.74952415	0.8141	5.3735	159.3748666
5	450	10	0.04	8	-10.03009414	0.95011	6.5173	110.435474
5	450	10	0.04	9	-1.689901744	1.1096	7.7269	82.28452335
5	450	10	0.04	10	4.97839395	1.2946	8.8392	63.77032913

5	450	10	0.05	5	-85.05967385	0.52284	4.9566	1048.012851
5	450	10	0.05	6	-60.05195741	0.58606	5.1325	593.3835145
5	450	10	0.05	7	-42.1819538	0.65887	5.2481	339.7666597
5	450	10	0.05	8	-28.78748907	0.74287	5.3275	248.5742296
5	450	10	0.05	9	-18.36385617	0.83963	5.5111	187.4804429
5	450	10	0.05	10	-10.03009414	0.95011	6.5173	125.3306317
5	450	20	0.02	5	9.987653686	1.111	7.5921	68.04777761
5	450	20	0.02	6	19.15736406	1.4601	9.5666	39.63753018
5	450	20	0.02	7	25.70991306	1.902	11.087	27.68472063
5	450	20	0.02	8	30.61628685	2.4448	12.104	20.23094212
5	450	20	0.02	9	34.44235815	3.1014	12.696	15.75443307
5	450	20	0.02	10	37.49636684	3.8821	12.965	12.84344157
5	450	20	0.03	5	-17.52147744	0.70337	5.2939	185.0710192
5	450	20	0.03	6	-3.766911878	0.84302	5.3996	122.1684237
5	450	20	0.03	7	6.058696435	1.0131	6.8583	80.04188713
5	450	20	0.03	8	13.42790267	1.2179	8.2941	55.15479623
5	450	20	0.03	9	19.15736406	1.4601	9.5666	39.63753018
5	450	20	0.03	10	23.74221925	1.7438	10.636	29.02355406
5	450	20	0.04	5	-45.0241782	0.56519	5.0406	342.5543339
5	450	20	0.04	6	-26.68475745	0.64403	5.219	223.8988042
5	450	20	0.04	7	-13.58608982	0.73582	5.3269	147.3488634
5	450	20	0.04	8	-3.766911878	0.84302	5.3996	122.1684237
5	450	20	0.04	9	3.87880035	0.96767	6.484	89.87205868
5	450	20	0.04	10	9.987653686	1.111	7.5921	68.04777761
5	450	20	0.05	5	-72.53330933	0.49556	4.7216	1008.336609
5	450	20	0.05	6	-49.60903339	0.55068	4.9913	559.2358544
5	450	20	0.05	7	-33.23730645	0.61113	5.1594	316.7582316
5	450	20	0.05	8	-20.95529605	0.67895	5.2673	230.4282666
5	450	20	0.05	9	-11.40619373	0.75586	5.3428	177.2432039
5	450	20	0.05	10	-3.766911878	0.84302	5.3996	138.6460814
5	450	30	0.02	5	11.59524667	0.91731	6.0386	83.05831017
5	450	30	0.02	6	20.49488142	1.1608	7.9852	46.10222555
5	450	30	0.02	7	26.85451927	1.4652	9.7287	30.6297089
5	450	30	0.02	8	31.62585524	1.8366	11.146	21.32894979
5	450	30	0.02	9	35.32974947	2.2813	12.196	15.92193202
5	450	30	0.02	10	38.30000257	2.8059	12.903	12.52872065
5	450	30	0.03	5	-15.11008797	0.62946	5.3315	178.405494
5	450	30	0.03	6	-1.754205463	0.72846	5.4001	118.5938709
5	450	30	0.03	7	7.782036113	0.84861	5.4489	97.80666441
5	450	30	0.03	8	14.9326097	0.99206	6.699	66.29580705
5	450	30	0.03	9	20.49488142	1.1608	7.9852	46.10222555
5	450	30	0.03	10	24.95112917	1.3566	9.1795	32.64775953
5	450	30	0.04	5	-41.80899223	0.53156	5.1846	323.3254822
5	450	30	0.04	6	-24.00972272	0.58712	5.2835	214.7142395

5	450	30	0.04	7	-11.29044704	0.65236	5.3515	142.3932139
5	450	30	0.04	8	-1.754205463	0.72846	5.4001	118.5938709
5	450	30	0.04	9	5.660013375	0.81647	5.4379	104.0351188
5	450	30	0.04	10	11.59524667	0.91731	6.0386	83.05831017
5	450	30	0.05	5	-68.51432687	0.48414	5.039	917.2629608
5	450	30	0.05	6	-46.26523998	0.52147	5.1598	525.19345
5	450	30	0.05	7	-30.36936056	0.56381	5.2484	302.3038445
5	450	30	0.05	8	-18.447451	0.61199	5.3137	221.753388
5	450	30	0.05	9	-9.174854674	0.66668	5.3625	171.4410002
5	450	30	0.05	10	-1.754205463	0.72846	5.4001	134.5894052
5	450	40	0.02	5	9.871906991	0.6415	4.5299	114.3043501
5	450	40	0.02	6	19.06090848	0.78279	5.0066	75.90961942
5	450	40	0.02	7	25.62631823	0.94318	6.5119	47.24131499
5	450	40	0.02	8	30.54555275	1.1332	7.9698	30.79449648
5	450	40	0.02	9	34.37805443	1.358	9.3082	21.53671668
5	450	40	0.02	10	37.43869926	1.6179	10.46	15.9550349
5	450	40	0.03	5	-17.68866711	0.43993	3.3965	289.1066217
5	450	40	0.03	6	-3.908380061	0.51553	3.9327	168.1145291
5	450	40	0.03	7	5.936519368	0.60006	4.3922	125.264266
5	450	40	0.03	8	13.31858635	0.68872	4.6987	97.5776472
5	450	40	0.03	9	19.06090848	0.78279	5.0066	75.90961942
5	450	40	0.03	10	23.65862441	0.88675	6.0114	51.46699383
5	450	40	0.04	5	-45.25567159	0.34713	2.481	697.5260717
5	450	40	0.04	6	-26.8776686	0.40374	3.0772	380.5912987
5	450	40	0.04	7	-13.75327949	0.462	3.6022	218.3881253
5	450	40	0.04	8	-3.908380061	0.51553	3.9327	168.1145291
5	450	40	0.04	9	3.750192911	0.5781	4.2853	136.2893666
5	450	40	0.04	10	9.871906991	0.6415	4.5299	114.3043501
5	450	40	0.05	5	-72.82267606	0.29056	1.8356	2599.514153
5	450	40	0.05	6	-49.85338752	0.33985	2.4136	1159.094625
5	450	40	0.05	7	-33.44307835	0.37919	2.8185	581.1450965
5	450	40	0.05	8	-21.13534647	0.43146	3.3731	360.6368479
5	450	40	0.05	9	-11.56695303	0.46846	3.609	262.9826727
5	450	40	0.05	10	-3.908380061	0.51553	3.9327	190.7892399
5	450	50	0.02	5	3.885230722	0.44428	3.8899	147.5910482
5	450	50	0.02	6	14.07093986	0.50285	4.3812	96.18197936
5	450	50	0.02	7	21.35012089	0.55991	4.685	72.8060024
5	450	50	0.02	8	26.80307629	0.62185	4.9177	55.33572179
5	450	50	0.02	9	31.05355214	0.6877	5.0661	43.87514079
5	450	50	0.02	10	34.44878852	0.76049	5.1784	35.7339421
5	450	50	0.03	5	-26.6718967	0.33803	2.5602	425.2681371
5	450	50	0.03	6	-11.39333299	0.38325	3.1896	229.8301097
5	450	50	0.03	7	-0.480991821	0.42493	3.6929	165.1919342
5	450	50	0.03	8	7.70487165	0.46381	4.072	124.8439124

5	450	50	0.03	9	14.07093986	0.50285	4.3812	96.18197936
5	450	50	0.03	10	19.16379443	0.54129	4.6078	74.44883202
5	450	50	0.04	5	-57.22902413	0.27719	1.6775	1143.85707
5	450	50	0.04	6	-36.85760584	0.31523	2.2302	582.2611952
5	450	50	0.04	7	-22.30567416	0.35028	2.7391	318.4461732
5	450	50	0.04	8	-11.39333299	0.38325	3.1896	229.8301097
5	450	50	0.04	9	-2.905242039	0.41417	3.567	181.546205
5	450	50	0.04	10	3.885230722	0.44428	3.8899	147.5910482
5	450	50	0.05	5	-87.78615155	0.23479	1.1305	4680.009652
5	450	50	0.05	6	-62.3218787	0.26983	1.5755	1968.851051
5	450	50	0.05	7	-44.1303565	0.30152	2.0315	893.9904314
5	450	50	0.05	8	-30.49153763	0.33007	2.4497	550.5965593
5	450	50	0.05	9	-19.88142394	0.35674	2.8289	372.000481
5	450	50	0.05	10	-11.39333299	0.38325	3.1896	260.8288062
10	150	10	0.02	5	44.99531869	24.422	56.145	10.03969531
10	150	10	0.02	6	48.33007099	32.579	56.661	7.301897284
10	150	10	0.02	7	50.71203508	43.011	59.641	5.615197413
10	150	10	0.02	8	52.49850815	55.962	70.343	3.798218017
10	150	10	0.02	9	53.88798935	71.715	81.625	2.673635826
10	150	10	0.02	10	54.99956917	90.434	93.374	1.945735151
10	150	10	0.03	5	34.98893976	15.075	55.112	19.39651611
10	150	10	0.03	6	39.99319024	18.241	55.538	12.95943525
10	150	10	0.03	7	43.56613638	22.151	55.943	10.70640823
10	150	10	0.03	8	46.24585241	26.903	56.333	8.860238753
10	150	10	0.03	9	48.33007099	32.579	56.661	7.301897284
10	150	10	0.03	10	49.99744714	39.264	56.9	5.919328032
10	150	10	0.04	5	24.9897114	12.014	54.199	34.75971293
10	150	10	0.04	6	31.6580071	13.739	54.84	23.24863066
10	150	10	0.04	7	36.4202441	15.801	55.225	15.50748475
10	150	10	0.04	8	39.99319024	18.241	55.538	12.95943525
10	150	10	0.04	9	42.77215263	21.101	55.843	11.38556817
10	150	10	0.04	10	44.99531869	24.422	56.145	10.03969531
10	150	10	0.05	5	14.98405268	10.573	52.832	98.32261691
10	150	10	0.05	6	23.3178147	11.702	53.994	56.40517258
10	150	10	0.05	7	29.27233911	13.011	54.63	32.64011361
10	150	10	0.05	8	33.74144761	14.522	55.011	24.07298919
10	150	10	0.05	9	37.21423427	16.26	55.294	18.68599611
10	150	10	0.05	10	39.99319024	18.241	55.538	14.7073594
10	150	20	0.02	5	46.66551777	21.211	55.901	9.241794108
10	150	20	0.02	6	49.72190571	27.532	56.422	6.720718801
10	150	20	0.02	7	51.90503627	35.547	56.847	5.399414175
10	150	20	0.02	8	53.54238258	45.395	63.446	3.859586474
10	150	20	0.02	9	54.81587916	57.3	73.2	2.732490194
10	150	20	0.02	10	55.83467514	71.413	83.382	1.997016382

10	150	20	0.03	5	37.49636684	13.81	54.872	17.85514412
10	150	20	0.03	6	42.08094552	16.354	55.354	11.9171265
10	150	20	0.03	7	45.35563815	19.438	55.72	9.851961137
10	150	20	0.03	8	47.81166084	23.147	56.081	8.157119086
10	150	20	0.03	9	49.72190571	27.532	56.422	6.720718801
10	150	20	0.03	10	51.25009646	32.677	56.722	5.442236186
10	150	20	0.04	5	28.32707444	11.296	53.568	32.23341128
10	150	20	0.04	6	34.44235815	12.73	54.526	21.43065435
10	150	20	0.04	7	38.80624646	14.404	55.028	14.26387767
10	150	20	0.04	8	42.08094552	16.354	55.354	11.9171265
10	150	20	0.04	9	44.62793225	18.616	55.634	10.47435792
10	150	20	0.04	10	46.66551777	21.211	55.901	9.241794108
10	150	20	0.05	5	19.15736406	10.032	51.454	92.52851352
10	150	20	0.05	6	26.79664592	11.032	53.272	52.397393
10	150	20	0.05	7	32.25603169	12.131	54.226	30.13835467
10	150	20	0.05	8	36.35022378	13.366	54.754	22.1670528
10	150	20	0.05	9	39.53395879	14.768	55.096	17.18772669
10	150	20	0.05	10	42.08094552	16.354	55.354	13.52446763
10	150	30	0.02	5	47.20127707	17.748	55.928	8.967885707
10	150	30	0.02	6	50.16836643	22.114	56.211	6.549171718
10	150	30	0.02	7	52.28772056	27.546	56.521	5.27215104
10	150	30	0.02	8	53.87723134	34.16	56.78	4.186905149
10	150	30	0.02	9	55.11352179	42.068	64.14	3.027500514
10	150	30	0.02	10	56.10255157	51.373	72.387	2.233247442
10	150	30	0.03	5	38.30000257	12.52	55.495	17.13972234
10	150	30	0.03	6	42.75063661	14.327	55.69	11.49970843
10	150	30	0.03	7	45.92966459	16.507	55.84	9.544031764
10	150	30	0.03	8	48.31393719	19.091	56.011	7.92907842
10	150	30	0.03	9	50.16836643	22.114	56.211	6.549171718
10	150	30	0.03	10	51.65191111	25.61	56.42	5.311770801
10	150	30	0.04	5	29.40094655	10.746	54.891	30.53894618
10	150	30	0.04	6	35.32974947	11.748	55.334	20.50172922
10	150	30	0.04	7	39.57161505	12.938	55.556	13.71620139
10	150	30	0.04	8	42.75063661	14.327	55.69	11.49970843
10	150	30	0.04	9	45.2232175	15.925	55.802	10.13821319
10	150	30	0.04	10	47.20127707	17.748	55.928	8.967885707
10	150	30	0.05	5	20.49488142	9.9232	54.008	85.58154458
10	150	30	0.05	6	27.91553063	10.567	54.758	49.48853434
10	150	30	0.05	7	33.21415711	11.325	55.192	28.74712816
10	150	30	0.05	8	37.18734246	12.201	55.438	21.25493304
10	150	30	0.05	9	40.27806214	13.2	55.587	16.53898148
10	150	30	0.05	10	42.75063661	14.327	55.69	13.05074963
10	150	40	0.02	5	46.62707701	12.687	50.74	10.20471572
10	150	40	0.02	6	49.68986959	15.259	52.8	7.197899632

10	150	40	0.02	7	51.87757858	18.153	53.84	5.713794931
10	150	40	0.02	8	53.51835871	21.59	54.695	4.48717393
10	150	40	0.02	9	54.7945239	25.681	55.483	3.613143957
10	150	40	0.02	10	55.81544833	30.42	56.106	2.974542207
10	150	40	0.03	5	37.43869926	8.8378	42.165	23.28828745
10	150	40	0.03	6	42.03289135	10.325	46.616	14.18277005
10	150	40	0.03	7	45.31445162	11.93	49.894	11.02709162
10	150	40	0.03	8	47.77562503	13.558	51.773	8.855737371
10	150	40	0.03	9	49.68986959	15.259	52.8	7.197899632
10	150	40	0.03	10	51.22126267	17.134	53.523	5.78048104
10	150	40	0.04	5	28.24990997	6.862	32.686	52.94505855
10	150	40	0.04	6	34.37805443	8.0943	39.153	29.91228117
10	150	40	0.04	7	38.75132466	9.3055	44.041	17.86239424
10	150	40	0.04	8	42.03289135	10.325	46.616	14.18277005
10	150	40	0.04	9	44.58521529	11.518	49.175	11.87678338
10	150	40	0.04	10	46.62707701	12.687	50.74	10.20471572
10	150	40	0.05	5	19.06090848	5.6311	24.711	193.098951
10	150	40	0.05	6	26.71948145	6.7353	32.028	87.34828236
10	150	40	0.05	7	32.1852976	7.5502	36.411	44.98523673
10	150	40	0.05	8	36.29015767	8.7112	42.102	28.89326283
10	150	40	0.05	9	39.48056099	9.4012	43.995	21.57300752
10	150	40	0.05	10	42.03289135	10.325	46.616	16.09569341
10	150	50	0.02	5	44.63176475	9.2284	47.567	12.06959485
10	150	50	0.02	6	48.02711045	10.264	50.672	8.316081622
10	150	50	0.02	7	50.45235737	11.267	52.318	6.5196705
10	150	50	0.02	8	52.27129096	12.363	53.441	5.092054398
10	150	50	0.02	9	53.6860178	13.541	54.091	4.109294536
10	150	50	0.02	10	54.81779541	14.848	54.562	3.391456431
10	150	50	0.03	5	34.44878852	7.151	36.303	29.9912262
10	150	50	0.03	6	39.53874942	8.0872	42.186	17.3769999
10	150	50	0.03	7	43.1766166	8.8783	46.171	13.21256403
10	150	50	0.03	8	45.90501698	9.5766	48.778	10.42200196
10	150	50	0.03	9	48.02711045	10.264	50.672	8.316081622
10	150	50	0.03	10	49.72478008	10.938	51.923	6.606808701
10	150	50	0.04	5	24.256649	5.7987	26.333	72.86751355
10	150	50	0.04	6	31.05355214	6.6558	32.816	39.57090802
10	150	50	0.04	7	35.90088225	7.4158	38.085	22.90287287
10	150	50	0.04	8	39.53874942	8.0872	42.186	17.3769999
10	150	50	0.04	9	42.3682031	8.6777	45.229	14.31770133
10	150	50	0.04	10	44.63176475	9.2284	47.567	12.06959485
10	150	50	0.05	5	14.07093986	4.8617	19.889	266.0139229
10	150	50	0.05	6	22.55903081	5.6374	25.066	123.7502925
10	150	50	0.05	7	28.62287155	6.3548	30.588	59.37431547
10	150	50	0.05	8	33.17557488	6.9857	35.179	38.34095316

10	150	50	0.05	9	36.70929575	7.5496	38.942	27.02357765
10	150	50	0.05	10	39.53874942	8.0872	42.186	19.72075002
10	300	10	0.02	5	24.9897114	8.054	29.523	19.09286635
10	300	10	0.02	6	31.6580071	10.753	33.648	12.29591066
10	300	10	0.02	7	36.4202441	14.2	42.004	7.972954693
10	300	10	0.02	8	39.99369824	18.479	50.826	5.256719986
10	300	10	0.02	9	42.77215263	23.686	60.022	3.635925566
10	300	10	0.02	10	44.99537013	29.905	69.533	2.612875527
10	300	10	0.03	5	4.97839395	4.9601	28.768	37.15867615
10	300	10	0.03	6	14.98405268	6.0072	29.127	24.71044442
10	300	10	0.03	7	22.12819589	7.3023	29.407	20.36755179
10	300	10	0.03	8	27.48469571	8.8755	30.927	16.13877291
10	300	10	0.03	9	31.6580071	10.753	33.648	12.29591066
10	300	10	0.03	10	34.98893976	12.962	39.161	8.600642604
10	300	10	0.04	5	-15.0329235	3.9485	27.946	67.41364349
10	300	10	0.04	6	-1.689901744	4.519	28.518	44.70702382
10	300	10	0.04	7	7.833479088	5.2001	28.869	29.66506791
10	300	10	0.04	8	14.98405268	6.0072	29.127	24.71044442
10	300	10	0.04	9	20.53989403	6.9542	29.343	21.66800543
10	300	10	0.04	10	24.9897114	8.054	29.523	19.09286635
10	300	10	0.05	5	-35.03781059	3.4684	26.88	193.2507625
10	300	10	0.05	6	-18.36385617	3.8451	27.778	109.6385949
10	300	10	0.05	7	-6.454807346	4.2784	28.326	62.95027207
10	300	10	0.05	8	2.476979268	4.7774	28.676	46.18075074
10	300	10	0.05	9	9.421780956	5.3517	28.928	35.71707235
10	300	10	0.05	10	14.98405268	6.0072	29.127	28.04330437
10	300	20	0.02	5	28.32707444	6.9726	29.379	17.58485763
10	300	20	0.02	6	34.44235815	9.0626	31.376	12.08555572
10	300	20	0.02	7	38.80624646	11.716	36.269	8.462888351
10	300	20	0.02	8	42.08099696	14.979	43.764	5.595359735
10	300	20	0.02	9	44.62793225	18.932	51.635	3.873695792
10	300	20	0.02	10	46.66551777	23.633	59.802	2.784442325
10	300	20	0.03	5	9.987653686	4.5353	28.513	34.36143052
10	300	20	0.03	6	19.15736406	5.3708	28.959	22.77912292
10	300	20	0.03	7	25.70991306	6.3873	29.254	18.76499879
10	300	20	0.03	8	30.61628685	7.6123	29.491	15.51183057
10	300	20	0.03	9	34.44235815	9.0626	31.376	12.08555572
10	300	20	0.03	10	37.49678481	10.766	33.856	9.117867466
10	300	20	0.04	5	-8.351767066	3.707	27.342	63.15117312
10	300	20	0.04	6	3.87880035	4.1804	28.183	41.46215304
10	300	20	0.04	7	12.61124543	4.73	28.657	27.38991034
10	300	20	0.04	8	19.15736406	5.3708	28.959	22.77912292
10	300	20	0.04	9	24.25021863	6.1159	29.189	19.96404222
10	300	20	0.04	10	28.32707444	6.9726	29.379	17.58485763

10	300	20	0.05	5	-26.68475745	3.2857	25.726	185.0642204
10	300	20	0.05	6	-11.40619373	3.6196	27.101	102.996713
10	300	20	0.05	7	-0.487422192	3.9832	27.909	58.55754131
10	300	20	0.05	8	7.698441278	4.3895	28.398	42.74015102
10	300	20	0.05	9	14.06450949	4.8497	28.723	32.96922291
10	300	20	0.05	10	19.15736406	5.3708	28.959	25.85149284
10	300	30	0.02	5	29.40094655	5.831	29.32	17.10627257
10	300	30	0.02	6	35.32974947	7.289	29.529	12.46691359
10	300	30	0.02	7	39.57161505	9.1124	32.779	9.09079743
10	300	30	0.02	8	42.75063661	11.339	36.314	6.546579125
10	300	30	0.02	9	45.2232175	14.007	42.616	4.556595714
10	300	30	0.02	10	47.20127707	17.153	49.203	3.285533048
10	300	30	0.03	5	11.59524667	4.1066	28.805	33.0209648
10	300	30	0.03	6	20.49488142	4.6999	29.069	22.03098704
10	300	30	0.03	7	26.85451927	5.4197	29.244	18.22386588
10	300	30	0.03	8	31.62585524	6.2787	29.392	15.11008476
10	300	30	0.03	9	35.32974947	7.289	29.529	12.46691359
10	300	30	0.03	10	38.30000257	8.4617	31.438	9.532734544
10	300	30	0.04	5	-6.204022841	3.5225	28.16	59.52817099
10	300	30	0.04	6	5.660013375	3.8533	28.605	39.65889476
10	300	30	0.04	7	14.14167395	4.2438	28.885	26.38107267
10	300	30	0.04	8	20.49488142	4.6999	29.069	22.03098704
10	300	30	0.04	9	25.43983744	5.2271	29.205	19.3710862
10	300	30	0.04	10	29.40094655	5.831	29.32	17.10627257
10	300	30	0.05	5	-24.00972272	3.2449	27.449	168.388213
10	300	30	0.05	6	-9.174854674	3.4629	28.043	96.63349725
10	300	30	0.05	7	1.422398272	3.7141	28.452	55.76449801
10	300	30	0.05	8	9.37033798	4.002	28.733	41.00967451
10	300	30	0.05	9	15.54992541	4.3296	28.928	31.78070948
10	300	30	0.05	10	20.49488142	4.6999	29.069	25.00245097
10	300	40	0.02	5	28.24990997	4.1274	25.16	20.57978043
10	300	40	0.02	6	34.37805443	4.9837	26.785	14.18887812
10	300	40	0.02	7	38.75132466	5.9435	27.612	11.14119655
10	300	40	0.02	8	42.03289778	7.0811	28.25	8.687645242
10	300	40	0.02	9	44.58521529	8.4319	31.33	6.398597708
10	300	40	0.02	10	46.62707701	9.995	33.983	4.910975049
10	300	40	0.03	5	9.871906991	2.8631	19.375	50.68132338
10	300	40	0.03	6	19.06090848	3.3448	22.21	29.76785271
10	300	40	0.03	7	25.62631823	3.8752	24.51	22.44739735
10	300	40	0.03	8	30.54555275	4.4178	25.954	17.66541153
10	300	40	0.03	9	34.37805443	4.9837	26.785	14.18887812
10	300	40	0.03	10	37.43869926	5.6061	27.368	11.30476055
10	300	40	0.04	5	-8.506095993	2.2555	14.185	121.999449
10	300	40	0.04	6	3.750192911	2.629	17.614	66.49003886

10	300	40	0.04	7	12.50192911	3.0101	20.501	38.37265035
10	300	40	0.04	8	19.06090848	3.3448	22.21	29.76785271
10	300	40	0.04	9	24.1666238	3.7383	23.987	24.3482229
10	300	40	0.04	10	28.24990997	4.1274	25.16	20.57978043
10	300	40	0.05	5	-26.8776686	1.8862	11.594	411.5635828
10	300	40	0.05	6	-11.56695303	2.2129	13.815	202.5038572
10	300	40	0.05	7	-0.628890375	2.4646	16.133	101.5283862
10	300	40	0.05	8	7.576264211	2.8174	19.283	63.08479757
10	300	40	0.05	9	13.95519317	3.0446	20.512	46.27069354
10	300	40	0.05	10	19.06090848	3.3448	22.21	33.78283853
10	300	50	0.02	5	24.256649	2.9626	22.416	25.61181381
10	300	50	0.02	6	31.05355214	3.3253	24.74	17.03284107
10	300	50	0.02	7	35.90088225	3.6708	26.101	13.0683162
10	300	50	0.02	8	39.53874942	4.0437	27.098	10.04223482
10	300	50	0.02	9	42.3682031	4.4384	27.709	8.021792586
10	300	50	0.02	10	44.63176475	4.8744	28.158	6.571654442
10	300	50	0.03	5	3.885230722	2.2699	15.471	70.37499092
10	300	50	0.03	6	14.07093986	2.5712	18.871	38.84617232
10	300	50	0.03	7	21.35012089	2.8407	21.446	28.44527155
10	300	50	0.03	8	26.80307629	3.0845	23.294	21.82383495
10	300	50	0.03	9	31.05355214	3.3253	24.74	17.03284107
10	300	50	0.03	10	34.44878852	3.5588	25.761	13.31646008
10	300	50	0.04	5	-16.48618756	1.8615	10.433	183.9183585
10	300	50	0.04	6	-2.905242039	2.1173	13.621	95.3350648
10	300	50	0.04	7	6.798189207	2.3527	16.458	52.99890103
10	300	50	0.04	8	14.07093986	2.5712	18.871	38.84617232
10	300	50	0.04	9	19.72966716	2.7714	20.814	31.11248742
10	300	50	0.04	10	24.256649	2.9626	22.416	25.61181381
10	300	50	0.05	5	-36.85760584	1.5788	8.9196	593.1601094
10	300	50	0.05	6	-19.88142394	1.8129	10.163	305.2174389
10	300	50	0.05	7	-7.753742476	2.026	12.49	145.407651
10	300	50	0.05	8	1.338803436	2.2177	14.859	90.77302586
10	300	50	0.05	9	8.412212562	2.3956	16.946	62.10032815
10	300	50	0.05	10	14.07093986	2.5712	18.871	44.08561073
10	450	10	0.02	5	4.97839395	5.1678	35.308	15.96461689
10	450	10	0.02	6	14.98405268	6.9759	42.527	9.728708867
10	450	10	0.02	7	22.12819589	9.277	47.295	7.081001986
10	450	10	0.02	8	27.48469571	12.128	49.902	5.354054948
10	450	10	0.02	9	31.6580071	15.592	51.03	4.276612274
10	450	10	0.02	10	34.98893976	19.723	53.502	3.39578098
10	450	10	0.03	5	-25.03215186	3.0882	21.353	50.06232359
10	450	10	0.03	6	-10.03009414	3.7926	26.032	27.64832186
10	450	10	0.03	7	0.689335871	4.6633	32.397	18.4877796
10	450	10	0.03	8	8.727300787	5.719	37.98	13.14175434

10	450	10	0.03	9	14.98405268	6.9759	42.527	9.728708867
10	450	10	0.03	10	19.98688204	8.4517	45.969	7.3268891
10	450	10	0.04	5	-55.04912804	2.4086	20.626	91.33819844
10	450	10	0.04	6	-35.03781059	2.7917	21.121	60.36432485
10	450	10	0.04	7	-20.74952415	3.2497	21.45	39.92544735
10	450	10	0.04	8	-10.03009414	3.7926	26.032	27.64832186
10	450	10	0.04	9	-1.689901744	4.4294	30.865	20.5995232
10	450	10	0.04	10	4.97839395	5.1678	35.308	15.96461689
10	450	10	0.05	5	-85.05967385	2.087	19.785	262.551453
10	450	10	0.05	6	-60.05195741	2.3394	20.488	148.6499848
10	450	10	0.05	7	-42.1819538	2.63	20.949	85.1176384
10	450	10	0.05	8	-28.78748907	2.9653	21.267	62.26920619
10	450	10	0.05	9	-18.36385617	3.3516	22.013	46.93696765
10	450	10	0.05	10	-10.03009414	3.7926	26.032	31.37743263
10	450	20	0.02	5	9.987653686	4.4349	30.326	17.03572949
10	450	20	0.02	6	19.15736406	5.8285	38.214	9.92297054
10	450	20	0.02	7	25.70991306	7.5925	44.287	6.930713247
10	450	20	0.02	8	30.61628685	9.7593	48.351	5.064534827
10	450	20	0.02	9	34.44235815	12.38	50.716	3.943889152
10	450	20	0.02	10	37.49636684	15.497	51.793	3.215013997
10	450	20	0.03	5	-17.52147744	2.8077	21.132	46.36321542
10	450	20	0.03	6	-3.766911878	3.3651	21.554	30.6050209
10	450	20	0.03	7	6.058696435	4.0443	27.395	20.03837469
10	450	20	0.03	8	13.42790267	4.8617	33.13	13.80801073
10	450	20	0.03	9	19.15736406	5.8285	38.214	9.92297054
10	450	20	0.03	10	23.74221925	6.9612	42.486	7.26579393
10	450	20	0.04	5	-45.0241782	2.2561	20.121	85.81478929
10	450	20	0.04	6	-26.68475745	2.5708	20.833	56.09023469
10	450	20	0.04	7	-13.58608982	2.9372	21.264	36.91274739
10	450	20	0.04	8	-3.766911878	3.3651	21.554	30.6050209
10	450	20	0.04	9	3.87880035	3.8628	25.9	22.49924434
10	450	20	0.04	10	9.987653686	4.4349	30.326	17.03572949
10	450	20	0.05	5	-72.53330933	1.9781	18.847	252.6111389
10	450	20	0.05	6	-49.60903339	2.1982	19.924	140.0980687
10	450	20	0.05	7	-33.23730645	2.4395	20.595	79.3533586
10	450	20	0.05	8	-20.95529605	2.7102	21.026	57.72542608
10	450	20	0.05	9	-11.40619373	3.0172	21.327	44.40263467
10	450	20	0.05	10	-3.766911878	3.3651	21.554	34.73292109
10	450	30	0.02	5	11.59524667	3.6617	24.12	20.79419203
10	450	30	0.02	6	20.49488142	4.6336	31.896	11.54174478
10	450	30	0.02	7	26.85451927	5.8487	38.861	7.66802833
10	450	30	0.02	8	31.62585524	7.3314	44.522	5.339662961
10	450	30	0.02	9	35.32974947	9.1068	48.717	3.985957324
10	450	30	0.02	10	38.30000257	11.201	51.542	3.136434026

10	450	30	0.03	5	-15.11008797	2.5126	21.282	44.69358572
10	450	30	0.03	6	-1.754205463	2.9078	21.556	29.7095362
10	450	30	0.03	7	7.782036113	3.3875	21.751	24.50180377
10	450	30	0.03	8	14.9326097	3.9601	26.758	16.59748903
10	450	30	0.03	9	20.49488142	4.6336	31.896	11.54174478
10	450	30	0.03	10	24.95112917	5.4152	36.667	8.173292296
10	450	30	0.04	5	-41.80899223	2.1218	20.695	81.00088403
10	450	30	0.04	6	-24.00972272	2.3436	21.09	53.79054929
10	450	30	0.04	7	-11.29044704	2.6041	21.362	35.67162645
10	450	30	0.04	8	-1.754205463	2.9078	21.556	29.7095362
10	450	30	0.04	9	5.660013375	3.2592	21.707	26.06221829
10	450	30	0.04	10	11.59524667	3.6617	24.12	20.79419203
10	450	30	0.05	5	-68.51432687	1.9326	20.113	229.8059991
10	450	30	0.05	6	-46.26523998	2.0816	20.596	131.5737601
10	450	30	0.05	7	-30.36936056	2.2506	20.95	75.73324569
10	450	30	0.05	8	-18.447451	2.4429	21.211	55.55282531
10	450	30	0.05	9	-9.174854674	2.6612	21.405	42.9503557
10	450	30	0.05	10	-1.754205463	2.9078	21.556	33.71665648
10	450	40	0.02	5	9.871906991	2.5607	18.083	28.63392554
10	450	40	0.02	6	19.06090848	3.1247	19.998	19.00435546
10	450	40	0.02	7	25.62631823	3.765	26.011	11.82694702
10	450	40	0.02	8	30.54555275	4.5234	31.835	7.70931296
10	450	40	0.02	9	34.37805443	5.421	37.182	5.391535318
10	450	40	0.02	10	37.43869926	6.4586	41.782	3.994295752
10	450	40	0.03	5	-17.68866711	1.7561	13.558	72.42592126
10	450	40	0.03	6	-3.908380061	2.0579	15.699	42.11376577
10	450	40	0.03	7	5.936519368	2.3953	17.533	31.38000964
10	450	40	0.03	8	13.31858635	2.7492	18.757	24.44357258
10	450	40	0.03	9	19.06090848	3.1247	19.998	19.00435546
10	450	40	0.03	10	23.65862441	3.5397	24.012	12.8847529
10	450	40	0.04	5	-45.25567159	1.3856	9.9031	174.7495414
10	450	40	0.04	6	-26.8776686	1.6116	12.283	95.34767927
10	450	40	0.04	7	-13.75327949	1.8442	14.379	54.71018185
10	450	40	0.04	8	-3.908380061	2.0579	15.699	42.11376577
10	450	40	0.04	9	3.750192911	2.3076	17.106	34.14245427
10	450	40	0.04	10	9.871906991	2.5607	18.083	28.63392554
10	450	40	0.05	5	-72.82267606	1.1598	7.3263	651.3066867
10	450	40	0.05	6	-49.85338752	1.3566	9.6339	290.3902664
10	450	40	0.05	7	-33.44307835	1.5136	11.25	145.5962182
10	450	40	0.05	8	-21.13534647	1.7223	13.464	90.34938737
10	450	40	0.05	9	-11.56695303	1.87	14.406	65.88258127
10	450	40	0.05	10	-3.908380061	2.0579	15.699	47.79392597
10	450	50	0.02	5	3.885230722	1.7735	15.527	36.97523142
10	450	50	0.02	6	14.07093986	2.0072	17.488	24.09609378

10	450	50	0.02	7	21.35012089	2.235	18.701	18.23945892
10	450	50	0.02	8	26.80307629	2.4822	19.63	13.8626836
10	450	50	0.02	9	31.05355214	2.7451	20.223	10.99124021
10	450	50	0.02	10	34.44878852	3.0357	20.671	8.951896172
10	450	50	0.03	5	-26.6718967	1.3493	10.219	106.5438384
10	450	50	0.03	6	-11.39333299	1.5298	12.731	57.58118905
10	450	50	0.03	7	-0.480991821	1.6962	14.74	41.38651925
10	450	50	0.03	8	7.70487165	1.8514	16.254	31.27626501
10	450	50	0.03	9	14.07093986	2.0072	17.488	24.09609378
10	450	50	0.03	10	19.16379443	2.1607	18.393	18.65086327
10	450	50	0.04	5	-57.22902413	1.1064	6.6957	286.575001
10	450	50	0.04	6	-36.85760584	1.2583	8.9016	145.8792709
10	450	50	0.04	7	-22.30567416	1.3982	10.933	79.78193663
10	450	50	0.04	8	-11.39333299	1.5298	12.731	57.58118905
10	450	50	0.04	9	-2.905242039	1.6532	14.238	45.48218242
10	450	50	0.04	10	3.885230722	1.7735	15.527	36.97523142
10	450	50	0.05	5	-87.78615155	0.93717	4.5125	1172.465576
10	450	50	0.05	6	-62.3218787	1.0771	6.2884	493.2772774
10	450	50	0.05	7	-44.1303565	1.2036	8.1085	223.9799669
10	450	50	0.05	8	-30.49153763	1.3175	9.7779	137.9433612
10	450	50	0.05	9	-19.88142394	1.424	11.292	93.1944882
10	450	50	0.05	10	-11.39333299	1.5298	12.731	65.34754223
15	150	10	0.02	5	44.99531869	54.897	126.29	4.463367592
15	150	10	0.02	6	48.33007099	73.217	127.43	3.24674568
15	150	10	0.02	7	50.71203508	96.656	134.06	2.498105243
15	150	10	0.02	8	52.49850815	125.75	158.11	1.689823857
15	150	10	0.02	9	53.88798935	161.15	183.47	1.189488877
15	150	10	0.02	10	54.99956917	203.21	209.88	0.865642624
15	150	10	0.03	5	34.98893976	33.887	123.95	8.624290404
15	150	10	0.03	6	39.99319024	41.001	124.91	5.762077613
15	150	10	0.03	7	43.56613638	49.788	125.82	4.760360798
15	150	10	0.03	8	46.24585241	60.465	126.7	3.939414599
15	150	10	0.03	9	48.33007099	73.217	127.43	3.24674568
15	150	10	0.03	10	49.99744714	88.239	127.97	2.631943151
15	150	10	0.04	5	24.9897114	27.01	121.9	15.45481281
15	150	10	0.04	6	31.6580071	30.886	123.34	10.33691345
15	150	10	0.04	7	36.4202441	35.519	124.21	6.894781785
15	150	10	0.04	8	39.99319024	41.001	124.91	5.762077613
15	150	10	0.04	9	42.77215263	47.427	125.59	5.062539083
15	150	10	0.04	10	44.99531869	54.897	126.29	4.463367592
15	150	10	0.05	5	14.98405268	23.77	118.83	43.71438607
15	150	10	0.05	6	23.3178147	26.308	121.44	25.07856463
15	150	10	0.05	7	29.27233911	29.249	122.87	14.51232528
15	150	10	0.05	8	33.74144761	32.644	123.73	10.7029759

15	150	10	0.05	9	37.21423427	36.551	124.36	8.308326382
15	150	10	0.05	10	39.99319024	41.001	124.91	6.539246868
15	150	20	0.02	5	46.66551777	47.675	125.72	4.109334493
15	150	20	0.02	6	49.72190571	61.876	126.9	2.98815127
15	150	20	0.02	7	51.90503627	78.885	127.85	2.400786059
15	150	20	0.02	8	53.54238258	102.01	142.61	1.717097843
15	150	20	0.02	9	54.81587916	128.76	164.53	1.215694902
15	150	20	0.02	10	55.83467514	160.47	187.42	0.888460249
15	150	20	0.03	5	37.49636684	31.044	123.41	7.938963361
15	150	20	0.03	6	42.08094552	36.761	124.5	5.298478879
15	150	20	0.03	7	45.35563815	43.691	125.32	4.380396382
15	150	20	0.03	8	47.81166084	52.025	126.13	3.626888095
15	150	20	0.03	9	49.72190571	61.876	126.9	2.98815127
15	150	20	0.03	10	51.25009646	73.438	127.57	2.419804977
15	150	20	0.04	5	28.32707444	25.394	120.48	14.33166812
15	150	20	0.04	6	34.44235815	28.618	122.64	9.52811366
15	150	20	0.04	7	38.80624646	32.379	123.76	6.342216067
15	150	20	0.04	8	42.08094552	36.761	124.5	5.298478879
15	150	20	0.04	9	44.62793225	41.844	125.12	4.65737235
15	150	20	0.04	10	46.66551777	47.675	125.72	4.109334493
15	150	20	0.05	5	19.15736406	22.554	115.73	41.1385305
15	150	20	0.05	6	26.79664592	24.803	119.82	23.29589317
15	150	20	0.05	7	32.25603169	27.272	121.96	13.40015104
15	150	20	0.05	8	36.35022378	30.048	123.15	9.855743474
15	150	20	0.05	9	39.53395879	33.197	123.92	7.641825288
15	150	20	0.05	10	42.08094552	36.761	124.5	6.013119528
15	150	30	0.02	5	47.20127707	39.893	125.78	3.98756489
15	150	30	0.02	6	50.16836643	49.703	126.42	2.912003571
15	150	30	0.02	7	52.28772056	61.908	127.12	2.344141354
15	150	30	0.02	8	53.87723134	76.768	127.7	1.861648194
15	150	30	0.02	9	55.11352179	94.535	144.17	1.346909086
15	150	30	0.02	10	56.10255157	115.44	162.71	0.993535017
15	150	30	0.03	5	38.30000257	28.145	124.82	7.620324397
15	150	30	0.03	6	42.75063661	32.208	125.26	5.112715649
15	150	30	0.03	7	45.92966459	37.105	125.59	4.243480641
15	150	30	0.03	8	48.31393719	42.911	125.97	3.525566495
15	150	30	0.03	9	50.16836643	49.703	126.42	2.912003571
15	150	30	0.03	10	51.65191111	57.558	126.89	2.361810297
15	150	30	0.04	5	29.40094655	24.16	123.46	13.57778467
15	150	30	0.04	6	35.32974947	26.411	124.45	9.115650338
15	150	30	0.04	7	39.57161505	29.086	124.95	6.098577704
15	150	30	0.04	8	42.75063661	32.208	125.26	5.112715649
15	150	30	0.04	9	45.2232175	35.798	125.5	4.507829262
15	150	30	0.04	10	47.20127707	39.893	125.78	3.98756489

15	150	30	0.05	5	20.49488142	22.31	121.47	38.05127241
15	150	30	0.05	6	27.91553063	23.758	123.16	22.00302991
15	150	30	0.05	7	33.21415711	25.461	124.14	12.78082405
15	150	30	0.05	8	37.18734246	27.428	124.69	9.45008403
15	150	30	0.05	9	40.27806214	29.674	125.02	7.353642327
15	150	30	0.05	10	42.75063661	32.208	125.26	5.802301191
15	150	40	0.02	5	46.62707701	28.52	114.12	4.537217627
15	150	40	0.02	6	49.68986959	34.301	118.75	3.200413478
15	150	40	0.02	7	51.87757858	40.804	121.09	2.540512999
15	150	40	0.02	8	53.51835871	48.527	123.01	1.995170946
15	150	40	0.02	9	54.7945239	57.719	124.78	1.606572096
15	150	40	0.02	10	55.81544833	68.366	126.18	1.322631678
15	150	40	0.03	5	37.43869926	19.869	94.837	10.35408797
15	150	40	0.03	6	42.03289135	23.212	104.85	6.305617632
15	150	40	0.03	7	45.31445162	26.819	112.22	4.902742017
15	150	40	0.03	8	47.77562503	30.478	116.44	3.937548015
15	150	40	0.03	9	49.68986959	34.301	118.75	3.200413478
15	150	40	0.03	10	51.22126267	38.513	120.38	2.570100405
15	150	40	0.04	5	28.24990997	15.427	73.517	23.53961919
15	150	40	0.04	6	34.37805443	18.197	88.062	13.29921583
15	150	40	0.04	7	38.75132466	20.92	99.055	7.941827316
15	150	40	0.04	8	42.03289135	23.212	104.85	6.305617632
15	150	40	0.04	9	44.58521529	25.893	110.6	5.280658433
15	150	40	0.04	10	46.62707701	28.52	114.12	4.537217627
15	150	40	0.05	5	19.06090848	12.66	55.59	85.83680839
15	150	40	0.05	6	26.71948145	15.142	72.037	38.83547049
15	150	40	0.05	7	32.1852976	16.974	81.896	20.00045734
15	150	40	0.05	8	36.29015767	19.584	94.695	12.84612864
15	150	40	0.05	9	39.48056099	21.135	98.952	9.591564252
15	150	40	0.05	10	42.03289135	23.212	104.85	7.1560977
15	150	50	0.02	5	44.63176475	20.747	106.98	5.366558406
15	150	50	0.02	6	48.02711045	23.074	113.97	3.697398332
15	150	50	0.02	7	50.45235737	25.33	117.67	2.898751774
15	150	50	0.02	8	52.27129096	27.793	120.19	2.264119137
15	150	50	0.02	9	53.6860178	30.441	121.66	1.827024912
15	150	50	0.02	10	54.81779541	33.377	122.71	1.507983422
15	150	50	0.03	5	34.44878852	16.077	81.652	13.33429046
15	150	50	0.03	6	39.53874942	18.182	94.884	7.725919205
15	150	50	0.03	7	43.1766166	19.96	103.85	5.874215635
15	150	50	0.03	8	45.90501698	21.53	109.71	4.633710796
15	150	50	0.03	9	48.02711045	23.074	113.97	3.697398332
15	150	50	0.03	10	49.72478008	24.589	116.78	2.937534922
15	150	50	0.04	5	24.256649	13.037	59.227	32.39772797
15	150	50	0.04	6	31.05355214	14.964	73.808	17.59374211

15	150	50	0.04	7	35.90088225	16.672	85.66	10.18276807
15	150	50	0.04	8	39.53874942	18.182	94.884	7.725919205
15	150	50	0.04	9	42.3682031	19.509	101.73	6.365627772
15	150	50	0.04	10	44.63176475	20.747	106.98	5.366558406
15	150	50	0.05	5	14.07093986	10.93	44.668	118.4461116
15	150	50	0.05	6	22.55903081	12.674	56.376	55.02208087
15	150	50	0.05	7	28.62287155	14.287	68.798	26.39817381
15	150	50	0.05	8	33.17557488	15.705	79.122	17.04704622
15	150	50	0.05	9	36.70929575	16.973	87.588	12.01479838
15	150	50	0.05	10	39.53874942	18.182	94.884	8.767964674
15	300	10	0.02	5	24.9897114	18.207	67.34	8.370636966
15	300	10	0.02	6	31.6580071	24.291	76.485	5.409332575
15	300	10	0.02	7	36.4202441	32.06	95.476	3.507645785
15	300	10	0.02	8	39.99369824	41.704	115.53	2.312629187
15	300	10	0.02	9	42.77215263	53.44	136.44	1.599498126
15	300	10	0.02	10	44.99537013	67.457	158.07	1.149371
15	300	10	0.03	5	4.97839395	11.23	65.583	16.29966296
15	300	10	0.03	6	14.98405268	13.592	66.418	10.836537
15	300	10	0.03	7	22.12819589	16.512	67.069	8.930334366
15	300	10	0.03	8	27.48469571	20.059	70.156	7.114485285
15	300	10	0.03	9	31.6580071	24.291	76.485	5.409332575
15	300	10	0.03	10	34.98893976	29.271	89.013	3.783826688
15	300	10	0.04	5	-15.0329235	8.9474	63.683	29.58311765
15	300	10	0.04	6	-1.689901744	10.235	65.004	19.61348387
15	300	10	0.04	7	7.833479088	11.772	65.818	13.011651
15	300	10	0.04	8	14.98405268	13.592	66.418	10.836537
15	300	10	0.04	9	20.53989403	15.727	66.921	9.500818629
15	300	10	0.04	10	24.9897114	18.207	67.34	8.370636966
15	300	10	0.05	5	-35.03781059	7.8633	61.232	84.83440843
15	300	10	0.05	6	-18.36385617	8.714	63.294	48.11737113
15	300	10	0.05	7	-6.454807346	9.6921	64.56	27.61972439
15	300	10	0.05	8	2.476979268	10.818	65.37	20.25821031
15	300	10	0.05	9	9.421780956	12.114	65.954	15.66581965
15	300	10	0.05	10	14.98405268	13.592	66.418	12.29813193
15	300	20	0.02	5	28.32707444	15.769	67.005	7.71025345
15	300	20	0.02	6	34.44235815	20.481	71.169	5.32811906
15	300	20	0.02	7	38.80624646	26.462	82.446	3.722927705
15	300	20	0.02	8	42.08099696	33.817	99.48	2.461553312
15	300	20	0.02	9	44.62793225	42.727	117.37	1.704168716
15	300	20	0.02	10	46.66551777	53.322	135.95	1.224826921
15	300	20	0.03	5	9.987653686	10.272	64.998	15.07350177
15	300	20	0.03	6	19.15736406	12.157	66.031	9.990165536
15	300	20	0.03	7	25.70991306	14.449	66.714	8.228426935
15	300	20	0.03	8	30.61628685	17.212	67.266	6.80075217

15	300	20	0.03	9	34.44235815	20.481	71.169	5.328111906
15	300	20	0.03	10	37.49678481	24.32	76.962	4.010999206
15	300	20	0.04	5	-8.351767066	8.4018	62.31	27.711111179
15	300	20	0.04	6	3.87880035	9.4708	64.239	18.19031833
15	300	20	0.04	7	12.61124543	10.711	65.331	12.01439838
15	300	20	0.04	8	19.15736406	12.157	66.031	9.990165536
15	300	20	0.04	9	24.25021863	13.837	66.564	8.754438262
15	300	20	0.04	10	28.32707444	15.769	67.005	7.71025345
15	300	20	0.05	5	-26.68475745	7.4499	58.611	81.2298397
15	300	20	0.05	6	-11.40619373	8.2044	61.756	45.19907248
15	300	20	0.05	7	-0.487422192	9.0255	63.609	25.69262872
15	300	20	0.05	8	7.698441278	9.9427	64.773	18.73828306
15	300	20	0.05	9	14.06450949	10.981	65.484	14.46116593
15	300	20	0.05	10	19.15736406	12.157	66.031	11.33760478
15	300	30	0.02	5	29.40094655	13.195	66.856	7.502032904
15	300	30	0.02	6	35.32974947	16.483	67.346	5.466330464
15	300	30	0.02	7	39.57161505	20.593	74.327	4.009138657
15	300	30	0.02	8	42.75063661	25.613	82.547	2.879965042
15	300	30	0.02	9	45.2232175	31.625	96.868	2.004623642
15	300	30	0.02	10	47.20127707	38.716	111.84	1.445440652
15	300	30	0.03	5	11.59524667	9.3047	65.653	14.48782068
15	300	30	0.03	6	20.49488142	10.643	66.267	9.664218423
15	300	30	0.03	7	26.85451927	12.267	66.678	7.992722243
15	300	30	0.03	8	31.62585524	14.205	67.026	6.626019924
15	300	30	0.03	9	35.32974947	16.483	67.346	5.466330464
15	300	30	0.03	10	38.30000257	19.126	71.269	4.205055615
15	300	30	0.04	5	-6.204022841	7.9861	64.164	26.12544877
15	300	30	0.04	6	5.660013375	8.733	65.19	17.40209671
15	300	30	0.04	7	14.14167395	9.6143	65.838	11.57412564
15	300	30	0.04	8	20.49488142	10.643	66.267	9.664218423
15	300	30	0.04	9	25.43983744	11.833	66.585	8.496396671
15	300	30	0.04	10	29.40094655	13.195	66.856	7.502032904
15	300	30	0.05	5	-24.00972272	7.3594	62.535	73.91201822
15	300	30	0.05	6	-9.174854674	7.8517	63.896	42.41099855
15	300	30	0.05	7	1.422398272	8.4189	64.836	24.47115024
15	300	30	0.05	8	9.37033798	9.0685	65.484	17.99418144
15	300	30	0.05	9	15.54992541	9.808	65.937	13.94289039
15	300	30	0.05	10	20.49488142	10.643	66.267	10.96769504
15	300	40	0.02	5	28.24990997	9.3468	57.372	9.025086726
15	300	40	0.02	6	34.37805443	11.281	61.086	6.22154177
15	300	40	0.02	7	38.75132466	13.447	62.981	4.88450039
15	300	40	0.02	8	42.03289778	16.013	64.444	3.808360407
15	300	40	0.02	9	44.58521529	19.059	71.055	2.821308369
15	300	40	0.02	10	46.62707701	22.584	77.113	2.164222182

15	300	40	0.03	5	9.871906991	6.4869	44.169	22.23167019
15	300	40	0.03	6	19.06090848	7.5772	50.638	13.05628202
15	300	40	0.03	7	25.62631823	8.777	55.887	9.844609822
15	300	40	0.03	8	30.54555275	10.003	59.184	7.746825002
15	300	40	0.03	9	34.37805443	11.281	61.086	6.22154177
15	300	40	0.03	10	37.43869926	12.685	62.423	4.95632518
15	300	40	0.04	5	-8.506095993	5.1097	32.329	53.52971586
15	300	40	0.04	6	3.750192911	5.9565	40.152	29.16805002
15	300	40	0.04	7	12.50192911	6.82	46.736	16.83237129
15	300	40	0.04	8	19.06090848	7.5772	50.638	13.05628202
15	300	40	0.04	9	24.1666238	8.4673	54.693	10.67852966
15	300	40	0.04	10	28.24990997	9.3468	57.372	9.025086726
15	300	40	0.05	5	-26.8776686	4.2716	26.431	180.5330172
15	300	40	0.05	6	-11.56695303	5.0134	31.483	88.86036233
15	300	40	0.05	7	-0.628890375	5.5837	36.771	44.54481669
15	300	40	0.05	8	7.576264211	6.3838	43.956	27.67458712
15	300	40	0.05	9	13.95519317	6.8977	46.764	20.29562197
15	300	40	0.05	10	19.06090848	7.5772	50.638	14.81726853
15	300	50	0.02	5	24.256649	6.7162	51.086	11.23819478
15	300	50	0.02	6	31.05355214	7.537	56.385	7.473485643
15	300	50	0.02	7	35.90088225	8.3182	59.494	5.733286066
15	300	50	0.02	8	39.53874942	9.1606	61.772	4.405304654
15	300	50	0.02	9	42.3682031	10.052	63.171	3.51863752
15	300	50	0.02	10	44.63176475	11.036	64.2	2.882315355
15	300	50	0.03	5	3.885230722	5.1463	35.252	30.88538195
15	300	50	0.03	6	14.07093986	5.8295	43.004	17.04646353
15	300	50	0.03	7	21.35012089	6.4402	48.874	12.48183684
15	300	50	0.03	8	26.80307629	6.9923	53.088	9.575881771
15	300	50	0.03	9	31.05355214	7.537	56.385	7.473485643
15	300	50	0.03	10	34.44878852	8.065	58.717	5.842351077
15	300	50	0.04	5	-16.48618756	4.2192	23.766	80.73803898
15	300	50	0.04	6	-2.905242039	4.8001	31.036	41.84040848
15	300	50	0.04	7	6.798189207	5.3342	37.503	23.25829702
15	300	50	0.04	8	14.07093986	5.8295	43.004	17.04646353
15	300	50	0.04	9	19.72966716	6.2831	47.434	13.65213377
15	300	50	0.04	10	24.256649	6.7162	51.086	11.23819478
15	300	50	0.05	5	-36.85760584	3.5769	20.186	262.1000155
15	300	50	0.05	6	-19.88142394	4.109	23.009	134.8135439
15	300	50	0.05	7	-7.753742476	4.5928	28.458	63.81831336
15	300	50	0.05	8	1.338803436	5.028	33.859	39.83568302
15	300	50	0.05	9	8.412212562	5.4314	38.615	27.25241903
15	300	50	0.05	10	14.07093986	5.8295	43.004	19.34563204
15	450	10	0.02	5	4.97839395	11.611	79.304	7.107821715
15	450	10	0.02	6	14.98405268	15.673	95.515	4.331600293

15	450	10	0.02	7	22.12819589	20.842	106.23	3.152555671
15	450	10	0.02	8	27.48469571	27.247	112.08	2.383815578
15	450	10	0.02	9	31.6580071	35.031	114.61	1.90415779
15	450	10	0.02	10	34.98893976	44.312	120.19	1.511615559
15	450	10	0.03	5	-25.03215186	6.9381	47.972	22.28343191
15	450	10	0.03	6	-10.03009414	8.5207	58.47	12.30957952
15	450	10	0.03	7	0.689335871	10.477	72.764	8.231386339
15	450	10	0.03	8	8.727300787	12.849	85.304	5.851118701
15	450	10	0.03	9	14.98405268	15.673	95.515	4.331600293
15	450	10	0.03	10	19.98688204	18.988	103.25	3.262080049
15	450	10	0.04	5	-55.04912804	5.4113	46.337	40.65739433
15	450	10	0.04	6	-35.03781059	6.2719	47.45	26.86943952
15	450	10	0.04	7	-20.74952415	7.3009	48.19	17.7713394
15	450	10	0.04	8	-10.03009414	8.5207	58.47	12.30957952
15	450	10	0.04	9	-1.689901744	9.9512	69.323	9.171621013
15	450	10	0.04	10	4.97839395	11.611	79.304	7.107821715
15	450	10	0.05	5	-85.05967385	4.6888	44.449	116.8660824
15	450	10	0.05	6	-60.05195741	5.2557	46.027	66.16857254
15	450	10	0.05	7	-42.1819538	5.9087	47.064	37.88733229
15	450	10	0.05	8	-28.78748907	6.662	47.777	27.71792302
15	450	10	0.05	9	-18.36385617	7.5299	49.442	20.89768757
15	450	10	0.05	10	-10.03009414	8.5207	58.47	13.96985337
15	450	20	0.02	5	9.987653686	9.9638	68.113	7.584830097
15	450	20	0.02	6	19.15736406	13.095	85.83	4.417993664
15	450	20	0.02	7	25.70991306	17.058	99.468	3.085821547
15	450	20	0.02	8	30.61628685	21.926	108.6	2.254837232
15	450	20	0.02	9	34.44235815	27.815	113.91	1.755932598
15	450	20	0.02	10	37.49636684	34.817	116.33	1.431403937
15	450	20	0.03	5	-17.52147744	6.3078	47.475	20.63712414
15	450	20	0.03	6	-3.766911878	7.5603	48.424	13.62259666
15	450	20	0.03	7	6.058696435	9.086	61.529	8.921829942
15	450	20	0.03	8	13.42790267	10.923	74.411	6.147738848
15	450	20	0.03	9	19.15736406	13.095	85.83	4.417993664
15	450	20	0.03	10	23.74221925	15.639	95.424	3.234977793
15	450	20	0.04	5	-45.0241782	5.0686	45.203	38.19833585
15	450	20	0.04	6	-26.68475745	5.7756	46.803	24.96694356
15	450	20	0.04	7	-13.58608982	6.5989	47.771	16.43073539
15	450	20	0.04	8	-3.766911878	7.5603	48.424	13.62259666
15	450	20	0.04	9	3.87880035	8.6783	58.171	10.01754188
15	450	20	0.04	10	9.987653686	9.9638	68.113	7.584830097
15	450	20	0.05	5	-72.53330933	4.4442	42.341	112.4433087
15	450	20	0.05	6	-49.60903339	4.9385	44.76	62.36179446
15	450	20	0.05	7	-33.23730645	5.4807	46.268	35.32208914
15	450	20	0.05	8	-20.95529605	6.0888	47.236	25.69512255

15	450	20	0.05	9	-11.40619373	6.7787	47.914	19.76405622
15	450	20	0.05	10	-3.766911878	7.5603	48.424	15.45996575
15	450	30	0.02	5	11.59524667	8.2266	54.174	9.258240333
15	450	30	0.02	6	20.49488142	10.41	71.639	5.138758099
15	450	30	0.02	7	26.85451927	13.14	87.283	3.414035367
15	450	30	0.02	8	31.62585524	16.471	99.996	2.37741984
15	450	30	0.02	9	35.32974947	20.46	109.42	1.774665353
15	450	30	0.02	10	38.30000257	25.165	115.76	1.396493457
15	450	30	0.03	5	-15.11008797	5.6451	47.812	19.89393648
15	450	30	0.03	6	-1.754205463	6.5329	48.427	13.22441535
15	450	30	0.03	7	7.782036113	7.6105	48.866	10.9061256
15	450	30	0.03	8	14.9326097	8.897	60.099	7.389733796
15	450	30	0.03	9	20.49488142	10.41	71.639	5.138758099
15	450	30	0.03	10	24.95112917	12.166	82.355	3.639003201
15	450	30	0.04	5	-41.80899223	4.767	46.493	36.05517594
15	450	30	0.04	6	-24.00972272	5.2653	47.381	23.94298737
15	450	30	0.04	7	-11.29044704	5.8504	47.991	15.87833727
15	450	30	0.04	8	-1.754205463	6.5329	48.427	13.22441535
15	450	30	0.04	9	5.660013375	7.3222	48.767	11.60072533
15	450	30	0.04	10	11.59524667	8.2266	54.174	9.258240333
15	450	30	0.05	5	-68.51432687	4.3418	45.186	102.2902682
15	450	30	0.05	6	-46.26523998	4.6766	46.27	58.56695836
15	450	30	0.05	7	-30.36936056	5.0563	47.066	33.71035349
15	450	30	0.05	8	-18.447451	5.4883	47.652	24.72783887
15	450	30	0.05	9	-9.174854674	5.9788	48.089	19.11772679
15	450	30	0.05	10	-1.754205463	6.5329	48.427	15.00807911
15	450	40	0.02	5	9.871906991	5.7519	40.612	12.74961281
15	450	40	0.02	6	19.06090848	7.0189	44.93	8.458693536
15	450	40	0.02	7	25.62631823	8.4571	58.44	5.26404379
15	450	40	0.02	8	30.54555275	10.161	71.527	3.431235451
15	450	40	0.02	9	34.37805443	12.177	83.541	2.399636899
15	450	40	0.02	10	37.43869926	14.508	93.878	1.777729235
15	450	40	0.03	5	-17.68866711	3.9445	30.45	32.24796849
15	450	40	0.03	6	-3.908380061	4.6224	35.258	18.75160272
15	450	40	0.03	7	5.936519368	5.3803	39.377	13.97226069
15	450	40	0.03	8	13.31858635	6.1753	42.125	10.88399029
15	450	40	0.03	9	19.06090848	7.0189	44.93	8.458693536
15	450	40	0.03	10	23.65862441	7.9511	53.949	5.734836359
15	450	40	0.04	5	-45.25567159	3.1125	22.242	77.80605089
15	450	40	0.04	6	-26.8776686	3.6201	27.587	42.45316796
15	450	40	0.04	7	-13.75327949	4.1424	32.294	24.35987195
15	450	40	0.04	8	-3.908380061	4.6224	35.258	18.75160272
15	450	40	0.04	9	3.750192911	5.1834	38.418	15.20227036
15	450	40	0.04	10	9.871906991	5.7519	40.612	12.74961281

15	450	40	0.05	5	-72.82267606	2.6053	16.455	289.9828732
15	450	40	0.05	6	-49.85338752	3.0472	21.638	129.2906363
15	450	40	0.05	7	-33.44307835	3.4	25.268	64.82339143
15	450	40	0.05	8	-21.13534647	3.8686	30.24	40.22698914
15	450	40	0.05	9	-11.56695303	4.2004	32.355	29.3340895
15	450	40	0.05	10	-3.908380061	4.6224	35.258	21.28075455
15	450	50	0.02	5	3.885230722	3.9835	34.871	16.46395051
15	450	50	0.02	6	14.07093986	4.5086	39.275	10.72928041
15	450	50	0.02	7	21.35012089	5.0202	42	8.12133622
15	450	50	0.02	8	26.80307629	5.5755	44.086	6.172582658
15	450	50	0.02	9	31.05355214	6.166	45.417	4.894111253
15	450	50	0.02	10	34.44878852	6.8187	46.424	3.98596945
15	450	50	0.03	5	-26.6718967	3.0309	22.951	47.43895624
15	450	50	0.03	6	-11.39333299	3.4363	28.593	25.63795747
15	450	50	0.03	7	-0.480991821	3.81	33.105	18.42734613
15	450	50	0.03	8	7.70487165	4.1585	36.504	13.92626593
15	450	50	0.03	9	14.07093986	4.5086	39.275	10.72928041
15	450	50	0.03	10	19.16379443	4.8532	41.307	8.304774692
15	450	50	0.04	5	-57.22902413	2.4854	15.039	127.589616
15	450	50	0.04	6	-36.85760584	2.8265	19.993	64.95067862
15	450	50	0.04	7	-22.30567416	3.1407	24.555	35.5225377
15	450	50	0.04	8	-11.39333299	3.4363	28.593	25.63795747
15	450	50	0.04	9	-2.905242039	3.7135	31.977	20.25128415
15	450	50	0.04	10	3.885230722	3.9835	34.871	16.46395051
15	450	50	0.05	5	-87.78615155	2.1052	10.137	521.9247225
15	450	50	0.05	6	-62.3218787	2.4195	14.124	219.6208462
15	450	50	0.05	7	-44.1303565	2.7035	18.211	99.72772289
15	450	50	0.05	8	-30.49153763	2.9595	21.961	61.41780389
15	450	50	0.05	9	-19.88142394	3.1986	25.36	41.49653631
15	450	50	0.05	10	-11.39333299	3.4363	28.593	29.09591719
20	150	10	0.02	5	44.99531869	96.759	222.77	2.530316889
20	150	10	0.02	6	48.33007099	129.06	224.84	1.840120984
20	150	10	0.02	7	50.71203508	170.38	236.39	1.416709628
20	150	10	0.02	8	52.49850815	221.67	278.79	0.958348757
20	150	10	0.02	9	53.88798935	284.07	323.49	0.674628348
20	150	10	0.02	10	54.99956917	358.22	370.05	0.490963583
20	150	10	0.03	5	34.98893976	59.74	218.69	4.88811009
20	150	10	0.03	6	39.99319024	72.278	220.37	3.266057606
20	150	10	0.03	7	43.56613638	87.766	221.97	2.698331286
20	150	10	0.03	8	46.24585241	106.58	223.52	2.233016418
20	150	10	0.03	9	48.33007099	129.06	224.84	1.840120984
20	150	10	0.03	10	49.99744714	155.54	225.77	1.491826926
20	150	10	0.04	5	24.9897114	47.618	215.07	8.759667462
20	150	10	0.04	6	31.6580071	54.45	217.61	5.858898512

20	150	10	0.04	7	36.4202441	62.615	219.13	3.908186216
20	150	10	0.04	8	39.99319024	72.278	220.37	3.266057606
20	150	10	0.04	9	42.77215263	83.605	221.58	2.869411876
20	150	10	0.04	10	44.99531869	96.759	222.77	2.530316889
20	150	10	0.05	5	14.98405268	41.907	209.65	24.77739326
20	150	10	0.05	6	23.3178147	46.381	214.26	14.21422985
20	150	10	0.05	7	29.27233911	51.566	216.78	8.225525449
20	150	10	0.05	8	33.74144761	57.549	218.29	6.066605012
20	150	10	0.05	9	37.21423427	64.435	219.41	4.709099261
20	150	10	0.05	10	39.99319024	72.278	220.37	3.706572248
20	150	20	0.02	5	46.66551777	84.041	221.81	2.329135442
20	150	20	0.02	6	49.72190571	109.07	223.87	1.693824077
20	150	20	0.02	7	51.90503627	140.81	225.56	1.360793126
20	150	20	0.02	8	53.54238258	179.82	251.46	0.973814219
20	150	20	0.02	9	54.81587916	226.97	290.11	0.689456696
20	150	20	0.02	10	55.83467514	282.86	330.45	0.503904433
20	150	20	0.03	5	37.49636684	54.729	217.74	4.499620962
20	150	20	0.03	6	42.08094552	64.804	219.64	3.003371975
20	150	20	0.03	7	45.35563815	77.019	221.09	2.48293127
20	150	20	0.03	8	47.81166084	91.708	222.52	2.055812491
20	150	20	0.03	9	49.72190571	109.07	223.87	1.693824077
20	150	20	0.03	10	51.25009646	129.45	225.06	1.371609886
20	150	20	0.04	5	28.32707444	44.771	212.58	8.122492122
20	150	20	0.04	6	34.44235815	50.454	216.37	5.400600172
20	150	20	0.04	7	38.80624646	57.082	218.36	3.594580786
20	150	20	0.04	8	42.08094552	64.804	219.64	3.003371975
20	150	20	0.04	9	44.62793225	73.764	220.75	2.639775441
20	150	20	0.04	10	46.66551777	84.041	221.81	2.329135442
20	150	20	0.05	5	19.15736406	39.766	204.2	23.31519165
20	150	20	0.05	6	26.79664592	43.728	211.41	13.20332018
20	150	20	0.05	7	32.25603169	48.081	215.18	7.594955016
20	150	20	0.05	8	36.35022378	52.973	217.28	5.586040173
20	150	20	0.05	9	39.53395879	58.523	218.62	4.331602734
20	150	20	0.05	10	42.08094552	64.804	219.64	3.40845648
20	150	30	0.02	5	47.20127707	70.324	221.91	2.260177152
20	150	30	0.02	6	50.16836643	87.613	223.03	1.650609745
20	150	30	0.02	7	52.28772056	109.13	224.26	1.32875791
20	150	30	0.02	8	53.87723134	135.32	225.29	1.055228702
20	150	30	0.02	9	55.11352179	166.63	254.21	0.763871929
20	150	30	0.02	10	56.10255157	203.49	286.89	0.56348455
20	150	30	0.03	5	38.30000257	49.62	220.22	4.319175784
20	150	30	0.03	6	42.75063661	56.777	220.98	2.898084724
20	150	30	0.03	7	45.92966459	65.41	221.57	2.40528381
20	150	30	0.03	8	48.31393719	75.634	222.24	1.998360383

20	150	30	0.03	9	50.16836643	87.613	223.03	1.650609745
20	150	30	0.03	10	51.65191111	101.46	223.86	1.338738982
20	150	30	0.04	5	29.40094655	42.595	217.83	7.695511615
20	150	30	0.04	6	35.32974947	46.561	219.58	5.166420824
20	150	30	0.04	7	39.57161505	51.277	220.46	3.456487726
20	150	30	0.04	8	42.75063661	56.777	220.98	2.898084724
20	150	30	0.04	9	45.2232175	63.107	221.42	2.555020199
20	150	30	0.04	10	47.20127707	70.324	221.91	2.260177152
20	150	30	0.05	5	20.49488142	39.336	214.33	21.56528745
20	150	30	0.05	6	27.91553063	41.888	217.31	12.4701724
20	150	30	0.05	7	33.21415711	44.889	219.02	7.244139792
20	150	30	0.05	8	37.18734246	48.356	219.99	5.356293366
20	150	30	0.05	9	40.27806214	52.313	220.58	4.167886317
20	150	30	0.05	10	42.75063661	56.777	220.98	3.288968446
20	150	40	0.02	5	46.62707701	46.67	196.67	2.632772032
20	150	40	0.02	6	49.68986959	55.498	205.37	1.85055802
20	150	40	0.02	7	51.87757858	65.148	210.1	1.464210943
20	150	40	0.02	8	53.51835871	76.395	214.01	1.146796776
20	150	40	0.02	9	54.7945239	89.601	217.54	0.921522783
20	150	40	0.02	10	55.81544833	104.74	220.37	0.757315719
20	150	40	0.03	5	37.43869926	32.919	162.54	6.041286086
20	150	40	0.03	6	42.03289135	38.306	180.07	3.671594429
20	150	40	0.03	7	45.31445162	44.026	193.14	2.848636787
20	150	40	0.03	8	47.77562503	49.701	200.89	2.282284289
20	150	40	0.03	9	49.68986959	55.498	205.37	1.85055802
20	150	40	0.03	10	51.22126267	61.773	208.65	1.482811822
20	150	40	0.04	5	28.24990997	25.642	125.7	13.76740003
20	150	40	0.04	6	34.37805443	30.196	150.78	7.767313599
20	150	40	0.04	7	38.75132466	34.631	169.82	4.632420827
20	150	40	0.04	8	42.03289135	38.306	180.07	3.671594429
20	150	40	0.04	9	44.58521529	42.567	190.26	3.069698427
20	150	40	0.04	10	46.62707701	46.67	196.67	2.632772032
20	150	40	0.05	5	19.06090848	22.32	98.127	48.62747438
20	150	40	0.05	6	26.71948145	26.697	127.12	22.00747945
20	150	40	0.05	7	32.1852976	29.926	144.51	11.33456131
20	150	40	0.05	8	36.29015767	34.528	167.09	7.280292965
20	150	40	0.05	9	39.48056099	37.262	174.6	5.435878957
20	150	40	0.05	10	42.03289135	39.306	180.07	4.166806485
20	150	50	0.02	5	44.63176475	34.466	182.62	3.143765296
20	150	50	0.02	6	48.02711045	38.23	194.84	2.162761691
20	150	50	0.02	7	50.45235737	41.828	201.58	1.692112914
20	150	50	0.02	8	52.27129096	45.701	206.36	1.318688113
20	150	50	0.02	9	53.6860178	49.793	209.36	1.061692065
20	150	50	0.02	10	54.81779541	54.258	211.65	0.874295515

20	150	50	0.03	5	34.44878852	26.824	139.34	7.813775546
20	150	50	0.03	6	39.53874942	30.279	161.85	4.529293283
20	150	50	0.03	7	43.1766166	33.185	177.19	3.442842676
20	150	50	0.03	8	45.90501698	35.736	187.35	2.713447619
20	150	50	0.03	9	48.02711045	38.23	194.84	2.162761691
20	150	50	0.03	10	49.72478008	40.654	199.91	1.71599884
20	150	50	0.04	5	24.256649	21.801	101.24	18.95318288
20	150	50	0.04	6	31.05355214	24.991	126.02	10.30438754
20	150	50	0.04	7	35.90088225	27.803	146.15	5.968223833
20	150	50	0.04	8	39.53874942	30.279	161.85	4.529293283
20	150	50	0.04	9	42.3682031	32.449	173.56	3.73113225
20	150	50	0.04	10	44.63176475	34.466	182.62	3.143765296
20	150	50	0.05	5	14.07093986	19.27	78.729	67.20205911
20	150	50	0.05	6	22.55903081	22.345	99.477	31.18233191
20	150	50	0.05	7	28.62287155	25.189	121.4	14.95997991
20	150	50	0.05	8	33.17557488	27.69	139.61	9.661173206
20	150	50	0.05	9	36.70929575	29.926	154.55	6.809137242
20	150	50	0.05	10	39.53874942	31.279	161.85	5.140188818
20	300	10	0.02	5	24.9897114	33.444	133.77	4.213790037
20	300	10	0.02	6	31.6580071	44.632	154.49	8.882266686
20	300	10	0.02	7	36.4202441	58.915	176.68	16.11997673
20	300	10	0.02	8	39.99369824	74.194	211.37	46.2315815
20	300	10	0.02	9	42.77215263	98.218	252.53	2.67805555
20	300	10	0.02	10	44.99537013	123.98	297.25	5.778732354
20	300	10	0.03	5	4.97839395	20.616	120.35	10.77730266
20	300	10	0.03	6	14.98405268	22.32	124.55	26.21849938
20	300	10	0.03	7	22.12819589	26.327	128.88	1.895494617
20	300	10	0.03	8	27.48469571	31.998	136.44	4.647335472
20	300	10	0.03	9	31.6580071	40.632	154.49	7.08354711
20	300	10	0.03	10	34.98893976	46.053	168.16	15.05004563
20	300	10	0.04	5	-15.0329235	16.421	116.87	1.264030137
20	300	10	0.04	6	-1.689901744	18.787	118.3	3.65819283
20	300	10	0.04	7	7.833479088	19.662	120.9	5.778732354
20	300	10	0.04	8	14.98405268	22.32	124.55	11.03933985
20	300	10	0.04	9	20.53989403	25.457	127.33	0.864196429
20	300	10	0.04	10	24.9897114	33.444	133.77	2.67805555
20	300	10	0.05	5	-35.03781059	14.429	112.36	4.993358073
20	300	10	0.05	6	-18.36385617	15.992	116.16	8.536920341
20	300	10	0.05	7	-6.454807346	17.789	118.48	0.611206304
20	300	10	0.05	8	2.476979268	19.858	119.96	2.002912494
20	300	10	0.05	9	9.421780956	21.51	121.03	4.213790037
20	300	10	0.05	10	14.98405268	22.32	124.55	6.558147943
20	300	20	0.02	5	28.32707444	28.963	129.93	3.976183579
20	300	20	0.02	6	34.44235815	37.628	143.67	2.639356833

20	300	20	0.02	7	38.80624646	48.628	161.12	1.90504281
20	300	20	0.02	8	42.08099696	62.152	184.1	1.330121257
20	300	20	0.02	9	44.62793225	78.534	217.24	0.920724923
20	300	20	0.02	10	46.66551777	98.012	251.62	0.661772593
20	300	20	0.03	5	9.987653686	18.854	119.3	8.212468301
20	300	20	0.03	6	19.15736406	22.01	123.18	5.355257513
20	300	20	0.03	7	25.70991306	24.535	126.41	4.342625382
20	300	20	0.03	8	30.61628685	31.615	128.28	3.566100682
20	300	20	0.03	9	34.44235815	37.628	143.67	2.639356833
20	300	20	0.03	10	37.49678481	44.688	156.03	1.978430564
20	300	20	0.04	5	-8.351767066	15.418	114.37	15.09731027
20	300	20	0.04	6	3.87880035	17.382	117.91	9.9103372
20	300	20	0.04	7	12.61124543	19.301	119.91	6.545848224
20	300	20	0.04	8	19.15736406	22.01	123.18	5.355257513
20	300	20	0.04	9	24.25021863	25.41	125.41	4.646602571
20	300	20	0.04	10	28.32707444	28.963	129.93	3.976183579
20	300	20	0.05	5	-26.68475745	13.67	107.58	44.25508584
20	300	20	0.05	6	-11.40619373	15.056	113.36	24.62344672
20	300	20	0.05	7	-0.487422192	16.564	116.76	13.99693748
20	300	20	0.05	8	7.698441278	18.25	118.82	10.21490329
20	300	20	0.05	9	14.06450949	20.159	120.19	7.87898319
20	300	20	0.05	10	19.15736406	22.01	123.18	6.077556269
20	300	30	0.02	5	29.40094655	24.23	122.68	4.088326637
20	300	30	0.02	6	35.32974947	30.277	127.4	2.889603543
20	300	30	0.02	7	39.57161505	37.838	149.41	1.994426403
20	300	30	0.02	8	42.75063661	47.07	166.14	1.430916542
20	300	30	0.02	9	45.2232175	58.128	179.26	1.083252722
20	300	30	0.02	10	47.20127707	71.17	206.99	0.78099465
20	300	30	0.03	5	11.59524667	17.076	120.5	7.893517769
20	300	30	0.03	6	20.49488142	19.6	121.62	5.265735588
20	300	30	0.03	7	26.85451927	22.523	122.36	4.355497987
20	300	30	0.03	8	31.62585524	26.086	122.98	3.611283228
20	300	30	0.03	9	35.32974947	30.277	127.4	2.889603543
20	300	30	0.03	10	38.30000257	35.14	142.67	2.100582523
20	300	30	0.04	5	-6.204022841	14.652	117.77	14.2337887
20	300	30	0.04	6	5.660013375	16.025	119.66	9.480550598
20	300	30	0.04	7	14.14167395	17.645	120.84	6.30600202
20	300	30	0.04	8	20.49488142	19.6	121.62	5.265735588
20	300	30	0.04	9	25.43983744	21.725	122.19	4.629941668
20	300	30	0.04	10	29.40094655	24.23	122.68	4.088326637
20	300	30	0.05	5	-24.00972272	13.5	114.77	40.27261531
20	300	30	0.05	6	-9.174854674	14.405	117.28	23.10618318
20	300	30	0.05	7	1.422398272	15.448	119.01	13.33174941
20	300	30	0.05	8	9.37033798	16.642	120.2	9.803086337

20	300	30	0.05	9	15.54992541	18.001	121.02	7.596697767
20	300	30	0.05	10	20.49488142	19.6	121.62	5.975959934
20	300	40	0.02	5	28.24990997	17.161	105.35	4.914924306
20	300	40	0.02	6	34.37805443	20.714	112.14	3.389059217
20	300	40	0.02	7	38.75132466	24.696	115.59	2.661395614
20	300	40	0.02	8	42.03289778	29.414	125.64	1.953406384
20	300	40	0.02	9	44.58521529	35.015	142.3	1.408770669
20	300	40	0.02	10	46.62707701	41.497	155.88	1.070629106
20	300	40	0.03	5	9.871906991	11.91	81.156	12.09954459
20	300	40	0.03	6	19.06090848	13.912	93.019	7.107623268
20	300	40	0.03	7	25.62631823	16.114	102.63	5.360866307
20	300	40	0.03	8	30.54555275	18.366	108.66	4.219474424
20	300	40	0.03	9	34.37805443	20.714	112.14	3.389059217
20	300	40	0.03	10	37.43869926	23.296	114.57	2.70043368
20	300	40	0.04	5	-8.506095993	9.383	59.417	29.12570786
20	300	40	0.04	6	3.750192911	10.937	73.783	15.8729727
20	300	40	0.04	7	12.50192911	12.521	85.863	9.162010468
20	300	40	0.04	8	19.06090848	13.912	93.019	7.107623268
20	300	40	0.04	9	24.1666238	15.546	100.45	5.814244129
20	300	40	0.04	10	28.24990997	17.161	105.35	4.914924306
20	300	40	0.05	5	-26.8776686	7.8441	48.89	97.60008547
20	300	40	0.05	6	-11.56695303	9.2061	57.862	48.34936206
20	300	40	0.05	7	-0.628890375	10.253	67.578	24.23802798
20	300	40	0.05	8	7.576264211	11.721	80.761	15.06251968
20	300	40	0.05	9	13.95519317	12.665	85.916	11.04688842
20	300	40	0.05	10	19.06090848	13.912	93.019	8.066275103
20	300	50	0.02	5	24.256649	12.327	93.814	6.119709407
20	300	50	0.02	6	31.05355214	13.833	103.53	4.070245223
20	300	50	0.02	7	35.90088225	15.267	109.23	3.12273296
20	300	50	0.02	8	39.53874942	16.814	113.4	2.399686764
20	300	50	0.02	9	42.3682031	18.452	115.96	1.916832104
20	300	50	0.02	10	44.63176475	20.261	117.83	1.570437459
20	300	50	0.03	5	3.885230722	9.4479	64.763	16.81162832
20	300	50	0.03	6	14.07093986	10.701	78.987	9.280845175
20	300	50	0.03	7	21.35012089	11.82	89.757	6.796542818
20	300	50	0.03	8	26.80307629	12.833	97.485	5.21479624
20	300	50	0.03	9	31.05355214	13.833	103.53	4.070245223
20	300	50	0.03	10	34.44878852	14.802	107.8	3.182238666
20	300	50	0.04	5	-16.48618756	7.7476	43.669	43.94010017
20	300	50	0.04	6	-2.905242039	8.8131	57.022	22.77294584
20	300	50	0.04	7	6.798189207	9.7925	68.892	12.66120759
20	300	50	0.04	8	14.07093986	10.701	78.987	9.280845175
20	300	50	0.04	9	19.72966716	11.532	87.115	7.433568424
20	300	50	0.04	10	24.256649	12.327	93.814	6.119709407

20	300	50	0.05	5	-36.85760584	6.5686	37.146	142.4312419
20	300	50	0.05	6	-19.88142394	7.5453	42.259	73.40270312
20	300	50	0.05	7	-7.753742476	8.433	52.286	34.73475809
20	300	50	0.05	8	1.338803436	9.231	62.203	21.6837836
20	300	50	0.05	9	8.412212562	9.9707	70.934	14.83565231
20	300	50	0.05	10	14.07093986	10.701	78.987	10.53261372
20	450	10	0.02	5	4.97839395	20.788	148.54	3.794793949
20	450	10	0.02	6	14.98405268	28.063	180.7	2.289611522
20	450	10	0.02	7	22.12819589	37.321	203.38	1.701539918
20	450	10	0.02	8	27.48469571	48.791	217.71	1.264408408
20	450	10	0.02	9	31.6580071	62.729	225.93	0.965943099
20	450	10	0.02	10	34.98893976	79.384	230.06	0.789711701
20	450	10	0.03	5	-25.03215186	12.421	85.856	12.4508572
20	450	10	0.03	6	-10.03009414	15.255	108.47	6.635393331
20	450	10	0.03	7	0.689335871	18.758	135.87	4.408247557
20	450	10	0.03	8	8.727300787	23.006	160.29	3.113880028
20	450	10	0.03	9	14.98405268	28.063	180.7	2.289611522
20	450	10	0.03	10	19.98688204	34.001	196.84	1.522872027
20	450	10	0.04	5	-55.04912804	9.687	82.927	22.7180735
20	450	10	0.04	6	-35.03781059	11.228	84.92	15.01359992
20	450	10	0.04	7	-20.74952415	13.071	86.969	9.847196651
20	450	10	0.04	8	-10.03009414	15.255	108.47	6.635393331
20	450	10	0.04	9	-1.689901744	17.817	129.24	4.919562701
20	450	10	0.04	10	4.97839395	20.788	148.54	3.794793949
20	450	10	0.05	5	-85.05967385	8.3934	79.546	65.30284988
20	450	10	0.05	6	-60.05195741	9.4084	82.372	41.57244366
20	450	10	0.05	7	-42.1819538	10.578	84.23	29.19199339
20	450	10	0.05	8	-28.78748907	11.927	85.507	20.19870647
20	450	10	0.05	9	-18.36385617	13.481	91.277	12.61054232
20	450	10	0.05	10	-10.03009414	15.255	108.47	6.635393331
20	450	20	0.02	5	9.987653686	17.839	127.01	4.067597295
20	450	20	0.02	6	19.15736406	23.447	161.34	2.350293766
20	450	20	0.02	7	25.70991306	30.544	188.69	1.68091498
20	450	20	0.02	8	30.61628685	39.262	208.25	1.211504383
20	450	20	0.02	9	34.44235815	49.808	221.26	0.903996575
20	450	20	0.02	10	37.49636684	62.348	229.26	0.72631606
20	450	20	0.03	5	-17.52147744	11.292	84.966	11.53105323
20	450	20	0.03	6	-3.766911878	13.535	88.502	7.453623879
20	450	20	0.03	7	6.058696435	16.267	114.42	4.797686371
20	450	20	0.03	8	13.42790267	19.557	139.13	3.28799968
20	450	20	0.03	9	19.15736406	23.447	161.34	2.350293766
20	450	20	0.03	10	23.74221925	28.004	180.44	1.522608304
20	450	20	0.04	5	-45.0241782	9.0728	80.897	21.34417068
20	450	20	0.04	6	-26.68475745	10.339	83.763	13.95040602

20	450	20	0.04	7	-13.58608982	11.813	85.497	9.180587161
20	450	20	0.04	8	-3.766911878	13.535	88.502	7.453623879
20	450	20	0.04	9	3.87880035	15.537	108.02	5.394653106
20	450	20	0.04	10	9.987653686	17.839	127.01	4.067597295
20	450	20	0.05	5	-72.53330933	7.9549	75.774	62.8310784
20	450	20	0.05	6	-49.60903339	8.8399	80.104	39.1809722
20	450	20	0.05	7	-33.23730645	9.8106	82.805	27.21562035
20	450	20	0.05	8	-20.95529605	10.9	84.538	18.72481369
20	450	20	0.05	9	-11.40619373	12.135	85.752	12.3025492
20	450	20	0.05	10	-3.766911878	13.535	88.502	7.453623879
20	450	30	0.02	5	11.59524667	14.728	100.15	5.008047048
20	450	30	0.02	6	20.49488142	18.639	133.48	2.757982405
20	450	30	0.02	7	26.85451927	23.528	163.78	1.880083998
20	450	30	0.02	8	31.62585524	29.494	189.05	1.295617502
20	450	30	0.02	9	35.32974947	36.638	208.67	0.930578823
20	450	30	0.02	10	38.30000257	45.064	222.98	0.724989158
20	450	30	0.03	5	-15.11008797	10.105	85.564	11.11646126
20	450	30	0.03	6	-1.754205463	11.695	86.669	7.389248315
20	450	30	0.03	7	7.782036113	13.625	88.873	5.996632652
20	450	30	0.03	8	14.9326097	15.929	111.42	3.985959535
20	450	30	0.03	9	20.49488142	18.639	133.48	2.757982405
20	450	30	0.03	10	24.95112917	21.784	154.17	1.730073795
20	450	30	0.04	5	-41.80899223	8.5323	83.199	20.1482385
20	450	30	0.04	6	-24.00972272	9.4247	84.791	13.37928182
20	450	30	0.04	7	-11.29044704	10.473	85.886	8.872427219
20	450	30	0.04	8	-1.754205463	11.695	86.669	7.389248315
20	450	30	0.04	9	5.660013375	13.108	87.278	6.481960773
20	450	30	0.04	10	11.59524667	14.728	100.15	5.008047048
20	450	30	0.05	5	-68.51432687	7.7707	80.857	57.16373424
20	450	30	0.05	6	-46.26523998	8.3703	82.8	36.7995546
20	450	30	0.05	7	-30.36936056	9.0503	84.226	25.97599018
20	450	30	0.05	8	-18.447451	9.824	85.277	18.02108971
20	450	30	0.05	9	-9.174854674	10.702	86.062	11.90067025
20	450	30	0.05	10	-1.754205463	11.695	86.669	7.389248315
20	450	40	0.02	5	9.871906991	10.299	72.714	7.120874599
20	450	40	0.02	6	19.06090848	12.568	82.937	4.58238302
20	450	40	0.02	7	25.62631823	15.144	108.47	2.930626684
20	450	40	0.02	8	30.54555275	18.196	133.36	1.896094248
20	450	40	0.02	9	34.37805443	21.807	156.46	1.281273592
20	450	40	0.02	10	37.43869926	25.982	176.7	0.944480278
20	450	40	0.03	5	-17.68866711	7.0625	54.521	18.01050312
20	450	40	0.03	6	-3.908380061	8.2765	63.129	10.47290483
20	450	40	0.03	7	5.936519368	9.6337	70.503	7.803720538
20	450	40	0.03	8	13.31858635	11.058	75.423	6.078889608

20	450	40	0.03	9	19.06090848	12.568	82.937	4.58238302
20	450	40	0.03	10	23.65862441	14.238	99.968	2.754453954
20	450	40	0.04	5	-45.25567159	5.5724	39.824	43.45525773
20	450	40	0.04	6	-26.8776686	6.4815	49.394	23.71048193
20	450	40	0.04	7	-13.75327949	7.4169	57.822	13.60516248
20	450	40	0.04	8	-3.908380061	8.2765	63.129	10.47290483
20	450	40	0.04	9	3.750192911	9.2811	68.787	8.490569769
20	450	40	0.04	10	9.871906991	10.299	72.714	7.120874599
20	450	40	0.05	5	-72.82267606	4.6639	29.46	161.9710855
20	450	40	0.05	6	-49.85338752	5.4555	38.741	81.19589853
20	450	40	0.05	7	-33.44307835	6.0873	45.242	49.92390083
20	450	40	0.05	8	-21.13534647	6.9265	54.145	29.30128213
20	450	40	0.05	9	-11.56695303	7.5207	57.932	18.25140718
20	450	40	0.05	10	-3.908380061	8.2765	63.129	10.47290483
20	450	50	0.02	5	3.885230722	7.132	62.43	9.196130359
20	450	50	0.02	6	14.07093986	8.0722	70.315	5.992924525
20	450	50	0.02	7	21.35012089	8.9884	75.193	4.6874841
20	450	50	0.02	8	26.80307629	9.983	78.929	3.552188364
20	450	50	0.02	9	31.05355214	11.041	81.312	2.733616819
20	450	50	0.02	10	34.44878852	12.21	83.116	2.226342049
20	450	50	0.03	5	-26.6718967	5.4263	41.088	26.49852718
20	450	50	0.03	6	-11.39333299	6.1523	51.19	14.32049459
20	450	50	0.03	7	-0.480991821	6.8213	59.268	10.29286113
20	450	50	0.03	8	7.70487165	7.4454	65.352	7.778865397
20	450	50	0.03	9	14.07093986	8.0722	70.315	5.992924525
20	450	50	0.03	10	19.16379443	8.6894	73.953	4.128457366
20	450	50	0.04	5	-57.22902413	4.4495	26.921	71.27596428
20	450	50	0.04	6	-36.85760584	5.0602	35.791	36.28171657
20	450	50	0.04	7	-22.30567416	5.6229	43.96	19.84203624
20	450	50	0.04	8	-11.39333299	6.1523	51.19	14.32049459
20	450	50	0.04	9	-2.905242039	6.6485	57.247	11.31195195
20	450	50	0.04	10	3.885230722	7.132	62.43	9.196130359
20	450	50	0.05	5	-87.78615155	3.7686	18.157	291.3890462
20	450	50	0.05	6	-62.3218787	4.3314	25.283	137.9505367
20	450	50	0.05	7	-44.1303565	4.84	32.602	76.8162575
20	450	50	0.05	8	-30.49153763	5.2984	39.315	44.74389451
20	450	50	0.05	9	-19.88142394	5.7266	45.401	25.82239604
20	450	50	0.05	10	-11.39333299	6.1523	51.19	14.32049459

